UNIVERSITY OF SOUTHAMPTON

FACULTY OF ENGINEERING, SCIENCE AND MATHEMATICS

School of Chemistry

Absolute Stereochemistry: The merits of VCD and XRD

by

Helen Louise Turner

Thesis for the degree of Doctor of Philosophy

March 2006

UNIVERSITY OF SOUTHAMPTON

ABSTRACT

FACULTY OF ENGINEERING, SCIENCE AND MATHEMATICS

SCHOOL OF CHEMISTRY

Doctor of Philosophy

ABSOLUTE STEREOCHEMISTRY: THE MERITS OF VCD AND XRD

By Helen Louise Turner

The active ingredients in drugs are frequently chiral. The traditional method of absolute stereochemistry determination in the pharmaceutical industry is using single crystal XRD; however, there are some common problems that mean that the determination is not always successful. VCD spectroscopy is an alternative technique that overcomes many of the problems experienced with single crystal XRD, although it is not currently widely practised. The aims of this research are to make the use of VCD for absolute stereochemistry determination desirable within the pharmaceutical industry and to investigate the limits of single crystal XRD.

A reliable VCD sampling methodology was developed using the nujol mull technique and provided good quality VCD spectra. Development of a straightforward method for prediction of accurate VCD spectra, proved to be a much harder target to achieve. Using published prior information was shown to provide a quicker route to an accurate predicted VCD spectrum. However, rotation of the non-chiral groups of the molecule was shown to invert bands in the VCD spectra, which had generally only been thought to occur when the absolute stereochemistry inverted. This degree of added complexity may mean that using VCD for absolute stereochemistry determination within the pharmaceutical industry would only prove useful for a specific subset of chiral compounds.

Increasing the number of heavy atoms in the chiral compound improved the reliability of the absolute stereochemistry determination. Increasing the redundancy of the data collection improved the Flack parameter and lowered its associated esd, thus making the absolute stereochemistry determination more reliable. The data collection itself took several days, so may not prove practical for routine use. However, it does provide an alternative route for accurate absolute stereochemistry determination when no other techniques are available.

Table of Contents

Abbreviations

ADP – Anisotropic Displacement Parameter
API – Active Pharmaceutical Ingredient
DFT – Density Functional Theory
DS – Dual Source
DSC – Differential Scanning Calorimetry
ECD – Electronic Circular Dichroism
FDA – Food and Drug Authority
FT – Fourier Transform
FT-IR – Fourier Transform Infrared
FT-VCD – Fourier Transform Vibrational Circular Dichroism
HF – Hartree Fock
IR – Infrared
LCP – Left Circularly Polarised
NDA – New Drug Application
NMR – Nuclear Magnetic Resonance
PEM – Photoelastic Modulator
PXRD – Powder X-Ray Diffraction
RCP – Right Circularly Polarised
SS – Single Source
TGA – Thermo Gravimetric Analysis
UV - Ultraviolet
VCD – Vibrational Circular Dichroism
VOA – Vibrational Optical Activity
XRD – X-Ray Diffraction

Acknowledgements

I would like to begin by thanking my supervisors whose help and advice have made this PhD possible. Firstly, Dr Andrea Russell who has been enthusiastic and supportive over the past seven and half years; Prof Chris Frampton who (despite his elusiveness) has taught me a lot about single crystal XRD and introduced me to the delights of bitterballen; Dr Mike Claybourn who has supported throughout my work at AstraZeneca and finally Ron Roberts who has been ever helpful and who stood in to read my thesis at the last minute, thank you all. I would also like to thank the staff at the University of Southampton, AstraZeneca and Bruker AXS for always being friendly and approachable. Special thanks go to Vicky and Caroline from AZ, Anita, Bram, Dietrich and Martin from Bruker, and the crystallography group at Southampton, who were always great company at the conferences I attended.

I would like to thank Prof. Larry Nafie and Dr Tess Freedman for allowing me to visit their wonderful labs at Syracuse University, and for making the visit extremely enjoyable. I gained a lot of valuable experience and could not have wished for nicer hosts.

Thanks go to the Russell group (Abbe, Colin, Richard, Dave, Peter, Suzanne, Kate and Piotr), past and present, for making coming to work fun! Without Abbe and Fabrice I would have killed several computers; Colin has helped me to see the true horror of mornings (especially Monday) and who I'm glad to say has decided that blonde really wasn't his colour; Dave has shown me a new way of dancing that I doubt I would have otherwise experienced; Peter who has cooked many a great curry and whose unfaltering devotion to Oasis and Manchester Utd disturbs me slightly; and finally Suzanne who saved me from being the only girl in the group and made moving to Lymington much easier than I expected. Thank you all for your friendship and making the group what it is!

Thanks go to my family, who have been supportive throughout PhD and university career. Finally I shall be leaving the student life and entering into the real world that has got to be a relief. My friends from home have also been unfalteringly supportive, despite the complete geeky-ness of me doing a chemistry degree. Charlie, Emily, Sam, Laura and all the old gang have been

wonderful friends and without them I would never have made it here. Thank you my wonderful ladies!

A great big thank you goes to my wonderful housemates, James, Richard, Marz and Megan. They all deserve medals for putting up with me and have all been great fun to live with. Jim has been a constant friend, an excellent chef and the font of all 'spanky' TV knowledge since the dawn of my university career. Richard who was a joy and a challenge to live with and with whom I will always associate pate and bread and swimming hamster attempts. Marz has shown me more bugs than I ever dreamt existed and whose enthusiasm is infectious, and finally Megan, a wonderful pie cook and a wonderful friend.

Last but not least I would like to thank Henry, who has been constantly supportive and a complete angel when I've been hell to live with. Thank you for correcting my ever so dodgy grammar and for being the best boyfriend a girl could ever wish for. I promise to find a job soon and stop being a kept woman!!

"I smile because I have no idea what's going on."

Anon

Chapter 1 - Introduction

1.1 Chirality & Absolute Stereochemistry

A chiral molecule is one that is not superimposable on its mirror image: it has the property of rotating the plane of polarisation of plane-polarised monochromatic light that is passed through it. This phenomenon is called optical activity. The term "absolute stereochemistry" [1] applies to chiral molecules where the substituents are defined as having an absolute position within space, making the molecule a specific chiral enantiomer of the compound. The enantiomers of a chiral compound are thus non-superimposable mirror images, illustrated in figure 1.1 below.

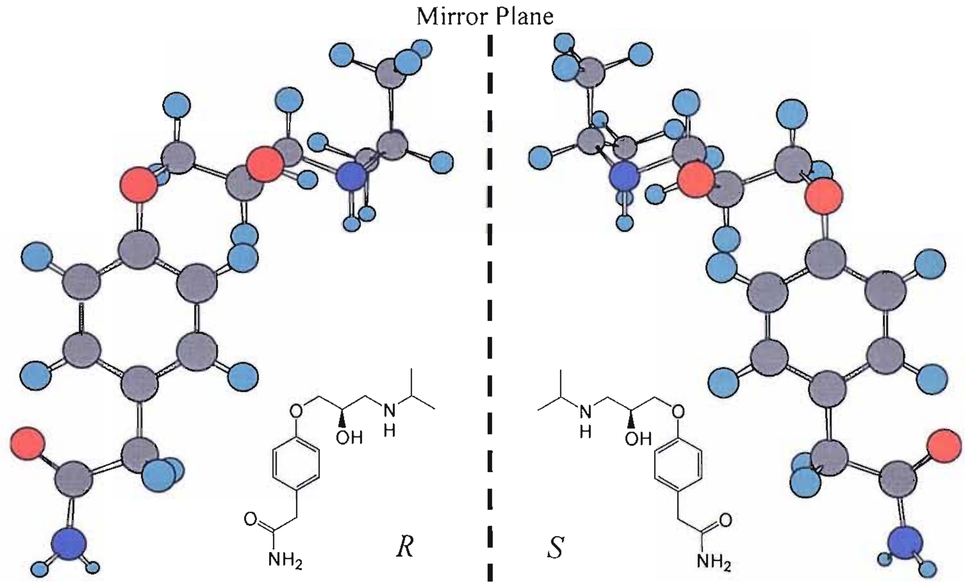

Figure 1.1. The two enantiomers of Atenolol, (*R*) & (*S*), are non-superimposable mirror images. The dashed line indicates a mirror plane

Cahn - Ingold - Prelog [2, 3] notation is used to define the arrangement of atoms within space around the chiral centre e.g. a carbon atom with four different groups around it. This gives the absolute configuration of the compound. There are two possible absolute configurations around any chiral centre, denoted either (*R*) or (*S*) in the Cahn - Ingold - Prelog notation.

To apply the correct (*R*) or (*S*) notation to the chiral centre under observation, the groups around it must first be prioritised. Priorities are decided initially on the higher mass having the higher priority, with the groups attached to these atoms being taken into consideration if two atoms are the same. The molecule is then rotated so as to have the group of lowest priority at the rear. A circle is then traced from the group of highest priority to the lowest. If the circle is moving clockwise its designation is (*R*), or if the circle is moving counter-clockwise its designation is (*S*). These define the absolute stereochemistry of the enantiomer. See figure 1.2 for an example.

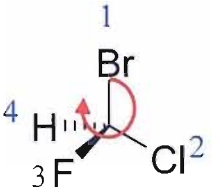

Figure 1.2. Illustration of the determination of stereogenic centre designation. Adjoining groups have been prioritised (labelled 1-4) and the circle moves clockwise, giving designation (*R*)

Enantiomers can also be labelled according to the direction in which they rotate the plane of polarisation of plane polarised light. Dextrorotatory or (+) if they give a positive optical rotation, levorotatory or (-) if they give a negative optical rotation. This nomenclature is known as the Fischer projections, or DL nomenclature, but as it does not give any information about the absolute structure of the chiral compound, the label is generally not important. An (*R*) or (*S*) enantiomer can be either (+) or (-).

When two or more chiral centres are present in a molecule, further complications can arise. Diastereoisomers are possible, which are non-enantiomeric isomers: i.e. (*R*, *R*) and (*S*, *S*) are enantiomers, but (*R*, *R*) and (*S*, *R*) are diastereoisomers. Diastereoisomers have different physical and chemical properties to each other and in relation to the enantiomers of the same compound.

A sample containing only one enantiomeric form of a chiral molecule is called enantiopure. A sample with equal amounts of each enantiomer is called a racemic mixture or racemate.

1.2 The Importance of Chirality in Pharmaceutical Applications

Chirality is a fundamental property of all living things; plants and animals naturally produce single enantiomers because living systems are inherently able to recognise and chose between mirror image forms.[4, 5] Many drugs are derived from natural substances, two examples are: morphine (figure 1.3) which is derived from the opium poppy and quinine (figure 1.4) which is obtained from the bark of the Cinchona tree. Natural products usually only occur as one enantiomer, and this natural chirality is often carried through to the active pharmaceutical ingredient (API) in drugs.

Figure 1.3. The structure of Morphine and its origins in nature, the opium poppy

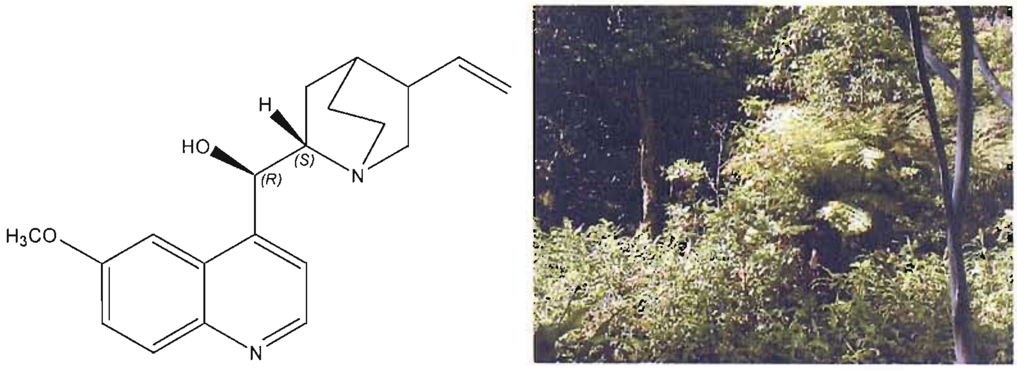

Figure 1.4. The structure of Quinine and its origins in nature, the bark of the Cinchona tree

Accurate determination of the absolute stereochemistry of chiral compounds is essential within the pharmaceutical industry; it enables comparison of the functionality, activity and safety of the different enantiomers of the API. Regulatory submission of an API to the Food & Drug Authority (FDA) requires the absolute stereochemistry to have been proven and also confirms the stereo control of the production process.

Approximately half of all drugs are chiral, with the importance of chirality first being realised within the pharmaceutical industry in the early 1960s in relation to the case of thalidomide.[6] Thalidomide was developed as a racemate: it was awaiting approval in the United States whilst prescribed to pregnant mothers as an anti-nausea drug for relief of morning sickness in Europe. During the US approval process it was discovered that the drug caused birth defects, when prescribed to pregnant women. The (*R*) enantiomer, figure 1.5, produced the desired therapeutic effect; however the (*S*) enantiomer caused birth defects because of its powerful angiogenesis-blocking effects. Studies now conclude that both enantiomers of thalidomide are unstable and spontaneously change form, but because of its powerful anti-angiogenesis activity its use was approved as a treatment for leprosy complications.[7]

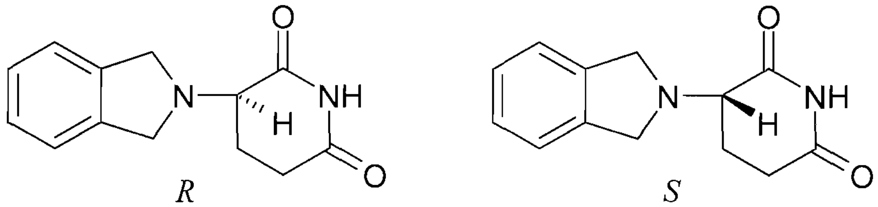

Figure 1.5. Thalidomide, the (*R*) and (*S*) enantiomers

Due to this tragic mistake, the guidelines for regulatory submissions were drastically altered and the single crystal X-ray diffraction (XRD) structure is currently required in order to prove the absolute stereochemistry of the submitted drug. Full pharmacological and toxicity profiles are also now required for New Drug Applications (NDA).

It is important to understand that a racemate or non-racemate is not a simple and predictable combination of the individual enantiomers with respect to pharmacodynamics and pharmacokinetics.[5] The simplistic idea that one enantiomer may be "good" and the other enantiomer may be "bad" or "inactive" does not exist. In reality the two enantiomers can influence, interact, and interfere with each other's activity and metabolism in subtle, unexpected ways. Rigorous preclinical and clinical study is essential to sort out the material therapeutic effects and so decide which compound to submit for approval.

Three distinct categories of the enantiomers of chiral compounds have now been classified for the purposes of drug regulation:[4]

- Both enantiomers have similar desirable properties, that are either identical or differ in the magnitude of the effect.
- One enantiomer is pharmacologically active, the other enantiomer is inactive.
- Each enantiomer has completely different pharmacological activity.

Enantiomers can differ considerably in potency, pharmacological activity and pharmacokinetic profile, since the molecules with which they interact in biological systems are also chiral. In fact the stereoisomeric discrimination within biological systems is remarkable: it is responsible for the differences in physiological responses to the individual enantiomers of a given substrate, and to the racemate as compared with the corresponding pure enantiomers. The degree of stereoselectivity of the drug increases with the number of interaction points of the drug with the active site. Consideration of the stereoselective properties of the enantiomers of chiral drugs may therefore suggest therapeutic advantages over the use of racemates.

A racemic drug can be considered as two separate drugs being given at the same time: each has potentially different pharmacodynamics and pharmacokinetics, and each influences the interactions and behaviour of the other. A racemate can be considered as containing up to 50% impurity, a situation that would usually be considered undesirable.[8] The reality of stereoisomers and their effects is not predictable by current technology: racemates are more than the sum of their halves, and enantiomers are more than one half of a racemate. Other considerations include the interaction with chiral pharmaceutical excipients. An excipient is a "filling" agent in a medication, which stabilises the active pharmaceutical ingredient, ensuring that it remains in its active form. Excipients may interact preferentially with one of the enantiomers. The dissolution rate of the individual enantiomers, from a formulation containing a racemate and a chiral excipient, may also differ considerably.

Development of a single enantiomer should be considered when both enantiomers are pharmacologically active but differ significantly in potency, specificity or maximum effect. So the decision to develop a stereochemically pure compound must be based on pharmacodynamic, safety, pharmacokinetic and pharmaceutical considerations, whilst preclinical development of racemic drugs should explore the pharmacological characteristics of each isomer separately, as well as together. In developing a single enantiomer from a racemic drug, development of a combination (non-racemate or fixed proportion) of the two enantiomers might be reasonable.[5]

Single enantiomers present challenging research and development problems and can offer significant scientific innovation with respect to the treatment of diseases. Applications for enantiomeric and racemic drug substances should include a stereochemically specific identity test and/or a stereochemically selective assay method. Chemical information is also required to assure the identity, quality, purity and strength of the drug substance.

Recent regulations from the FDA [4, 5, 9] have stressed that chiral pharmaceuticals must be tested in an optically pure form, or, if the racemate is to be marketed, both enantiomers and the racemate must be tested separately. In order to ensure that small amounts of the undesired enantiomer are not present in the final product, new methods for the routine measurement of enantiomeric purity and absolute configuration are necessary. Enantiopurity is typically determined by separation of enantiomers with column chromatography and absolute configuration from single crystal XRD. A chiral column can require a great deal of time and development, and if single crystals cannot be obtained an impasse is reached.

Medical treatment with drugs has always involved a risk-benefit analysis of the curative properties of a drug compared to its short- and long-term side effects. One drive for the pharmaceutical industry towards stereochemically pure drugs is the additional exclusivity gained (from three to five years) when a currently marketed racemic drug is switched to an enantiopure compound.

1.3 Determination of Absolute Stereochemistry

Conventional analytical techniques, such as infrared (IR) spectroscopy (figure 1.6), nuclear magnetic resonance (NMR) spectroscopy (except in the use of chiral Shift reagents), mass spectroscopy, and differential scanning calorimetry (DSC) are unable to detect the differences between the enantiomers of a chiral compound and so cannot be used to determine the absolute stereochemistry. This same is true for powder X-ray diffraction (PXRD), as the enantiomers of a chiral compound have identical unit cell parameters and space groups and differ only in the fractional co-ordinates of the atoms within space. Hence the 2θ values for each enantiomer are the same and the powder diffraction patterns measured are identical.

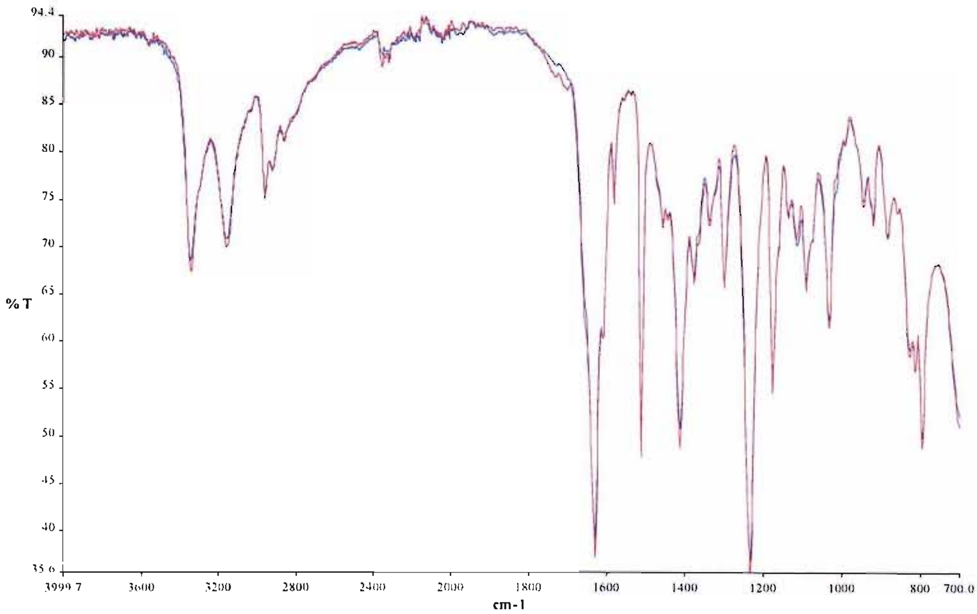

Figure 1.6. The infrared spectra of (*R*)-Atenolol (red line) and (*S*)-Atenolol (blue line), appear identical

The current preferred methodology for absolute stereochemistry determination is single crystal X-ray diffraction,[10, 11] using anomalous dispersion techniques and the Flack parameter.[12-14] The Flack parameter is a measure of the likelihood of the enantiomer modelled in the XRD collection being the correct enantiomer and gives an indication of the confidence of the absolute stereochemistry determination (it is described in more detail in chapter 2, section 2.1.3). Use of the Flack parameter has drawbacks when the compound under investigation contains only light atoms, such as oxygen, nitrogen and carbon or when the crystals produced are of poor quality, i.e. they may be too small, contain disorder, or may be twinned. The loss of information when studying compounds containing solely light atoms can be partially compensated for by the use of longer wavelength radiation, i.e. Copper instead of Molybdenum, in conjunction with a very large data collection (i.e. many reflections over a large 2θ range). Pharmaceuticals often contain only light atoms and can also prove very difficult to re-crystallise to a high enough quality, for example in the case of Atenolol (figure 1.7).

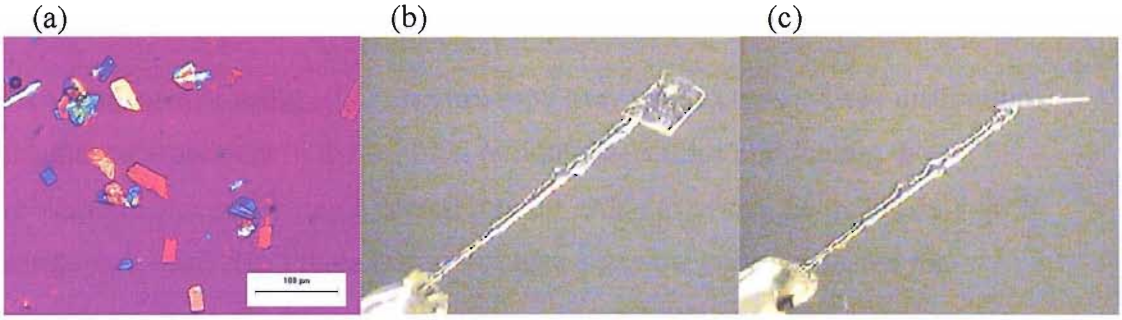

Figure 1.7. (a) Crystals of Atenolol under a polarising microscope, colours indicate stress and strain in the crystals; (b) & (c) front and side views of a crystal of Atenolol. Thin and plate-like crystals, such as those shown, cause problems when using single crystal XRD for absolute stereochemistry determination

Due to these difficulties a new technique is necessary to support XRD data when the results are not completely reliable, and also to determine the absolute stereochemistry when XRD fails to do so, either due to the problem of light atoms or the lack of crystallinity in the sample. One possible technique is vibrational circular dichroism (VCD) spectroscopy.

1.4 Vibrational Circular Dichroism

Vibrational circular dichroism spectroscopy [15, 16] is a relatively new technique in its application to absolute stereochemistry determination. For small chiral pharmaceutical compounds it is ideal,[17] as measurements can be carried out on both solution and liquid phases, and the atomic weight of the compound has no impact on signal strength. Hence typical pharmaceuticals that contain only light atoms such as carbon, nitrogen and oxygen can be measured as easily as compounds containing heavier atoms. The technique derives from the optical activity of the chiral compounds, and indeed can only be applied to chiral compounds. The different enantiomers of a chiral compound will interact in different ways when they encounter either left- or right-handed circularly polarised radiation. By measuring the differential interaction of each enantiomer with left- and right-handed circularly polarised light we can observe differences in the spectrum obtained, and through use of this technique in the infrared region of the spectrum we also gain valuable structural information. A detailed description of the VCD technique is given in chapter 2, section 2.2.

The advantages of using VCD spectroscopy over single crystal X-ray diffraction includes measurement in the solution or liquid state, thus eliminating the problematic process of single crystal growth. Also for a sample that is only 90 % enantiopure, with XRD there is a 10 % chance that the crystal selected for diffraction will be the minority enantiomer. With VCD spectroscopy the signal observed is from the majority enantiomer and the minority enantiomer simply causes a reduction in the VCD signal strength observed. In fact VCD signal scales linearly and directly with the enantiomeric excess of a sample, making it a very convenient measure of enantiomeric excess.

One disadvantage of VCD spectroscopy is that in order to interpret the measured results, *ab initio* calculations must be performed to predict the VCD spectrum of one of the possible enantiomers of the chiral compound under study. These calculations are carried out using density functional theory (DFT) methods [18, 19] and can be time consuming if the molecule is large and has many possible conformers. However, methods have been devised to overcome these size constraints, such as use of the chiral fragments of the molecule to determine key marker bands.[20] In addition, the availability of calculation software along with computing power is increasing all the time.

1.5 Project Aims

The aim of this research project is to develop a usable, reliable methodology for absolute stereochemistry determination of small chiral pharmaceutical-type compounds via VCD spectroscopy. This requires both development of the practical measurements involved, and the prediction of VCD spectra through computational molecular modelling, necessary to determine which enantiomer is which. Although many results have been published within the research sector, the pharmaceutical industry has yet to take on the powerful possibilities of this technique, due to its perceived complexity. Collection of reliable experimental data and prediction of VCD spectra for easy use within the pharmaceutical industry are the main targets of this project. Details of the VCD results are found in chapters 3 and 4.

Within XRD the aims of this project were to examine the effect of data redundancy on the Flack parameter, i.e. does collecting more data than strictly necessary to solve the structure, lead to an improved Flack parameter and hence accurate determination of the absolute stereochemistry. This target is aimed at improving XRD absolute stereochemistry determinations of pharmaceutical-type compounds, i.e. those containing only light atoms, and has not been previously studied. Details of the XRD results are found in chapter 5.

1.6 References

1. *Stereochemistry.* 2002, http://www.chem.umd.edu/courses/chem233/Handouts&Topics/stereo.html.
2. R.S. Cahn and C. Ingold, *Specification of Configuration about Quadricovalent Asymmetric Atoms.* Journal of the Chemical Society, 1951: p. 612 - 622.
3. R.S. Cahn, C. Ingold, and V. Prelog, *Specification of Molecular Chirality.* Angewante Chemie International Edition, 1966. **5**(4): p. 385 - 415.
4. J. Tomaszewski and M.M. Rumore, *Stereoisomeric Drugs - FDA's Policy Statement and the Impact on Drug Development.* Drug Development and Industrial Pharmacy, 1994. **20**(2): p. 119-139.
5. M. Strong, *FDA policy and regulation of stereoisomers: Paradigm shift and the future of safer, more effective drugs.* Food and Drug Law Journal, 1999. **54**(3): p. 463-487.
6. CelgenePharmacueticals, *THALOMID® (thalidomide).* 2003, http://www.celgene.com/thalomid/.
7. FDA, *FDA Approves Thalidomide for Hansen's Disease Side Effect, Imposes Unprecidented Restrictions on Distribution*, in *FDA Talk Paper.* 1998.
8. M.R. Islam, J.G. Mahdi, and I.D. Bowen, *Pharmacological importance of stereochemical resolution of enantiomeric drugs.* Drug Safety, 1997. **17**(3): p. 149-165.
9. W.H. De Camp, *Chiral Drugs - The FDA Perspective on Manufacturing and Control.* Journal of Pharmaceutical and Biomedical Analysis, 1993. **11**(11-12): p. 1167-1172.
10. J.M. Bijvoet, A.F. Peerdeman, and J. Van Bommel, *Determination of the Absolute Configuration of Optically Active Compounds by means of X-rays.* Nature, 1951. **168**: p. 271 - 272.
11. W. Clegg, *Crystal Structure Determination.* 1998: Oxford Chemistry Primers.

12. H.D. Flack, *On Enantiomorph-Polarity Estimation.* Acta Cryst. A, 1983. **39**: p. 876-881.

13. H.D. Flack and G. Bernardinelli, *Absolute structure and absolute configuration.* Acta Crystallographica Section A, 1999. **55**: p. 908-915.

14. H.D. Flack and G. Bernardinelli, *Reporting and evaluating absolute-structure and absolute- configuration determinations.* Journal of Applied Crystallography, 2000. **33**: p. 1143-1148.

15. L.A. Nafie and T.B. Freedman, *Vibrational circular dichroism: An incisive tool for stereochemical applications.* Enantiomer, 1998. **3**(4-5): p. 283-297.

16. L. Nafie, T.A. Keiderling, and P.J. Stephens, *Vibrational Circular Dichroism.* Journal of the American Chemical Society, 1976. **98**: p. 2715 - 2723.

17. L.A. Nafie, T.B. Freedman, F.J. Long, and E. Lee, *Applications of vibrational optical activity to biological and pharmaceutical.* Biophysical Journal, 1998. **74**(2): p. A29-A29.

18. F.J. Devlin, C.A. Ashvar, J. Finley, P.J. Stephens, and M.J. Frisch, *Ab-Initio Calculation of Vibrational Absorption and Circular- Dichroism Spectra Using Density-Functional Theory.* Abstracts of Papers of the American Chemical Society, 1995. **209**: p. 160-PHYS.

19. F.J. Devlin, J.W. Finley, P.J. Stephens, and M.J. Frisch, *Ab-Initio Calculation of Vibrational Absorption and Circular- Dichroism Spectra Using Density-Functional Force-Fields - a Comparison of Local, Nonlocal, and Hybrid Density Functionals.* Journal of Physical Chemistry, 1995. **99**(46): p. 16883-16902.

20. T.B. Freedman, F.J. Long, M. Citra, and L.A. Nafie, *Hydrogen-stretching vibrational circular dichroism spectroscopy: Absolute configuration and solution conformation of selected pharmaceutical molecules.* Enantiomer, 1999. **4**(2): p. 103-119.

Chapter 2 - Technical Background

In chapter 1 the property of chirality was shown to be ever-present in nature, and thus an important factor in the activity and functionality of drugs often derived from natural products. As such determination of accurate absolute stereochemistry plays a fundamental role in the pharmaceutical industry. Three topics are discussed in this chapter: (1) single crystal x-ray diffraction, the predominant technique used for absolute stereochemistry determination within the pharmaceutical industry; (2) vibrational circular dichroism (VCD) spectroscopy, a complementary technique for absolute stereochemistry determination with great potential for development within the pharmaceutical industry; (3) *ab initio* quantum mechanical methods, a technique required for determination of absolute stereochemistries of chiral compounds using VCD.

2.1 Single Crystal X-ray Diffraction

X-ray crystallography can be used to determine the structure of a compound within a single crystal. X-ray crystallography is an extremely useful and well practiced technique within chemical and biological areas, both in research and industry. There are two principal methods within X-ray diffraction (XRD) powder and single crystal, and both have their relative advantages and disadvantages. Powder X-ray diffraction (PXRD) is simple to use and does not require single crystals, however it can not give any information on the 3D spatial arrangement of the atoms within the compound. In contrast, single crystal XRD can give the 3D arrangement of the atoms within space when used in conjunction with anomalous dispersion techniques [1] and the Flack parameter.[2-5]

X-rays are beams of electromagnetic radiation with a wavelength (λ) of ~ 1 Å (10^{-8} cm) and are emitted when electrons of high energy are incident upon a metal surface. Any metal will give a continuous band of varying wavelengths, known as white radiation, but within this band will be some very intense lines of specific wavelengths, known as the characteristic radiation for that metal. In X-ray crystallography the wavelengths most commonly used are Mo $K\alpha = 0.70930$ Å and Cu $K\alpha = 1.54056$ Å.

When a beam of X-rays irradiates an atom, the component electrons are caused to vibrate, and they become excited. As the electrons vibrate they become secondary emitters, with most of the X-radiation emitted having a wavelength equal to that of the incident radiation and occurring in all directions. If the spacing between the atoms is of the same order as the wavelength of the X-rays, as is true in crystals, diffraction effects will occur.

2.1.1 The Origins of X-ray Diffraction

The diffraction pattern (figure 2.1) that results when an X-ray beam is incident upon a single crystal corresponds to the pattern of the scattered waves. Experimentally the diffraction pattern is partially measurable, with the amplitudes obtainable from directly measured intensities, but with the relative phases of the scattered waves getting lost. For a known structure the diffraction pattern can be calculated giving both amplitudes and phases, as the diffraction pattern is the Fourier transform of the crystal structure. In turn the crystal structure is the Fourier transform of the diffraction pattern and can be expressed in terms of electron density distribution concentrated on atoms. The electron density distribution can not be measured by direct experiment, because the scattered X-rays can not be refracted by lenses to form an image, as is done with light in an optical microscope, and can not be obtained directly by calculation, because the required relative phases are unknown. A diffraction pattern (figure 2.1 (a)) consists of discrete spots with a range of intensities: the pattern has a definite geometry, and contains symmetry in the positions and intensities of the spots.

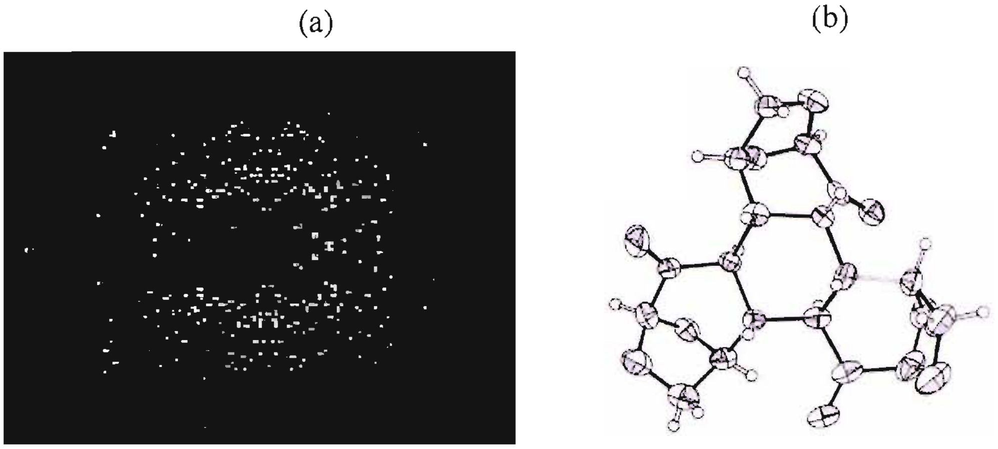

Figure 2.1 (a) An example of an x-ray diffraction pattern produced by a randomly oriented single crystal (b) Thermal ellipsoid plot of the final structure of an organic compound ($C_{18}H_{18}O_9$) determined using single crystal XRD.

All perfect crystals display translation symmetry in three dimensions: they display a regular pattern of an individual structural unit, in an identical form and orientation. This smallest repeating unit is called the unit cell; this can be further broken down to the unique asymmetric unit, if symmetry is present within the unit cell. It is the translation symmetry of crystalline materials that gives rise to X-ray diffraction. Any regularly spaced arrangement of objects can act as a diffraction grating for waves having a wavelength comparable to the repeat distance between the identical objects. Unit cell dimensions in crystals are comparable to the wavelength of X-rays, so the crystal structure acts as a three-dimensional diffraction grating.

Every crystal structure can be assigned to a specific space group, depending on the symmetry elements present in the solid state. The symmetry of the diffraction pattern is closely related to the symmetry of the structure producing it, which allows deduction of something about the space group from the observed pattern. Every diffraction pattern has inversion symmetry, whether or not the crystal structure is centrosymmetric; this is known as Friedels Law and is true in the absence of anomalous scattering. Friedels Law produces the condition that the reflections $F(hkl)$ and its opposite $F(-h-k-l)$ should have the same magnitude and opposite phases. These pairs of reflections are known as Friedel pairs. Enantiomers which are related by inversion of their fractional co-ordinates, x, y, z, to $-x, -y, -z$, will then give identical diffraction patterns with conventional XRD.

An X-ray diffraction pattern has a particular geometry that is related to the lattice and unit cell geometry of the crystal structure and so can tell us the repeat distances between molecules. The pattern also has a symmetry, which is closely related to the symmetry of the unit cell. Apart from the symmetry, there is no apparent relationship among the intensities of the individual diffracted beams, which vary widely. The intensities hold all the available information about the positions of atoms in the unit cell of the crystal structure. Determination of the full molecular structure involves the measurement of all the many individual intensities and these can only be measured when the directions of the diffracted beams (the diffraction pattern geometry) have first been established.

For diffraction by a single row of regularly spaced points (one dimensional, the dots in figure 2.2), in any particular direction, the radiation scattered by the row of points will have zero intensity by destructive interference of the individual scattered rays unless they are all in phase. The individual rays have different path lengths (except in the straight through direction) which must be whole numbers of wavelengths to keep the rays in phase.

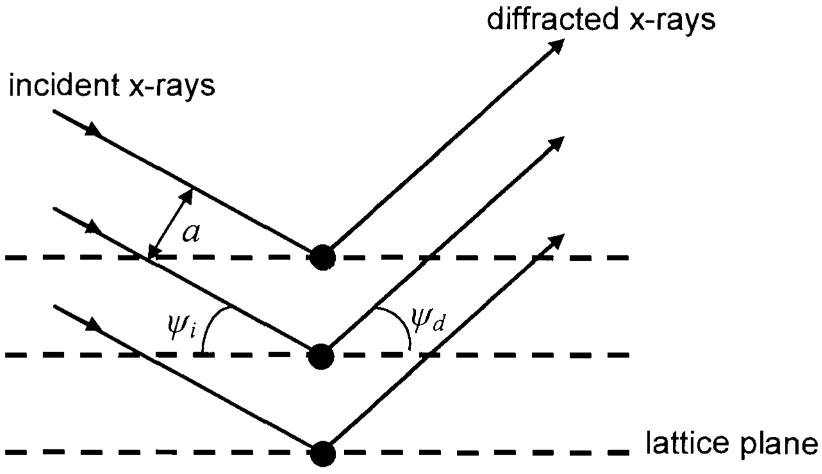

Figure 2.2 Diffraction in one-dimension, the first Laue condition

For rays scattered by two adjacent points in a row, where ψ_i and ψ_d are the angles of the incident and diffracted beams (as shown in figure 2.2) and, a is the one-dimensional lattice spacing. The path difference is then given by equation 2.1, with h being an integer, obtained from the Miller indices.

$$\text{path difference} = a\sin\psi_i + a\sin\psi_d = h\lambda \qquad [2.1]$$

For a given value of ψ_i (a fixed incident beam), each value of h corresponds to an observed diffraction maximum and the equation can be used to calculate the permitted values of ψ_d (i.e., the directions in which intensity is observed). For a significant diffraction effect, the spacing must be comparable to the wavelength. This is why X-rays are used for diffraction by crystals.

For diffraction by a three-dimensional lattice there are three such equations (such as equation 2.1), which all have to be satisfied simultaneously in order to observe a diffraction maximum. The first equation contains the lattice a spacing, angles relative to this a axis of the unit cell and the integer h. The other two equations, correspondingly, contain the unit cell axes b and c and the integers k and l respectively. Thus each allowed diffracted beam (spot seen in the diffraction pattern) can be labelled by three integers, h, k, l, which specifies its position if the unit cell geometry is known. These three equations are known as the Laue conditions.

An alternative, equivalent, description was described by Bragg.[6] He showed that every diffracted beam that can be produced by an appropriate orientation of a crystal in an X-ray beam can be regarded geometrically as if it were a reflection from sets of parallel planes passing through lattice points (figure 2.3). Analogous to the reflection of light by a mirror, the angle of incidence and reflection must be equal and the incoming and outgoing beams and the normal to the reflecting planes must themselves all lie in one plane. The reflection by adjacent planes in the set gives interference effects, equivalent to those of the Laue equations; to define a plane we need three integers to specify its orientation with respect to the three unit cell edges, the indices h, k, l and the spacing between successive planes is determined by the lattice geometry, and so is a function of the unit cell parameters.

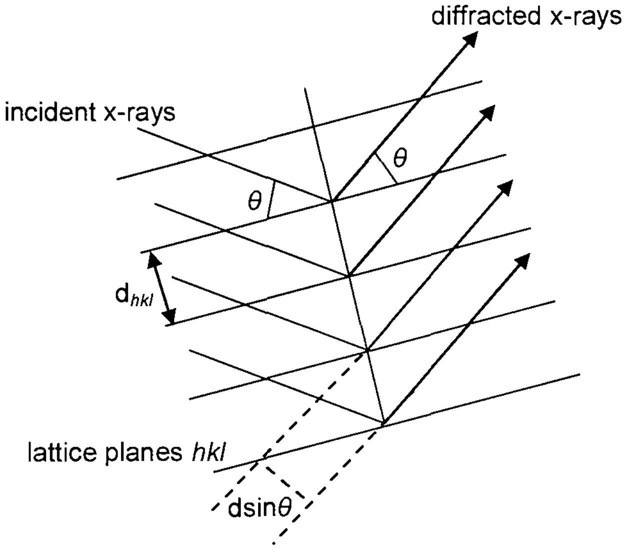

Figure 2.3 The Bragg conditions for diffraction by a three-dimensional crystal structure; one set of parallel lattice planes is seen edge-on

For rays reflected by two adjacent parallel planes,

$$\text{path difference} = 2d_{hkl}\sin\theta = n\lambda \qquad [2.2]$$

The value of n can always be set equal to one by considering planes with a smaller spacing: i.e., $n = 2$ for planes *hkl* is equivalent to $n = 1$ for planes *2h,2k,2l*, which have exactly half the spacing. It is in this form that the Bragg equation (equation 2.3) is always used.

$$\lambda = 2d_{hkl}\sin\theta \qquad \text{Braggs Law} \qquad [2.3]$$

The Bragg equation allows each observed diffracted beam (known as a 'reflection') to be uniquely labelled with its three indices and for its net scattering angle (2θ from the beam direction) to be calculated from the unit cell geometry, of which each d_{hkl} is a function.

2.1.2 Determination of Single Crystal X-ray Structure

The crystal structure and its XRD pattern are related to each other by Fourier transform. X-rays are scattered by the electrons in the crystal structure, and so it is possible to determine the electron density distribution as an average over time, and hence over the vibrations of the atoms. The electron density, $\rho(xyz)$, is a smoothly varying continuous function, with units of e Å^{-3}. However, it is easier to work by describing the structure in terms of the positions and displacements (vibrations) of discrete atoms, each with its own electron density distribution about its centre. Atoms are generally taken to be spherical in shape when stationary, and their individual contributions to X-ray scattering, known as atomic scattering factors, are calculated from electron densities derived from quantum mechanics. The X-ray scattering effects of atoms are modified by atomic displacements, which cause the at rest electron density to be spread over a larger volume, described by a set of anisotropic displacement parameters (adp) for each atom. Each symmetry independent atom in the asymmetric unit is described by the following parameters: a known atomic scattering factor (f), a set of displacement parameters (U values) and three co-ordinates (x, y, z) specifying its position.

The diffraction pattern is a set of discrete reflections, each a wave with its own amplitude and relative phase. The structure factor, F, shows how each reflection is related to the crystal structure (equation 2.4).

$$F(hkl) = \sum_{j=1}^{N} f_j \exp\left[2\pi i\left(hx_j + ky_j + lz_j\right)\right] \qquad [2.4]$$

Here f_j is the atomic scattering factor for the jth atom in the unit cell, with co-ordinates x_j, y_j, z_j. The integer's hkl are the indices for the particular reflection, occurring at a certain direction. Every part of the structure contributes to every reflection. $F(hkl)$ is a complex number, with an amplitude and a phase. The relative phases of the scattered waves depend upon the positions of the atoms relative to one other.

The structure factor equation (equation 2.4) can be used to calculate the expected diffraction pattern for any known structure. It is used at various stages during crystal structure determination, even when the known structure is incomplete, and is referred to as the set of calculated structure factors, $F_c(hkl)$ or F_c. From experiment, only the amplitudes of the reflections are obtained and not their relative phases: we have a set of observed structure factors, $|F_o|$, but with no observed phases the observed diffraction pattern is incomplete.

One important reflection that can not be measured is the $F(000)$, as it is not physically separable from the un-diffracted x-ray beam. By setting all indices to zero in the structure factor equation (equation 2.4), and noting that atomic displacement parameters have no effect at zero Bragg angle, the reflection $F(000)$ has an amplitude equal to the total number of electrons in one unit cell and has a phase of zero.

The Fourier transform of the diffraction pattern (equation 2.5), provides an expression which describes the crystal structure in terms of electron density $\rho(xyz)$. Where V is the unit cell volume.

$$\rho(xyz) = \frac{1}{V}\sum_{hkl} F(hkl)\exp[-2\pi i(hx + ky + lz)] \qquad [2.5]$$

This is the basis of all Fourier synthesis calculations in crystallography. It shows how, in principle, the electron density can be obtained from the diffraction pattern. The equation says that, in order to find the electron density at a particular point in the structure, we have to take all the individual scattered X-ray waves (reflections F) and add them together, allowing for their different relative phases. The phase differences vary with the position at which we are finding the electron density, because the waves will have different path lengths converging on that point, but the waves will also have different phases from their initial production in the diffraction process and these have to be included as well. As this physical process can not actually be carried out we emulate it via calculation with equation 2.5. However, this is not possible directly as we do not have the relative phase information for the reflections, although we have the structure factor amplitudes. Solving the crystal structure mostly involves recovering this lost phase information.

Equation 2.5 can be separated into its amplitude and phase (equation 2.6).

$$\rho(xyz)=\frac{1}{V}\sum_{hkl}|F(hkl)|\exp[i\phi(hkl)]\exp[-2\pi i(hx+ky+lz)] \qquad [2.6]$$

The measured amplitudes are $|F(hkl)|$, the unknown phases are $\exp[i\varphi(hkl)]$ and the values of $\exp[-2\pi i(hx+ky+lz)]$ are easily calculated. As the amplitudes are known but the phases unknown, it is not possible to carry out the Fourier synthesis directly: this is known as the phase problem.

There are two main ways for solving the phase problem. One is by direct methods,[7] which attempts to estimate approximate phases from relationships among the structure factors with no prior knowledge of the crystal structure itself. The second is the use of Patterson synthesis,[8] which can provide information on the approximate positions of some of the atoms in the structure. Patterson synthesis is most useful when there are a few heavy atoms amongst many light atoms. The amplitudes $|F_o|$ are replaced by their squares, $|F_o|^2$, and the unknown phases are set to zero. We then get equation 2.7, the result of which is no longer the desired electron density, but is closely related to it in a useful way.

$$P(uvw)=\frac{1}{V}\sum_{hkl}|F(hkl)|^2\cos[2\pi(hu+kv+lw)] \qquad [2.7]$$

The peaks in a Patterson map do not correspond to the positions of the individual atoms, but instead to the vectors between pairs of atoms in the structure, $P(uvw)$. A peak in the Patterson map at (u,v,w) means that there must be two atoms whose x co-ordinates differ by u, y co-ordinates differ by v, and z co-ordinates differ by w. The objective is to work out some atom co-ordinates by knowing only the differences between them.

Direct methods attempt to derive the structure factor phases by mathematical means from a single set of X-ray intensities. Structure factor amplitudes and phases are linked through knowledge of the electron density. If nothing was known about the electron density, then neither phases nor amplitudes could be calculated from the other. However, something is always known about the electron density, otherwise the correct answer would not be recognised when it was achieved. Constraints on the electron density impose corresponding constraints on the structure factors. The structure amplitudes are known, so most constraints restrict the values of structure factor phases and in favourable cases are sufficient to determine the phase values directly. Constraints on the electron density include that the correct electron density must always possess certain features like discrete atomic peaks, and can never possess features such as negative electron density.

Refinement of the resulting model is next undertaken, for a number of reasons: Firstly, to improve the calculated phases so that the computed electron density maps more closely represent the actual electron density. Secondly, to try to verify that the structure is 'correct': as there is no way of directly and unambiguously computing the structure from the data, there is the possibility that the proposed structure is 'wrong'. In order to assess the validation of the structure, comparisons are either made with the X-ray data alone or with known properties of structures. Thirdly, to obtain the 'best' values for the parameters in the model.

Following refinement, interpretation of the results begins, in order to try and detect patterns, common features, significant differences and variations. This involves checking of bond lengths, bond angles and torsion angles, placement of hydrogen atoms and H-bonding and modelling of thermal motion and geometrical corrections.

Once the final structure has been obtained we can check the reliability of the overall crystal structure through calculation of the *residual factor* or *R-factor* [9] (equation 2.8). If the atoms in the model structure are in approximately the right positions, there should be at least some degree of resemblance between the calculated diffraction pattern and the observed one: i.e., between the sets of $|F_c|$

and $|F_o|$ values. The value of the *R-factor* can give an idea of the goodness of fit between these values. An R value of < 10 generally indicates a correct model, < 8 indicates a good fit of the data and < 5 indicates a very good fit of the data.

$$R = \frac{\sum \left\| F_o \right| - \left| F_c \right\|}{\sum \left| F_o \right|} \qquad [2.8]$$

There are two main XRD techniques, PXRD and single crystal XRD. PXRD takes the diffraction pattern of a polycrystalline / powder sample, with randomly distributed crystallites. This ideally gives a random distribution of all possible *hkl* planes. Only the crystallites that have reflecting planes parallel to the surface of the sample will contribute to the reflected intensities. Hence, if the crystallites are completely randomly oriented, each possible reflection from the set of *hkl* planes will have an equal number of crystallites contributing to it. Thus changing the angle θ will produce all possible reflections. PXRD has the advantages of not needing a single crystal and having a quick collection time, with the disadvantage being that it cannot be used to distinguish between the enantiomers of a chiral compound. This is because for both sets of co-ordinates, x, y, z and $-x$, $-y$, $-z$, the same 2θ values are observed and hence the same diffraction pattern is observed for each enantiomer.

Single crystal XRD can be used to determine the absolute stereochemistry of a chiral compound using anomalous dispersion techniques. Bijvoet et al [1] first applied the anomalous scattering technique to establish the absolute configuration of (+)-tartaric acid in its sodium rubidium double salt (its absolute configuration was completely unknown at the time). When anomalous scattering occurs deviations from Friedels law are seen. Friedels law states that pairs of reflections $F(hkl)$ and $F(-h\text{-}k\text{-}l)$ should be equal.

Considering the mechanics of X-ray diffraction,[10, 11] an atom is driven to vibrate by an X-ray wave and then re-emits the radiation, which leads to a phase change between the driving wave and the scattered wave. If this phase change is the same for all atoms, then it has no influence on how the scattered waves reinforce one another to generate the net scattered wave and so can effectively be ignored. In reality however, this phase shift can differ for different atoms, owing to the effect known as anomalous scattering. Within the sample different amounts of phase change are generated between the driving X-ray and scattered waves and will depend upon the relative geometric positions. So the overall phase difference, influencing the amplitude of the scattered wave, will be slightly greater when one atom is in front compared to when the other atom is in front. Rotation of the sample through 180° to scatter from the opposite side of the same set of planes changes the atom which is in front and by comparing the scattered intensity, you can tell the sign of the difference between the atoms and thus the handedness of the crystal system.

2.1.3 Anomalous Scattering

Anomalous scattering [1] relies on the anomalous part of the X-ray scattering factor, f, which is atom sensitive and takes place in a crystal when an atom absorbs X-rays more strongly than is usual. This strong absorption is a result of the frequency of the incident radiation being similar to the natural absorption frequency of the atom. Hence a slight phase change occurs for the X-rays scattered by that atom relative to the rest of the atoms in the structure. Slight differences are then observed between the pairs of reflections $F(hkl)$ and $F(-h\text{-}k\text{-}l)$ (figure 2.4) and these differences are used to compute the absolute configuration.

In figure 2.4 the reflections Fn_{hkl} and Fn_{-h-k-l} are shown in the absence of anomalous scattering, with these reflections being opposite in sign but equal in magnitude (dark blue lines on the left) (they are represented as vectors with both a magnitude and direction to aid the illustration). However, in the presence of anomalous scattering changes to the magnitude of these reflections occur, due to the real and imaginary parts of the X-ray scattering factor, f' and f'', respectively. Hence the actual reflections observed in the presence of anomalous scattering are F_{hkl} and F_{-h-k-l} (orange and green lines on the left). If we now compare these reflections (right hand side of figure 2.4) the magnitudes are no longer equal in size (the F_{-h-k-l} reflection has been inverted for ease of comparison) and the differences can be measured and recorded during a single crystal X-ray diffraction collection.

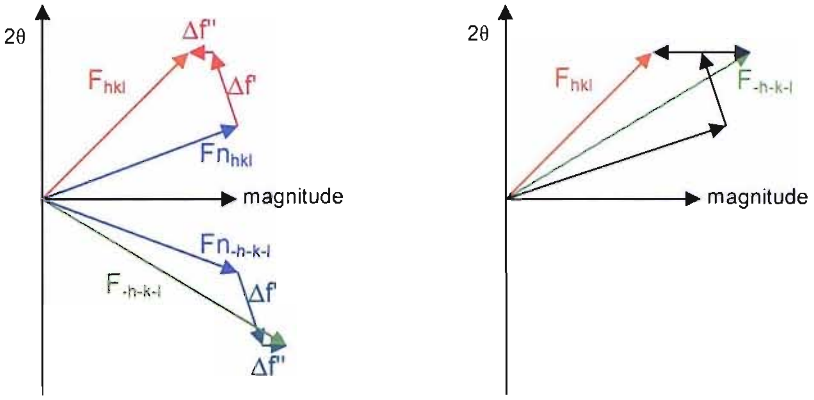

Figure 2.4 The reflections Fn_{hkl} and Fn_{-h-k-l} are shown in the absence of anomalous scattering. In the presence of anomalous scattering phase changes occur due to the real and imaginary parts of the X-ray scattering factor, where $\Delta f'$ = real part of the anomalous scattering and $\Delta f''$ = imaginary part of the anomalous scattering. These phase changes give rise to slight differences between the observed reflections F_{hkl} and F_{-h-k-l}.

The X-ray scattering factor, f, is defined as the ratio between the amplitude scattered by an atom and that scattered by a free classical electron when all other conditions remain unchanged. It is made up of three component parts (equation 2.9): f^0 is the Thomson scattering factor, which is the sole component in the absence of anomalous scattering, and f' and f'' are respectively the real and imaginary anomalous scattering correction terms, which are zero unless anomalous scattering occurs.

$$f = f^0 + f' + if'' \qquad [2.9]$$

The magnitudes of the anomalous scattering deviations that occur depend both on the wavelength of the incident radiation and on the type of atom that is anomalously scattering. Use of longer wavelength radiation or the presence of heavier atoms in the molecule makes the deviations between $F(hkl)$ and $F(-h-k-l)$ larger and thus easier to detect. The dependence on atom size is related to the component f'', the imaginary part of the scattering factor. Table 2.1 shows the dependence of f'' on both the atom size and the wavelength of the incident radiation.

Table 2.1 Effect of the change in atom size and wavelength on the real and imaginary parts of the anomalous scattering factor. Red indicates that the differences are almost impossible to detect, yellow indicates that the differences are difficult to detect and green indicates that the differences can be detected. The characteristic wavelengths for the different metals used in X-ray generation are also shown.

	Ag *Kα*		Mo *Kα*		Cu *Kα*		Cr *Kα*	
	Δf′	*Δf″*	*Δf′*	*Δf″*	*Δf′*	*Δf″*	*Δf′*	*Δf″*
B	0.000	0.000	0.000	0.001	0.008	0.004	0.018	0.009
C	0.000	0.001	0.002	0.002	0.017	0.009	0.035	0.021
N	0.001	0.002	0.004	0.003	0.029	0.018	0.059	0.042
O	0.003	0.004	0.008	0.006	0.047	0.032	0.090	0.073
F	0.006	0.006	0.014	0.010	0.069	0.053	0.129	0.119
P	0.055	0.058	0.090	0.095	0.283	0.434	0.377	0.900
S	0.068	0.076	0.110	0.124	0.319	0.557	0.364	1.142
Cl	0.084	0.099	0.132	0.159	0.348	0.702	0.335	1.423
Br	0.090	1.643	-0.374	2.456	-0.767	1.283	-0.198	2.563
I	-1.144	1.187	-0.726	1.182	-0.579	6.835	-5.852	12.850

Ag *Kα* = 0.55941 Å
Mo *Kα* = 0.70930 Å
Cu *Kα* = 1.54056 Å
Cr *Kα* = 2.28970 Å

In order to determine if the crystal we have modelled is the correct or incorrect enantiomer we use the Flack parameter,[2-5] $x(u)$, where u is the uncertainty in x. With the Flack parameter in the structure factor equation the value for x can show if the correct or incorrect enantiomer has been modelled (equation 2.10).

$$|F(hlkx)|^2 = (1-x)|F(hkl)|^2 + x|F(-h-k-l)|^2 \qquad [2.10]$$

For a correct model, x has a value of zero and for the inverted model x has a value of +1. The uncertainty (u) must have a value of < 0.04 for strong enantiopure distinguishing power; with (u) < 0.10, the structure is enantiopure and has sufficient distinguishing power. For values of $(u) > 0.10$ the absolute configuration can not be confidently assigned and further investigation is required, possibly with the use of longer wavelength X-rays or conducted at a lower temperature to minimise thermal vibration. Collection of high-angle data (i.e. large θ value) is of much more use in absolute stereochemistry determination studies: in general the scattering factor, f, falls off with sin θ/λ, but the components f' and f'' do not. Therefore high angle data contains proportionally more absolute structure data than that collected at lower angles.

The technique of single crystal XRD with anomalous scattering methods for the determination of absolute configuration of chiral compounds is a well established procedure and is required by the FDA (Food & Drug Administration) as part of the process of submitting a new drug for testing.[12-14] However, there are certain limitations which can be very difficult if not impossible to overcome. Firstly, a single crystal of sufficient size and quality is necessary to perform the experiment. Single crystals can prove difficult to grow, especially with pharmaceutical compounds, and often thin plate like crystals or long needle crystals are produced which are not of good enough quality to gain the data needed on the compound. Disorder and twinning may also be present in crystals that superficially appear ideal: collecting at low temperature can significantly reduce thermal disorder, and simple twins may be solvable. Secondly, not all chiral pharmaceutical compounds contain enough heavy atoms to enable detection of the anomalous scattering differences present from just the lower weight component atoms. It may be necessary to go to a longer wavelength, but when longer wavelength X-rays are used the absorption of the beam between the collimator and the sample increases, so that lower intensity radiation is present at the sample: for example, with Cr radiation it is necessary to position an evacuated glass tube between the collimator and the sample so that sufficient X-ray radiation reaches the sample. Thirdly if the sample is only 90 % enantiopure there is a 10 % chance that the crystal selected for the diffraction experiment may not be the predominant enantiomer.

Even if a reliable crystal structure (low *R-factor*) can be collected, the Flack parameter and its uncertainty may not necessarily give conclusive results. Thus, there is a real need for the development of additional techniques to support and confirm the XRD data. One such technique is vibrational circular dichroism, which gives complementary data on the absolute configuration of chiral compounds in solution and solid state.

2.2 Vibrational Circular Dichroism, VCD

Vibrational circular dichroism (VCD) is one of the primary forms of natural vibrational optical activity (VOA) [15] present in all chiral molecules. VCD has been a developing spectroscopic field since the early 1970s.[16, 17] VCD spectroscopy combines the stereochemical sensitivity of natural optical activity with the large amount of structural information obtainable from vibrational spectroscopy. It operates in the infrared region of the spectrum where vibrational transitions occur. All chiral molecules are optically active, and the enantiomers of a chiral compound give an opposite interaction when exposed to either left-handed or right-handed circularly polarised light. The differential interaction of an enantiomer with left- versus right-circularly polarised light is called circular dichroism, and when the infrared region of the spectrum is used the method is called VCD.

VCD is defined as the difference in the IR absorbance, ΔA, for left circularly polarised (LCP) radiation, A_L, versus that for right circularly polarised (RCP) radiation, A_R, given by equation 2.11, as a function of the wavenumber, $\tilde{\nu}$, of the incident radiation.

$$\Delta A(\tilde{\nu}) = A_L(\tilde{\nu}) - A_R(\tilde{\nu}) \qquad [2.11]$$

The effects of path length, l, and concentration, c, may be removed by use of the absorptivity, ε (equation 2.12).

$$\Delta\varepsilon(\tilde{\nu}) = \frac{\Delta A(\tilde{\nu})}{lc} = \varepsilon_L(\tilde{\nu}) - \varepsilon_R(\tilde{\nu}) \qquad [2.12]$$

The physical process associated with VCD is a simple one-photon quantum transition which is induced by both LCP and RCP radiation. VCD is the difference in absorption of LCP and RCP, if just one is present then only an IR spectrum is obtained. The transitions are between vibrational energy levels g_0 and g_1, for a fundamental transition of a normal mode of vibration in the ground electronic state (figure 2.5).

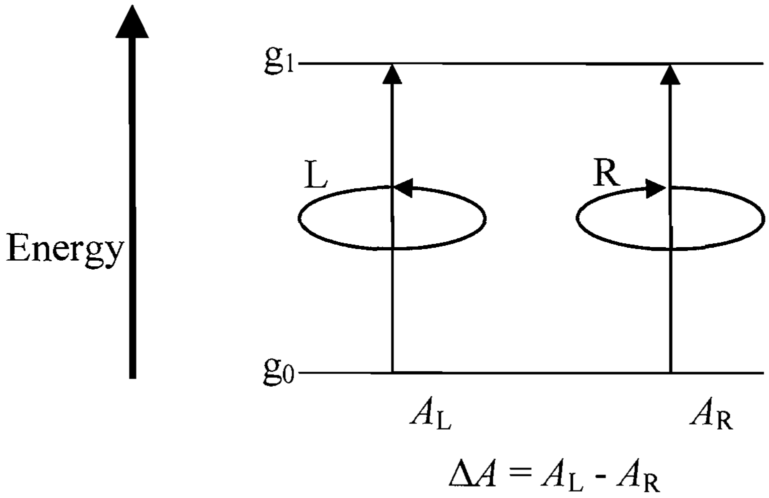

Figure 2.5 Energy-level polarization-state diagram for the measurement of VCD defined as the difference in absorbance (ΔA) for left (A_L) minus right (A_R) circularly polarised radiation for a vibrational transition from vibrational energy level g_0 to g_1.

The VCD spectrum of a chiral molecule is dependent upon the three-dimensional structure of the molecule.[18] Hence it is a sensitive function of a chiral molecule's absolute configuration and, in the case of flexible molecules, its conformation. This three-dimensional property of VCD spectra is due to the fact that VCD is sensitive to both the linear (electric-dipole) oscillation of charge and the circular (magnetic-dipole) oscillation of charge during vibrational motion. Traditional IR is only sensitive to the linear oscillation of charge during vibrational motion and hence is only a two-dimensional technique. Standard IR spectra consist of characteristic bands for each type of bond vibration. The position of such characteristic bands in the spectrum does not depend upon the orientation or position of the relevant bonds. However, the position of the band is affected by the interactions that the bond is involved in, such as hydrogen-bonding. VCD produces a characteristic band that may be positive or negative in sign, which depends on the type of bond vibration and its chiral conformation (i.e. its *x*, *y*, *z* position in space), as the chiral conformation of the bond can alter its interaction with the circularly polarised radiation.

The VCD signal is very small compared to standard IR intensities, approximately 10^{-4} of the absorbance. This can be rationalised if we compared electronic circular dichroism (ECD) and VCD; ECD is circular dichroism operating in the ultraviolet (UV) region of the spectrum and VCD is circular dichroism operating in the IR region. By comparing the ratio of the size of a typical molecule, 10 Å, to UV wavelength (for ECD) 1000 Å we get 10^{-2}, a good signal strength. Whereas in the IR 1000 $\text{cm}^{-1} \equiv 100000$ Å, giving a ratio of 10^{-4}, which is the VCD signal strength at its best. The degree of chirality of a site, i.e. how different the groups attached to the chiral centre are, can also lead to varying amounts of VCD intensity. If the groups appear to be very similar electronically, the VCD signal in this region may be weak, and so requires a longer collection time.

2.2.1 The Origins of VCD

VCD arises from simultaneous linear and angular oscillation of charge produced by vibrational motion. The angular oscillation of charge of the electrons results from the motion of the nuclei, which results in the need to consider the movement of both nuclei and electrons. Thus, the Born-Oppenheimer approximation can not be used to describe VCD spectra. For VCD to be observed, the electric and magnetic dipole transition moments for a given vibrational mode need to be non-zero and non-orthogonal to one another. Depending on the orientation of these two components, parallel or anti-parallel, positive or negative rotational strengths, respectively, are observed. For achiral molecules, the derivatives of the components for a given vibrational mode are either zero for magnetic or electric dipole moments, both zero, or orthogonal if both are non-zero. The non-zero dipole moment changes and the orientations of the two changing moments represent the selection rules for VCD active vibrational modes and the factors determining the sign of the VCD active vibrational mode respectively.

We have seen that the intensity for the absorption of IR radiation during vibrational excitation is expressed as absorbance, A, or absorptivity, ε, and that VCD intensity is expressed as differential absorbance, ΔA, or differential absorptivity, $\Delta\varepsilon$. A molecule with N atoms is known to have 3N-6 normal modes of vibration. Quantum mechanics tells us that a fundamental vibrational transition for a normal mode, a, corresponds to quantum excitation for a molecule in the ground electronic state and ground vibrational state, $\psi_0^a \equiv |0^a\rangle$, to the first excited vibrational state of a mode in the ground electronic state, $\psi_1^a \equiv |1^a\rangle$. So the absorption intensity of normal mode a is proportional to the dipole strength, D_{01}^a, the absolute square of the electric dipole transition moment, equation 2.13;

$$D_{01}^a = \left|\int \psi_0^{a*} . \hat{\mu} . \psi_1^a d\tau\right|^2 \equiv \left|\langle 0^a|\hat{\mu}|1^a\rangle\right|^2 \qquad [2.13]$$

Where the electric-dipole moment operator is $\hat{\mu} = \sum q_i \vec{r}_i$ for all charged particles in the molecule with charge q_i (Ze for a nucleus with atomic number Z and $-e$ for an electron) and position $\vec{r}$. Experimentally we obtain the dipole strength from the integrated area of the absorption band for mode a,

$$D_{01}^a = 9.184 \times 10^{-39} \int^{band} \frac{\varepsilon(\tilde{\nu})}{\tilde{\nu}} \approx \frac{9.2 \times 10^{-39}}{\tilde{\nu}_0 \int^{band} \varepsilon(\tilde{\nu}) d\tilde{\nu}} \qquad [2.14]$$

In practice the wavenumber frequency $\tilde{\nu}$ can be considered constant over the absorption band, replaced by the frequency $\tilde{\nu}_0$ at the band maximum and removed from the integration as shown in equation 2.15. If we assume a Lorentzian band shape with half-width, γ, at one-half the band maximum, ε_0, the dipole strength is further approximated as,

$$D \approx 9.2 \times 10^{-39} \frac{\varepsilon_0 \gamma}{\tilde{\nu}_0 \pi} \qquad [2.15]$$

In these equations D is given in the Gaussian units of esu^2 cm^2, where esu represents electrostatic units. To convert these to SI units for absorption intensity, km mol^{-1} multiplication by $3.987\text{x}10^{-37}/\tilde{\nu}$ is necessary.

Absorption intensities require a linear oscillation of charge to be present during a vibrational transition, an electric dipole contribution, as seen above. However, VCD intensities require, in addition to a linear oscillation of charge, an angular oscillation of charge, which is a contribution from the magnetic-dipole transition moment. VCD intensity is, thus, proportional to the rotational or rotatory strength, the scalar product of the electric and magnetic dipole transition moments,

$$R_{01}^{a} = \mathrm{Im}\left(\int \psi_0^{a*} \hat{\mu} \psi_1^{a} d\tau . \int \psi_0^{a*} \hat{m} \psi_1^{a} d\tau\right) \equiv \mathrm{Im}\left(\langle 0^a|\hat{\mu}|1^a\rangle . \langle 1^a|\hat{m}|0^a\rangle\right) \qquad [2.16]$$

Here $\hat{m} = \sum_i (q_i/2m_i c)\vec{r}_i \times \vec{p}_i$ is the magnetic dipole moment operator, a pure imaginary operator proportional to the angular momentum operator $\vec{r}_i \times \vec{p}_i \equiv -i\hbar\vec{r}_i \times d/d\vec{r}_i$ for the ith particle with mass, m_i, and linear momentum, p_i. The imaginary part of the scalar product is taken to obtain the rotational strength as a real quantity. Experimentally the rotational strength is obtained from the integrated intensity of the VCD differential absorption band (equation 2.17),

$$R_{01}^{a} = 2.296\times10^{-39} \int^{band} \frac{\Delta\varepsilon(\tilde{\nu})}{\tilde{\nu}} \approx \frac{2.296\times10^{-39}}{\tilde{\nu}_0 \int^{band} \Delta\varepsilon(\tilde{\nu}) d\tilde{\nu}} \qquad [2.17]$$

and this can also be approximated for a Lorentzian band from the half-width at half-height and the frequency and intensity at the band maximum,

$$R \approx \frac{2.3\times10^{-39}\,\Delta\varepsilon\gamma}{\tilde{\nu}_0 \pi} \qquad [2.18]$$

Expressing both D and R in esu^{2}cm^2 allows definition of the dimensionless parameter g, the anisotropy ratio, as,

$$g = \frac{\Delta\varepsilon}{\varepsilon} = \frac{4R}{D} \qquad [2.19]$$

which connects experiment to theory. g can be seen as a measure of the intrinsic strength of a VCD band and for measurable VCD bands g values are typical within the range $10^{-4} - 10^{-6}$.

The first measured VCD spectra were published in the early to mid-1970s [16, 17, 19, 20] after some key technological developments were made. The spectrometers use solid-state electronics and lock-in amplifiers, liquid nitrogen cooled semiconductor detectors and IR polarisation modulators. Some key instrumental developments for the modern-day measurement of VCD include the advent of Fourier transform - infrared (FT-IR) VCD in 1979,[21, 22] followed 18 years later by the first dedicated commercial VCD spectrometer.[23] In the 1980s the theoretical formalism and methodology were developed for calculating VCD [24-27] from first principles without reliance on approximate models. With more powerful computers and the availability of commercial software for carrying out *ab initio* quantum calculations, VCD spectra can now be simulated at a high level of accuracy for medium sized molecules. A typical VCD measurement yields the spectra seen in figure 2.6. The small amplitude of the VCD is shown by looking at the units for the VCD spectra which are multiplied by 10^5. The noise spectrum shown gives an indication of how accurate the VCD signal is likely to be, if the noise signal is large at a certain point in the spectrum, then the VCD signal at that same point is likely to be unreliable.

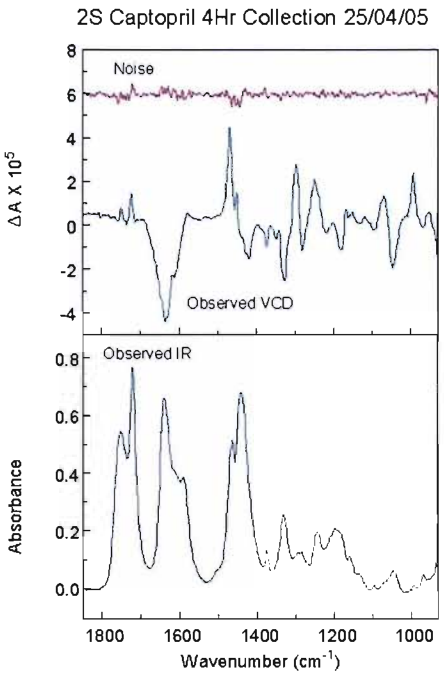

Figure 2.6 Typical IR (lower frame), VCD and noise (upper frame) for (2*S*)-Captopril from a standard VCD data collection on the dual PEM FT-VCD spectrometer

For calculation of a VCD spectrum for an enantiomer, simplifications are possible by breaking the molecule down into key fragments, which retain both the chiral centres and the hydrogen-bonding capabilities of the original molecule. This can reduce calculation time and enables the identification of key marker bands, specific for the chiral centre with that specific configuration. The same calculations can then be used for different chiral compounds that contain the same chiral centre.[28]

One of the first VCD measurements was made on crystalline samples α-$NiSO_4.6H_2O$ and α-$ZnSeO_4.6H_2O$.[19] However, it was found that the measurement of optical activity in crystals was limited to cases in which light propagates down the unique axis of a uniaxial crystal. Biaxial and uniaxial crystals viewed in directions other than the optical axis exhibit linear birefringence and linear dichroism, which are several orders of magnitude larger than vibrational optical activity, thereby obscuring the measurement of the VCD spectrum. Subsequent measurements were made in the liquid phase,[16, 20] which gave higher instrumental sensitivity and improved on earlier work, with observation of VCD over a greater spectral region and better signal-to-noise ratio.

2.2.2 Data Acquisition

In order to measure a VCD spectrum it is first necessary to ensure that an IR spectrum of good quality can be measured, as the magnitude of the signal strength of the VCD is approximately 10^{-4} of the parent IR signal. It is recommended that an IR spectrum with decadic absorbance in the range 0.1 – 1.0 be obtained, where the absorbance, A, for a band at wavenumber, $\tilde{v}$, can be expressed as per equation 2.20.

$$A(\tilde{v}) = -\log_{10}\left[\frac{I(\tilde{v})}{I_0(\tilde{v})}\right] \qquad [2.20]$$

Where $I(\tilde{v})$ is the intensity of the light after it has passed through the sample and $I_0(\tilde{v})$ is the intensity of the radiation incident upon the sample, at wavenumber $\tilde{v}$. An absorbance of 1.0 corresponds to approximately 10% percentage transmission, whereas an absorbance of 0.1 corresponds to about 80% percentage transmission. If the absorbance is greater than 1.0 too little light reaches the detector, but if the absorbance is less than 0.1 the sample absorbs too little of the incident IR beam and so insufficient signal is detected. Additional factors that influence the quality of the VCD spectrum include the quality of the VCD baseline, the selection of the spectral region and the setting of the polarization modulator.

2.2.2.1 Fourier Transform VCD

The introduction of FT-VCD measurements [22] produced great advances in the improvement of the signal-to-noise ratio and led to the separate collection of the polarisation modulated (ac) and unmodulated (dc) interferograms. Also seen were higher attainable spectral resolution and increased sharpening of peaks with subsequent lessening of spectral overlap.

A Fourier transform spectrometer is simply a Michelson interferometer with a moveable mirror (figure 2.7). By scanning the moveable mirror over some distance, an interference pattern is produced that encodes the spectrum of the source (as its Fourier transform). In most commercial Fourier transform spectrometers the interferometer consists of two mirrors located at right angles to one another; with a beam splitter placed at the vertex of the right angle and oriented 45 ° relative to the two mirrors. Radiation incident upon the beam splitter is divided into two parts, each of which propagates down one of the two arms and is reflected off one of the mirrors. The two beams then recombine and are transmitted out onto the detector. When the position of one mirror is continuously varied along the axis of the corresponding arm, the interference pattern is swept out as the two phase-shifted beams interfere with one another.

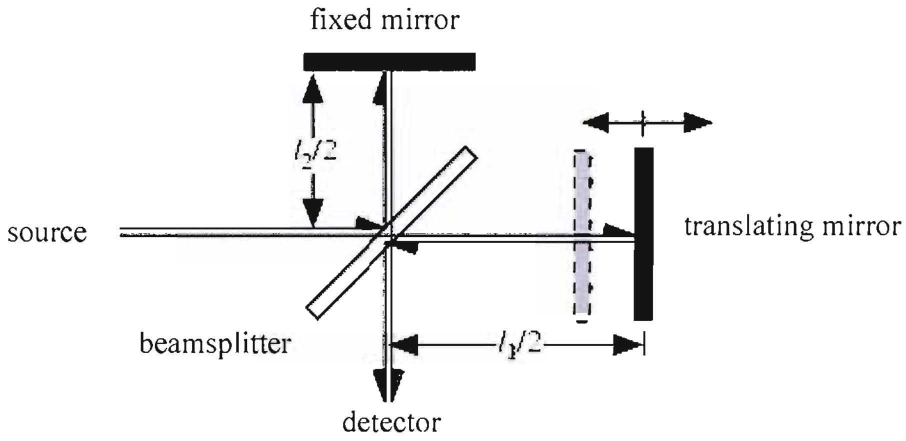

Figure 2.7 Schematic of the basics of a Fourier transform spectrometer

Fourier transform spectrometers have a multiplex advantage over dispersive spectral detection techniques for signal, but a multiplex disadvantage for noise. An instrument simultaneously measuring a signal over a range of frequencies obtains a $t^{1/2}$ advantage in time, t, required to obtain a given signal-to-noise ratio, compared to that which would be necessary using dispersive methods if the noise is detector limited.

The basic schematic for a standard FT-VCD for measurement in the mid-IR region is shown in figure 2.8. IR radiation from an interferometer initially passes through an optical filter to isolate the spectral region of interest e.g. 2000 – 800 cm^{-1}. The beam then goes through a linear polariser, which defines a single state of polarisation, and into a photoelastic modulator (PEM) (ZnSe in the case of the spectrometers used in this thesis) that modulates the polarisation between LCP and RCP states at a frequency of 50 kHz. The chiral sample is placed directly after the PEM and the beam is focused with a lens onto the MCT liquid nitrogen cooled detector. The detector signal is amplified and divided into two paths: one is the ordinary IR path that represents the FT-IR interferogram of the sample, the other path is to the lock-in amplifier, referenced to the PEM modulation frequency. The output of the lock-in amplifier is the VCD interferogram.

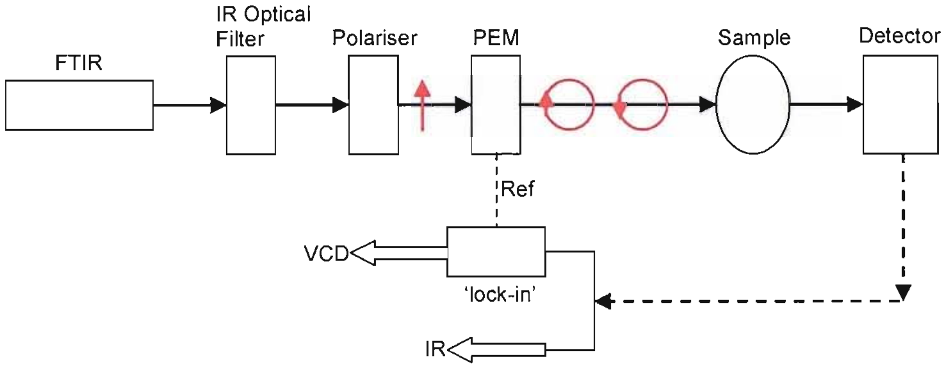

Figure 2.8 Optical-electronic diagram for a typical single PEM FT-VCD spectrometer

To carry out VCD measurements with an FT-IR spectrometer [21] the double modulation technique was developed.[22, 29] In this technique two interferograms are present simultaneously at the detector: one for the parent IR, the other for the VCD (encoded at the PEM frequency). Here the IR beam is first polarised at 45 ° to the stress axis of a PEM that converts the polarisation state of the light to left and right circular states at the PEM frequency, generally in the tens of kHz range. The beam passes through a chiral sample and onto a semi-conductor detector that can follow the high frequency polarisation modulation signal (figure 2.8).

The signal at the detector has two types of modulation, one at the Fourier frequencies associated with the unpolarised IR spectrum and one at the PEM modulation frequency associated with the VCD spectrum. To obtain the VCD spectrum, the signal is first demodulated at the PEM frequency and the resulting VCD interferogram is Fourier transformed to yield the VCD spectrum. If the linear polariser prior to the PEM is rotated by 90 °, right circularly polarised

(RCP) and left circularly polarised (LCP) states of radiation are interchanged and the resulting VCD spectrum has the opposite sign for all of its bands. For single-source FT-VCD measurements using the double modulation method, a PEM is placed in the beam after a linear polariser and before the sample. If the sample is chiral, there will be differences in the transmitted light at the PEM modulation frequency due to differences in the absorbance of the sample for left- versus right-circularly polarised radiation. Therefore, at the detector, there will be DC terms and Fourier modulated terms, as well as terms that are double-modulated at the Fourier frequencies and the PEM frequency. The interferogram associated with the VCD is obtained by demodulating the double-modulated term with respect to the PEM frequency using a lock-in amplifier tuned to this frequency. The output of the lock-in amplifier, with a sufficiently fast time constant; typically in the microsecond range, yields a VCD interferogram.

2.2.2.2 Dual Source Fourier Transform Polarisation Modulation Spectroscopy

In single source (SS) FT-VCD, VCD intensities are commonly in the range 10^{-4} to 10^{-6} absorbance units, and are often limited in quality by the low signal-to-noise ratios. One obvious way to improve the signal quality is to increase the instrumental throughput for the spectral region of interest. At high levels of IR intensity however, detector non-linearity occurs, limiting any further improvement of the signal-to-noise ratio for the FT-VCD measurement.

In the dual source (DS) method a four-port dual-source interferometer is combined with double-modulation FT-VCD measurements to obtain a spectrometer with enhanced signal quality and lower susceptibility to detector saturation (figure 2.9).[30] The interferogram is equipped with two sources, A and B. Source A is in the normal source position and has a BaF_2 wire grid polariser placed in front of it to pass vertically polarised radiation with respect to the plane of the interferometer. Source B is located beneath the beam port that normally goes to the sample.

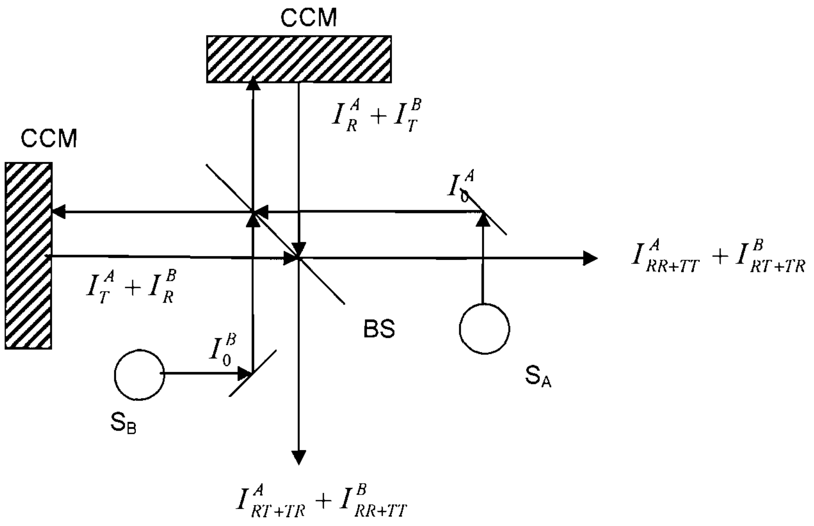

Figure 2.9 Diagram illustrating the optical layout of a dual-source interferometer. The two sources are labelled S_A and S_B, and the ZnSe beamsplitter is labelled BS. The reflections occur at the cube-corner mirrors (CCM) that displace the outgoing parallel beam relative to the incoming beam but do not change the final linear polarisation state.[30]

The method involves placing a linear polariser in front of each of the two sources in the interferometer and setting the polarisation state of one to be vertical and the other to be horizontal. In this way, the ordinary IR interferograms from the two sources combine negatively since they are simply out of Fourier phase with respect to one another. However, the polarisation-modulation interferograms combine positively since they are both out of Fourier phase and out of polarisation-modulation phase with respect to each other. The polarisation phase inversion created by orthogonal linear polarisers in front of the two sources undoes the Fourier phase reversal so the VCD interferograms become larger at the same time as the ordinary IR-transmission interferograms become smaller, thus avoiding saturation limits normally encountered in single source operation.

For dual source FT-VCD, the VCD contributions from the two sources have opposite signs due to the orthogonal orientations of their polarisers, whereas the relative orientation of the polarisers has no such effect for the ordinary IR intensity or absorbance spectrum. The signals from the two sources carry intrinsically opposite Fourier phase for their contributions to a given output beam, the VCD contributions add rather than subtract. The VCD interferograms associated with the two output beams are identical in magnitude but opposite in sign.

The gain in VCD intensity for dual source operation significantly outweighs the small increase in the VCD noise. The increase in the signal-to-noise ratio of the DS-VCD relative to the SS-VCD is due to the additivity of the VCD intensities coming from the two sources without an increase in the noise contribution from the detector. There is a significant reduction in collection time to achieve the same signal-to-noise ratio; these are very significant reductions, and represent a significant advantage of DS as compared to SS-VCD measurement. A second advantage of the DS is the reduction of the large interferogram associated with the ordinary IR spectrum. This reduction in magnitude allows the normal saturation level of the detector to be avoided. It is therefore possible to increase the absorbance of the sample well beyond the saturation limit, as long as the contributions of both sources are sufficiently well balanced to prevent their difference contribution from exceeding the normal SS saturation limit.

When the contributions of the two sources are the same level, the DS-IR interferogram cancels and the DS-VCD doubles compared to the SS-VCD interferogram. The doubling of the VCD interferogram signal against a constant noise background leads to a doubling of the signal-to-noise ratio and a four fold improvement in signal averaging time. The suppression of the DS-IR interferogram is maximised when the contributions from each source are equal. At the same time this limit is inconvenient, since the single-beam IR interferogram is needed to obtain the proper VCD spectrum.

Adjusting the baseline is simpler with one source compared to two. Quality of baseline obtained is the same for two sources as it is for one. While the overall alignment is more difficult, there is an additional degree of freedom that can be utilized before arriving at the final alignment, namely the baseline of the second source can be used to balance that of the first source. Finally, the quality of any baseline achieved with DS operation can be improved by approximately one order of magnitude by using a dual PEM set up.[29]

2.2.2.3 Dual PEM Set-Up

The dual PEM FT-VCD method [29] uses a second PEM, positioned after the sample, to reduce the artefacts observed to those solely derived from the components in between the two PEMs. Figure 2.10 shows the optical set-up of a dual PEM spectrometer. Positioning the second PEM after the sample eliminates any artefacts that arise from the optics before the first PEM, so that any artefacts now observed are purely due to the sampling conditions between the two PEMs, i.e. the sample and its cell.

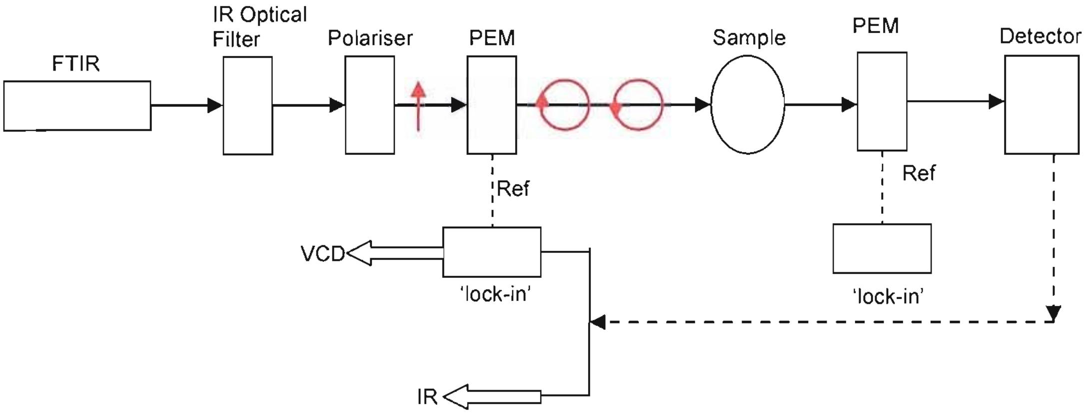

Figure 2.10 Optical-electronic diagram for the Chiral*IR* dual PEM VCD spectrometer

The baseline of the instrument with no sample or cell present can be adjusted to zero by altering the retardation of the second PEM, changing it from 0.25 (quarter-wave) to a slightly higher or lower value. This improves the spectra collected as prior to collection of data the baseline is now zero, so any baseline effects now observed are reduced as compared to VCD spectra collected from the single PEM spectrometer.[29]

2.2.2.4 VCD Calibration Procedure

The PEM is an essential piece of hardware for a VCD spectrometer, as it produces the alternating left- and right-circularly polarised light. A calibration curve is necessary as the effect of the PEM is not linear across the spectrum and the calibration curve corrects for this non-linearity. A PEM works by applying a periodic stress to an isotropic crystal, which cause synchronous variation of the difference in the refractive indexes along two mutually perpendicular axes of the crystal. One of these axes coincides with the axis along which the stress is applied. When the polarisation direction of the linearly polarised incident light is at 45 ° to the optical axes of the crystal, the periodic variation in the birefringence of the crystal introduces a time-dependent phase lag into the electric vector components. The phase variation in time, *t*, follows the relation

$$\delta_t = \delta^0_{\tilde{\nu}_i} \sin 2\pi\omega_m t \qquad [2.21]$$

where ω_m is the frequency of the stress modulation, and $\delta^0_{\tilde{\nu}_i}$ is the maximum phase shift introduced for wavelength λ_i or wavenumber $\tilde{\nu}_i$. When the maximum stress applied corresponds to a phase shift $\delta^0_{\tilde{\nu}_i} = \pi/2$, then the radiation of $\tilde{\nu}_i$ is said to be circularly polarised. Alternatively, one of the two electric vectors incident on and parallel to the optical axes of the PEM is said to have undergone a 90 ° phase shift or quarter-wave retardation relative to the other. For a given maximum stress on the PEM, one quarter-wave retardation is achievable at only one wavenumber, $\tilde{\nu}_q$. For other wavenumbers at the same PEM frequency, the maximum phase shift becomes

$$\delta^0_{\tilde{\nu}_i} = \delta^0_{\tilde{\nu}_q} \frac{\tilde{\nu}_i}{\tilde{\nu}_q} = \frac{\pi}{2}\frac{\tilde{\nu}_i}{\tilde{\nu}_q} = \frac{\pi}{2}\frac{\lambda_q}{\lambda_i} \qquad [2.22]$$

As $\sin 2\pi\omega_m t$ goes through +1, 0 and -1, δ_t for wavenumber $\tilde{\nu}_q$ goes through $+\pi/2$, 0 and $-\pi/2$, which means that the $\tilde{\nu}_q$ component goes through right circularly polarised, linearly polarised and left circularly polarised states, respectively. For the intermediate values of $\sin 2\pi\omega_m t$, corresponding intermediate polarisation states are achieved. Thus, only for a very small amount of the cycle is the wavenumber component $\tilde{\nu}_q$ circularly polarised. The remaining portion of the cycle contains polarisation states of an unwanted intermediate nature.

There are two types of experimental set-up to be discussed; sample and calibration set-up. Sample set-up consists of monochromatic light of wavenumber $\tilde{\nu}_i$ passing through a linear polariser, a PEM and an optically active sample, and then onto the detector. In the calibration step the optically active sample is replaced by a quarter-wave plate and a second polariser. The z axis is the direction of light propagation, and the optical axes of the PEM are set to coincide with the x and y axes. The polarisation direction of the first linear polariser is at 45 ° to the x and y axes.

The first set-up to be discussed is the sample set-up. The electric vector of the monochromatic light of wavenumber $\tilde{\nu}_i$, after passing through the first polariser is given as $\left[E^0(\tilde{\nu}_i)/\sqrt{2}\right](\mathbf{u}+\mathbf{v})$, where **u** and **v** are the unit vectors parallel to the x and y axes respectively, and $E^0(\tilde{\nu}_i)$ is the amplitude of the initial electronic vector. As the PEM induces a time-dependent relative phase lag δ_t into one of the electric vector components, the resulting electric vector after passing through the PEM becomes,

$$E(\tilde{\nu}_i)=\left[E^0(\tilde{\nu}_i)/\sqrt{2}\right]\left(\mathbf{u}+\mathbf{v}e^{i\delta_t}\right) \qquad [2.23]$$

If the right and left circularly polarised vectors are denoted by $\left[E^0(\tilde{\nu}_i)/\sqrt{2}\right](\mathbf{u}+i\mathbf{v})$ and $\left[E^0(\tilde{\nu}_i)/\sqrt{2}\right](\mathbf{u}-i\mathbf{v})$, respectively, it can be seen that equation 2.23 is equivalent to (equation 2.24),

$$E(\tilde{\nu}_i)=\left[E^0(\tilde{\nu}_i)/\sqrt{8}\right]\left[\left(1-ie^{i\delta_t}\right)(\mathbf{u}+i\mathbf{v})+\left(1+ie^{i\delta_t}\right)(\mathbf{u}+i\mathbf{v})\right] \qquad [2.24]$$

When this electric vector passes through an optically active sample, the right and left circularly polarised components are absorbed to different extents, and these absorbances are denoted by $A_R(\tilde{\nu}_i)$ and $A_L(\tilde{\nu}_i)$, respectively. The resulting electric vector, then, is

$$E(\tilde{\nu}_i) = \left[E^0(\tilde{\nu}_i)/\sqrt{8} \right] [(1 - ie^{i\delta_t})(\mathbf{u} + i\mathbf{v})e^{-2.303 A_R(\tilde{\nu}_i)/2} + (1 + ie^{i\delta_t})(\mathbf{u} + i\mathbf{v})e^{-2.303 A_L(\tilde{\nu}_i)/2}]$$

[2.25]

The intensity at the detector is calculated as the product of this electric vector with the complex conjugate. The voltage output of a linearly responding detector can be represented by the intensity falling on it, which in the present case is,

$$I(\tilde{\nu}_i) = \left[I^0(\tilde{\nu}_i)/2 \right] \left[(e^{-\alpha R} + e^{-\alpha L}) + (e^{-\alpha R} - e^{-\alpha L})\sin\delta_t \right] \qquad [2.26]$$

where $I^0(\tilde{\nu}_i)$ is the initial intensity of the wavenumber component $\tilde{\nu}_i$, $\alpha_L = 2.303 A_L(\tilde{\nu}_i)$ and $\alpha_R = 2.303 A_R(\tilde{\nu}_i)$. Because δ_t is time variant, sin δ_t can be expressed in a Fourier series as

$$\sin\delta_t = \sin(\delta^0_{\tilde{\nu}_i} \sin 2\pi\omega_m t) = 2\sum_{n=1}^{\infty} J_{2n-1}(\delta^0_{\tilde{\nu}_i}) \sin[(2n-1)2\pi\omega_m t] \qquad [2.27]$$

where n is an integer and $J_n(\delta^0_{\tilde{\nu}_i})$ are Bessel functions. From equations 2.26 and 2.27 it can be seen that the detector would notice a time-independent signal, dc signal and, time-varying signals at frequency ω_m, $3\omega_m$ etc. The signal at the fundamental frequency, ω_m, the ac signal, can be isolated by passing the detector signal through a 'lock-in' amplifier tuned to ω_m. Similarly the dc signal can be isolated by eliminating the signal frequencies at ω_m, $3\omega_m$, etc, using the appropriate electronic filters. The ratio of the ac signal demodulated at ω_m to the dc signal becomes

$$\frac{I_{\omega_m}(\tilde{\nu}_i)}{I_{dc}(\tilde{\nu}_i)} = 2J_1(\delta^0_{\tilde{\nu}_i}) \left(\frac{e^{-\alpha R} - e^{-\alpha L}}{e^{-\alpha R} + e^{-\alpha L}} \right) \frac{G_l}{G_f} \qquad [2.28]$$

where G_l and G_f are the gains introduced by the lock-in amplifier and filters, respectively. Multiplying the numerator and denominator of equation 2.28 by $e^{(\alpha_R+\alpha_L)/2}$ and noting that $(e^{\beta} - e^{-\beta})/(e^{\beta} + e^{-\beta}) = \tanh\beta$ and that for small values of β, $\tanh\beta \approx \beta$, equation 2.29 is obtained,

$$\frac{I_{\omega_m}(\tilde{\nu}_i)}{I_{dc}(\tilde{\nu}_i)} = 2J_1\left(\delta^0_{\tilde{\nu}_i}\right)\{1.15[A_L(\tilde{\nu}_i) - A_R(\tilde{\nu}_i)]\}\frac{G_l}{G_f} \qquad [2.29]$$

If $\tilde{\nu}_i$ is equal to $\tilde{\nu}_q$, then $\delta^0_{\tilde{\nu}_i} = \pi/2$ and $J_1(\pi/2) \approx 0.57$. It is not possible to know a priori the wavenumber $\tilde{\nu}_q$ precisely, however, and therefore $J_1\left(\delta^0_{\tilde{\nu}_i}\right)$ is not known. So the value of $J_1\left(\delta^0_{\tilde{\nu}_i}\right)G_l/G_f$ should be determined from a calibration spectrum to obtain the circular dichroism of a sample from equation 2.29.

In the calibration arrangement, the optically active sample is replaced by a birefringent plate and analyser together. There are four different ways that these two components can be oriented with respect to the preceding PEM and first polariser. Firstly, with the fast axes of the birefringent plate oriented parallel to that of the PEM and the direction of the second polariser oriented parallel to that of the first. The electric vector of light after passing through the PEM is $\left[E^0(\tilde{\nu}_i)/\sqrt{2}\right]\left(\mathbf{u} + \mathbf{v}e^{i\delta_t}\right)$. The birefringent plate induces further phase lag $\delta^B_{\tilde{\nu}_i}$, which is static in nature. The final electric vector after passing through the analyser becomes,

$$E(\tilde{\nu}_i) = \left[E^0(\tilde{\nu}_i)/2\right]\left(\mathbf{u} + \mathbf{v}e^{i\left(\delta_t + \delta^B_{\tilde{\nu}_i}\right)}\right)(\mathbf{u} + \mathbf{v}) \qquad [2.30]$$

and intensity,

$$I(\tilde{\nu}_i) = \left[I^0(\tilde{\nu}_i)/2\right]\left(1 + \cos\delta_t\cos\delta^B_{\tilde{\nu}_i} - \sin\delta_t\sin\delta^B_{\tilde{\nu}_i}\right) \qquad [2.31]$$

Using equation 2.27 and a similar expression for cos δ_t,

$$\cos\delta_t = \cos\left(\delta^0_{\tilde{\nu}_i}\sin 2\pi\omega_m t\right) = J_0\left(\delta^0_{\tilde{\nu}_i}\right) + 2\sum_{n=1}^{\infty} J_{2n}\left(\delta^0_{\tilde{\nu}_i}\right)\cos 4n\pi\omega_m t \qquad [2.32]$$

The expression analogous to equation 2.29 becomes,

$$\frac{I_{\omega_m}(\tilde{\nu}_i)}{I_{dc}(\tilde{\nu}_i)} = \left(\frac{-2J_1\left(\delta^0_{\tilde{\nu}_i}\right)\sin\delta^B_{\tilde{\nu}_i}}{1+J_0\left(\delta^0_{\tilde{\nu}_i}\right)\cos\delta^B_{\tilde{\nu}_i}}\right)\frac{G_l}{G_f} \qquad [2.33]$$

Secondly, if the polarisation direction of the second polariser is perpendicular to that of the first polariser, whereas the fast axis of the birefringent plate is parallel to that of the PEM, then (**u** + **v**) in equation 2.30 becomes (**u** - **v**) and the expressions analogous to equations 2.31 and 2.33 become,

$$I(\tilde{\nu}_i) = \left[I^0(\tilde{\nu}_i)/2\right]\left(1-\cos\delta_t\cos\delta^B_{\tilde{\nu}_i}+\sin\delta_t\sin\delta^B_{\tilde{\nu}_i}\right) \qquad [2.34]$$

$$\frac{I_{\omega_m}(\tilde{\nu}_i)}{I_{dc}(\tilde{\nu}_i)} = \left(\frac{2J_1\left(\delta^0_{\tilde{\nu}_i}\right)\sin\delta^B_{\tilde{\nu}_i}}{1-J_0\left(\delta^0_{\tilde{\nu}_i}\right)\cos\delta^B_{\tilde{\nu}_i}}\right)\frac{G_l}{G_f} \qquad [2.35]$$

Thirdly, if in addition to the second polariser being perpendicular to the first polariser, the fast axis of the birefringent plate is also perpendicular to that of the PEM, then the $e^{i\left(\delta_t+\delta^B_{\tilde{\nu}_i}\right)}$ and (**u** + **v**) terms become $e^{i\left(\delta_t-\delta^B_{\tilde{\nu}_i}\right)}$ and (**u** - **v**), respectively, and the expressions analogous to equations 2.31 and 2.33 become,

$$I(\tilde{\nu}_i) = \left[I^0(\tilde{\nu}_i)/2\right]\left(1-\cos\delta_t\cos\delta^B_{\tilde{\nu}_i}-\sin\delta_t\sin\delta^B_{\tilde{\nu}_i}\right) \qquad [2.36]$$

$$\frac{I_{\omega_m}(\tilde{\nu}_i)}{I_{dc}(\tilde{\nu}_i)} = \left(\frac{-2J_1\left(\delta^0_{\tilde{\nu}_i}\right)\sin\delta^B_{\tilde{\nu}_i}}{1-J_0\left(\delta^0_{\tilde{\nu}_i}\right)\cos\delta^B_{\tilde{\nu}_i}}\right)\frac{G_l}{G_f} \qquad [2.37]$$

In the fourth arrangement, the polarisation direction of the second polariser is parallel to the first but the fast axis of the birefringent plate is perpendicular to that of the PEM. Then the expressions analogous to equations 2.31 and 2.33 become,

$$I(\tilde{\nu}_i) = \left[I^0(\tilde{\nu}_i)/2\right]\left(1+\cos\delta_t\cos\delta^B_{\tilde{\nu}_i}+\sin\delta_t\sin\delta^B_{\tilde{\nu}_i}\right) \qquad [2.38]$$

$$\frac{I_{\omega_m}(\tilde{\nu}_i)}{I_{dc}(\tilde{\nu}_i)} = \left(\frac{-2J_1\left(\delta^0_{\tilde{\nu}_i}\right)\sin\delta^B_{\tilde{\nu}_i}}{1-J_0\left(\delta^0_{\tilde{\nu}_i}\right)\cos\delta^B_{\tilde{\nu}_i}}\right)\frac{G_l}{G_f} \qquad [2.39]$$

Equations 2.33 and 2.39 are equal but opposite in sign, as are equations 2.35 and 2.37. Also equations 2.33 and 2.37, like 2.35 and 2.39, are equal to each other with a non-zero magnitude of $\pm 2J_1\left(\delta^0_{\tilde{\nu}_i}\right)G_l/G_f$ at $\cos\delta^B_{\tilde{\nu}_i} = 0$ and $\sin\delta^B_{\tilde{\nu}_i} = \pm 1$. This is applicable when,

$$\delta^B_{\tilde{\nu}_i} = \frac{\tilde{\nu}_i}{\tilde{\nu}_B}\frac{\pi}{2} = (2n+1)\frac{\pi}{2} \qquad [2.40]$$

where $\tilde{\nu}_B$ is the wavenumber for which the birefringent plate introduces one quarter-wave retardation and n is an integer. Further more, equations 2.33, 2.35, 2.37 and 2.39 are equal to each other with zero magnitude, when $\sin\delta^B_{\tilde{\nu}_i} = 0$. This condition is met when $\delta^B_{\tilde{\nu}_i} = \frac{\tilde{\nu}_i}{\tilde{\nu}_B}\frac{\pi}{2} = n\pi$.

In practical terms, if the maximum stress setting on the PEM corresponds to one quarter-wave retardation for the wavenumber $\tilde{\nu}_q$ and the light components of various wavenumbers are investigated using the calibration arrangement, then four curves are obtained. The non-zero crossings of the curves provide the values of $\pm 2J_1\left(\delta^0_{\tilde{\nu}_i}\right)G_l/G_f$. These can be interpolated to the desired wavenumber and used in equation 2.29 to determine the circular dichroism of a given sample. Two of the four possible calibration curves are shown in figure 2.11 (the green and purple lines), together with the interpolated curve of their non-zero crossings (the red line), which is the final calibration curve used to obtain the final VCD spectrum of a sample.

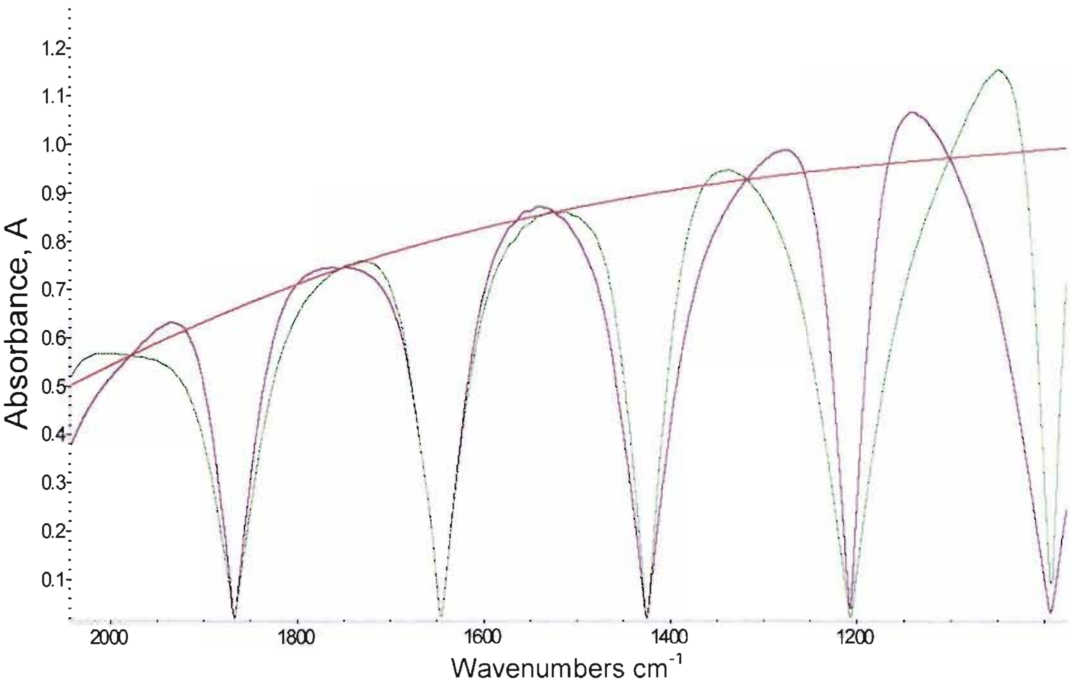

Figure 2.11 The two calibration curves (red and purple lines) are shown obtained from two different arrangements of the calibration set-up, with the interpolated non-zero crossings giving the calibration curve (red line) used to obtain the final VCD spectrum of a sample.

2.2.2.5 Comparison of FT-VCD Instruments

The two types of FT-VCD spectrometer available are the single PEM and dual PEM as discussed above. There are relative advantages and disadvantages of each instrument, and the choice of spectrometer can influence the quality of VCD spectrum obtained, and the ease of VCD measurement. The data reprocessing aspect is discussed below, but sampling issues and optimum measurement conditions are discussed in chapter 3.

The dual PEM holds the advantage with regards to data reprocessing as the end output of a data collection is the parent IR spectrum, VCD spectrum and associated noise spectrum. For the dual PEM instrument the data is collected in one hour increments and then averaged at the end of the total collection time, so that if a spectrum begins to look poor towards the end of the data collection the later data collection can be excluded from the average.

The single PEM spectrometer collects the data as a single unit, and so if the detector heats up or the compound comes out of solution the whole data collection is wasted. However, this is not normally a problem as the data collections tend to take approximately an hour.

The problem with reprocessing the data from the single PEM spectrometer is that it is a very convoluted process. There are several steps to the reprocessing; firstly a calibration curve has to be obtained, as described in section 2.2.2.4 of this chapter. Secondly, after the data collection itself, which produces two interferograms, these interferograms have to be Fourier transformed to give the parent IR spectrum and the uncorrected VCD spectrum. The VCD Fourier transform requires phase correction using the phase information from the parent IR interferogram. Thirdly, the uncorrected VCD has to be adjusted to correct for the instrument gain (this puts the parent IR and VCD spectra on the same scale). The VCD spectrum is then divided by the parent IR, to give the corrected VCD spectrum. The division of the raw VCD spectrum by the parent IR is necessary to convert the transmission experiment to a measurement of differential absorption i.e. corrected VCD spectrum. However, one further step is necessary; this is correction of the VCD spectrum by division by the calibration curve, which corrects for the varying effect of the PEM across the spectrum. There is no intrinsic measurement of the noise from the collected VCD data (as occurs with the dual PEM spectrometer), but an estimate can be made by collecting a VCD measurement of an empty cell. There is no need for the calibration step with the dual PEM spectrometer as baseline correction is achieved by setting the retardation of the second PEM prior to data collection, to give a zero baseline.

The VCD data from both spectrometers can also be corrected by subtraction of the solvent spectra, collected under the same conditions as the sample measurement.

2.2.3 Applications of VCD

2.2.3.1 Enantiomeric Excess

One of the most straight forward applications of VCD is the determination of the enantiomeric excess (ee) of a sample which consists of some mixture of enantiomers of a chiral molecule.[31-34] The % ee (percentage enantiomeric excess) of a sample is defined as the excess amount of one enantiomer over the other, relative to the total amount of both enantiomers, illustrated in equation 2.41, where N_A and N_B are a measure of the number of moles of A and B, respectively.

$$\%ee(A) = (N_A - N_b) \times 100\% / (N_A + N_B) \qquad [2.41]$$

For an optically pure sample of enantiomer A, % ee(A) = 100%; for the racemic mixture, % ee(A) = 0%; for an optically pure sample of enantiomer B, % ee(A) = -100%. The magnitude of a VCD spectrum of enantiomer A scales directly and linearly with the % ee of enantiomer A.[35] Hence the VCD signal of a band is at a maximum for 100% ee, is zero across the whole spectrum at 0% ee, and is at the negative of the maximum at -100% ee.

VCD can measure % ee without separation or further derivitisation, if a sample of known optical purity is available. Alternatively in the absence of a standard of known % ee, relative % ee can be determined. Use of VCD for determination of % ee is advantageous over traditional methods, such as optical rotation (OR), due to the multiplicity of spectral bands that can be measured simultaneously in the spectrum. These bands carry not only the VCD intensity, allowing determination of % ee, but also information about the structural specificity of the chiral molecule being measured, and permit simultaneous determinations of the % ee of more than one chiral species in a given sample.

From the concentrations of the A and B enantiomers of a chiral molecule in solution (C_A and C_B respectively), the ee of the sample is given by $(C_A - C_B)/(C_A$

$+ C_B$) or ($C_B - C_A$)/($C_A + C_B$), depending on the enantiomer selected for reference. The data collected in the spectral measurements give us this information, with the sum ($C_A + C_B$) obtained from the IR measurement and the difference ($C_A - C_B$) from the VCD measurement. Hence ee is obtained by the combination of the IR and VCD measurements.

2.2.3.2 Absolute structure determination

Determination of absolute configuration from VCD spectroscopy for a chiral compound consists of four basic steps: first, a configuration is chosen e.g. *R*; secondly, the IR and VCD spectra are calculated via *ab initio* quantum mechanical calculations for the chosen configuration; next, the experimental IR and VCD of the available enantiomer are measured in solution, as a liquid or in a KBr disc or Nujol mull; lastly, the observed and calculated VCD spectra are compared, which unambiguously determines the absolute configuration of the enantiomer under study.

2.2.4 Practical Solution State Measurements

Solution/liquid state measurements in the mid-IR region (2000 - 800 cm^{-1}) are the most commonly performed VCD measurements. A solution or neat liquid can be placed in a solution cell of variable path length and the VCD spectrum obtained. The choice of solvent is important, as it must not be chiral and should be free from absorbances in the IR in the region of interest. The concentration of the analyte in solution must be carefully controlled. If it is too high intermolecular interactions such as hydrogen bonding can complicate comparison with predicted VCD spectra. If the concentration is too low, the VCD signal will simply not be observed. To get a solution of the correct concentration it is easiest to ensure that an IR spectrum of the correct absorption can be measured before measuring the VCD spectrum. Variation of the path length of the cell performs essentially the same task as adjustment of the concentration; however, at longer path lengths internal reflection can occur within the cell which can obscure the small VCD signal. Neat liquids are the simplest measurements to perform, with choice of path length, resolution of the instrument, and data collection time / number of scans being the only variables.

In the solution state it is possible that the chiral molecule can adopt several low energy conformations, depending upon the possibility of hydrogen bonding, which may occur, both inter- and intra-molecularly and with the solvent. When trying to compare predicted VCD spectra with those obtained experimentally, it may be necessary to combine the predicted VCD spectra for several different conformers in order to obtain a better fit. This should enable determination of the dominant solution conformations; however, for a simple determination of absolute stereochemistry it is unnecessary.

VCD can be used to determine the preferred conformation of flexible chiral molecules in solution. This is done through calculation of the lowest energy conformers of the enantiomer, followed by a geometry optimisation and a vibrational frequency calculation for each possible conformer. The energy of each conformer produced by the calculation can then be used in conjunction with the Boltzmann population distribution to determine the relative amounts of each conformer in solution. The VCD spectra of the conformers are then combined in the same relative proportions and compared to the experimentally obtained VCD spectrum of the compound in solution. It may be necessary to increase the proportions of some of the higher energy conformers if specific bands, due only to that specific conformer, are present in the experimental VCD spectrum. Overestimation of the differences in energy between the conformers can occur as calculations assume that the molecules are in the gas phase, rather than solution phase and in solution certain conformers may be stabilised by solvent effects, leading to the adjustment of the relative proportions.

Other considerations regarding the calculations include the possibility of dimer formation, which is especially favourable for molecules with the COOH group present. Key marker bands can be seen for this functional group when compared to some of the compounds studied (e.g. ibuprofen) and these bands can be used to determine the absolute stereochemistry. Intra-molecular hydrogen bonding can also be seen in some cases and conformers which promote this may well be stabilised in non-polar solvents. The presence of dimer formation in solution for the COOH group can be confirmed by study of the OH stretching region of the observed IR spectrum. A broad band ~3000 cm^{-1} indicates hydrogen bonding (intra- or inter-molecular), while a sharper peak at ~3200 cm^{-1} indicates the presence of free –OH. Whilst in the fingerprint region a band at ~900 cm^{-1} can be indicative of the presence of the COOH group.

The measurement of the VCD of solid state samples, such as a nujol mull or KBr disc, is possible as long as the particle size of the solid is smaller than the wavelength of the incident radiation. The conformation of the molecules in the solid state will be different to that in the solution state, and calculations starting with the crystal structure, obtained from XRD, are more likely to yield good matches. These aspects of data collection and prediction are discussed further in chapters 3 and 4, respectively.

2.3 *Ab Initio* Quantum Mechanical Calculations

In order to perform an absolute stereochemistry determination or to determine the solution conformation of a chiral compound using VCD, it is necessary to predict the VCD spectrum for one possible enantiomer of that chiral compound. This is done through *ab initio* quantum mechanical calculations, performed using density functional theory (DFT) with varying levels of complexity in both the method and basis set.[36-40] The experimentally obtained VCD spectrum can then be compared to the predicted VCD spectrum in order to determine the correct absolute stereochemistry or solution conformation of the chiral compound under investigation.

The VCD calculations are carried out completely independently from the experimental VCD measurements and involve no adjustable parameters, other than the choice of quantum mechanical method and basis set, and the spectral bandwidths for converting numerical VCD intensities into simulated spectra, that can be compared directly to experimental spectra.

A basic VCD calculation begins with a geometry optimisation; geometry optimisations locate the lowest energy molecular structure in closest proximity to the specified starting structure. Geometry optimisations depend primarily on the gradient of the energy - the first derivative of the energy with respect to the atomic positions. This is followed by a frequency calculation; molecular frequencies depend on the second derivative of the energy with respect to the nuclear positions. A frequency calculation must use the same theoretical model and basis set as produced the optimised geometry. Frequencies computed with a different basis set or procedure have no validity.

Ab initio molecular orbital theory predicts the properties of both atomic and molecular systems. The fundamental laws of quantum mechanics form its basis, using a variety of mathematical approximation and transformation techniques. Quantum mechanics [41, 42] are used to explain how electrons have both particle-like and wave-like properties. Molecular mechanics simulations use the laws of classical physics to predict the structures and properties of molecules; they don't explicitly treat the electrons in a molecular system. Instead they perform computations based upon the interactions among the nuclei. Electronic effects are implicitly included in the force fields through parameterisation. Electronic structure methods use the laws of quantum mechanics rather than classical physics as the basis for their computations. Quantum mechanics states that the energy and other related properties of a molecule may be obtained by solving the Schrodinger equation (equation 2.42):

$$H\Psi = E\Psi \qquad [2.42]$$

where H is the Hamiltonian operator, E is the energy for the system and Ψ is the wavefunction. For any but the smallest systems, however, exact solutions to the Schrodinger equation are not computationally practical. Electronic structure methods are characterised by their various mathematical approximations to its solution. One of the major classes of electronic structure methods is *ab initio* methods. *Ab initio* methods use no experimental parameters in their computations. Instead, their computations are based solely upon the laws of quantum mechanics - the first principles referred to in the name *ab initio* - and on the values of a small number of physical constants: the speed of light, the masses and charges of electrons and nuclei and Planck's constant.

Another, relatively new, class of electronic structure methods is DFT methods; these are similar to *ab initio* methods in many ways. DFT methods include the effects of electron correlation in the model; the fact that electrons in a molecular system react to one another's motion and attempt to keep out of one another's way. Methods including electron correlation account for the instantaneous interactions of pairs of electrons with opposite spin.

Traditional methods in electronic structure, like Hartree-Fock (HF) theory are based on the complicated many-electron wavefunction. The main objective of DFT is to replace the many-body electronic wavefunction with the electron density as a basic quantity. Whereas the many-body wavefunction is dependent on 3N variables, three spatial variables for each of the N electrons, the density is only a function of three variables and is a simpler quantity to deal with both conceptually and practically.

DFT methods compute electron correlation via general functionals (in DFT functionals are functions of the electron density, itself a function of coordinates in real space) of the electron density. DFT functionals partition the electronic energy into several components which are computed separately: the kinetic energy, the electron-nuclear interaction, the Coulomb repulsion and an electron-correlation term which accounts for the remainder of the electron-electron interaction.

Traditional functionals are generally distinguished by the way that they treat exchange and correlation components. Local exchange and correlation functionals involve only the values of the electron spin densities, e.g., Slater and Xα. Gradient corrected functionals involve both the values of the electron spin densities and their gradients, e.g., B-LYP.

There are also several hybrid functionals, which define the exchange functional as a linear combination of Hartree-Fock, local and gradient-corrected exchange terms; this exchange functional is then combined with a local and/or gradient-corrected correlation functional, e.g., B3LYP and B3PW91.

The DFT approach is based upon a strategy of modelling electron correlation via general functionals of the electron density. DFT methods partition the electronic energy into several terms:

$$\mathrm{E} = \mathrm{E}^{\mathrm{T}} + \mathrm{E}^{\mathrm{V}} + \mathrm{E}^{\mathrm{J}} + \mathrm{E}^{\mathrm{XC}} \qquad [2.43]$$

where E^{T} is the kinetic energy term (arising from the motion of the electrons), E^{V} includes terms describing the potential energy of the nuclear-electron attraction and of the repulsion between pairs of nuclei, E^{J} is the electron-electron repulsion term, and E^{XC} is the exchange-correlation term and includes the remaining part of the electron-electron interactions.

All terms except the nuclear repulsion are functions of ρ, the electron density, with the electron positions given by $\bar{r}_1$ and $\bar{r}_2$, and their displacements by $d\bar{r}_1$ and $d\bar{r}_2$. E^{J} is given by the following expression:

$$\mathrm{E}^{\mathrm{J}} = \frac{1}{2} \int\int \rho(\bar{r}_1)(\Delta r_{12})^{-1} \rho(\bar{r}_2) d\bar{r}_1 d\bar{r}_2 \qquad [2.44]$$

$\mathrm{E}^{\mathrm{T}} + \mathrm{E}^{\mathrm{V}} + \mathrm{E}^{\mathrm{J}}$ corresponds to the classical energy of the charge distribution ρ. The E^{XC} term accounts for the remaining energy, including the exchange energy arising from antisymmetry of the quantum mechanical wavefunction and the dynamic correlation in the motion of the individual electrons.

E^{XC} is usually approximated as an integral involving only the spin densities, ρ_α and ρ_β, and possibly their gradients, $\nabla\rho_\alpha$ and $\nabla\rho_\beta$, as a function of position, $\bar{r}$:

$$\mathrm{E}^{\mathrm{XC}}(\rho) = \int f(\rho_\alpha(\bar{r}), \rho_\beta(\bar{r}), \nabla\rho_\alpha(\bar{r}), \nabla\rho_\beta(\bar{r})) d^3\bar{r} \qquad [2.45]$$

We use ρ_α to refer to the α spin density, ρ_β to refer to the β spin density and ρ refers to the total electron density $(\rho_\alpha + \rho_\beta)$.

E^{XC} is usually divided into separate parts, referred to as the exchange and correlation parts, but actually corresponding to same-spin and mixed-spin interactions, respectively:

$$E^{XC}(\rho) = E^{X}(\rho) + E^{C}(\rho) \qquad [2.46]$$

All three terms are again functionals of the electron density, $E^{X}(\rho)$ and $E^{C}(\rho)$ are the exchange functionals and correlation functionals, respectively.

Pure DFT methods are defined by pairing an exchange functional with a correlation functional, e.g. BLYP. Hybrid functionals, such as B3LYP, include a mixture of Hartree-Fock and DFT exchange along with DFT correlation.

The first report on using density functional theory (DFT) in *ab initio* calculations of VCD spectra was in 1994.[43] These calculations yielded results of similar accuracy to those calculated with MP2 force fields in regards to calculation of accurate harmonic force fields, but for substantially less computational effort. This advance in prediction of VCD spectra was proceeded by two important developments: Firstly hybrid functionals, such as B3LYP: Secondly, implementation of efficient analytical derivative techniques. Frequencies, dipole strengths and rotational strengths derived from harmonic force fields, atomic polar tensors (APT) and atomic axial tensors (AAT) can thus be used to synthesise absorption and VCD spectra, using Lorentzian band shapes.

2.3.1 Methodology of VCD Calculations

The infrared absorption intensity is proportional to the dipole strength, the square of the electric dipole transition moment. In the harmonic approximation, the dipole strength, D_{01}^{a}, is proportional to the square of the derivative of the electric dipole moment, $\vec{\mu}$, of the molecule with respect to the nuclear displacement in the normal mode, Q_a, equation 2.47. Where $\hbar$ is the reduced Planck constant, and ω_a is the angular frequency.

$$D_{01}^{a} = \frac{\hbar}{2\omega_a}\left|\left(\frac{\partial\vec{\mu}}{\partial Q_a}\right)_0\right|^2 \qquad [2.47]$$

The VCD intensity is proportional to the rotational / rotatory strength, the scalar product of the electric dipole and magnetic dipole transition moments. In the harmonic approximation, the rotational strength, R_{01}^{a}, is proportional to the scalar product between the derivative of the electric dipole moment with respect to the normal mode displacement and the derivative of the magnetic dipole moment, $\vec{m}$, of the molecule with respect to the nuclear velocities of the normal mode, expressed in terms of the conjugate momentum, P_a:

$$R_{01}^{a} = \frac{\hbar}{2}\left(\frac{\partial\vec{\mu}}{\partial Q_a}\right)_0 \cdot \left(\frac{\partial\vec{m}}{\partial P_a}\right)_0 \qquad [2.48]$$

From equations [2.47] and [2.48] it can be seen that non-zero IR intensity requires linear oscillation of charge and non-zero VCD intensity requires simultaneous linear (electric) and angular (magnetic) oscillation of charge, produced by nuclear motion. Quantum chemistry programs calculate these intensities by taking derivatives of the energy of the molecule with respect to the electric field, **E**, or magnetic field, **H**, and vibrational normal mode displacement or momentum:

$$\left(\frac{\partial\vec{\mu}}{\partial Q_a}\right)_0 = -\left(\frac{\partial^2 E_{el}}{\partial\mathbf{E}\partial Q_a}\right)_0 \qquad [2.49]$$

$$\left(\frac{\partial\vec{m}}{\partial P_a}\right)_0 = -\left(\frac{\partial^2 E_{el}}{\partial\mathbf{H}\partial P_a}\right)_0 \qquad [2.50]$$

The calculations then proceed, first via optimisation of the geometry, then calculation of the normal vibrational modes, and then calculation of the VCD intensities.

2.3.2 Basis Sets

Mathematical descriptions of the orbitals within a molecular system are know as basis sets, they combine to give an approximation of the total wavefunction, and are used in the calculations described above. Larger basis sets more accurately approximate the orbitals by imposing fewer restrictions on the locations of the electrons in space. In the true quantum mechanical picture, electrons have a finite probability of existing anywhere in space; this limit corresponds to the infinite basis set expansion.

Standard basis sets for electronic structure calculations use linear combinations of gaussian functions to form the orbitals. A basis set can be classified by the number and types of basis functions that it contains. Basis sets assign a group of basis functions to each atom within a molecule to approximate its orbitals. These basis functions themselves are composed of a linear combination of gaussian functions.

Minimal basis sets contain the minimum number of basis functions needed for each atom. They use fixed size atomic type orbitals, e.g. STO-3G, which approximates Slater orbitals with gaussian functions. Split valence basis sets increase in size by using a higher number of basis functions per atom, e.g. 3-21G and 6-31G have two (or more) sizes of basis function for each valence orbital. Similarly triple split valence basis sets, like 6-311G, use three sizes of functions for each orbital type.

Split valence basis sets allow orbitals to change in size but not in shape. Polarised basis sets remove this limitation by adding orbitals with angular momentum beyond what is required for the ground state description of each atom. For example, polarised basis sets add d functions to carbon atoms and f functions to transition metals, and some of them add p functions to hydrogen atoms. For example, 6-31G(d), otherwise known as 6-31G*, is the 6-31G basis set with d functions added to heavy atoms. 6-31G(d, p) or 6-31G** adds p functions to hydrogen atoms in addition to the d functions on heavy atoms.

Another basis set expansion is the addition of diffuse functions, which are large-size versions of s- and p-type functions. They allow orbitals to occupy a larger region of space. These basis sets are important for systems where the electrons are relatively far from the nucleus: molecules with lone pairs, anions and other systems with low ionisation potentials. The 6-31+G* basis set is the 6-31G* basis set with diffuse functions added to heavy atoms. The double plus version, 6-31++G* adds diffuse functions to the hydrogen atoms as well. Diffuse functions on hydrogen atoms seldom make a significant difference in accuracy. It is often found that hydrogen-bonded systems require basis sets with additional diffuse or polarisation functions.

2.3.3 Calculation Output

Once the predicted VCD spectrum has been obtained it can be directly compared to the experimental VCD spectrum. However, vibrational frequencies are consistently over-estimated by calculation from DFT, through neglect of anharmonicity. The effect is found to be relatively uniform and as such generic frequency scaling factors may be applied to the values of the vibrational frequencies. Application of a generic scale factor causes a shift of the spectrum along the x-axis to lower wavenumber, without altering the overall appearance of the spectrum (figures 2.12 and 2.13 show a comparison of the experimental IR spectrum for (*S*)-ibuprofen with the raw predicted IR spectrum and the scaled predicted IR spectrum respectively). For different basis sets and levels of calculation there are published scale factors.[44-47] Within chapter 3, calculation of individual scale factors is made to improve the fit of the predicted spectra to the experimental spectra, for subsequent use with a goodness of fit parameter developed in this thesis.

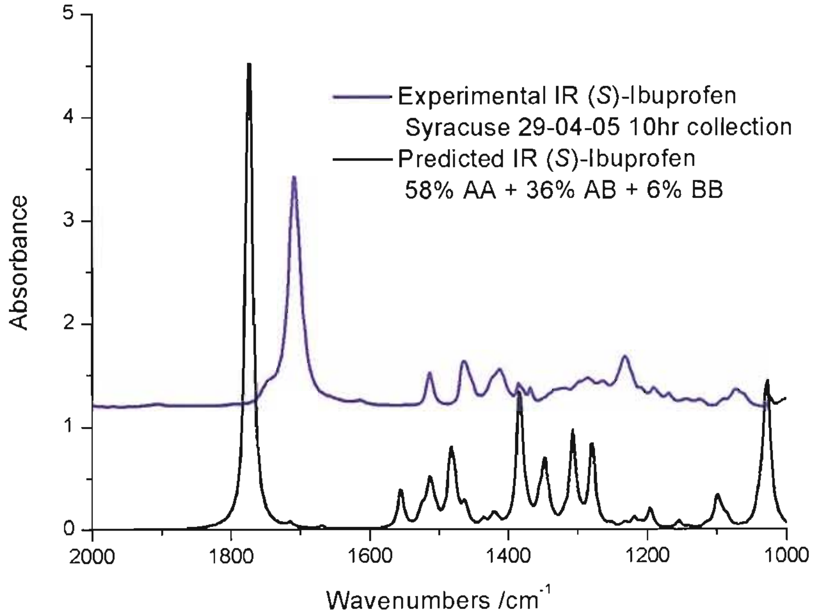

Figure 2.12 Comparison of the experimental IR spectrum (purple line) and predicted combined IR spectrum (black line) of (*S*)-ibuprofen in the range 2000 - 1000 cm^{-1}

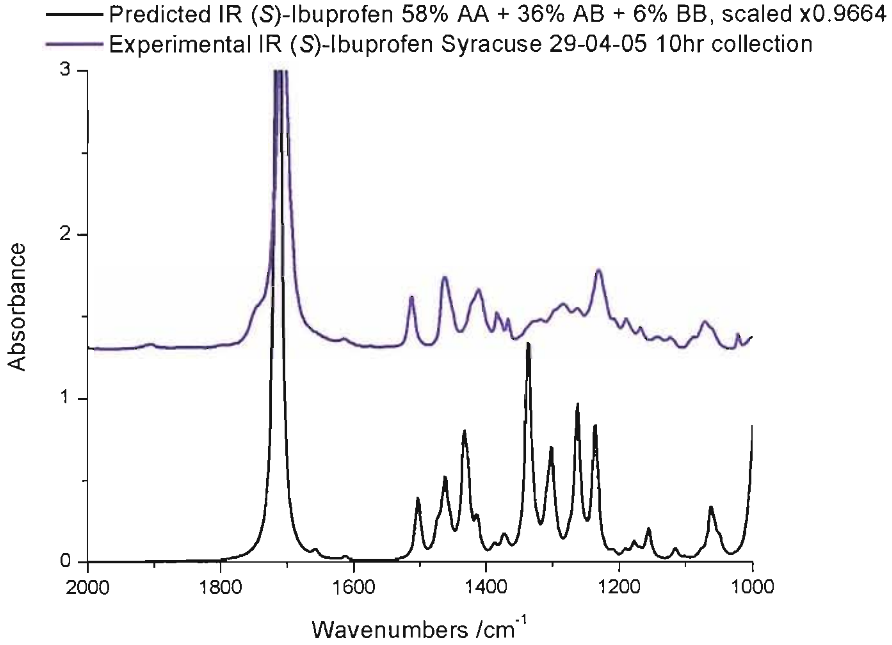

Figure 2.13 Comparison of the experimental IR spectrum (purple line) and the scaled (x0.9664) predicted combined IR spectrum (black line) of (*S*)-ibuprofen in the range 2000 - 1000 cm^{-1}

The completeness of a calculation can be assessed by comparing the structures for two enantiomers of the chiral compound under study. The calculation can be seen to be optimised if the calculations for the two enantiomers give mirror image structures, and the two calculated VCD spectra are also mirror images. A calculation will sometimes not complete properly if the geometry optimisation gets stuck in a local minimum, rather than finding the global minimum. Additionally, comparison of the IR spectra is a useful guide to the quality of agreement between experimental and calculated VCD spectra.

2.3.4 Analysis Using Fragments

A limitation to the widespread application of VCD to pharmaceuticals has been the interpretation of the VCD spectra, and the reliance on *ab initio* molecular orbital calculations of VCD intensities to identify absolute configuration and solution conformations from the broad VCD features.[36, 48] Such calculations are computationally demanding both in terms of time and hardware resources. Techniques that focus on fragments of the drugs and, where appropriate, simplified models,[49, 50] reduce those computational demands and allow application of VCD to larger molecules with numerous low-energy solution conformations. An interpretational approach that avoids calculations is the identification of VCD marker bands for both configuration and conformation, based on studies of similar molecules with similar chiral centres.[28]

In the mid-IR region, vibrational modes consist of highly coupled nuclear displacements distributed throughout the molecule. This complication can limit the *ab initio* molecular orbital calculations of VCD intensities to low energy conformers of the molecules and to fairly small molecular size (the largest compound studied in this project was 5α-cholestane, $C_{27}H_{48}$, a frequency only calculation for this compound took 62 hours at the B3LYP 6-31G* level). However, the hydrogen-stretching-modes are largely decoupled from the lower frequency deformation, heavy atom stretching and torsional motions. In addition, hydrogen stretches can be highly localised. For hydrogen stretching VCD, intense VCD marker bands have been used to identify absolute configuration and solution conformation, without the need for high level calculations.[51] Additionally, in the hydrogen stretching region, simplification of a large molecule into fragments of the molecule encompassing the chiral centres can be used with high reliability for hydrogen stretches, reducing computational demands and allowing application to larger molecules. This is facilitated by the fact that although the hydrogen stretching vibrations from C-H bands in locally achiral portions of the molecule contribute to the absorption spectrum, such modes generate little or no VCD intensities.

The use of such a fragment analysis is described in chapter 4, where the VCD spectra of atenolol have been predicted.

2.4 References

1. J.M. Bijvoet, A.F. Peerdeman, and J. Van Bommel, *Determination of the Absolute Configuration of Optically Active Compounds by means of X-rays.* Nature, 1951. **168**: p. 271 - 272.
2. H.D. Flack, *On Enantiomorph-Polarity Estimation.* Acta Cryst. A, 1983. **39**: p. 876-881.
3. H.D. Flack and G. Bernardinelli, *Absolute structure and absolute configuration.* Acta Crystallographica Section A, 1999. **55**: p. 908-915.
4. H.D. Flack and G. Bernardinelli, *Reporting and evaluating absolute-structure and absolute- configuration determinations.* Journal of Applied Crystallography, 2000. **33**: p. 1143-1148.
5. H.D. Flack, *Chiral and achiral crystal structures.* Helvetica Chimica Acta, 2003. **86**(4): p. 905-921.
6. W.L. Bragg and W.H. Bragg, *The Reflection of X-rays by Crystals.* Nature, 1913. **91**: p. 410.
7. J. Karle, *Isomorphous Substitution and Formulas for Phase Determination.* Acta Cryst., 1966. **21**: p. 273 - 276.
8. A.L. Patterson, *A Fourier Series Method for the Determination of the Components of Interatomic Distances in Crystals.* Physical Review, 1934. **46**: p. 372 - 376.
9. W.C. Hamilton, *Significance Tests on the Crystallogrphic R Factor.* Acta Cryst., 1965. **18**: p. 502 - 510.
10. C. Giacovazzo, H.L. Monaco, D. Viterbo, F. Scordari, G. Gilli, G. Zanotti, and M. Catti, *Fundamentals of Crystallography*, ed. C. Giacovazzo. 1992: Oxford University Press.
11. W. Clegg, *Crystal Structure Determination.* 1998: Oxford Chemistry Primers.
12. W.H. De Camp, *Chiral Drugs - The FDA Perspective on Manufacturing and Control.* Journal of Pharmaceutical and Biomedical Analysis, 1993. **11**(11-12): p. 1167-1172.

13. J. Tomaszewski and M.M. Rumore, *Stereoisomeric Drugs - FDA's Policy Statement and the Impact on Drug Development.* Drug Development and Industrial Pharmacy, 1994. **20**(2): p. 119-139.
14. M. Strong, *FDA policy and regulation of stereoisomers: Paradigm shift and the future of safer, more effective drugs.* Food and Drug Law Journal, 1999. **54**(3): p. 463-487.
15. A.D. Buckingham, *The Theoretical Background to Vibrational Optical-Activity - Introductory Lecture.* Faraday Discussions, 1994(99): p. 1-12.
16. L. Nafie, J.C. Cheng, and P.J. Stephens, *Vibrational Circular Dichroism of 2,2,2-Trifluoro-1-phenylethanol.* Journal of the American Chemical Society, 1975. **97**(13): p. 3842 - 3843.
17. L. Nafie, T.A. Keiderling, and P.J. Stephens, *Vibrational Circular Dichroism.* Journal of the American Chemical Society, 1976. **98**: p. 2715 - 2723.
18. P.L. Polavarapu, *New Spectroscopic Tool - Absolute-Configuration Determination of Pharmaceutical Compounds by Vibrational Circular-Dichroism.* Spectroscopy, 1994. **9**(9): p. 48-55.
19. C. Hsu E and H. G, *Vibrational circular dichroism observed in crystalline a-NiSO4.6H2O and a-ZnSeO4.6H2O between 1900 and 5000 cm-1.* Journal of Chemical Physics, 1973. **59**: p. 4678 - 4685.
20. G. Holzwarth, E.C. Hsu, H.S. Mosher, T.R. Faulkner, and A. Moscowitz, *Infrared Circular Dichroism of Carbon - Hydrogen and Carbon - Deuterium Stretching Modes.* Journal of the American Chemical Society, 1974. **96**(1): p. 251 - 252.
21. L. Nafie, M. Diem, and D.W. Vidrine, *Fourier Transform Infrared Vibrational Circular Dichroism.* Journal of the American Chemical Society, 1979. **101**(2): p. 496 - 498.
22. E.D. Lipp, C.G. Zimba, and L. Nafie, *Vibrational Circular Dichroism in the Mid-Infrared using Fourier Transform Spectroscopy.* Chemical Physics Letters, 1982. **90**(1): p. 1 - 5.
23. L. Nafie, F. Long, T. Freedman, H. Buijs, A. Rilling, J.-R. Roy, and R.K. Dukor. *The Determination of Enantiomeric Purity and Absolute Configuration by Vibrational Circular Dichroism Spectroscopy.* in

Fourier Transform Spectroscopy; Eleventh International Conference. 1997. Athens: Woodbury.

24. L.A. Nafie and T.B. Freedman, *Vibronic Coupling Theory of Infrared Vibrational Transitions.* Journal of Chemical Physics, 1983. **78**(12): p. 7108-7116.
25. P.J. Stephens, *Theory of Vibrational Circular-Dichroism.* Journal of Physical Chemistry, 1985. **89**(5): p. 748-752.
26. L. Nafie, *Adiabatic molecular properties beyond the Born-Oppenheimer approximation. Complete adiabatic wave functions and vibrationally induced electronic current density.* Journal of Chemical Physics, 1983. **79**(10): p. 4950 - 4957.
27. A.D. Buckingham, P.W. Fowler, and P.A. Galwas, *Velocity-dependent property surfaces and the theory of vibrational circular dichroism.* Chemical Physics, 1987. **112**: p. 1 - 14.
28. F. Long, T. Freedman, and L. Nafie. *Fourier Transform Vibrational Circular Dichroism of Small Pharmaceutical Molecules.* in *Fourier Transform Spectroscopy; Eleventh International Conference.* 1997. Athens: Woodbury.
29. L.A. Nafie, *Dual polarization modulation: A real-time, spectral-multiplex separation of circular dichroism from linear birefringence spectral intensities.* Applied Spectroscopy, 2000. **54**(11): p. 1634-1645.
30. L.A. Nafie, H. Buijs, A. Rilling, X.L. Cao, and R.K. Dukor, *Dual source Fourier transform polarization modulation spectroscopy: An improved method for the measurement of circular and linear dichroism.* Applied Spectroscopy, 2004. **58**(6): p. 647-654.
31. S.J. Cianciosi, N. Ragunathan, T.B. Freedman, L.A. Nafie, and J.E. Baldwin, *Racemization and Geometrical Isomerization of (-)-(R,R)-Cyclopropane-1,2-2h2.* Journal of the American Chemical Society, 1990. **112**(22): p. 8204-8206.
32. S.J. Cianciosi, N. Ragunathan, T.B. Freedman, L.A. Nafie, D.K. Lewis, D.A. Glenar, and J.E. Baldwin, *Racemization and Geometrical Isomerization of (2s,3s)- Cyclopropane-1-C-13-1,2,3-D3 at 407-Degrees-C - Kinetically Competitive One-Center and 2-Center Thermal*

Epimerizations in an Isotopically Substituted Cyclopropane. Journal of the American Chemical Society, 1991. **113**(5): p. 1864-1866.

33. L.A. Nafie and T.B. Freedman, *Vibrational circular dichroism: An incisive tool for stereochemical applications.* Enantiomer, 1998. **3**(4-5): p. 283-297.

34. R.D. Shah and L. Nafie, *Spectroscopic Methods for Determining Enantiomeric Purity and Absolute Configuration in Chiral Pharmacuetical Molecules.* Drug Discovery and Development, 2001. **4**(6): p. 764 - 775.

35. C.N. Guo, R.D. Shah, R.K. Dukor, X.L. Cao, T.B. Freedman, and L.A. Nafie, *Determination of enantiomeric excess in samples of chiral molecules using Fourier transform vibrational circular dichroism spectroscopy: Simulation of real-time reaction monitoring.* Analytical Chemistry, 2004. **76**(23): p. 6956-6966.

36. F.J. Devlin, P.J. Stephens, J.R. Cheeseman, and M.J. Frisch, *Ab initio prediction of vibrational absorption and circular dichroism spectra of chiral natural products using density functional theory: alpha-pinene.* Journal of Physical Chemistry A, 1997. **101**(51): p. 9912-9924.

37. A. Aamouche, F.J. Devlin, and P.J. Stephens, *Structure, vibrational absorption and circular dichroism spectra, and absolute configuration of Troger's Base.* Journal of the American Chemical Society, 2000. **122**(10): p. 2346-2354.

38. T.B. Freedman, X.L. Cao, R.V. Oliveira, Q.B. Cass, and L.A. Nafie, *Determination of the absolute configuration and solution conformation of gossypol by vibrational circular dichroism.* Chirality, 2003. **15**(2): p. 196-200.

39. J.E. Rode and J.C. Dobrowolski, *VCD technique in determining intermolecular H-bond geometry: a DFT study.* Journal of Molecular Structure-Theochem, 2003. **637**: p. 81-89.

40. P.J. Stephens, D.M. McCann, F.J. Devlin, T.C. Flood, E. Butkus, S. Stoncius, and J.R. Cheeseman, *Determination of molecular structure using vibrational circular dichroism spectroscopy: The keto-lactone product of Baeyer- Villiger oxidation of (+)-(1R,5S)-bicyclo 3.3.1 nonane-2,7- dione.* Journal of Organic Chemistry, 2005. **70**(10): p. 3903-3913.

41. H.G. Grant and W.G. Richards, *Computational Chemistry.* 1995: Oxford Chemistry Primers.

42. P.W. Atkins and R.S. Friedman, *Molecular Quantum Mechanics.* 2000: Oxford University Press.

43. P.J. Stephens, F.J. Devlin, C.S. Ashvar, C.F. Chabalowski, and M.J. Frisch, *Theoretical Calculation of Vibrational Circular-Dichroism Spectra.* Faraday Discussions, 1994(99): p. 103-119.

44. A.P. Scott, Radom, L., *Harmonic vibrational frequencies: An evaluation of Hartree- Fock, Moller-Plesset, quadratic configuration interaction, density functional theory, and semiempirical scale factors.* Journal of Physical Chemistry, 1996. **100**(41): p. 16502-16513.

45. M.D. Halls, J. Velkovski, and H.B. Schlegel, *Harmonic frequency scaling factors for Hartree-Fock, S-VWN, B- LYP, B3-LYP, B3-PW91 and MP2 with the Sadlej pVTZ electric property basis set.* Theoretical Chemistry Accounts, 2001. **105**(6): p. 413-421.

46. G. Rauhut and P. Pulay, *Transferable Scaling Factors for Density-Functional Derived Vibrational Force-Fields (Vol 99, Pg 3096, 1995).* Journal of Physical Chemistry, 1995. **99**(39): p. 14572-14572.

47. R.D. Johnson, *Computational Chemistry Comparison and Benchmark DataBase.* October 2003.

48. F.J. Devlin, J.W. Finley, P.J. Stephens, and M.J. Frisch, *Ab-Initio Calculation of Vibrational Absorption and Circular- Dichroism Spectra Using Density-Functional Force-Fields - a Comparison of Local, Nonlocal, and Hybrid Density Functionals.* Journal of Physical Chemistry, 1995. **99**(46): p. 16883-16902.

49. T.B. Freedman, F.J. Long, M. Citra, and L.A. Nafie, *Hydrogen-stretching vibrational circular dichroism spectroscopy: Absolute configuration and solution conformation of selected pharmaceutical molecules.* Enantiomer, 1999. **4**(2): p. 103-119.

50. V. Andrushchenko, H. Wieser, and P. Bour, *B-Z conformational transition of DNA monitored by vibrational circular dichroism. Ab initio interpretation of the experiment.* Journal of Physical Chemistry B, 2002. **106**(48): p. 12623-12634.

51. T. Freedman, D. Gigante, E. Lee, and L. Nafie. *C-H Stretching VCD of alpha-Hydroxy Acids and Related Molecules.* in *Fourier Transform Spectroscopy; Eleventh International Conference.* 1997. Athens: Woodbury.

Chapter 3 - Development of the VCD Method

The use of VCD as a standard method of absolute stereochemistry determination within the pharmaceutical industry has been hindered by both the experimental difficulties encountered in obtaining the VCD spectra and the complexity encountered in modelling VCD data. A more straightforward and reliable method of data collection is required for the technique to become standard practice. In this chapter the development of such a method is described. The challenges to overcome in developing this VCD data collection protocol include instrumental aspects, sample preparation and handling, and prediction or modelling of the data.

The design of the VCD spectrometer plays a major role in determining the quality of VCD spectra that the user is able to collect. A good VCD spectrometer requires a clean optical path that avoids signal artefacts originating from the optics, and a detector of sufficient sensitivity to detect the relatively weak VCD signal. As will be seen in this chapter and was seen in chapter 2, having a zero baseline provides an excellent foundation for collection of good quality VCD spectra; however, not all commercially available spectrometers include this capacity. Optimisation of the sample collection parameters for the particular instrument is an important part of being able to collect reliable VCD spectra. Simply using the experimental conditions from published works may not be possible when a different instrument to that used in the publication is being employed.

Sample preparation and handling can vary for the type of sample being investigated. One of the most important aspects of VCD spectroscopy for absolute stereochemistry determination within the pharmaceutical industry is that it provides an alternate / complementary technique to single crystal XRD. Most importantly, the sample does not have to be a single crystal, which can often be difficult to grow. Favoured sampling methods include using neat liquids, which generally give clear strong VCD spectra, or solutions. The use of solution sampling methods requires an achiral solvent, which will not interfere with the collection of the VCD spectrum in the region of interest. As such, the solvent cannot have strong absorption bands in the infrared in the area of study. Problems are also encountered when aggregation of the chiral sample in solution occurs, altering the conformation of the molecule that is dominant in solution and leading to changes in the observed VCD spectrum. These changes have to be accounted for in the modelling and prediction of the VCD spectrum for that molecule. This requires the modelling of dimer pairs and inter- and intra-molecular hydrogen bonding within the calculation. Traditionally, quantum mechanical calculations have been seen as a specialised field, too complex for the standard chemist to undertake. However, the development of programs such as Gaussian with a user friendly interface and clearly displayed results has lead to quantum mechanical calculations being available to a much wider audience. Knowing how to adjust the calculation for each molecule, however, still requires time and experience, as certain classes of compounds need to be handled with certain types of methods, as will be illustrated in this chapter and the next.

3.1 Sample Preparation and Sampling Techniques

3.1.1 Measurement of Pure Liquids

Collection of the VCD spectra of pure liquids is the simplest measurement to perform, as there are no solvent effects or concentration issues to contend with. A schematic of the standard type of solution cell used for this technique (and for the solution state measurements, discussed in the next section) is shown in figure 3.1. These cells can either be demountable, like the one shown, or be sealed with a fixed path length. The demountable cells allow the path length to be altered by changing the spacer. The spacer is generally made of Teflon and can be purchased in many different thicknesses, from about 5 to 100 μm. Using a larger path length cell increases the amount of sample present in the alternating IR beam, and so increases the amplitude of the VCD signal seen. However, as previously discussed, if the total IR absorbance is too high the VCD signal is hidden.

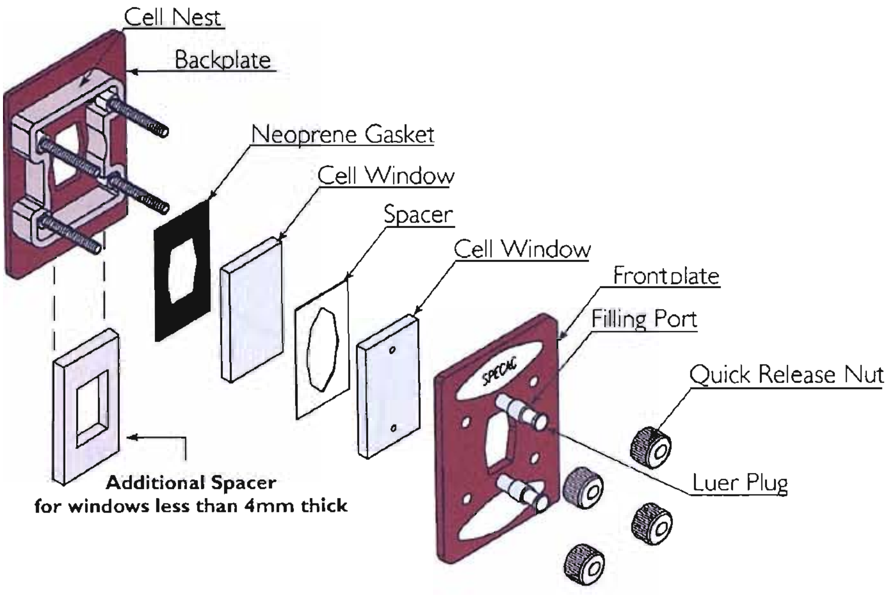

Figure 3.1 Schematic of the Specac Omni Cell^{TM} demountable solution cell

α-Pinene (figure 3.2) gives an ideal VCD spectrum from a neat liquid, as demonstrated in the comparison of the VCD spectra for the two enantiomers, which gives a perfect mirror image as shown in figure 3.3.

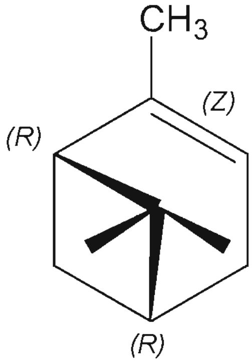

Figure 3.2 (*R*)-(+)-α-Pinene

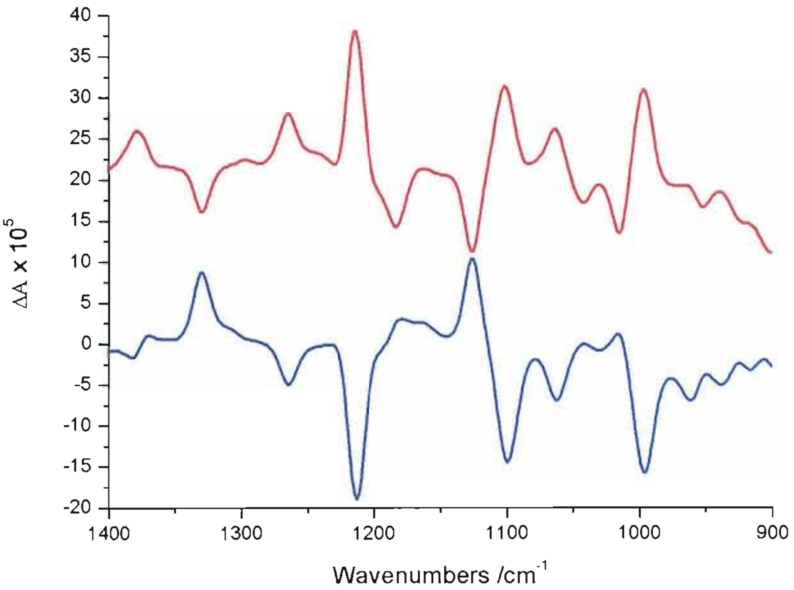

Figure 3.3 Comparison of experimental VCD spectra for (*R*)-(+)-α-pinene (red line) and (*S*)-(-)-α-pinene (blue line), collected on a single PEM spectrometer, in a 25 μm path length solution cell, 1024 scans and 16 cm^{-1} resolution. Spectra offset for clarity.

Due to the ease of this data collection, α-pinene is commonly used as a reference standard within VCD spectroscopy and can be measured to determine if the spectrometer is performing correctly.

3.1.2 Solution Method

Solution state measurements are the ideal technique for VCD spectroscopy as the sample is completely randomly oriented within the solvent. The majority of published VCD spectra have been collected in this way,[1-5] the exception being the VCD spectra of protein films.[6-8]

The solution cell (figure 3.1) is used for this technique; however, problems can be experienced with these cells, as leaking can occur during data collection. If this happens, the concentration of the sample in solution alters, and the presence of air in the cell, with its associated water vapour, can disrupt the spectra collected.

Solution state measurements are highly dependent upon the concentration of sample in solution. This sensitivity of the VCD spectra to the concentration was highlighted by comparing the VCD spectra of (*R*)-(+)-α-pinene as varying concentration solutions in methanol and acetone. Experiments were performed at 16 cm^{-1} resolution, 4096 scans, 25 μm path length cell and with a collection time of ~20 minutes on the single PEM spectrometer. The results of this study are shown in figure 3.4 and are compared to the VCD spectrum of neat (*R*)-(+)-α-pinene collected under identical conditions. The parent IR from these measurements did not contribute any additional information to that shown below, as a simple decrease in the intensity of the bands was observed. However, where bands in the IR are no longer observed, VCD signal is also no longer observed at this band. The methanol spectra are shown over a reduced range, due to a large solvent absorption band at ~1000 cm^{-1}.

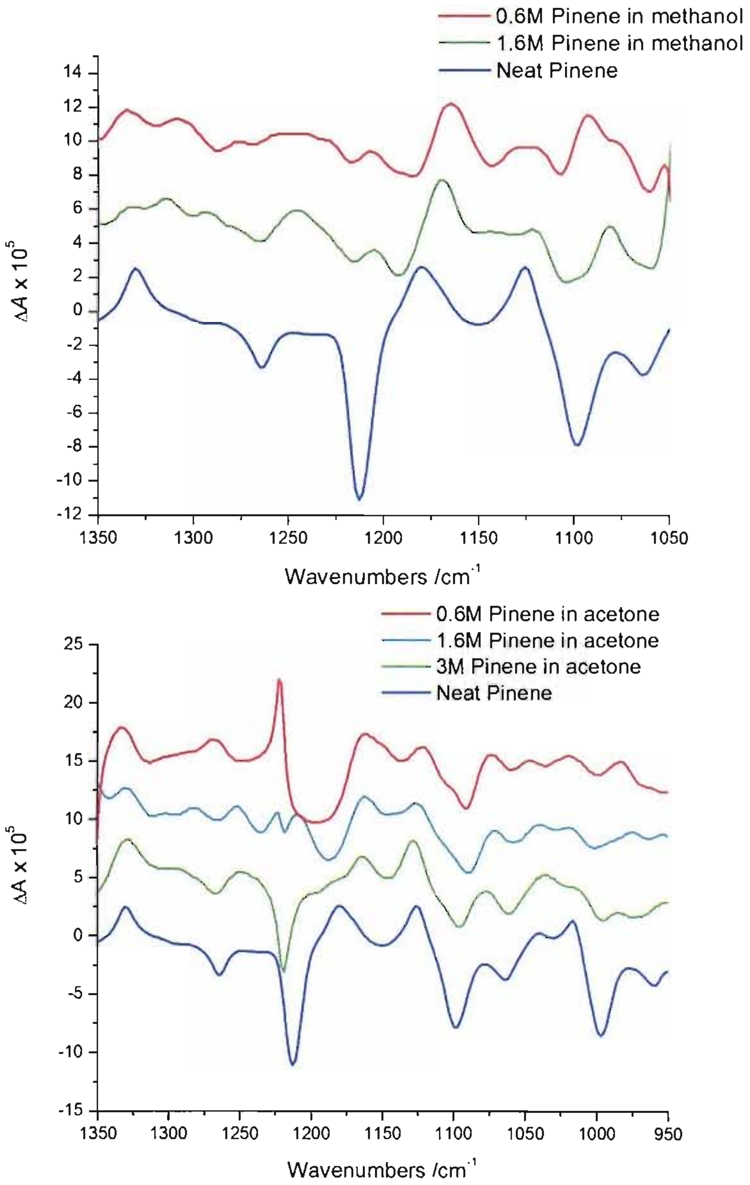

Figure 3.4 Effect of decreasing concentration of (*R*)-(+)-α-pinene as solutions in methanol (top) and acetone (bottom) on its VCD spectrum. Spectra offset for clarity.

In comparing the VCD spectra of the neat liquid and the solutions differences are observed. As expected the amplitudes of the VCD spectra are dependent upon the concentration of the solute. In addition the apparent noise levels increase as the concentration decreases. In fact the reliability of the VCD spectrum of 0.6 M α-pinene in acetone is fairly poor and the peak at 1220 cm^{-1} is thought to be due to a large solvent absorption band distorting the spectra. A shift in the band positions is also observed, which is dependent on the nature of the solvent, as illustrated in figure 3.5 where the spectra in methanol and acetone are compared. The positions of bands in the IR spectra of molecules are known to be sensitive to the environment in which the molecules are located owing to the sensitive changes in the bonding brought about by intermolecular interactions. These shifts are reflected in the VCD spectra.

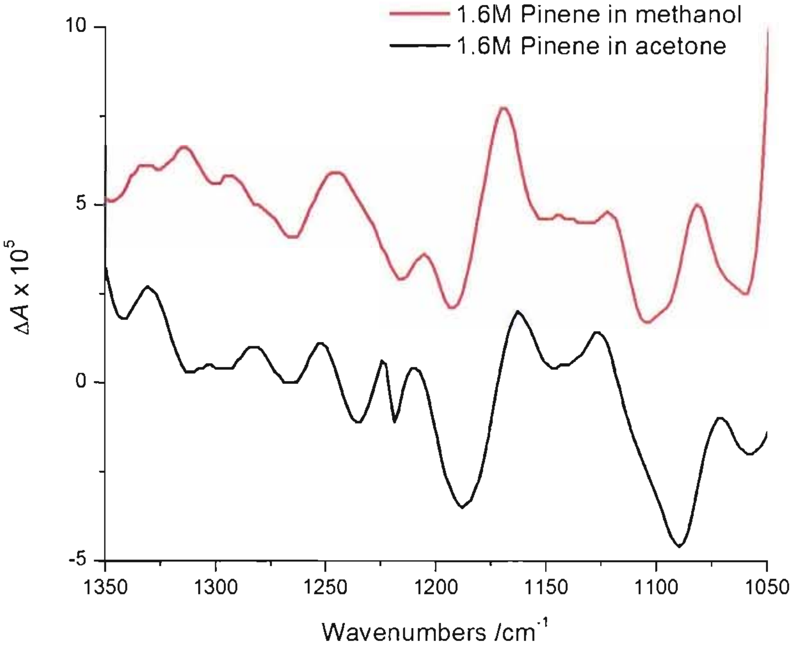

Figure 3.5 Comparison of the 1.6M solutions of α-pinene in methanol (red line) and acetone (black line)

Two of the stronger bands that show a shift in the VCD spectra are at 1210 and 1100 cm^{-1} in the spectrum of the neat liquid. These shift to 1180 and 1110 cm^{-1} in the spectrum of the solution in acetone, and to 1240 and 1095 cm^{-1} in the spectrum of the solution in methanol. Figures 3.6 and 3.7 show the vibrations responsible for these bands; the band at 1210 cm^{-1} derives from a combined vibration, whereas the 1100 cm^{-1} band is from a simple antisymmetric ring breathing. As the band at 1210 cm^{-1} is more complicated it is more easily perturbed when solvated, leading to the larger differences between the positions of the band in the solutions as compared to the neat liquid. There is a much smaller difference between the positions of the 1100 cm^{-1} band between the neat liquid and the solutions.

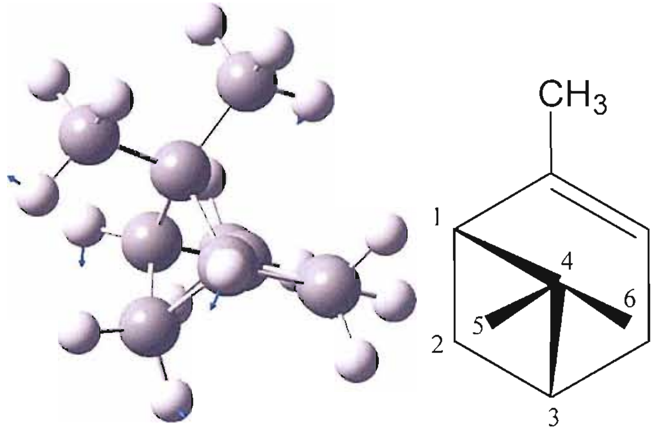

Figure 3.6 Illustration of the vibrations responsible for the band in the (*R*)-(+)-α-pinene VCD spectrum at 1210cm^{-1} for the neat liquid, 1180 cm^{-1} for the acetone solution and 1240 cm^{-1} in the methanol solution. The picture on the left shows the displacement vectors in blue that happen during the vibration. The vibrations are responsible for the band are a symmetric ring breathing for the ring comprising atoms 1-2-3-4, and an antisymmetric stretch of atoms 5-4-6.

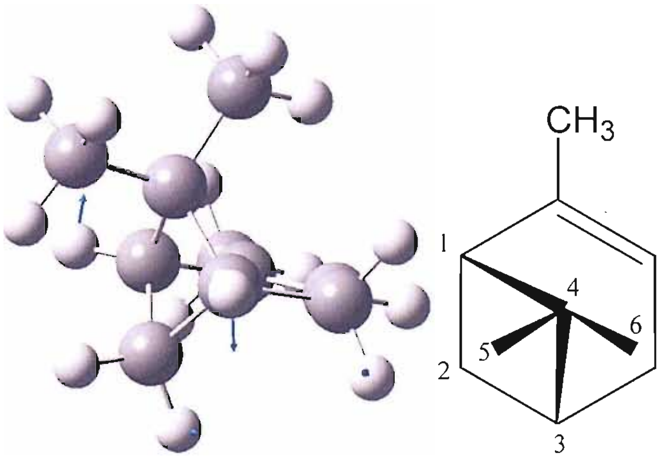

Figure 3.7 Illustration of the vibrations responsible for the band in the (*R*)-(+)-α-pinene VCD spectrum at 1100cm^{-1} for the neat liquid, 1110 cm^{-1} for the acetone solution and 1095 cm^{-1} for the methanol solution. The picture on the left shows the displacement vectors in blue that happen during the vibration. The vibration responsible for this band is an antisymmetric ring breathing for the ring comprising atoms 1-2-3-4.

A further study of the effect of concentration on the VCD spectrum was carried out using (*R*) and (*S*)-methyl mandelate (figure 3.8). Here the VCD spectra for the enantiomer pairs were compared at three different concentrations (figure 3.9).

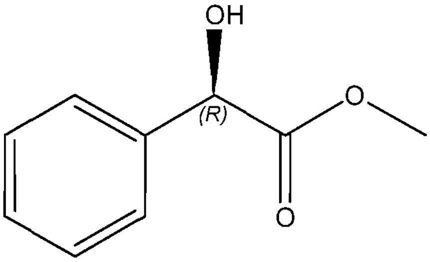

Figure 3.8 Methyl-(*R*)-mandelate

The 2 M spectra show clear mirror image spectra for the band at 1275 cm^{-1}, this peak is also seen as a mirror image for the two lower concentrations. However, the peak at 1180 cm^{-1} is not a mirror image for the 2 M concentration spectra, but is a mirror image for both the lower concentrations, and increases in relative intensity on going to the lower concentrations. This information suggests that the vibration causing this band is being perturbed as the concentration increases, possibly due to dimer formation and hydrogen bonding. It is interesting to observe the increase in relative intensity of the 1275 and 1180 cm^{-1} bands in the 0.5 M solution spectra.

The noise levels for each of the (*R*) enantiomer VCD spectra have been shown by the black lines to the left of the picture. Comparison of the size of the noise to the size of the largest VCD peak gives an idea of the reliability of the VCD spectrum observed (signal to noise ratio). The signal to noise ratio for the 0.5 M solutions is very poor and only the two largest peaks (at 1275 and 1180 cm^{-1}) can be thought of as reliable. However, this reliability is confirmed by the presence of these bands in the higher concentration spectra and by the fact that the two enantiomers show mirror image bands at these positions.

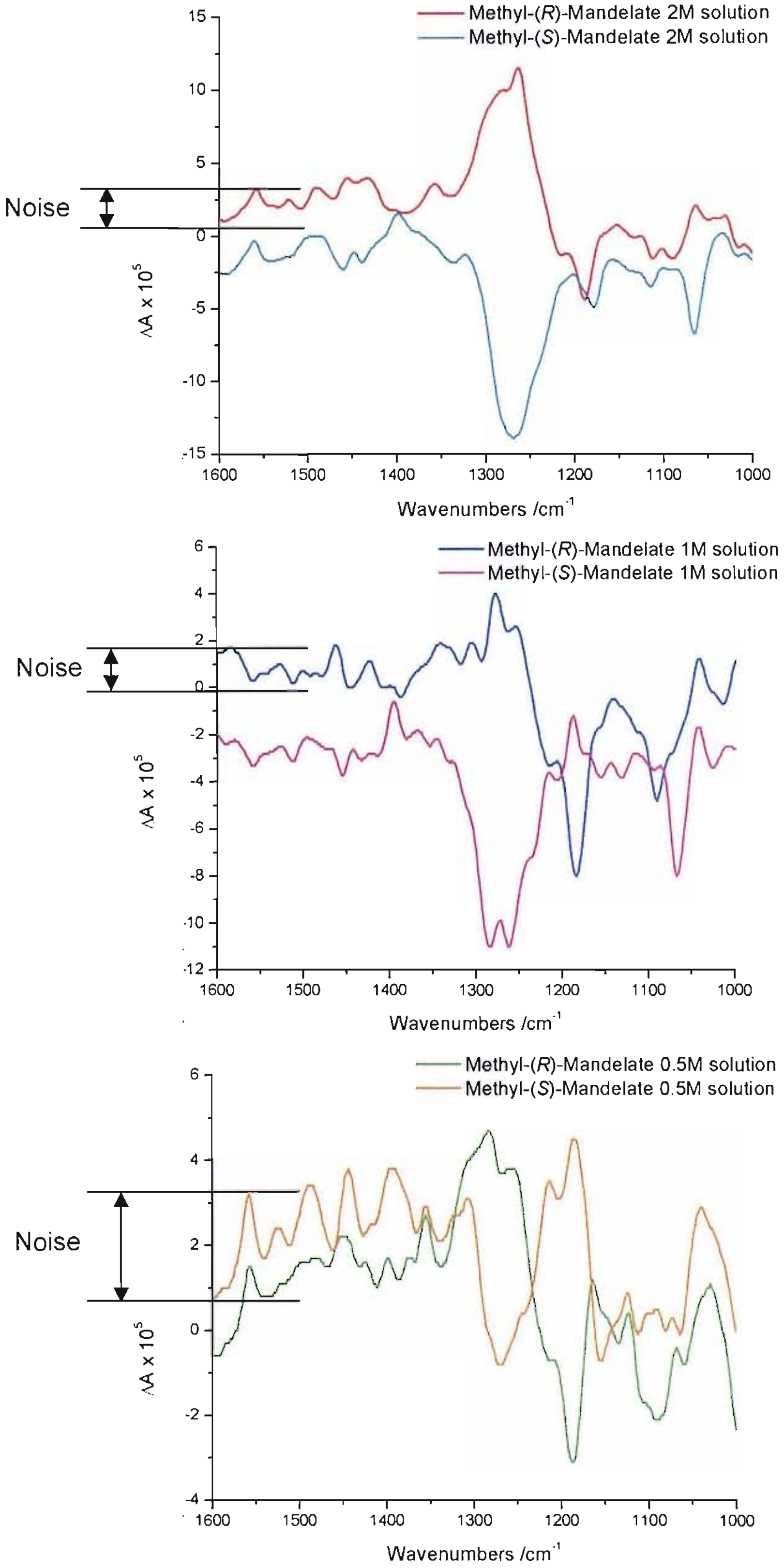

Figure 3.9 VCD spectra of (*R*)- and (*S*)-methyl mandelate at 2 M (top), 1 M (middle) and 0.5 M (bottom) concentrations in $CDCl_3$. Spectra collection on single PEM spectrometer at 16 cm^{-1} resolution, 4096 scans, 25 μm path length cell. Solvent spectrum subtracted.

Comparison of the parent IR spectra for the (*R*) and (*S*) enantiomers at 2M concentration shows nearly identical spectra, figure 3.10.

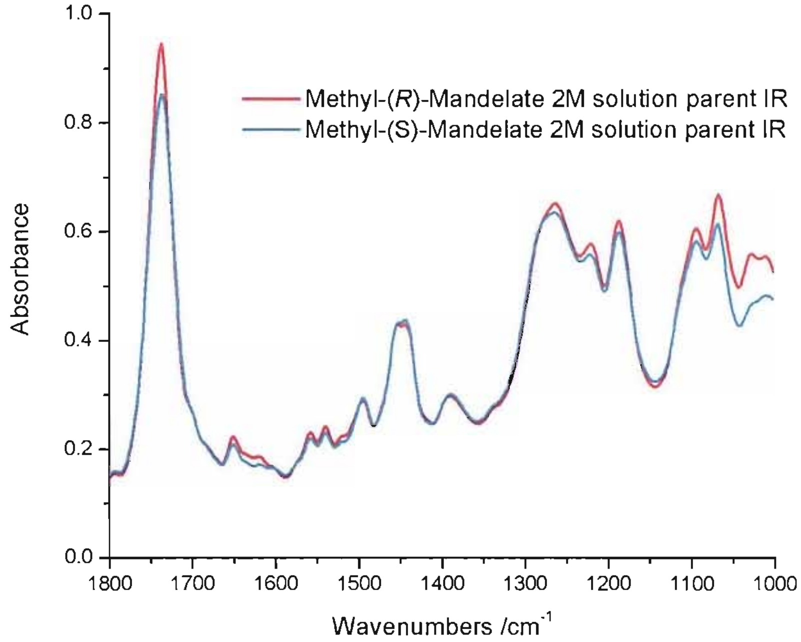

Figure 3.10 Parent IR spectra seen from (*R*)- and (*S*)-methyl mandelate, corresponding to the VCD spectra in the top frame of figure 3.7.

As well as the sensitivity of solution state measurements to concentration, which can make the measurements tricky and time-consuming, there are other problems associated with this technique. These include times when no suitable achiral solvent is available for the compound under study; compounds may be highly insoluble, so that a high enough concentration can not be put in solution for the VCD signal to be observed; and aggregation in solution may occur. There is also the possibility that samples in solution will aggregate if the concentration is too high. As we have seen however, concentrations need to be high if a signal is to be observed with the single PEM spectrometer.

Using the dual PEM spectrometer a VCD measurement was carried out on (-)-ephedrine (figure 3.11) in C_2Cl_4.

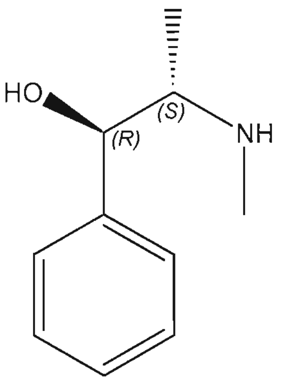

Figure 3.11 (-)-Ephedrine

Aggregation of the compound in solution can lead to changes in the IR and VCD spectra over time, as can be seen during a collection in the hydrogen stretching region (figure 3.12). Clear changes in the IR and VCD spectra are taking place as the collection time increases, both in peak intensity and in relative intensity. However, in this case, it is interesting to see in the VCD spectra that while the amplitudes of the peaks changes, the positions remain the same. Further details of these changes will be discussed in chapter 4.

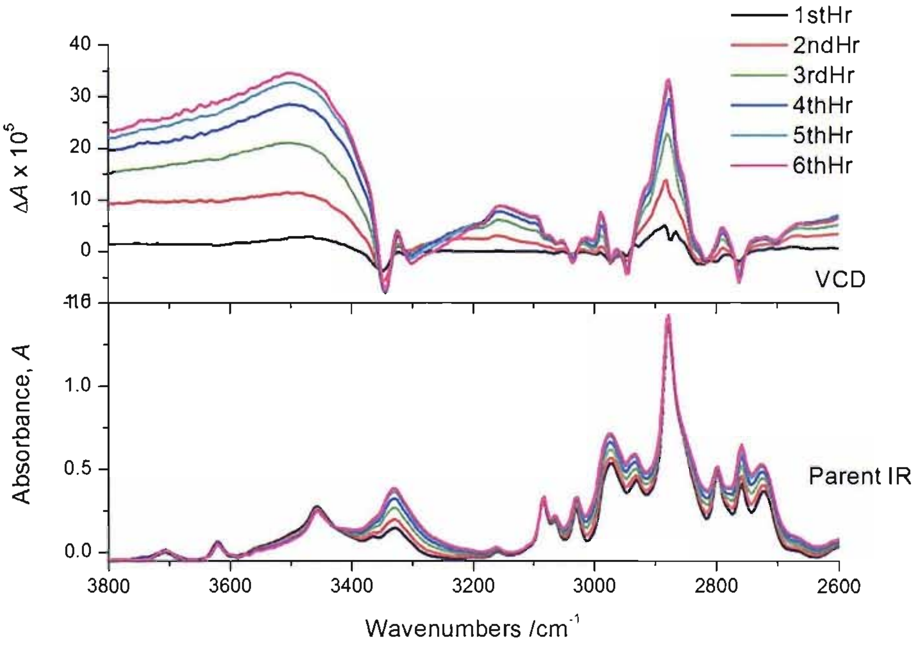

Figure 3.12 Aggregation of (-)-ephedrine in C_2Cl_4 during a data collection causes changes in both the parent IR (lower frame) and VCD (upper frame) spectra. Data collected on a dual PEM spectrometer, in a 1 cm path length cell, at 4 cm^{-1} resolution, six hour collection time and a concentration of 0.0024 M.

One of the key components in determining whether a good solution VCD spectrum can be obtained is the choice of instrument. The differences and relative advantages and disadvantages of the spectrometers were discussed in chapter 2. These differences are amplified when handling tricky solution state measurements. The dual PEM spectrometer is shown to be much more sensitive, as illustrated in figure 3.13 below, where the spectra for (2*S*)-captopril are compared for the single PEM and dual PEM spectrometers.

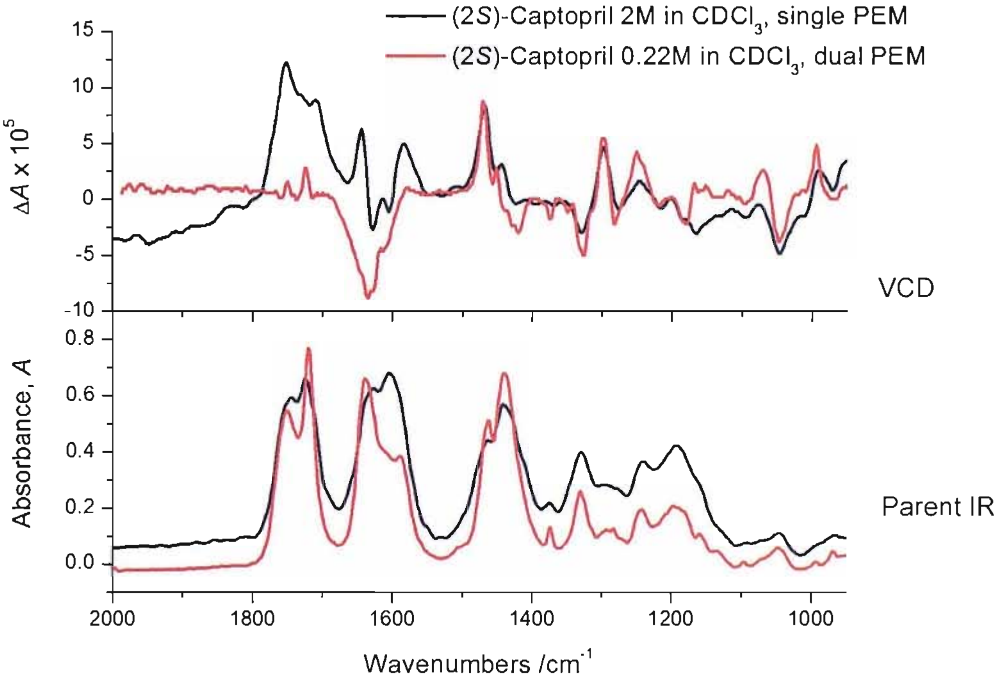

Figure 3.13 Comparison of the IR (lower frame) and VCD (upper frame) spectra of (2*S*)-Captopril, from a 2 M solution in CDCl$_3$ measured on the single PEM spectrometer and a 0.22 M solution in CDCl$_3$ measured on the dual PEM spectrometer.

These spectra also illustrate the improved baseline of the dual PEM spectrometer, as the VCD spectrum from the dual PEM spectrometer has a flat baseline, whereas the VCD spectrum from the single PEM spectrometer appears to have a curve to it, making assignment of the directions of the peaks difficult.

As we have seen, the effect of concentration of sample in solution on the VCD spectrum is a very important one. The more sensitive the instrument is, the lower the concentration of sample in solution necessary to observe a reliable VCD spectrum. The length of data collection (i.e. number of scans / time), and the path length of the cell (which is effectively another way of increasing the concentration of solution, by putting more sample in the path of the beam) also affect the quality of the VCD spectrum. Increasing path length may be preferable to increasing concentration in solution for some molecules that are prone to aggregation or hydrogen-bonding in solution. Aggregation or hydrogen-bonding can alter the band position within the spectrum, hence more complicated calculations are required to take into account these effects and accurately predict the VCD spectrum.

Due to the problems experienced with solution state techniques, alternative techniques are required. The obvious choice is to use techniques which are routinely used within the field of IR spectroscopy, such as KBr disc and nujol mull techniques. No reference to the use of such standard IR techniques within the area of VCD measurements could be found in the literature, and hence an investigation into using both of these methods was carried out. With the advantage of being able to use different sampling techniques, a suitable method should work for even the most troublesome compounds.

3.1.3 KBr Disc Technique

The KBr disc technique has long been used in the field of IR spectroscopy and is one of the basic methods taught in undergraduate chemistry labs. As such this technique is standard practice for characterisation within the pharmaceutical industry. In KBr discs the concentrations are generally kept low, ~0.25 % w/w (weight per weight), again to avoid saturation of the IR absorbance.

Although the technique of using KBr disc for VCD has not been published to our knowledge, there are instances where it has been used for measurement of circular dichroism (CD) spectra, which are taken in the electronic region of the spectrum.[9, 10] Kuroda and Honma [9] have discussed possible problems that might be encountered in solid state CD, including depolarisation: this can occur if the particle size is not small enough and homogeneous, and may adversely affect the CD signal. Also during the preparation of KBr discs, the pressure exerted upon the disc occasionally influences the CD spectra, through interaction of the compound with the K^+ or Br^- ions (although the occurrence of this phenomenon is rare). In the paper by Minguet et al.,[10] extensive experimental detail is given: enabling accurate reproduction of the experimental conditions that need to be employed to obtain reproducible CD spectra. Preparation of the KBr disc was given much consideration, and the effects of grinding time of the KBr-compound mixture, thickness and concentration of discs, pressure in disc preparation, band-width of the incident light and rotation of the disc in the machine and averaging of spectra were noted. The success of the technique is stated as requiring a random orientation of the crystallites in order to avoid the linear dichroic effects, which may swamp the circular dichroism. It was concluded that simple grinding of the KBr-compound mixture in an agate pestle and mortar for 10 minutes gave reproducible results. Thickness of the sample was found to be optimum at 0.8 mm, with a range of 0.4 - 1.0 mm providing good results. Discs prepared under the highest pressure employed, 10 ton for 10 minutes, were found to be more transparent and gave better spectra than those prepared at lower pressure. It was noted that application of such high pressures may cause conversion of one polymorph to the other. This should not be a problem for application to VCD spectra collection as our main target is to establish the absolute stereochemistry of the compound rather than its conformation.

For the KBr disc technique, very little sample preparation is required; grinding of the sample in a pestle and mortar is the only step required before addition to the microcognised KBr powder. A disc is then pressed, and the VCD measurement can then be made. For background subtraction, a blank KBr disc of the same thickness has to be pressed, the VCD and IR spectra of which can then be directly subtracted from the sample spectra. Providing that the sample is well dispersed within the KBr, there should be no orientation effects and the spectra obtained from any part of the sample KBr disc should be identical.

A good example of a successful KBr disc data collection is shown in figure 3.14. The solution and KBr data show good similarities in both the IR and VCD spectra, showing that the KBr disc technique is a valid method for VCD measurements. However, some of the peaks in the solution VCD are not found in the KBr disc VCD spectrum. It is important to note that the peak at 1260 cm^{-1}

seen clearly in the KBr disc IR spectra is possibly due to the presence of a silicon grease contaminant, which is not present in the solution spectra or the blank KBr disc spectra.

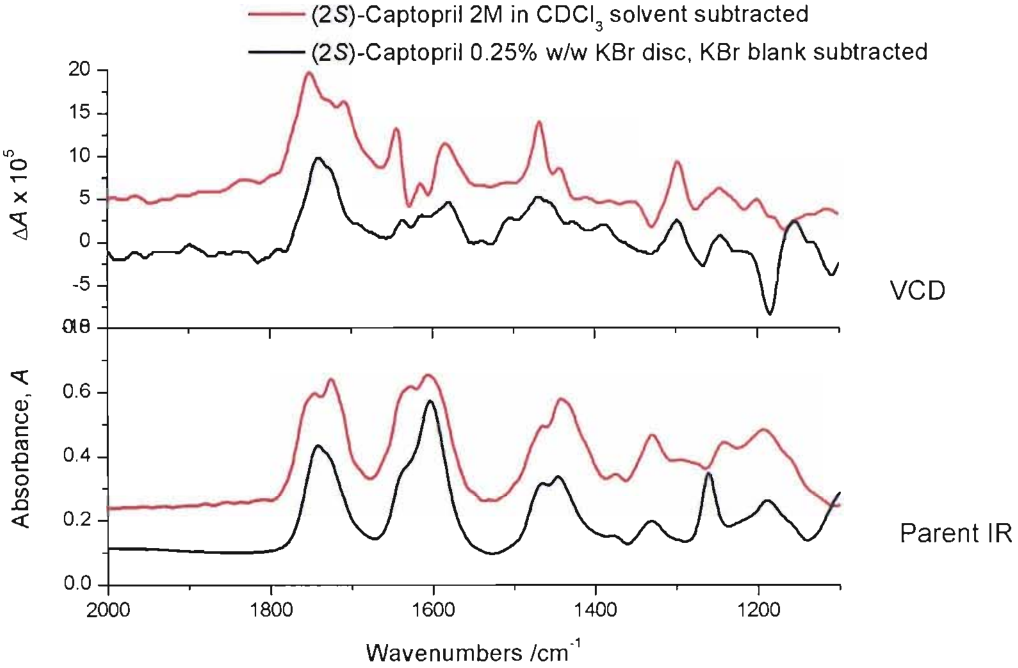

Figure 3.14 Comparison of (2S)-Captopril IR (lower frame) and VCD (upper frame) spectra, from 2 M solution in $CDCl_3$ and a 0.25 % w/w KBr disc. Collected on single PEM spectrometer, 4096 scans, 16 cm^{-1} resolution, with solution spectrum in 25 μm path length cell. Spectra offset for clarity.

Unfortunately, reproducibility is an issue when using the KBr disc technique. For example, the VCD spectra from one KBr disc was not found to be identical when measured from two different points on the disc. The two data collections of (2*S*)-captopril from the same KBr disc, rotated by 180 ° are shown in figure 3.15.

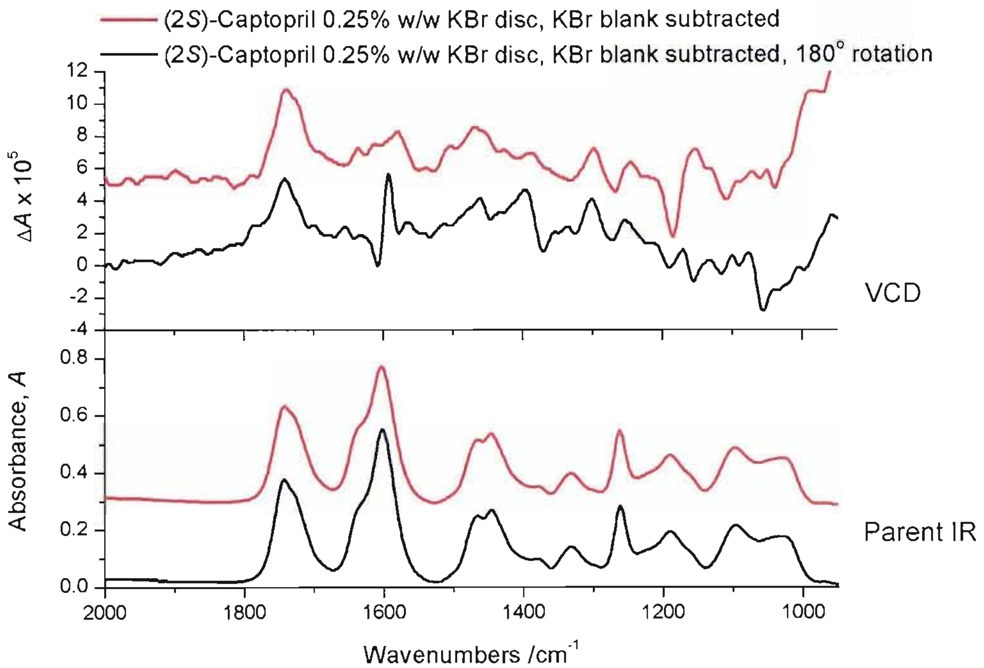

Figure 3.15 IR (lower frame) and VCD (upper frame) of (2*S*)-Captopril as a 0.25 % w/w KBr disc, two collections shown differ by a 180 ° rotation of the disc. Data collected upon a single PEM spectrometer, 4096 scans, 16 cm^{-1} resolution, with blank KBr spectra subtracted. Spectra offset for clarity.

Following these instances where KBr disc measurements do not give good VCD spectra, either due to extremely small VCD signal leading to irreproducible results or possibly due to poor dispersion of the sample within the KBr, which can occur if the sample does not grind up well, the KBr disc technique was abandoned.

3.1.4 Nujol Mull Technique

The nujol mull sampling method is again a well practised technique within the field of IR spectroscopy and taught in undergraduate chemistry labs. The method again involves grinding the sample, followed by mixing it with a couple of drops of nujol oil: this paste is then spread onto a BaF_2 window, and sandwiched between that and another window. The sample is then ready for measurement of the VCD spectra. This method involves the quickest sample preparation of the three techniques mentioned. For background subtraction a blank nujol oil spectrum is required, with the amount of nujol oil being of the same thickness layer as the sample mull. To ensure reproducibility a thin Teflon spacer may be used. Nujol^{TM} oil is a high purity mineral oil with a relatively straightforward IR spectrum having absorptions only at 1380 - 1380 cm^{-1} and at 720 cm^{-1}.

Atenolol (figure 3.16) proved an extremely difficult compound to obtain a good solution VCD spectrum from, mostly due to solubility issues and the extremely small VCD signal present when the compound is solvated. Atenolol is insoluble in $CDCl_3$, which is the ideal solvent for VCD measurements as it is not chiral and has no IR absorbances in the region of interest (2000 – 800 cm^{-1}). D4 methanol proved the only suitable solvent, although it has strong absorbances in the region of interest, which hides the VCD signal at this point, limiting the spectral range to 1800 – 1200 cm^{-1}. The small signal in solution is partly due to the solvent IR absorbances hiding the signal, and may also be due to the presence of a large number of conformers in solution with overlapping VCD bands; if this were the case then a longer data collection would be necessary as the overlapping bands, if opposite in sign, will cause the VCD signal to shrink even more. However, even a 12-hour collection, such as the one shown in figure 3.17, is insufficient in the case of atenolol.

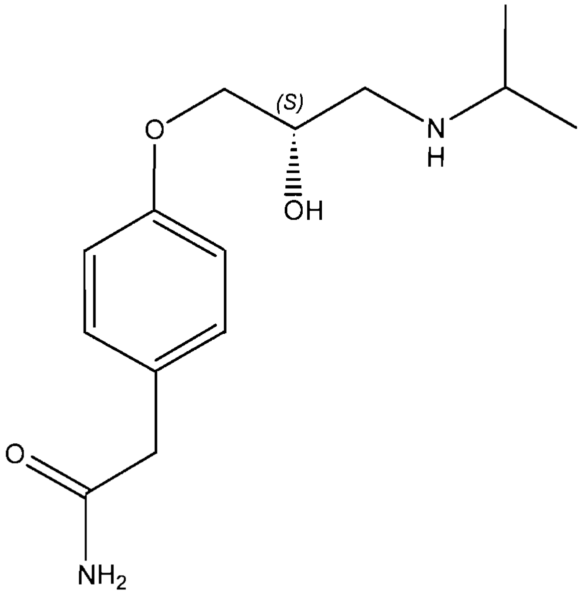

Figure 3.16 (*S*)-Atenolol

Collection of a VCD spectrum from a nujol mull in this case provided data of sufficient quality for comparison with the predicted spectra, whereas the solution data had such a poor signal-to-noise ratio that no conclusions could be drawn from the VCD spectrum. Figure 3.17 shows the solution in D_4 methanol and nujol mull spectra for (*S*)-atenolol.

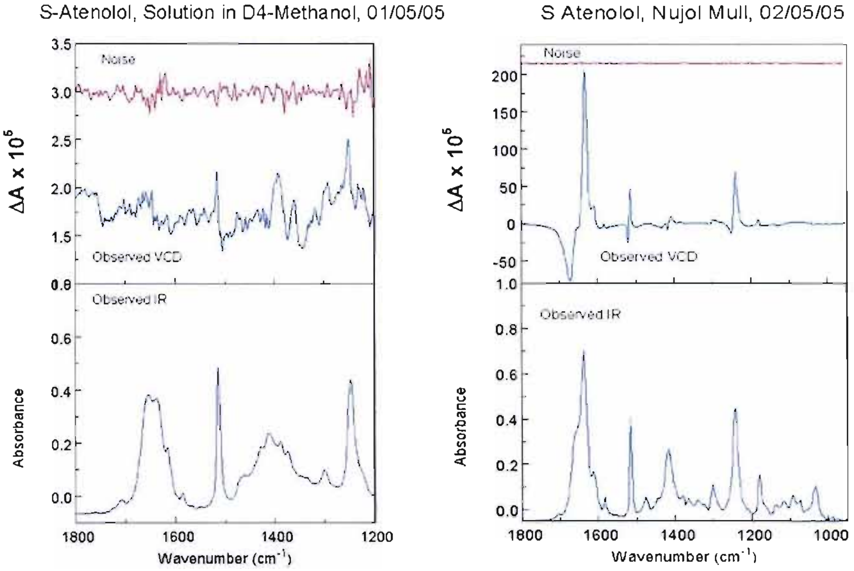

Figure 3.17 IR and VCD spectra with signal-to-noise ratio, for (a) (*S*)-atenolol as a solution in D_4-methanol and (b) (*S*)-atenolol as a nujol mull.

Figure 3.18 shows the nujol mull data for both enantiomers of atenolol. Despite being of different intensities (attributed to the different concentrations of the compound in the nujol mull) the VCD spectra still show excellent mirror image peaks (see close up of VCD on the right).

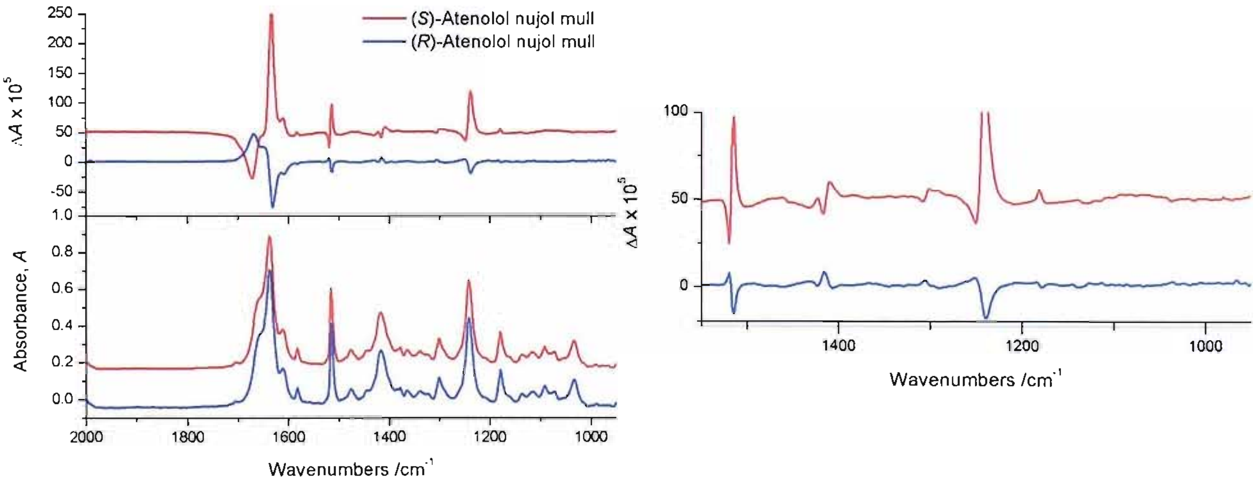

Figure 3.18 Comparison of IR (lower frame) and VCD (upper frame) spectra of (*R*) and (*S*) atenolol, from a nujol mull. Data collected on a dual PEM spectrometer, 1 hour collection, 4 cm^{-1} resolution, nujol background subtracted. Spectra are offset for clarity. Close up of VCD spectra shown to the right.

The VCD spectra using the nujol mull are generally of higher signal to noise ratio than from a sample in solution, despite the shorter collection time for the nujol mull data. This is because there is a high concentration of sample in the nujol mull technique and no solvent bands are present that interfere with the measurement of the VCD signal. This is well illustrated in figure 3.18.

3.1.5 Comparison of Sampling Techniques

The advantage of being able to use three different sampling techniques is that for problem compounds, one of the three methods is likely to work. If, for example, the sample is not soluble in a suitable solvent, i.e. $CDCl_3$ or CCl_4, a solid state technique can be used. Likewise if the sample is a liquid at room temperature we can use a solution cell; such a compound would have been very problematic for determination of absolute stereochemistry via single crystal XRD. Also it is advantageous to be able to determine the dominant conformation whilst the sample is in different states, either solid or solution, as this can help to investigate how an active pharmaceutical ingredient (API), for example, interacts within the body and what may be the best method of delivery.

The nujol mull technique would be especially good for the pharmaceutical industry, due to the simplicity of the sample preparation and the ease of data collection. This technique has also given the best results for a large number of compounds studied, and is a great method for otherwise problematic compounds.

3.2 Modelling of VCD Spectra

In order to determine the absolute stereochemistry of a compound using VCD spectroscopy, it is necessary to predict the VCD spectrum of one of the possible enantiomers of the compound under study. The predicted spectrum is then compared to the experimental VCD spectrum, and if the spectra match or are opposite, then the absolute stereochemistry can be determined. One simple way of assessing the prediction accuracy is by comparing the predicted and experimental IR spectra. If the predicted IR spectrum has not been correctly modelled then the predicted VCD spectrum will also not be accurate.

3.2.1 Commercial Software

The marketing of chiral pharmaceuticals requires study of the individual enantiomers for full safety testing, and represents examples where VCD spectroscopy can be usefully and conveniently applied.[2, 11, 12] In order to identify the absolute stereochemistry of a compound from its VCD spectrum, it is necessary to compare it to the predicted VCD for each possible enantiomer. DFT now provides reliable prediction of the VCD spectra of chiral compounds, hence the process of absolute stereochemistry determination is increasingly available to non-theoretical chemists.[13]

Commercial quantum mechanical calculation programs such as Gaussian 03 [14] have made the prediction of VCD spectra available to non-experts. The procedure for the prediction of vibrational frequencies first requires a suitable conformer of the compound being investigated. This conformer can simply be drawn, and put in a suitable conformation using chemical knowledge, or the conformers of a compound can be determined from a search of conformation space performed in a program such as Spartan.[15] Once a suitable conformer has been found, a geometry optimisation is performed with Gaussian 03, followed by calculation of the vibrational frequencies. It is important that the vibrational frequencies are predicted at the same level of calculation as the geometry optimisation was performed; otherwise the results are not valid.

Before proper comparison between the predicted and experimental vibrational spectra is possible, the predicted frequencies need to be scaled to correct for the neglect of anharmonicity within the calculations. To do this a uniform scale factor is applied; published scale factors are available for most basis sets and models of calculation.[16-19] They multiply the whole spectrum by a value of less than one, which shifts the entire spectrum to a lower wavenumber and corrects for the over estimation.

Consideration of possible dimer formation and intra-molecular hydrogen bonding is very important if accurate predictions are to be made. This information can be determined either through knowledge of hydrogen bonding formation or through use of XRD data. Alternatively, if the compound exists as a dimer within its crystal structure, this dimer can be extracted from the XRD data (powder or single crystal) and used as a starting point for calculation of the predicted VCD spectrum.

Within solution state VCD measurements there is the possibility for more than one prominent conformer in solution, and proportions of predicted VCD spectra of these various conformers may need to be combined to give a reasonable representation of the experimental spectra obtained. The relative amounts of each conformer can be extracted from a Boltzmann distribution using the single point energies determined in the calculations.

3.2.2 Goodness of Fit Parameter

The technique of VCD spectroscopy for absolute stereochemistry determination is not standard practice within the pharmaceutical industry, but has great potential to become so. A goodness of fit parameter to correlate the predicted VCD spectrum with the experimental VCD spectrum would make the use of VCD spectroscopy for absolute stereochemistry determination a much more desirable technique. This would be equivalent to the *R*-factor [20-22] or Flack parameter [23-26] in single crystal XRD, which gives a measure of how accurate the calculated model fits the experimental data.

In this section, a method of providing a goodness of fit parameter will be described. α-Pinene was used as a model / test system for the goodness of fit parameter due to its excellent experimental VCD spectra and its rigid structure which makes calculations easier to perform to an accurate level.

Vibrational circular dichroism measurements for α-pinene (figure 3.2) as a neat liquid were carried out on a single PEM spectrometer. Solution spectra were collected in a variable path length Omni transmission solution cell (figure 3.1), equipped with BaF_2 windows and Teflon spacer. The path length used was 25 μm and spectra were collected at 16 cm^{-1} resolution, with 4096 scans. α-Pinene in the (*R*)-(+) and (*S*)-(-) forms was purchased from Sigma Aldrich and used without further purification. The experimental VCD spectra for (*S*)-(-)-α-pinene and (*R*)-(+)-α-pinene have been shown in figure 3.3, the spectra show the ideal situation with the two enantiomers producing mirror image VCD spectra about the x-axis. The collection of the VCD spectrum of α-pinene is relatively straight forward, as the compound is liquid at room temperature, and so there are no solvent effects to contend with.

Calculations were performed using the Gaussian 03 [14] package and included geometry optimisation followed by frequency calculation. The theoretical IR and VCD spectra were visualised using GaussView 3.0, where the Gaussian band width at half-height was set to 10 cm^{-1}. Prediction of the IR and VCD spectra of the two enantiomers of α-pinene (the predicted VCD spectrum of α-pinene has previously been published)[27] was carried out using Gaussian 03. The completeness of the calculations was judged by whether the geometry optimisation step for each enantiomer had produced mirror image structures: if mirror image structures have been obtained, the frequency calculations give mirror image predicted VCD spectra (figure 3.19). Prediction of the VCD for α-pinene is relatively straightforward due to the rigid structure and limited conformational flexibility of the molecule.

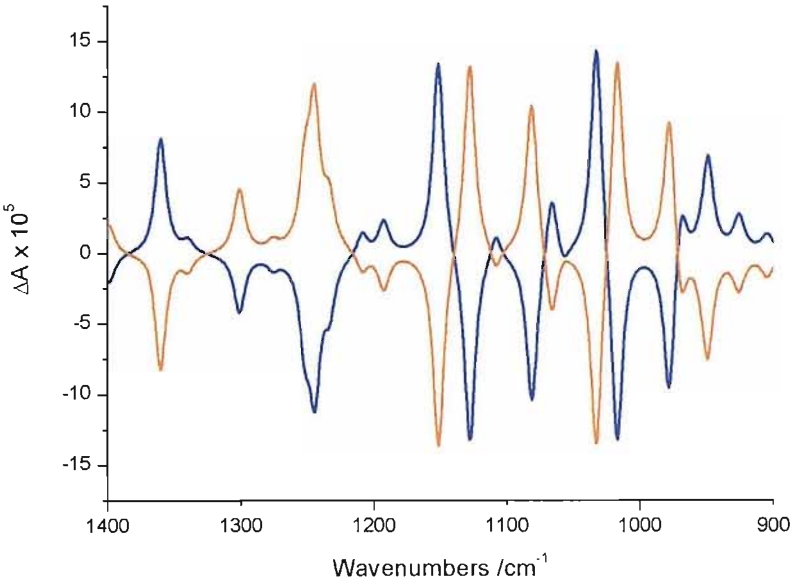

Figure 3.19 Predicted VCD spectra of (1*R*)-(+)-α-pinene (navy blue line) and (1*S*)-(-)-α-pinene (orange line), calculated at DFT B3PW91 6-31+G level.**

As previously discussed, before a predicted spectrum (either IR or VCD) can be directly compared to the experimental spectrum, the frequencies need to be corrected for the neglect of anharmonicity; this is done through application of a uniform scale factor. Published scale factors are available for predicted frequencies calculated from various basis sets.[16-19] However, these scale factors do not always lead to having the best fit between the predicted and experimental spectrum. Simultaneous measurement and calculation of the parent IR spectrum gives a secondary reference to changes in the VCD spectrum, and comparison of these spectra can provide a convenient way to calculate a scale factor that compensates for the neglect of anharmonicity in the calculation of the vibrational frequencies. Hence, a scale factor is calculated for each VCD spectrum / compound studied.

In the example of (*R*)-(+)- and (*S*)-(-)-α-pinene described here the scale factor has been determined from the average of the ratios of corresponding bands from the experimental IR vs. the predicted IR for (*R*)-(+)-α-pinene. For several corresponding bands in the IR the ratio ν_{exp} / ν_{calc} was determined and the average of these ratios gave the scale factor. This scale factor was initially applied to the predicted IR vibrational spectra and subsequently applied to the predicted VCD vibrational spectra.

Figure 3.20 shows the experimental and predicted (*R*)-(+)-α-pinene IR spectra from which the corresponding bands were taken, the black arrows indicating the corresponding bands. The effect of the number of corresponding bands used on the average scale factor has been discovered to have little effect. However, the more bands used, the more accurate the scale factor is likely to be.

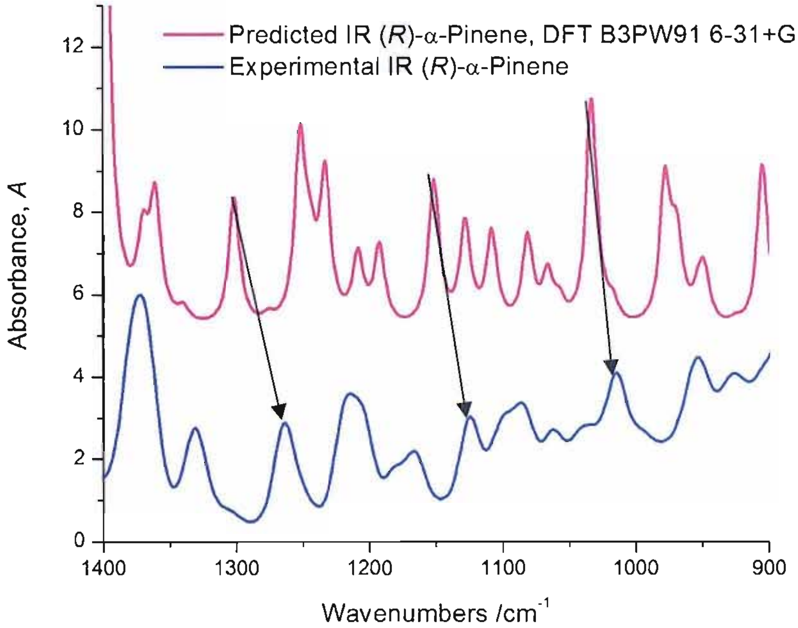

Figure 3.20 Comparison of the experimental IR spectrum of (*R*)-(+)-α-pinene (blue line) and the unscaled predicted IR spectrum of (*R*)-(+)-α-pinene from the DFT B3PW91 6-31+G level calculation (pink line). Spectra offset for clarity.**

Table 3.1 shows the tabulated corresponding bands for the predicted and experimental IR for (*R*)-α-pinene, the ratios ν_{exp} / ν_{calc} and the average of these ratios.

Table 3.1 Tabulated corresponding bands for the predicted and experimental IR spectra of (*R*)-(+)-α-pinene

(*R*)-Pinene Predicted IR, DFT B3PW91 6-31+G** Band Position	(*R*)-Pinene Experimental IR Spectrum Band Position	Ratio
1399	1372	0.9807
1360	1331	0.9786
1301	1264	0.9716
1251	1214	0.9696
1208	1167	0.9660
1151	1124	0.9765
1128	1087	0.9636
1108	1062	0.9585
1033	1014	0.9816
978	954	0.9755
949	926	0.9757
905	884	0.9768
	Average	0.9730

Figure 3.21 shows the experimental and the scaled predicted (*R*)-(+)-α-pinene IR spectra, which shows a much improved match, this spectrum was produced using the scale factor calculated above. Figure 3.21 also includes a comparison of the experimental spectrum with the predicted spectrum, scaled using the published scale factor for the DFT B3PW91 6-31+G** calculation level.[19] The published scale factor (0.9601) for the calculation used in the prediction of the above spectrum gives a worse fit than the calculated scale factor. It goes too far in correction of the overestimation of the neglect of anharmonicity

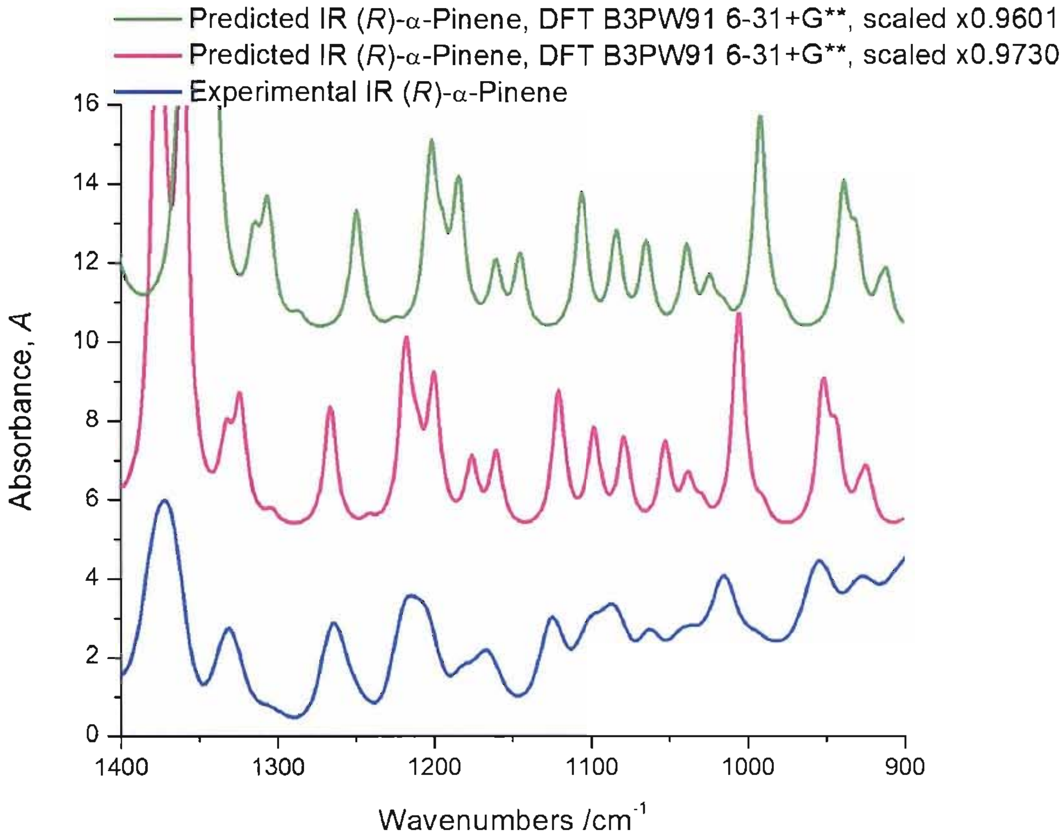

Figure 3.21 Comparison of the experimental IR spectrum of (R)-(+)-α-pinene (blue line) and the scaled predicted IR spectrum of (R)-(+)-α-pinene calculated at the DFT B3PW91 6-31+G level with applied calculated scale factor of 0.9730 (pink line), and applied published scale factor of 0.9601 (green line). Spectra offset for clarity.**

The calculated scale factor was then applied to the predicted VCD frequencies and the scaled predicted VCD spectrum compared to the experimental VCD spectrum. This is shown for (*R*)-(+)-α-pinene in figure 3.22. A comparison of the experimental data with the scaled predicted spectrum using the published scale factor is also included, again the scale factor has over-corrected for the neglect of anharmonicity.

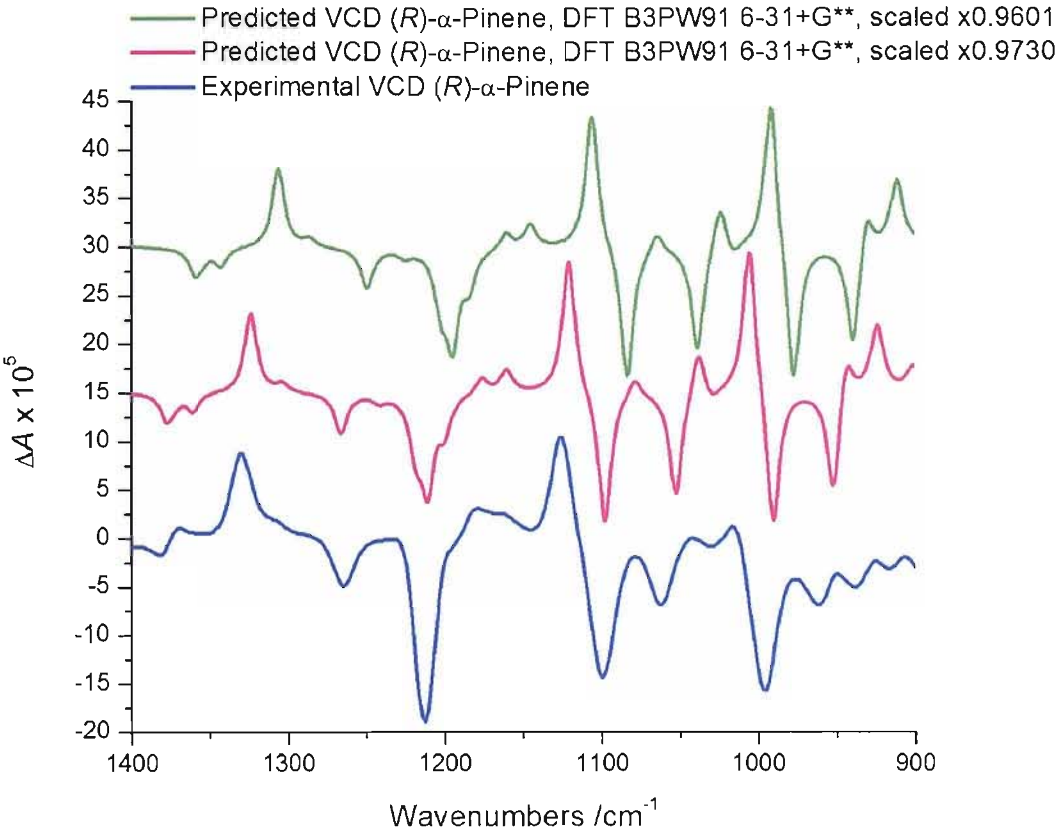

Figure 3.22 Comparison of the experimental VCD spectrum of (R)-(+)-α-pinene (blue line) and the scaled predicted VCD spectrum of (R)-(+)-α-pinene calculated at the DFT B3PW91 6-31+G level with applied calculated scale factor of 0.9730 (pink line), and applied published scale factor of 0.9601 (green line). Spectra offset for clarity.**

Although visually this appears to give a good fit between the experimental and calculated VCD spectra for (*R*)-(+)-α-pinene, a quantitative measurement of the fit would be preferable. A goodness of fit parameter can be defined as in equation 3.1 below; using the positions of the peaks in the VCD spectra.

$$R = \frac{\sum_{n} \left| |y_i| - |y_p| \right|}{\sum_{n} |y_i|} \qquad [3.1]$$

Where y_i is the ideal peak position, equivalent to the experimental peak position, y_p is the scaled predicted peak position, and n is the number of peaks used in the comparison. Table 3.2 shows the peak positions for (*R*)-(+)-α-pinene, and the associated *R*-factor when comparing the experimental spectrum with the scaled predicted VCD spectrum, using both the calculated scale factor and the published scale factor.

Table 3.2 Calculation of the goodness of fit parameter, *R*, for (*R*)-(+)-α-pinene

(*R*)-Pinene, Experimental VCD Spectrum	Predicted (*R*)-Pinene DFT B3PW91 6-31+G**, Scale factor 0.9730	Predicted (*R*)-Pinene DFT B3PW91 6-31+G**, Scale factor 0.9601
1330	1323	1306
1265	1265	1249
1213	1210	1194
1124	1120	1105
1099	1098	1083
1063	1052	1038
1041	1037	1023
1016	1005	992
995	990	976
960	952	939
R-Factor	**0.05302**	**0.18443**

For the experimental and predicted VCD (scaled with the calculated scaling factor 0.9730) spectra in figure 3.22 the *R*-factor is 5.3%. Zero is a perfect fit, and so a low *R*-factor corresponds to a very good fit; in the case of single crystal XRD, an *R*-value of <15% is the correct model, <10% is a good fit and <5% is a very good fit. The ranges of good and bad fit however, need to be calculated for the VCD technique, as are unlikely to not be the same as those used for the single crystal XRD technique. However, where we see a much poorer fit of the scaled predicted spectrum using the published scale factor to the experimental spectrum (figure 3.22), the goodness of fit parameter has a value of 18.4%. This gives us some idea of the ranges of goodness of fit that give a good estimation of the accuracy of the predicted spectra.

As validation of the technique a goodness of fit parameter was calculated for (*S*)-ibuprofen. This is shown in chapter 4.

3.3 Conclusions

A clear path for obtaining good quality, reliable VCD spectra has now been determined. Choice of sampling technique depends not only on the compound under investigation, but also on the spectrometer being used. A dual PEM spectrometer, with its increased sensitivity and improved baseline, allows for excellent data collection with all three sampling techniques, especially the nujol mull, where larger VCD signals are seen due to the high concentrations of sample in the mull. An additional advantage of the solid state techniques, especially when using the dual PEM spectrometer, is the quick data collection time. Choice of sampling technique also has an influence on the method necessary to predict accurate VCD spectra, as does the structure and conformational flexibility of the sample under investigation.

The goodness of fit parameter means that a reliability index, comparable to that for single crystal XRD absolute stereochemistry determinations, is available to the pharmaceutical industry and may provide additional confidence in the use of VCD as proof of absolute stereochemistry, to the regulatory boards. A combination of the nujol mull technique, accurate predicted VCD and the goodness of fit parameter should now prove a tempting method for the pharmaceutical industry, where single crystal XRD of certain compounds is either unreliable or impossible.

3.4 References

1. T.B. Freedman, X.L. Cao, R.K. Dukor, and L.A. Nafie, *Absolute configuration determination of chiral molecules in the solution state using vibrational circular dichroism.* Chirality, 2003. **15**(9): p. 743-758.
2. T.B. Freedman, F.J. Long, M. Citra, and L.A. Nafie, *Hydrogen-stretching vibrational circular dichroism spectroscopy: Absolute configuration and solution conformation of selected pharmaceutical molecules.* Enantiomer, 1999. **4**(2): p. 103-119.
3. L.A. Bodack, T.B. Freedman, B.Z. Chowdhry, and L.A. Nafie, *Solution conformations of cyclosporins and magnesium- cyclosporin complexes determined by vibrational circular dichroism.* Biopolymers, 2004. **73**(2): p. 163-177.
4. V. Baumruk and T.A. Keiderling, *Vibrational Circular-Dichroism of Proteins in H2o Solution.* Journal of the American Chemical Society, 1993. **115**(15): p. 6939-6942.
5. S. Abdali, K.J. Jalkanen, H. Bohr, S. Suhai, and R.M. Nieminen, *The VA and VCD spectra of various isotopomers of L-alanine in aqueous solution.* Chemical Physics, 2002. **282**(2): p. 219-235.
6. A.G. Petrovic, P.K. Bose, and P.L. Polavarapu, *Vibrational circular dichroism of carbohydrate films formed from aqueous solutions.* Carbohydrate Research, 2004. **339**(16): p. 2713-2720.
7. G. Shanmugam and P.L. Polavarapu, *Vibrational circular dichroism of protein films.* Journal of the American Chemical Society, 2004. **126**(33): p. 10292-10295.
8. G. Shanmugam and P.L. Polavarapu, *Film techniques for vibrational circular dichroism measurements.* Applied Spectroscopy, 2005. **59**(5): p. 673-681.
9. R. Kuroda and T. Honma, *CD spectra of solid-state samples.* Chirality, 2000. **12**(4): p. 269-277.
10. M. Minguet, D.B. Amabilino, K. Wurst, and J. Veciana, *Circular dichroism studies of crystalline chiral and achiral alpha-nitronyl nitroxide*

radicals in a KBr matrix. Journal of the Chemical Society-Perkin Transactions 2, 2001(5): p. 670-676.

11. R.K. Dukor and L. Nafie, *Vibrational Optical Activity of Pharmaceuticals and Biomolecules*, in *Encyclopedia of Analytical Chemistry*, R.A. Meyers, Editor. 2000, John Wiley & Sons Ltd. p. 662 - 676.
12. P.L. Polavarapu, *New Spectroscopic Tool - Absolute-Configuration Determination of Pharmaceutical Compounds by Vibrational Circular-Dichroism.* Spectroscopy, 1994. **9**(9): p. 48-55.
13. P.J. Stephens and F.J. Devlin, *Determination of the structure of chiral molecules using ab initio vibrational circular dichroism spectroscopy.* Chirality, 2000. **12**(4): p. 172-179.
14. G.W.T. M. J. Frisch, H. B. Schlegel, G. E. Scuseria, , et al., *Gaussian 03.* 2003, Gaussian, Inc.: Pittsburgh PA.
15. *Spartan '02.* 2002, Wavefunction Inc.: Irvine.
16. A.P. Scott, Radom, L., *Harmonic vibrational frequencies: An evaluation of Hartree- Fock, Moller-Plesset, quadratic configuration interaction, density functional theory, and semiempirical scale factors.* Journal of Physical Chemistry, 1996. **100**(41): p. 16502-16513.
17. G. Rauhut and P. Pulay, *Transferable Scaling Factors for Density-Functional Derived Vibrational Force-Fields (Vol 99, Pg 3096, 1995).* Journal of Physical Chemistry, 1995. **99**(39): p. 14572-14572.
18. M.D. Halls, J. Velkovski, and H.B. Schlegel, *Harmonic frequency scaling factors for Hartree-Fock, S-VWN, B- LYP, B3-LYP, B3-PW91 and MP2 with the Sadlej pVTZ electric property basis set.* Theoretical Chemistry Accounts, 2001. **105**(6): p. 413-421.
19. R.D. Johnson, *Computational Chemistry Comparison and Benchmark DataBase.* October 2003.
20. W.C. Hamilton, *Significance Tests on the Crystallogrphic R Factor.* Acta Cryst., 1965. **18**: p. 502 - 510.
21. A.T. Brunger, J. Kuriyan, and M. Karplus, *Crystallographic R Factor Refinement by Molecular Dynamics.* Science, 1987. **235**: p. 458 - 466.
22. W.C. Hamilton, *Statistics in Physical Science; Estimation, Hypothesis Testing and Least Squares.* 1964: The Ronald Press Company.

23. G. Bernardinelli and H.D. Flack, *Least-Squares Absolute-Structure Refinement. Practical Experince and Ancillary Calculations.* Acta Cryst. A, 1985. **41**: p. 500-511.
24. H.D. Flack and G. Bernardinelli, *Absolute structure and absolute configuration.* Acta Crystallographica Section A, 1999. **55**: p. 908-915.
25. H.D. Flack and G. Bernardinelli, *Reporting and evaluating absolute-structure and absolute- configuration determinations.* Journal of Applied Crystallography, 2000. **33**: p. 1143-1148.
26. H.D. Flack, *Chiral and achiral crystal structures.* Helvetica Chimica Acta, 2003. **86**(4): p. 905-921.
27. F.J. Devlin, P.J. Stephens, J.R. Cheeseman, and M.J. Frisch, *Ab initio prediction of vibrational absorption and circular dichroism spectra of chiral natural products using density functional theory: alpha-pinene.* Journal of Physical Chemistry A, 1997. **101**(51): p. 9912-9924.

Chapter 4 – VCD Results

If VCD is to be employed in the pharmaceutical industry, the technique requires a reliable and straightforward method of sample collection accompanied by a routine procedure to predict accurate VCD spectra. The results presented in this chapter illustrate the progressive development of the VCD methodology for use in the pharmaceutical industry enabled by this PhD project. The examples included were chosen to provide a gradual progression in the complexity of the experimental measurements; and problems experienced in sampling methodology are presented in detail. The effect of various parameters within the measurements on the VCD spectra will be explored. Examples have been selected to illustrate problems and limitations of the instrumentation. The development of modelling methods has been explored by examining the influence of functional, basis set, rigidity of the molecule, number of possible conformers and effect of hydrogen bonding on the predicted spectra. With increased complexity of the molecule different approaches to enable quicker prediction of more accurate spectra are required.

4.1 α-Pinene

α-Pinene is used as the standard reference compound in VCD spectroscopy, as the measurement of the spectrum is straightforward (being from a neat liquid) [1-3] and it is, therefore, used to determine if the VCD spectrometer is performing correctly. The experimental results have been presented in chapter 3.

A key component for using VCD spectroscopy as a tool for absolute stereochemistry determination is the prediction of the spectra using density functional theory (DFT) calculations.[1, 4-6] α-Pinene has a very rigid structure (figure 4.1) which means that prediction of the vibrational spectra is relatively simple: there are only a limited number of possible conformers, making the lowest energy conformer much easier to find. The predicted spectra have been compared to the experimental spectra in chapter 3; section 3.3, where the goodness of fit parameter was also calculated to give a measure of the accuracy of the match of the predicted and experimental spectra. This goodness of fit parameter then allows a measure of the confidence in the absolute stereochemistry determination.

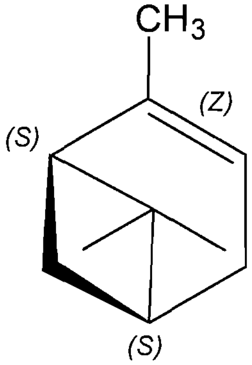

Figure 4.1 (*S*)-(-)-α-Pinene

In developing the VCD technique for the pharmaceutical industry, a comparison of the predicted VCD spectra for α-pinene calculated at different levels of complexity was performed. This was carried out to observe the full effect of changing the basis set on the vibrational frequencies and to give a better idea of what level of calculation may be necessary to obtain the best possible predicted spectrum. The results of these comparisons are shown in figures 4.2 & 4.3 below, for two different functionals, B3LYP and B3PW91 respectively, and four different basis sets. A table comparing the properties of the different basis sets is shown in table 4.1, with increasing complexity down the table. The two functionals B3LYP and B3PW91 are hybrid functionals, which define the exchange functional as a linear combination of Hartree-Fock (HF), local and gradient-corrected exchange terms; this exchange functional is then combined with a local and/or gradient-corrected correlation functional.

Table 4.1 Comparison of the properties of four different basis sets.[7]

Basis Set	Properties
6-31G	Split-valence basis set, where the core orbitals are represented in terms of six Gaussians and the valence orbitals split into three and one Gaussian components.
6-31G*	Addition of polarisability provides d-type functions on main-group elements, where the valence orbitals are of s and p type. This allows displacement of electron distributions away from the nuclear positions, can be thought of in terms of hybrid orbitals.
6-31G**	Addition of polarisability to the hydrogen atoms occurs in terms of p-type functions. This is necessary for an accurate description of the hydrogen bonding in many systems.
6-31+G**	Diffuse functions add large s- or p-type functions to heavy atoms in the system. They are necessary for systems containing extra electrons that are loosely associated with specific atoms.

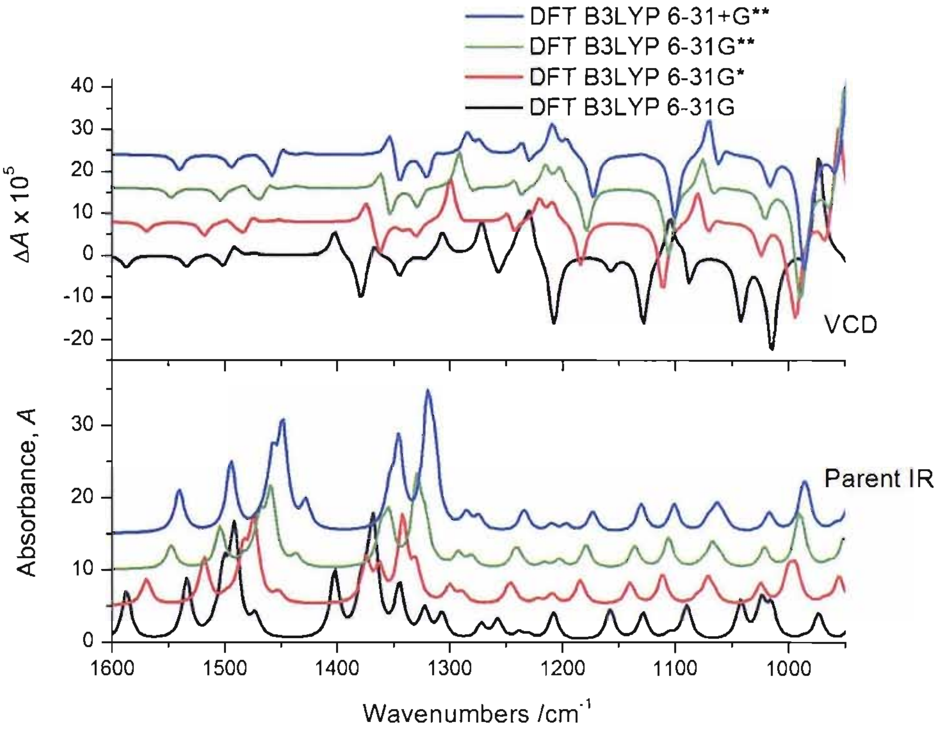

Figure 4.2 Comparison of the predicted IR (lower frame) and VCD (upper frame) spectra of (*S*)-(-)-α-pinene, calculated at using the B3LYP functional, with varying basis sets. Spectra offset for clarity.

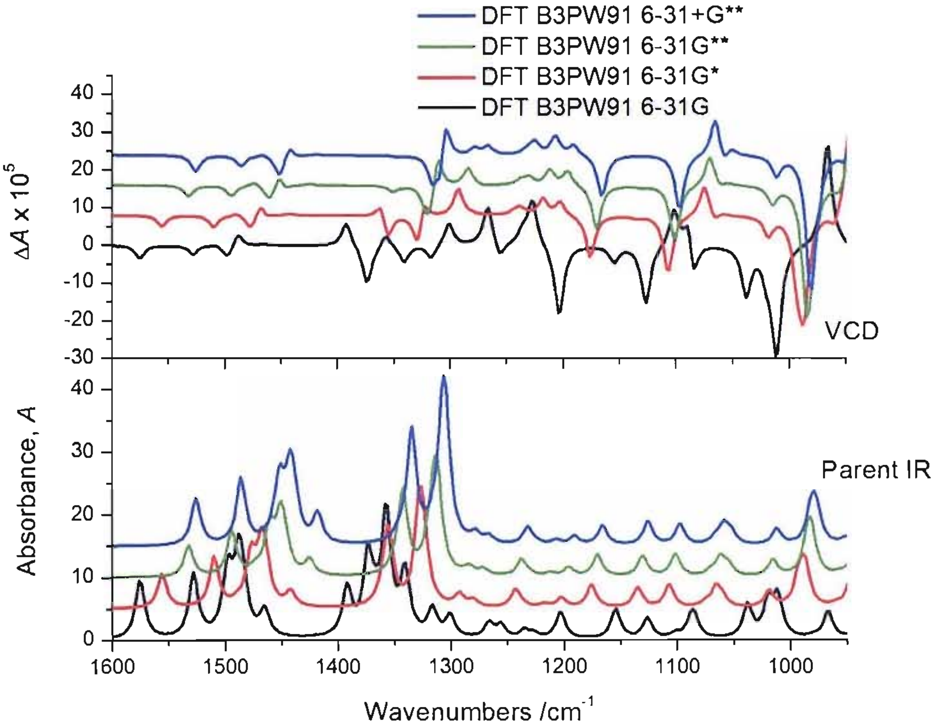

Figure 4.3 Comparison of the predicted parent IR (lower frame) and VCD (upper frame) spectra of (*S*)-(-)-α-pinene, calculated using the B3PW91 functional, with varying basis sets. Spectra offset for clarity.

There are some clear changes in the vibrational spectra that occur as the complexity of the basis sets increases. The most significant is the addition of polarised orbitals (see section 3.3.2, chapter 2 for further details) indicated by the addition of * to the basis set. The differences between the spectra for the 6-31G and 6-31G* basis set calculations include changes in both the position and relative intensity of the predicted bands in both the IR and VCD spectra. The spectra from the basis set calculations for 6-31G*, 6-31G** and 6-31+G** show fewer differences. The overall shape of these spectra is the same, but the whole spectrum shifts to lower wavenumber as the basis set used increases in complexity and therefore in accuracy: i.e., the more complex basis sets more accurately predict the vibrational frequencies as they more closely model the conditions within the molecule. This results in a scale factor (which corrects for neglect of anharmonicity) for calculations from a larger basis set, which is closer to a value of one.

Comparison of the predicted and experimental spectra for (R)-(+)-α-pinene (section 3.3.2, chapter 3) showed that a very good match was obtained using the

DFT B3PW91 6-31+G** calculation, i.e. the highest level calculation of those compared. However, as we have seen above, the spectra from the 6-31G* and 6-31G** only differ from the 6-31+G** in their shift of the spectrum along the x-axis. The choice of functional for this prediction has also made very little difference to the overall spectra. The predicted spectra from the 6-31+G** basis set, for both the B3LYP and B3PW91 functionals, are shown in figure 4.4. They are slightly offset along the x-axis, as the B3PW91 prediction has better approximated the vibrational frequencies and the relative intensities show slight differences. However, the lower level calculation gives a good enough result to obtain a good fit to the experimental spectra, which is advantageous as the calculation time required for an accurate prediction is significantly reduced.

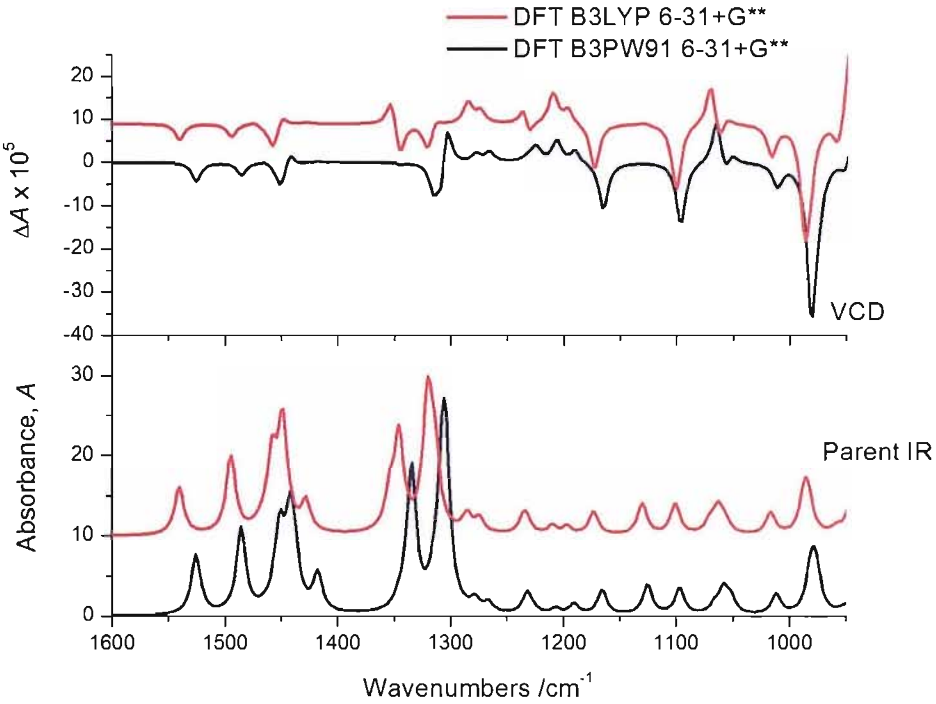

Figure 4.4 Comparison of the predicted IR (lower frame) and VCD (upper frame) spectra of (*S*)-(-)-α-pinene, at the B3LYP and B3PW91 levels, with the 6-31+G basis set. Spectra offset for clarity.**

This preliminary study of the reference compound α-pinene has shown that the highest level of basis set may not always be necessary, but the addition of polarisability to the basis set is essential. It is expected that when more flexible molecules are being studied, the influence of basis set and calculation model used will be greater.

4.2 (*S*)-Naproxen

(*S*)-Naproxen (figure 4.5) is also a fairly rigid structure, with one chiral centre, which has limited conformational flexibility. Experimental VCD spectra have been collected from both solution and as a nujol mull. (*S*)-Naproxen has very limited solubility in the solvent of choice, $CDCl_3$, but is soluble in D_6 DMSO. DMSO is not an ideal choice of solvent for VCD as it has a large absorption band in the IR at ~1100 cm^{-1} obscuring the VCD signal and limiting the usable range of the spectrum to 2000 – 1200 cm^{-1}.

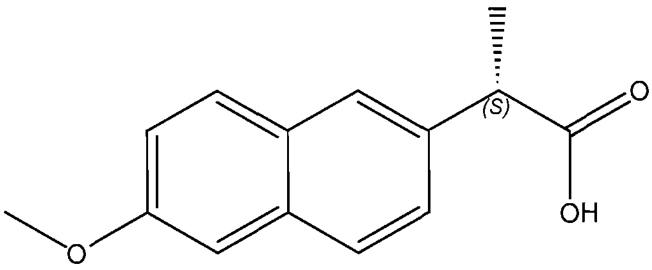

Figure 4.5 (*S*)-Naproxen

The IR and VCD spectra as a function of concentration of (*S*)-naproxen in both $CDCl_3$ and D_6 DMSO are shown in figures 4.6 and 4.7, respectively. The VCD spectra from the $CDCl_3$ solutions have two clearly defined bands at 1710 and 1605 cm^{-1}. However, the VCD spectra from the D_6 DMSO solutions show progressively improving spectra as the concentration increases. The bands at 1240 and 1210 cm^{-1} particularly show this improvement, and the 2 M concentration in D_6 DMSO has a VCD spectrum that is of good enough quality to compare to a prediction. These spectra highlight the importance of both solvent choice and concentration on the clarity of the VCD spectra. The spectra shown have been offset for easier comparison but have not been scaled. With the solutions in D_6 DMSO we would expect the infrared spectrum to double in size when the concentration is doubled (Beer's Law, $A = \varepsilon cl$, where A is the absorbance, ε is the absorptivity, c is the concentration and l is the path length of the cell). However, this is not the case, which may be due to problems within the reprocessing when the infrared spectrum is converted from percentage transmittance to absorbance.

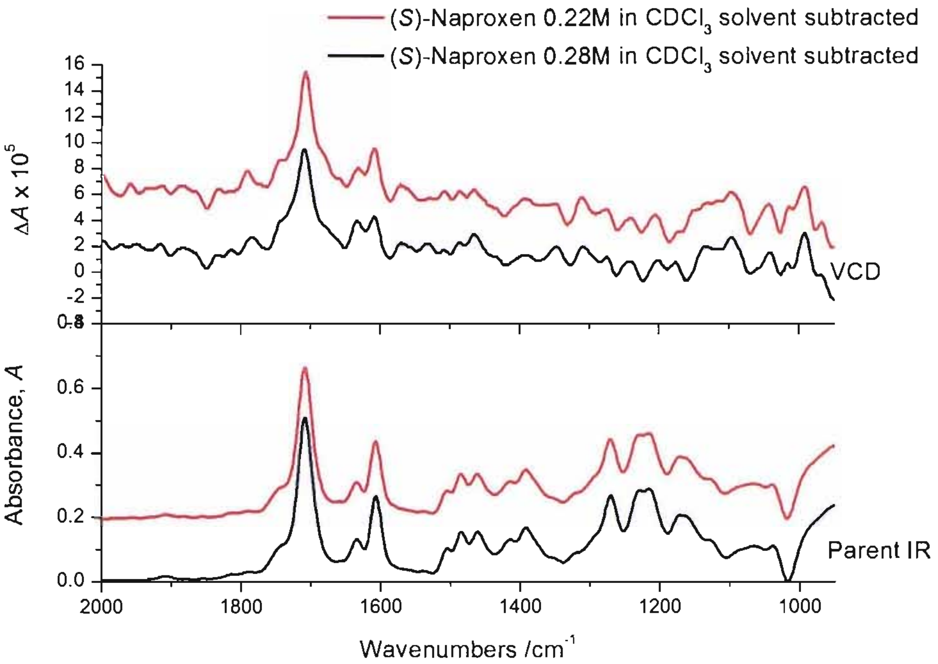

Figure 4.6 Comparison of the parent IR (lower frame) and VCD (upper frame) spectra of (*S*)-naproxen as 0.22 M and 0.28 M solutions in $CDCl_3$. Collected on single PEM spectrometer, 4096 scans, 25 μm path length cell, 16 cm^{-1} resolution. Solvent subtracted. Spectra offset for clarity.

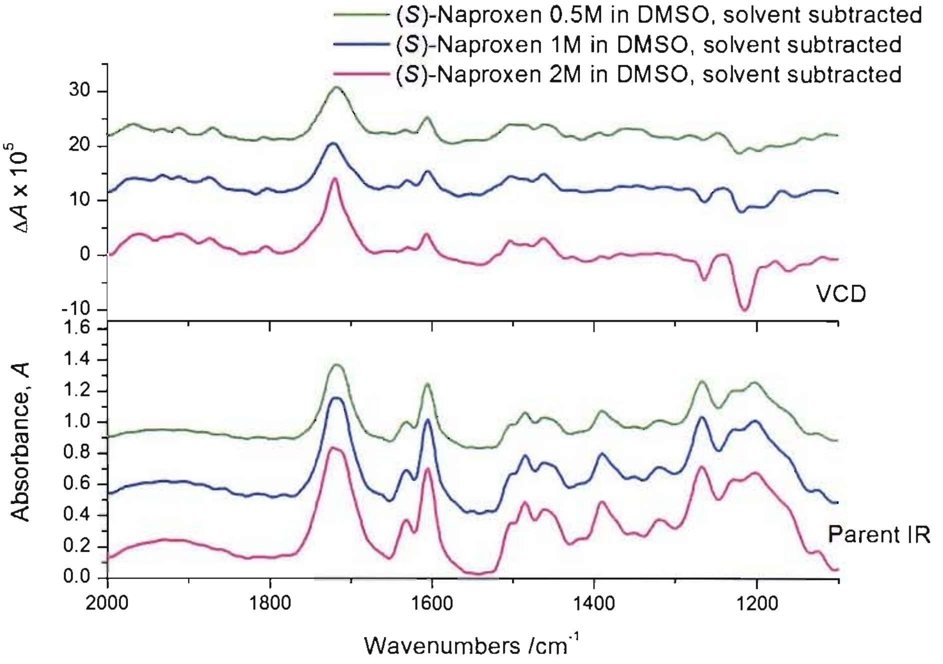

Figure 4.7 Comparison of the parent IR (lower frame) and VCD (upper frame) spectra of (*S*)-naproxen as 0.5 M, 1 M and 2 M solutions in D_6 DMSO. Collected on single PEM spectrometer, 4096 scans, 25 μm path length cell, 16 cm^{-1} resolution. Solvent subtracted. Spectra offset for clarity.

VCD spectra of (*S*)-naproxen were also collected experimentally from a nujol mull. If the spectra are proven to be as good as the spectra attainable from a solution collection, then it is very likely that this sampling technique will become the preferred method for the pharmaceutical industry. The nujol mull spectrum for (*S*)-naproxen is compared to the 2 M solution in D_6 DMSO spectra in figure 4.8.

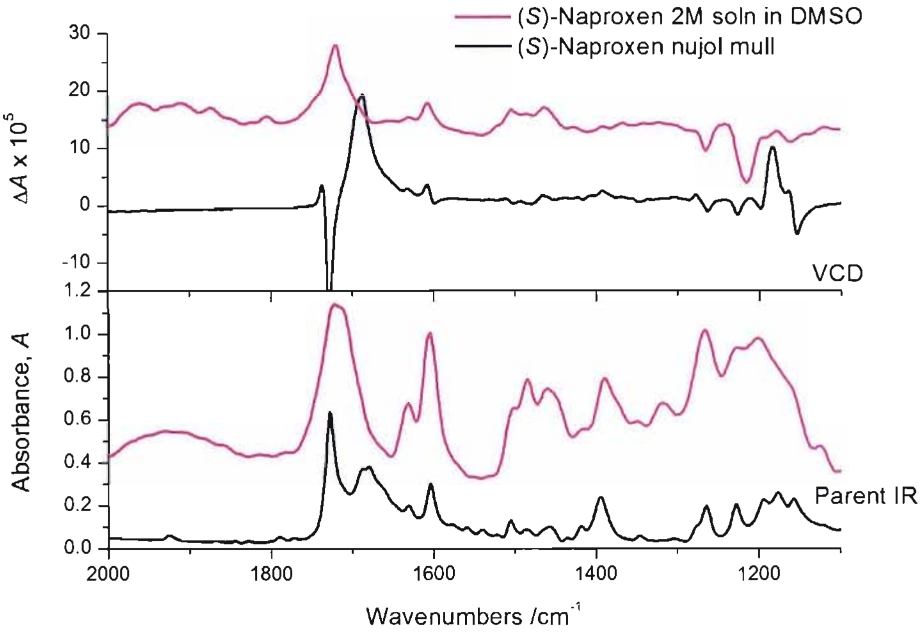

Figure 4.8 Comparison of parent IR (lower frame) and VCD (upper frame) of (*S*)-naproxen as a 2 M solution in D_6 DMSO (pink line) and from a nujol mull (black line). Collected on single PEM spectrometer, 4096 scans, 16 cm^{-1} resolution, solution in a 25 μm path length cell. Solvent and blank nujol subtracted. Spectra offset for clarity.

Comparison of the spectra collected via the two sampling techniques (figure 4.8) shows good peak position correlation in the parent IR and VCD spectra. However, the peak in the VCD at 1715 cm^{-1} changes significantly between the solution and nujol mull spectra. As seen in the parent IR for this peak, due to the C=O stretch, in solution there is just one broad band at 1715 cm^{-1}, whilst in the nujol mull there is an additional band at 1690 cm^{-1}. It is possible that in the nujol mull there are now two environments one hydrogen-bonded, and one not. These two environments lead to two bands in the parent IR which in turn gives two bands in the VCD spectrum, one negative and one positive.

The predicted spectra were calculated at two different levels DFT B3PW91 6-31G** and DFT B3PW91 6-31+G** (output geometry figure 4.9). Comparison of these spectra with the experimental spectra is shown in figure 4.10. The two predicted spectra are almost identical, with only a very small shift in the band position seen. The IR spectra show a good correlation between the predicted and experimental spectra, with a slightly better match seen with the experimental parent IR spectrum from the solution state data. The corresponding bands are highlighted in figure 4.10 by the red lines. The starting geometry for these calculations was simply drawn using no prior additional information such as XRD structure.

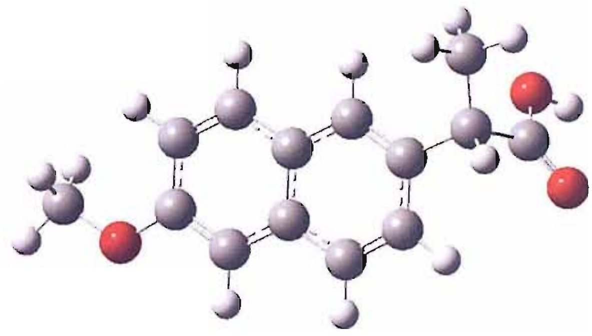

Figure 4.9 Output geometry from (*S*)-naproxen calculation DFT B3PW91 6-31G level**

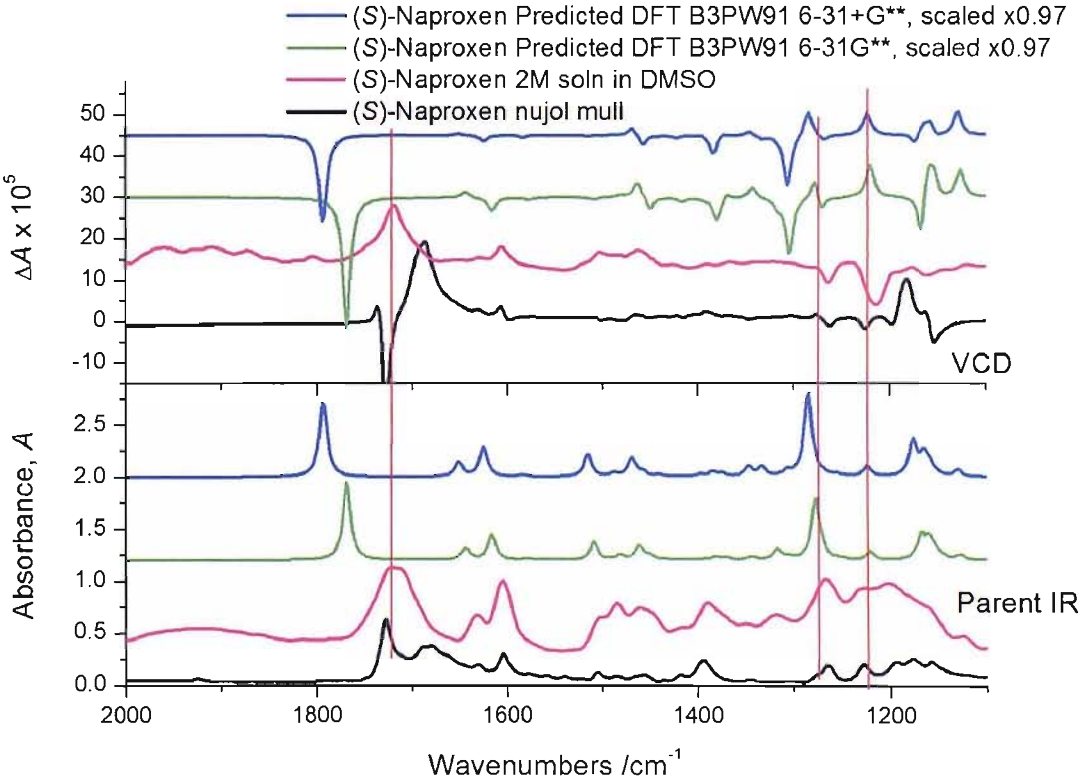

Figure 4.10 Comparison of parent IR (lower frame) and VCD (upper frame) spectra of (*S*)-naproxen. Predicted spectra calculated at DFT B3PW91 6-31G (blue line) and DFT B3LYP 6-31+G** (green line) scaled x0.97. Experimental spectra from 2 M solution in D_6 DMSO (pink line) and nujol mull (black line). Spectra offset for clarity.**

The negative band present in the VCD spectrum collected from a nujol mull is present in the predicted VCD spectra at 1775 cm^{-1}, indicating that the conditions in the prediction are more similar to the nujol mull than in solution. As the calculation is on an isolated gas phase molecule it seems logical that the negative peak in the experimental nujol mull VCD spectrum at 1715 cm^{-1} is due to the C=O stretch of the isolated molecule. The positive peak at 1690 cm^{-1} in the nujol mull VCD and at 1715 cm^{-1} in the solution VCD is from a C=O stretch which is involved in hydrogen-bonding.

An alternative option to simply drawing the starting geometry for the calculation is first to perform a search of conformational space and use the resultant minimum energy conformer from this as the starting geometry for the Gaussian calculation. The search of conformational space was performed using Spartan [8] at the semi-empirical AM1 level. The output geometry from the calculation using this starting structure is shown in figure 4.11 and the predicted spectra are compared to the experimental spectra in figure 4.12.

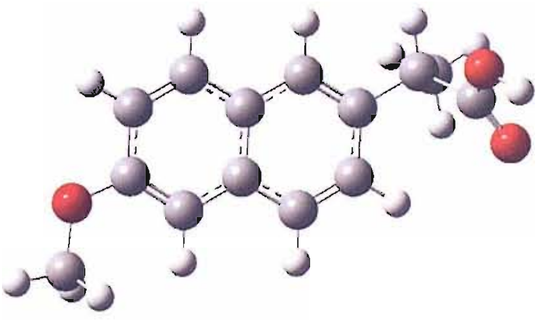

Figure 4.11 (*S*)-Naproxen end geometry of calculation performed using starting geometry from Spartan search of conformational space.

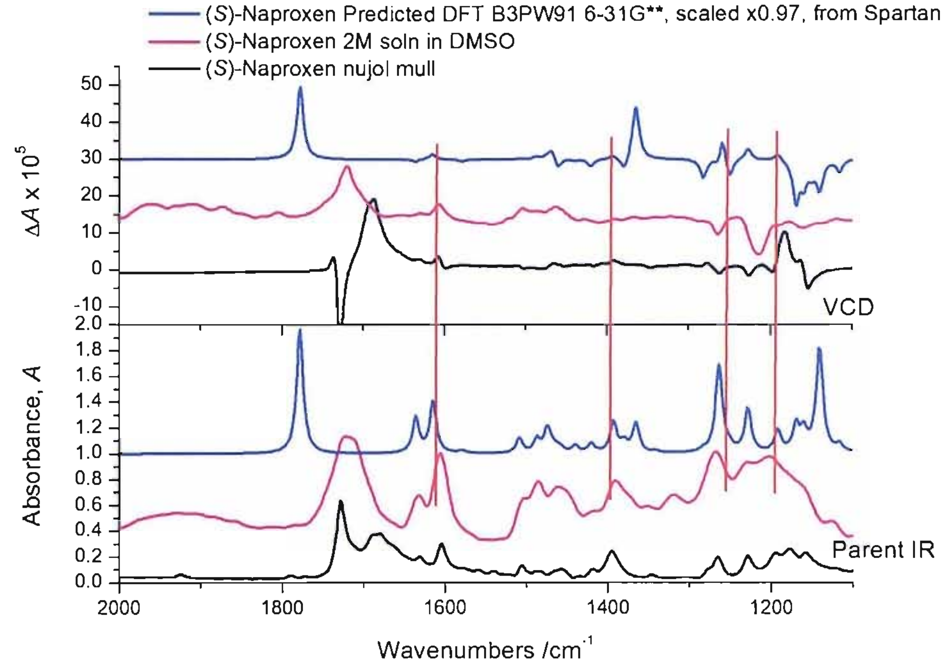

Figure 4.12 Comparison of parent IR (lower frame) and VCD (upper frame) spectra of (*S*)-naproxen. Predicted spectra calculated at DFT B3PW91 6-31G (blue line), scaled x0.97, starting geometry from Spartan. Experimental spectra from 2 M solution in DMSO (pink line) and nujol mull (black line). Spectra offset for clarity. The red lines indicate the corresponding bands seen between the predicted and solution state experimental spectra.**

An obvious change in the predicted VCD spectrum is the negative band at 1775 cm^{-1} seen in the previous prediction (DFT B3LYP 6-31G**), has been replaced by a positive band at 1785 cm^{-1}, which is due to the C=O stretch. The differences between the two optimised geometries can be observed by comparing figures 4.9 and 4.11, where the methyl group situated on the oxygen atom has undergone a rotation of 180 °, as has the carboxylic acid group.

The predicted spectra from both of these calculations are compared in figure 4.13, where considerable differences can be seen between both the parent IR and VCD spectra. This is slightly surprising as the spectra were calculated at the same calculation level, and illustrates the importance of choosing the correct starting structure. The predicted spectra from the starting geometry from Spartan also show a better match to the experimental spectra from solution (shown in figure 4.12, highlighted by the red lines). Additionally the band at 1785 cm^{-1} in the predicted spectra corresponds to the band at 1710 cm^{-1} in the experimental spectra and is due to the C=O stretch.

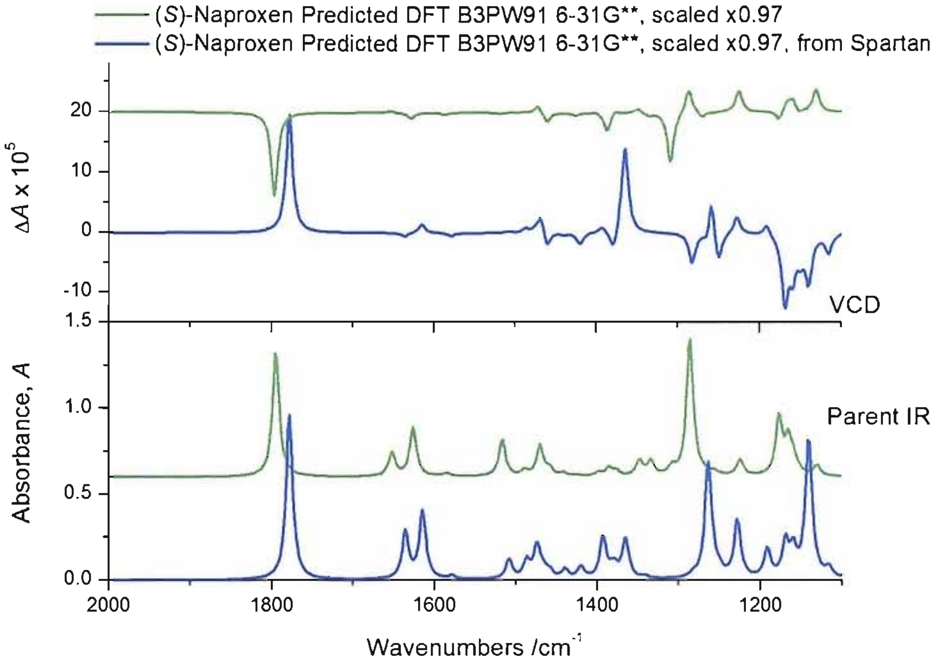

Figure 4.13 Comparison of the predicted parent IR (lower frame) and VCD (upper frame) spectra of (S)-naproxen, calculated at the DFT B3PW91 6-31G level, scaled by 0.97. Predictions differ in starting structure; no prior information (green line), minimum energy conformer from Spartan (blue line). Spectra offset for clarity.**

The effect of rotation of groups within a molecule has thus been shown to lead to important changes in the VCD spectrum, to the extent that the sign of a band has been inverted. Generally inversion is assumed only to be seen when the absolute stereochemistry of a molecule has been changed.

4.3 (-)-Ephedrine

(-)-Ephedrine (figure 4.14) is a more complex molecule, as it has two chiral centres, and the possibility for more conformational flexibility as compared to (*S*)-naproxen.

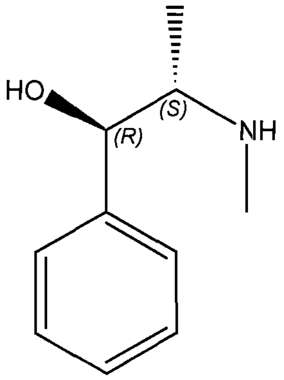

Figure 4.14 (-)-Ephedrine

The solution VCD spectra of (-)-ephedrine illustrate the sensitivity limitations of the single PEM spectrometer. The two single PEM data collections for two solutions of (-)-ephedrine in $CDCl_3$ at 1 M and 2 M concentration have very high noise levels and do not provide a useful VCD spectrum (figure 4.15). The four hour data collection from the dual PEM spectrometer for a 0.86 M solution in $CDCl_3$ shows a much improved VCD spectrum (figure 4.15). The dual PEM spectrum has clear bands and a good zero baseline, and comparison to the single PEM spectra shows that these spectra, despite being more noisy, do show the same structural features. It is possible that a higher concentration in solution with the single PEM spectrometer may provide a reliable spectrum, but it is also possible that by using a higher concentration the compound may aggregate and disrupt the VCD features expected. This has been observed in the hydrogen stretching region for (-)-ephedrine as shown in chapter 3, section 3.1.2 in figures 3.9 and 3.10.

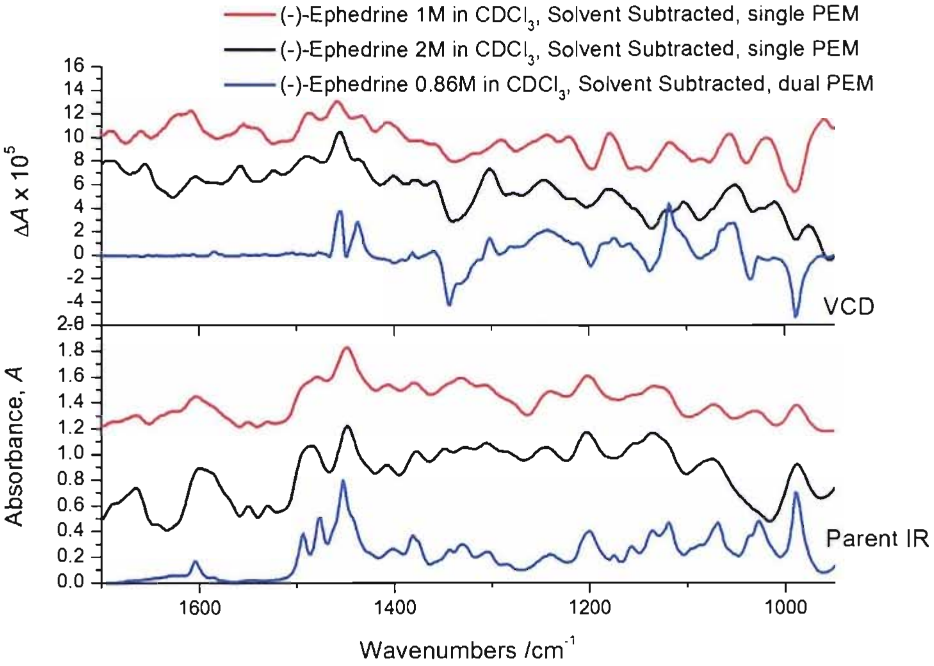

Figure 4.15 Comparison of (-)-ephedrine IR (lower frame) and VCD (upper frame) spectra, from solutions in CDCl$_3$. Single PEM data collected in 25 μm path length cell, 16 cm^{-1} resolution and 4096 scans, 1 M (red line) and 2 M (black line) solutions in CDCl$_3$. Dual PEM data collected in a 96 μm path length cell, 4 cm^{-1} resolution and 4 hour collection time, with a 0.86 M solution in CDCl$_3$ (blue line). Solvent subtracted. Spectra offset for clarity.

Looking at the dual PEM spectrometer data alone, presented in figure 4.16 with its associated noise spectrum, it is possible to estimate the confidence in the VCD spectrum. The noise spectrum shows no peaks and indicates that the VCD spectrum is accurate, with negligible noise levels. This noise spectrum is presented at the end of the data collection with the parent IR and VCD spectrum when using the dual PEM spectrometer. It is an extremely useful component as it provides an accurate reliability index for the VCD spectrum. It is calculated by separating the VCD data collection into two halves, and subtracting one from the other leaves the residual noise spectrum.

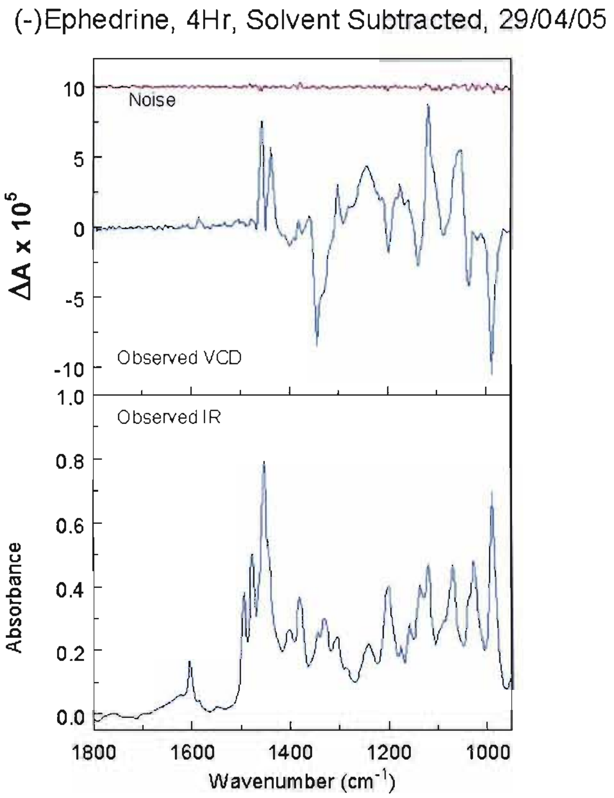

Figure 4.16 Observed parent IR (lower frame), VCD and associated noise (upper frame) spectra of (-)-ephedrine as a 0.86 M solution in $CDCl_3$. Collected on a dual PEM spectrometer, in a 96 μm path length cell, 4 cm^{-1} resolution and a four hour collection time. Solvent subtracted.

The data collection for the hydrogen stretching region (4000 – 2500 cm^{-1}) was problematic (as discussed in chapter 3) the compound aggregated in solution over time. The data from the first hour of the collection only is shown in figure 4.17. Peaks are observed in the noise spectrum at the same points the VCD signal is strong, but they are not large enough to compromise the reliability of the VCD spectrum.

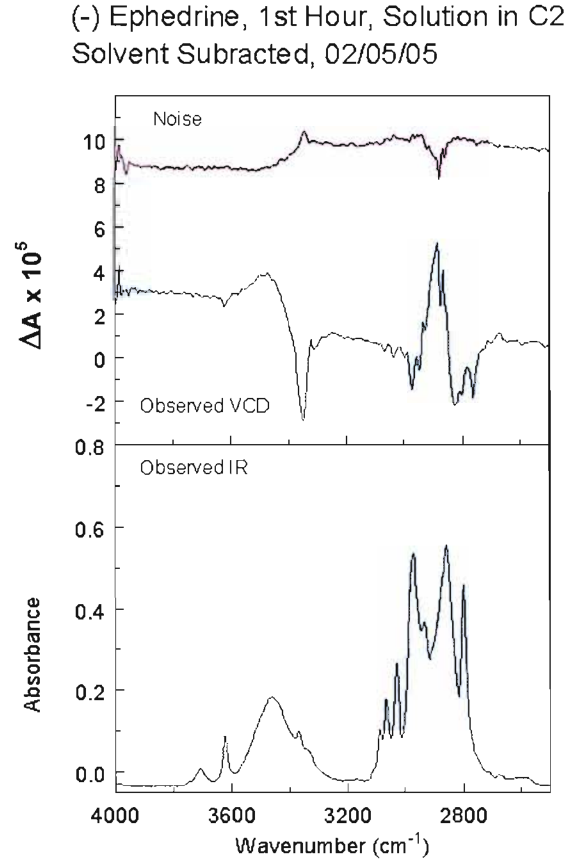

Figure 4.17 Observed parent IR (lower frame), VCD and associated noise (upper frame) spectra of (-)-ephedrine as a 0.0024 M solution in C_2Cl_4. Collected on a dual PEM spectrometer, in a 1 cm path length cell, 4 cm^{-1} resolution and a one hour collection time. Solvent subtracted.

Looking at the structure of (-)-ephedrine (figure 4.14) there are two possible places for hydrogen-bonding to occur, at either the NH or OH group. It is important to take these hydrogen-bonding possibilities into consideration when performing the prediction of the VCD spectra, as hydrogen-bonding alters the position of the bands involved.

The first three calculations for (-)-ephedrine were performed from an arbitrary starting geometry. The predicted spectra are compared with the experimental spectra below (figure 4.18). Predicted spectra calculated at three different levels, and all the predicted spectra have been scaled by 0.97 for better comparison to the experimental spectra.

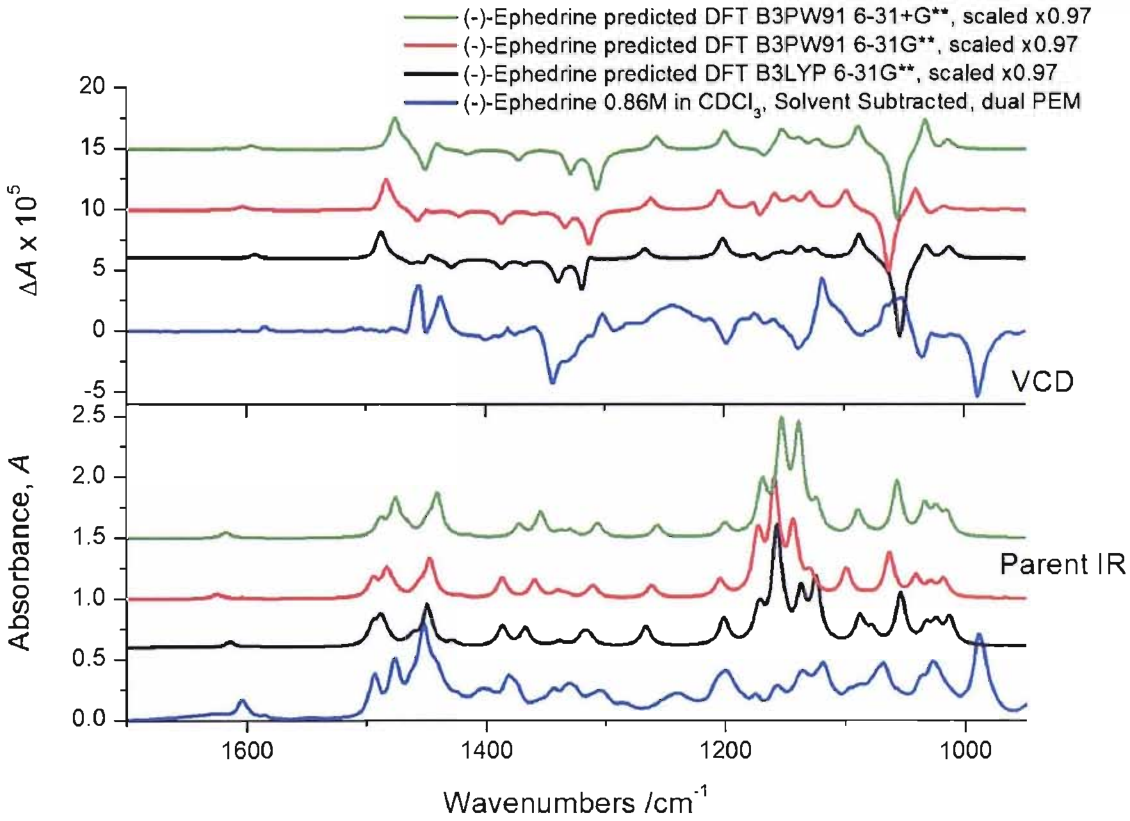

Figure 4.18 Comparison of experimental (blue line) and predicted spectra for (-)-ephedrine with parent IR (lower frame) and VCD (upper frame). Predicted spectra calculated using DFT B3LYP 6-31G (black line), using DFT B3PW91 6-31G** (red line) and using DFT B3PW91 6-31+G** (green line) scaled x0.97. Starting geometry from no prior information. Spectra offset for clarity.**

The predicted parent IR show quite a good agreement with the experimental parent IR spectrum around the bands at 1450, 1480 and 1490 cm^{-1}. However, beyond this there are no other particularly good matches. Also the VCD bands at these positions do not show matching peaks.

Comparison of the predicted spectra from the higher level calculation with the experimental spectra from the first hour of the hydrogen-stretching region data collection is shown in figure 4.19. The IR spectra compare well and show corresponding structural features including the very tiny band in the predicted IR at 3450 cm^{-1} due to the N-H stretch. Although there are no predicted structural features below 2800 cm^{-1} as seen in the experimental data. These experimental bands below 2800 cm^{-1} are most probably due to overtone and combination bands, which would not be calculated for in the prediction. However, the VCD spectra do not show any corresponding bands, although broadening of the bands in the predicted spectra may help.

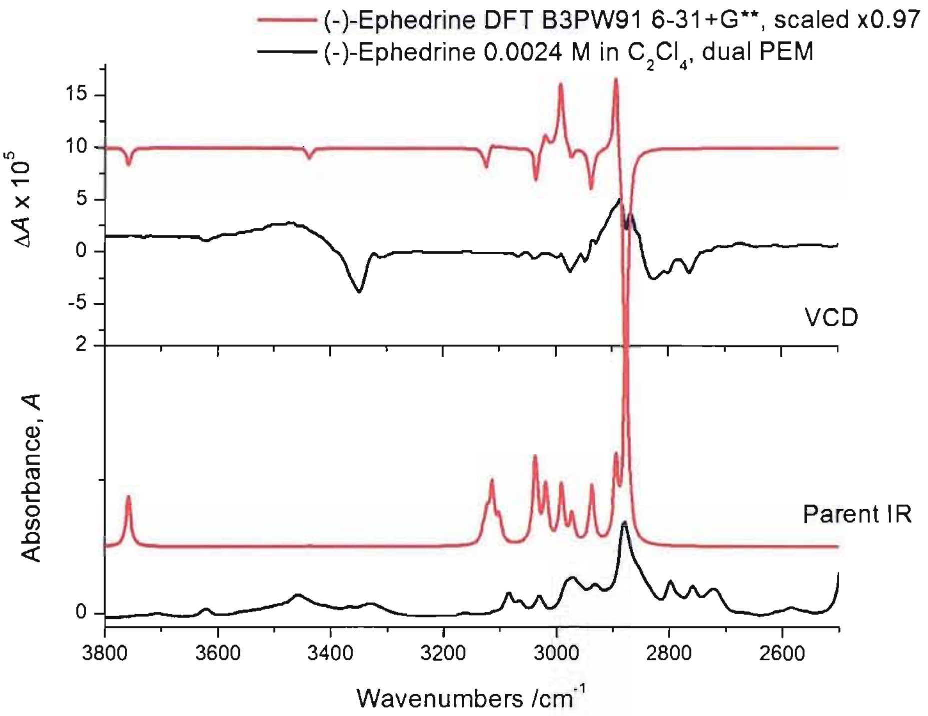

Figure 4.19 Comparison of experimental (-)-ephedrine data with predicted parent IR (lower frame) and VCD (upper frame) calculated using DFT B3PW91 6-31+G scaled x0.97, in the hydrogen stretching range. Starting geometry from no prior information. Spectra offset for clarity**

There are definite similarities between the predicted and experimental spectra shown above, but the match between the two is not good enough to decisively prove the absolute stereochemistry.

The geometry as optimised from a Spartan search of conformational space gave the conformer in figure 4.20, and using this as the starting structure for the calculation gave the predicted spectra in figure 4.21, where they are compared to the experimental spectra. The predicted spectra have been scaled by 0.98 for easier comparison to the experimental spectra.

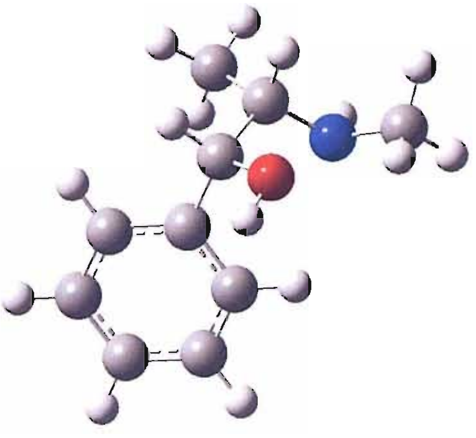

Figure 4.20 (-)-Ephedrine output geometry of calculation performed using starting geometry from Spartan search of conformational space.

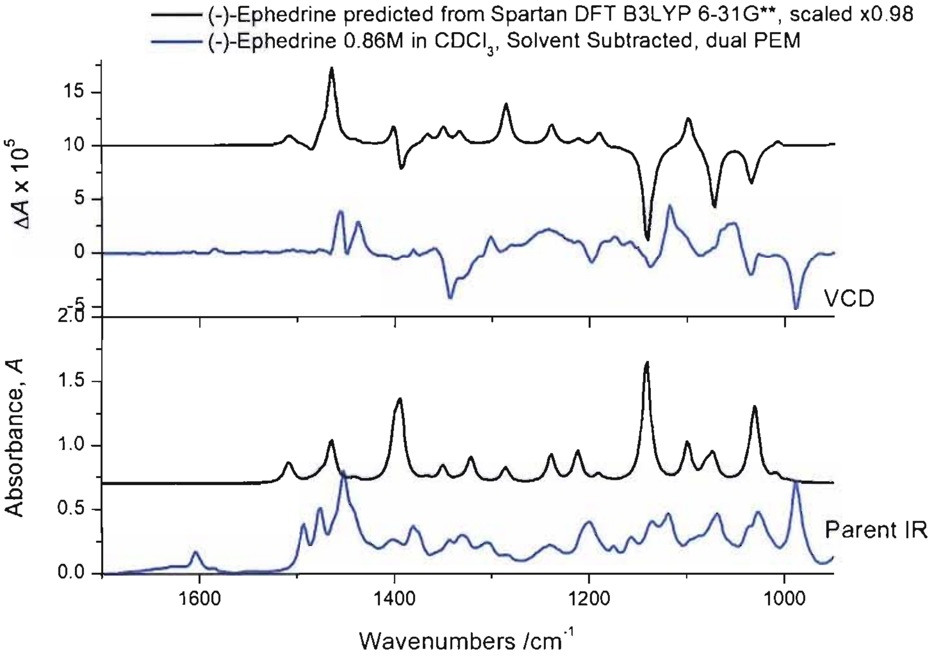

Figure 4.21 Comparison of experimental (blue line) (-)-ephedrine data with predicted parent IR (lower frame) and VCD (upper frame) spectra calculated from the optimised geometry from Spartan using DFT B3LYP 6-31G (black line) scaled x0.98. Spectra offset for clarity.**

The predicted spectra from this calculation show a much improved fit to the experimental spectra over the previous calculations and would allow a far more confident assignment of the absolute stereochemistry. Comparison of the predicted spectra from this calculation with the experimental spectra for the hydrogen-stretching region is shown in figure 4.22, where the predicted spectra have been scaled by 0.98. The band at 3350 cm^{-1} in the experimental spectra is still not present in the predicted spectrum, but is possibly the predicted band at

3720 cm^{-1}. The prominent broad band in the experimental VCD spectrum at 2890 cm^{-1} is a very sharp band in the predicted VCD spectrum and broadening of the predicted bands may improve this. Overall comparison of the spectra from the fingerprint region shows a better match and contains more useful information.

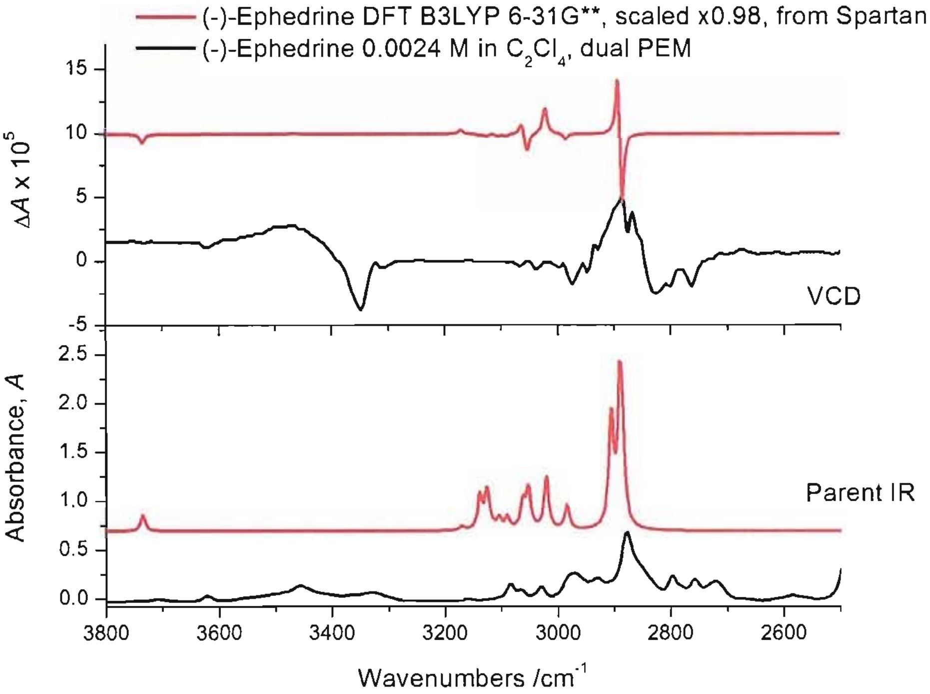

Figure 4.22 Comparison of experimental (black line) (-)-ephedrine spectra with predicted parent IR (lower frame) and VCD (upper frame) calculated from the optimised geometry from Spartan using DFT B3LYP 6-31G (red line) scaled x0.98, in the hydrogen-stretching region. Spectra offset for clarity.**

In the area of prediction of spectra, the first comparison with data from the hydrogen-stretching region has been shown. This region typically contains less information than the fingerprint region and the peaks are generally broader as they are frequently involved in hydrogen-bonding. Use of a geometry minimised structure from a search of conformational space has again proven a better choice for the starting geometry of the calculation. Once scaled, the predicted spectra show a good match to the experimental spectra from the dual PEM measurement. It seems that the use of a program such as Spartan to locate the minimum energy conformer is essential for the accurate prediction of spectra.

4.4 (2*S*)-Captopril

Captopril (figure 4.23) is the most complex molecule studied so far, it has two chiral centres and a large amount of conformational flexibility. Experimentally a wide range of sampling techniques have been used to try to obtain reliable VCD spectra. The solution state spectra were compared in chapter 3, section 3.1.2, figure 3.13, for data collections from the single and dual PEM spectrometers. They illustrated the improved baseline attainable with the dual PEM spectrometer. The KBr disc technique gave a VCD spectrum that contained slightly less structural information than the solution state spectrum (chapter 3, section 3.1.3, figure 3.15) and it was shown that when the disc was rotated the VCD spectra obtained, that should have been identical, were not (figure 3.13).

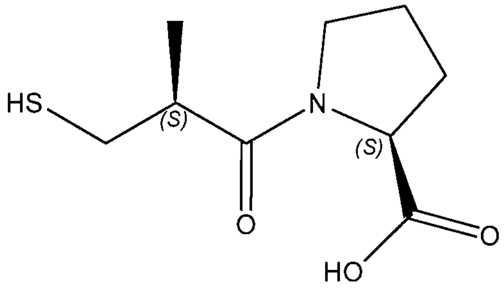

Figure 4.23 (2*S*)-Captopril

The solution state measurements of a 0.22 M solution in $CDCl_3$ from the dual PEM spectrometer are shown in figure 4.24. They show a very clear VCD spectrum, with low noise indicating its reliability.

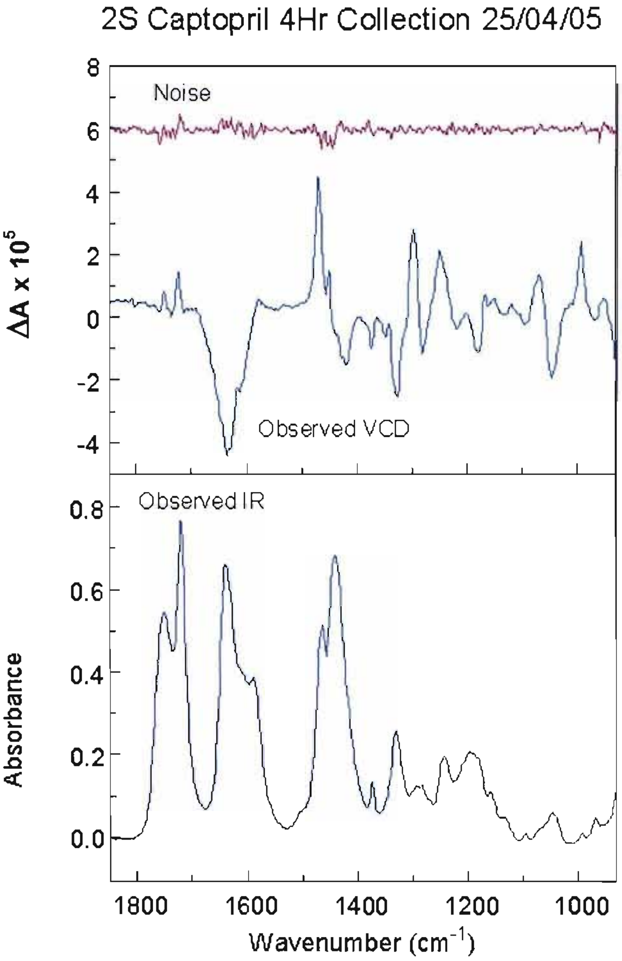

Figure 4.24 Experimental parent IR (lower frame), VCD and associated noise (upper frame) spectra of (2*S*)-captopril as a 0.22 M solution in $CDCl_3$, 4 hour collection, 94 μm path length cell, 4 cm^{-1} resolution. Solvent spectra subtracted.

The experimental spectra have also been measured from a nujol mull spectra on the single PEM spectrometer, and are compared to the solution spectra from the dual PEM spectrometer in figure 4.25. The nujol mull spectra in this case seem to contain less information than the solution spectra. This can be highlighted by comparing the IR spectra from both the data collections; the parent IR from the nujol mull contains fewer bands, which are at slightly different positions to the solution spectra IR. This is due to the solution state molecules being solvated and to the higher concentration of the nujol mull as compared to the solution state. An interesting point is that the KBr disc spectra (chapter 3, section 3.1.3, figure 3.14) are much more similar to the solution state spectra than the nujol mull spectra. This may again be attributed to the higher concentration of the nujol mull samples.

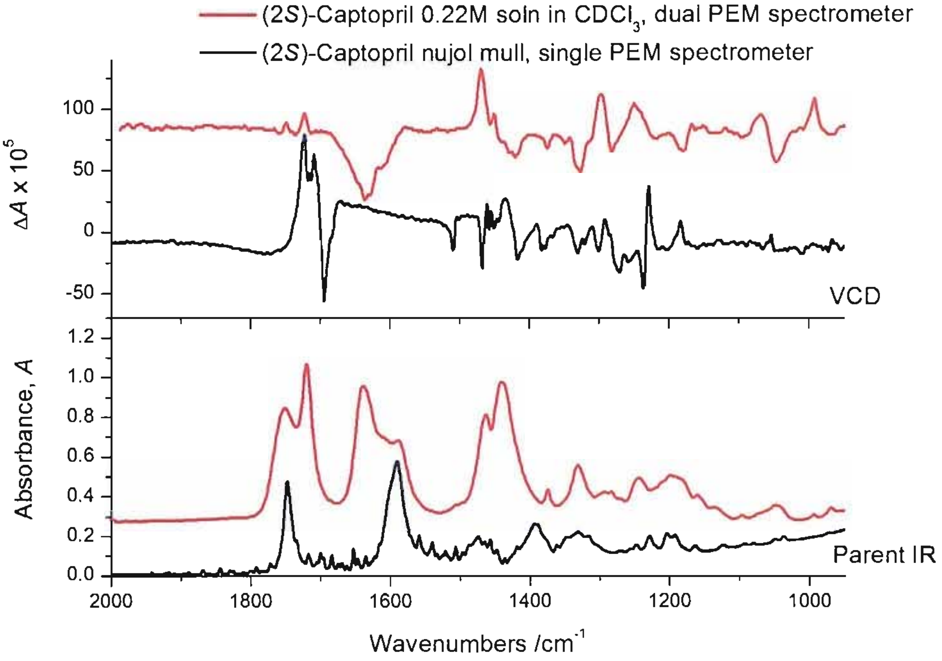

Figure 4.25 Comparison of parent IR (lower frame) and VCD (upper frame) spectra for (2*S*)-Captopril as a nujol mull (black line) and as a 0.22 M solution in $CDCl_3$ (red line). Nujol mull spectra collected on single PEM spectrometer, 4096 scans and 16 cm^{-1} resolution. Solution spectra collected on dual PEM spectrometer, 4 hour collection, 94 μm path length cell, 4 cm^{-1} resolution. Nujol and solvent subtracted. Spectra offset for clarity.

Some of the different methods of calculating the best predicted VCD spectra have been discussed; these include starting from an arbitrary structure with no prior knowledge and using the lowest energy conformer from a search of conformation space, using a program such as Spartan. There are three other approaches for choice of starting structure; the structure obtained from a single crystal XRD collection can be used by assigning the absolute stereochemistry at random, or the structure may be dimerised or lastly, the possible hydrogen bonding regions of the molecule can be hydrogen bonded using water or acetic acid.

The first technique to be applied to the prediction of the spectra of (2*S*)-captopril was the use of the XRD structure (see chapter 5 for XRD details) as the starting geometry for the calculations. Five different methods of using the XRD data were attempted; first using the XRD structure and a frequency only calculation; secondly using the XRD structure and an optimisation and frequency calculation; next, as the second calculation but using a higher level of calculation; fourth, a molecule of H_2O was added to the starting structure from the XRD to fulfil the hydrogen-bonding possibilities of the carbonyl group first with a frequency only calculation (figure 4.26 (a)) and then with an optimisation and frequency calculation (figure 4.26 (b)).

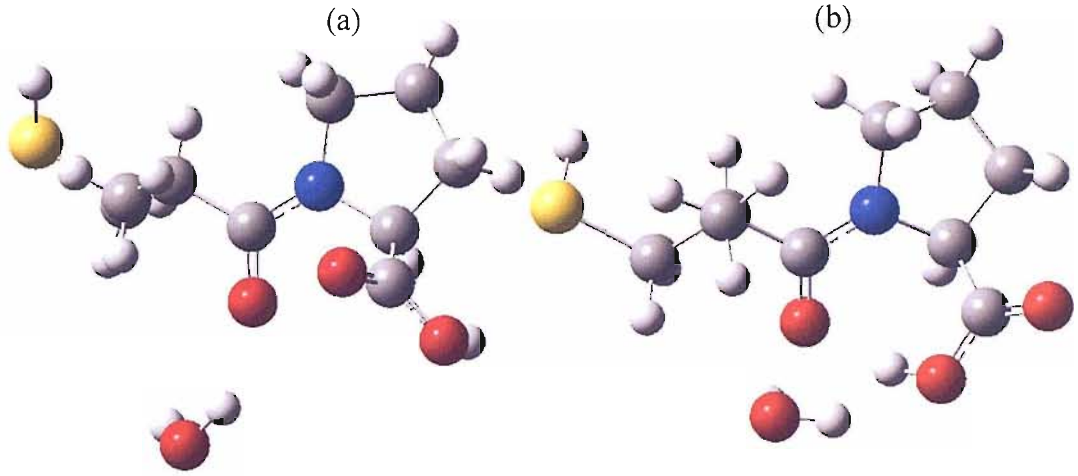

Figure 4.26 Final structures from the calculations with XRD structure plus H_2O for (2*S*)-captopril, (a) frequency only calculation and (b) optimisation plus frequency calculation.

A comparison of the predicted parent IR spectra from these calculations and the experimental parent IR from the 0.22 M solution in $CDCl_3$, measured on the dual PEM spectrometer, is shown in figure 4.27. The predicted spectra have been scaled by 0.97 for easier comparison to the experimental spectra.

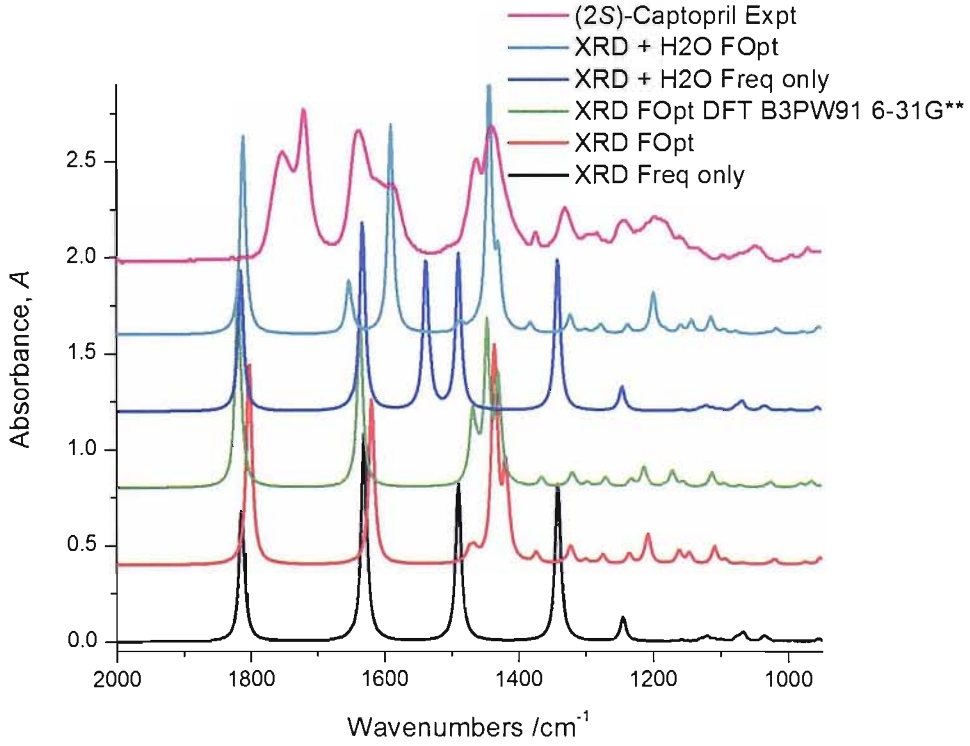

Figure 4.27 Comparison of predicted IR spectra of (2*S*)-Captopril from basic XRD structure, with experimental IR from 0.22 M solution in $CDCl_3$. Predicted spectra scaled by 0.97. Spectra offset for clarity.

The two frequency only calculations (there was no geometry optimisation prior to calculation of the frequencies) above (figure 4.27, black and dark blue lines) show identical IR spectra, apart from the additional band at 1585 cm^{-1} due to bending vibration of the water molecule, they do not show a good match to the experimental IR spectra and are proof that a geometry optimisation is always required to accurately predict vibrational spectra. The optimisation and frequency calculations (figure 4.27, red, green and light blue lines) show a better fit to the experimental IR spectra, particularly for the bands at 1620 and ~1410 cm^{-1} from the predicted spectra. However, the bands at 1800 cm^{-1} in the predicted IR spectra should be modelling the experimental peak at 1720 cm^{-1}. This band in the predicted IR spectrum is from the C=O stretch of the carboxylic acid group. The reason for the poor predicted position of this band is that in the solution it is probably hydrogen-bonded, which leads to a lower peak position in the IR due to the reduced strength of the C=O bond.

Following use of the XRD data for the starting structure, a calculation was performed using no prior information, in order to compare the two techniques. These calculations were performed at the DFT B3LYP 6-31G* and DFT B3PW91 6-31G** level and the predicted spectra were scaled by 0.98 and 0.97, respectively, for comparison to the experimental spectra in figure 4.28.

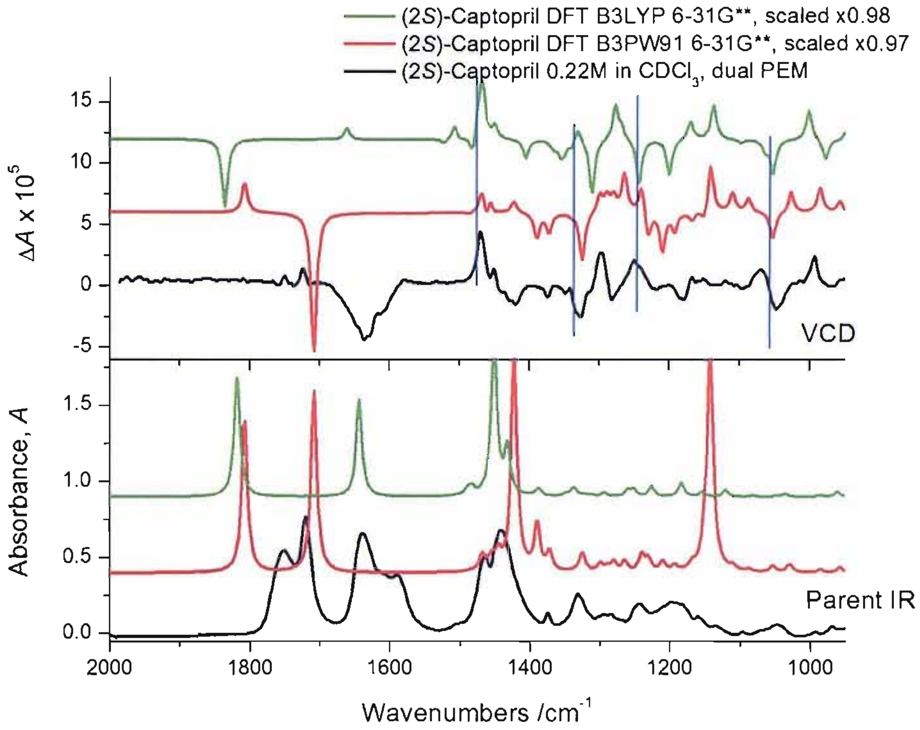

Figure 4.28 Comparison of experimental (black line) and predicted parent IR (lower frame) and VCD (upper frame) spectra of (2*S*)-captopril. Predicted spectra calculated at DFT B3LYP 6-31G* level (green line) and DFT B3PW91 6-31G (red line) scaled by 0.98 and 0.97, respectively. Spectra offset for clarity. Blue lines indicate corresponding bands in the VCD.**

Looking at the DFT B3PW91 6-31G** predicted spectra (figure 4.28, red line) it is possible to see that the two carbonyl C=O stretches with bands at 1810 cm^{-1} (from the COOH group) and 1700 cm^{-1} (from the lone carbonyl) in the predicted spectra need a larger scaling factor than the rest of the spectra. There are several corresponding bands in the rest of the spectrum, indicated by the blue lines on the figure above. So if the carbonyl bands are scaled further, to align with the corresponding experimental bands at 1710 and 1630 cm^{-1}, the predicted VCD peaks are seen to show a perfect match to the experimental VCD peaks for the carbonyl bands. These spectra are good enough to allow a confident determination of the absolute stereochemistry. The additional scaling is required as the prediction has not taken into account the hydrogen-bonding state of the bonds; a hydrogen bonded group produces a band shifted to a lower wavenumber in the spectrum, as compared to a group that is not hydrogen-bonded. In this case it has been found that calculations made from a starting structure drawn from no prior information gives a better match to the experimental spectra, than when XRD information is used.

A calculation was also performed using the minimum energy conformer from a search of conformational space using Spartan. The output geometry for this calculation is shown in figure 4.29 below, and the predicted spectra from this calculation are shown in figure 4.30.

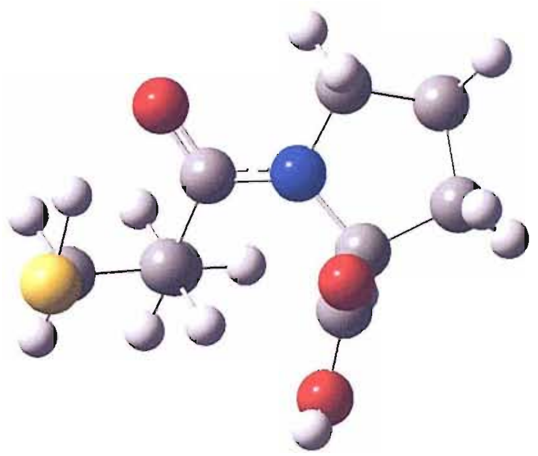

Figure 4.29 Output geometry from (2*S*)-captopril calculation at DFT B3LYP 6-31G level, starting geometry from minimum energy conformer produced by a Spartan search of conformational space.**

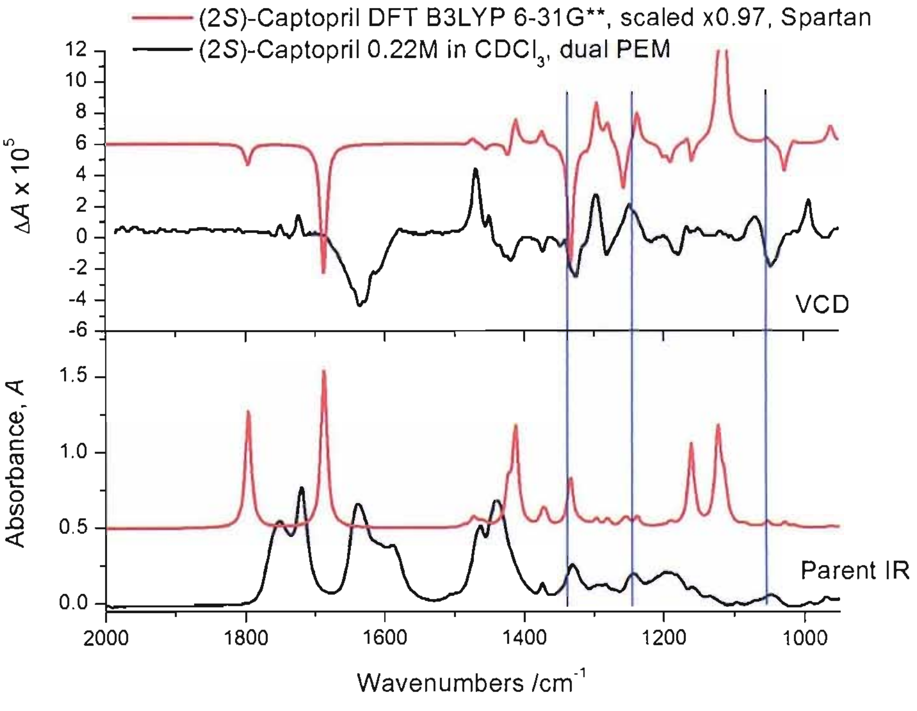

Figure 4.30 Comparison of experimental (black line) and predicted (red line) parent IR (lower frame) and VCD (upper frame) spectra of (2*S*)-captopril. Predicted spectra calculated at the DFT B3LYP 6-31G level, scaled by 0.97, starting geometry from Spartan. Spectra offset for clarity. Blue lines indicate corresponding bands.**

Starting the calculation using the minimum energy conformer from a search of conformational space has given an improved match to the experimental spectra (figure 4.30). Again the predicted C=O stretch bands at 1690 and 1800 cm^{-1}, are much overestimated as was seen in the previous calculation, but the VCD bands match well to the experimental VCD bands for these vibrations at 1640 and 1740 cm^{-1}. This calculation would again allow a confident assignment of the absolute stereochemistry as (*S*).

The components of a VCD spectrum come from certain parts of the molecule, and with a two chiral centre compound each chiral centre is responsible for certain bands in the VCD spectrum. By looking at the VCD spectra from the enantiomers and diastereoisomers of captopril, which chiral centres are responsible for which VCD bands can be assessed. The enantiomers and diastereoisomers are shown in figure 4.31.

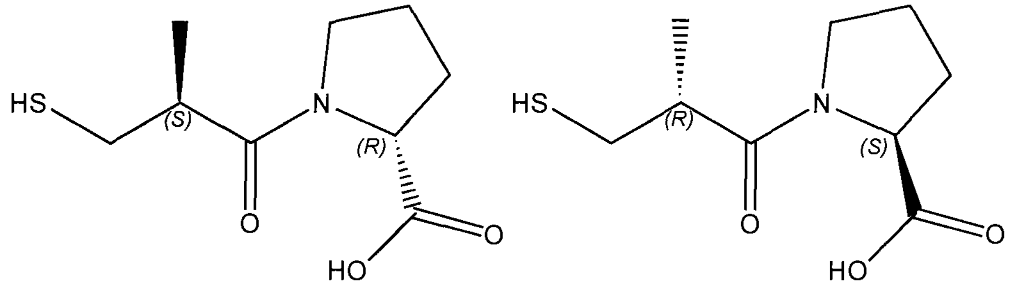

(*S*,*R*)-Captopril (*R*,*S*)-Captopril

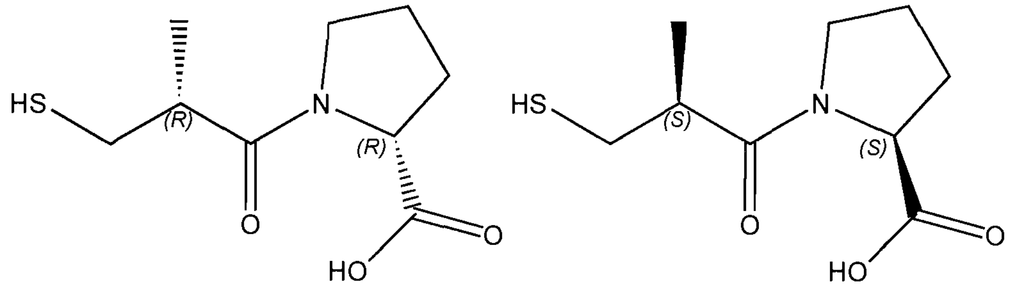

(2*R*)-Captopril (2*S*)-Captopril

Figure 4.31 The four possible stereoisomers of captopril

The predicted spectra from the two enantiomers (2*S* and 2*R*) and two diastereoisomers (*S*,*R* and *R*,*S*) of captopril are shown in figure 4.32, calculated at the DFT B3LYP 6-31G** level. The predicted parent IR spectra for the four compounds are virtually identical, as IR spectroscopy is a two dimensional technique. These identical IR give a good indication that the predicted VCD spectra are reliable, and that the calculations have optimised to mirror image structures. Comparison of the VCD spectra for the four compounds now enables observation of which chiral centre is responsible for which bands in the VCD spectra. This is a very useful tool for understanding which components are responsible for the different responses in the VCD spectrum. The (2*S*) and (2*R*) enantiomers are perfect mirror image spectra, and the (*S*,*R*) and (*R*,*S*) diastereoisomers spectra share aspects of each of the enantiomers spectra.

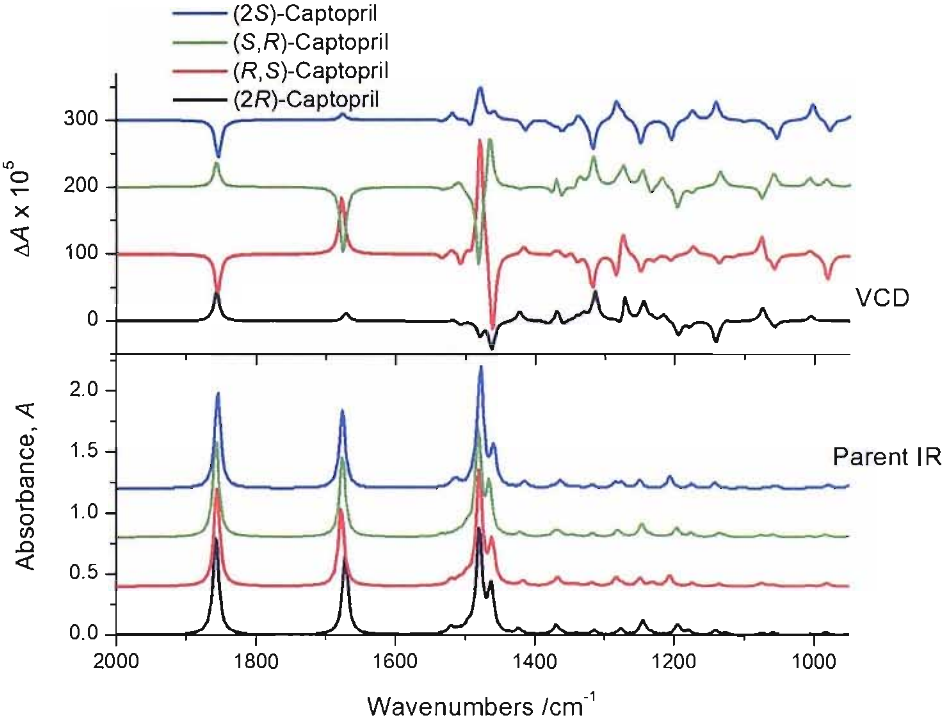

Figure 4.32 Comparison of predicted spectra of the enantiomers and diastereoisomers of captopril, calculated at the DFT B3LYP 6-31G level. Spectra offset for clarity.**

The band at 1870 cm^{-1} is from the carboxylic acid group chiral centre, we can tell this as the band is in the same negative direction for (2*S*) and (*R*,*S*), and is in the same positive direction for the (*S*,*R*) and (2*R*) molecules. It is easier to see these correlations by over-laying the spectra for pairs of the molecules, figures 4.33 and 4.34. The (*S*,*R*) and (2*S*) compounds share the same methyl chiral centre, the (*R*,*S*) and (2*R*) compounds also share this. Figures 4.35 and 4.36 the (*R*,*S*) and

(2*S*) share the same carboxylic acid chiral centre, as do the (*S*,*R*) and (2*R*) molecules.

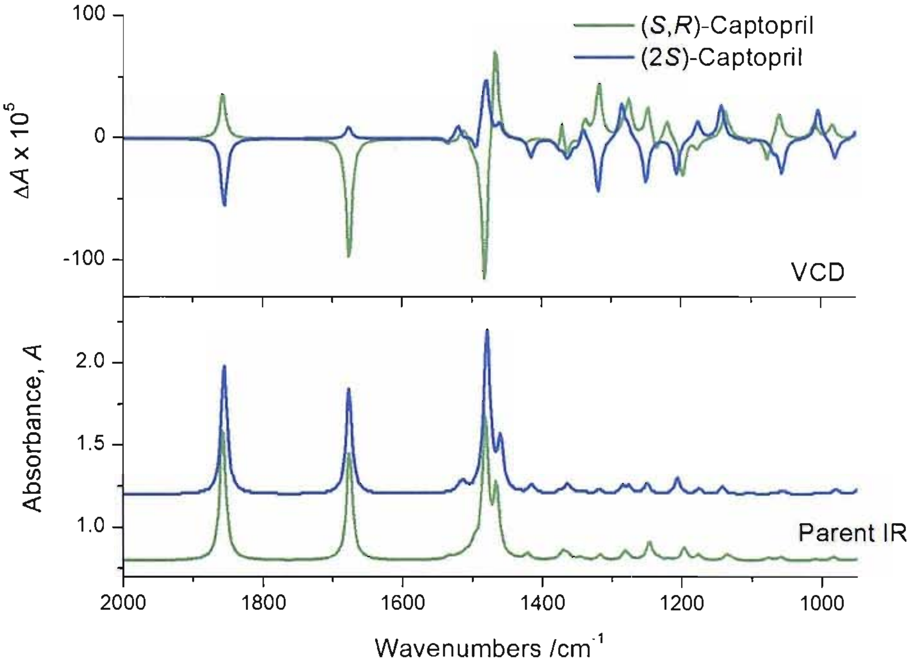

Figure 4.33 Comparison of (*S*,*R*) and (2*S*)-captopril predicted parent IR (lower frame) and VCD (upper frame) spectra, calculated using DFT B3LYP 6-31G. IR spectra offset for clarity.**

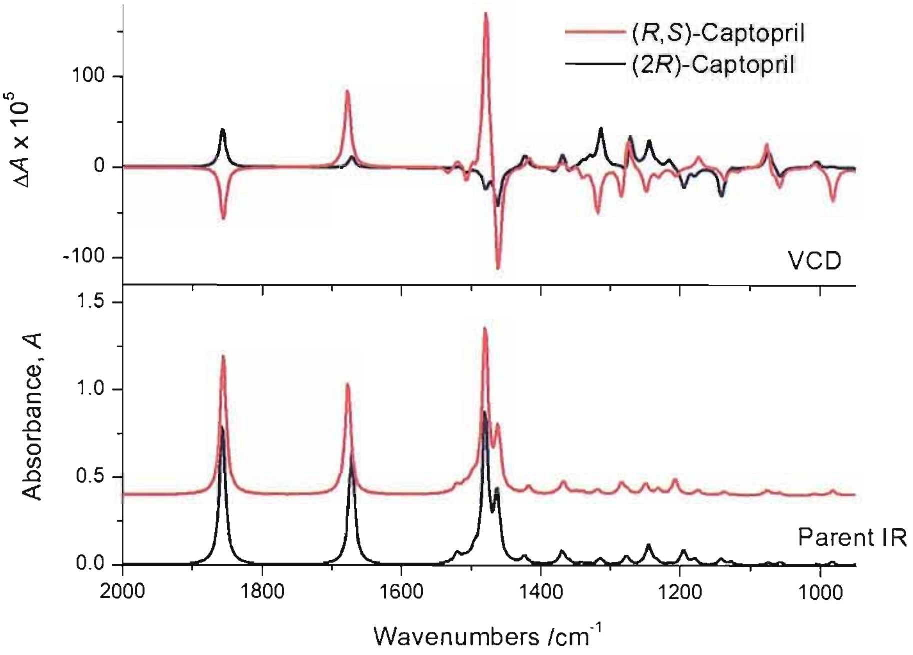

Figure 4.34 Comparison of (*R*,*S*) and (2*R*)-captopril predicted parent IR (lower frame) and VCD (upper frame) spectra, calculated using DFT B3LYP 6-31G. IR spectra offset for clarity.**

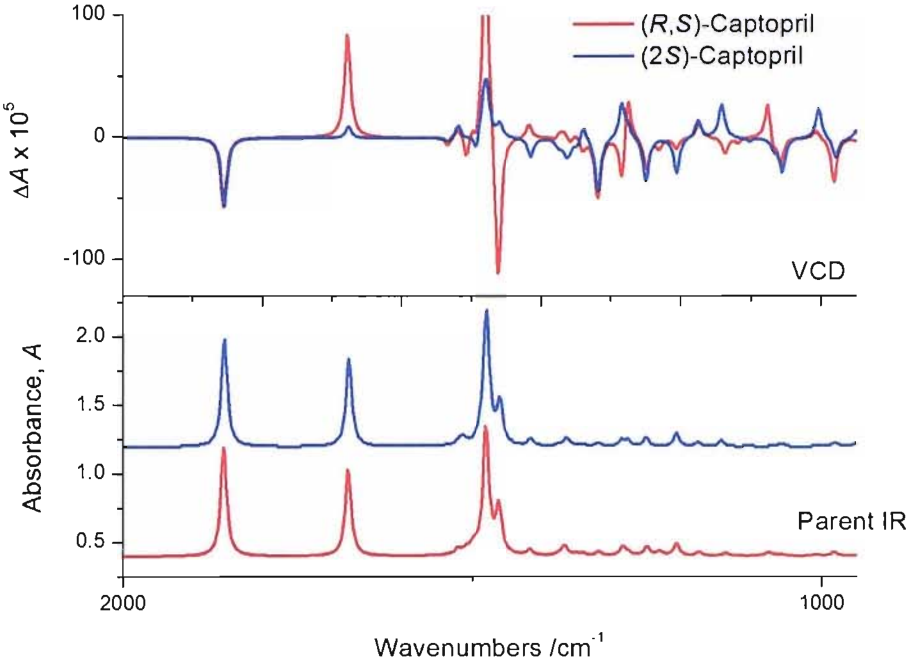

Figure 4.35 Comparison of (*R,S*) and (2*S*)-captopril predicted parent IR (lower frame) and VCD (upper frame) spectra, calculated using DFT B3LYP 6-31G. IR spectra offset for clarity.**

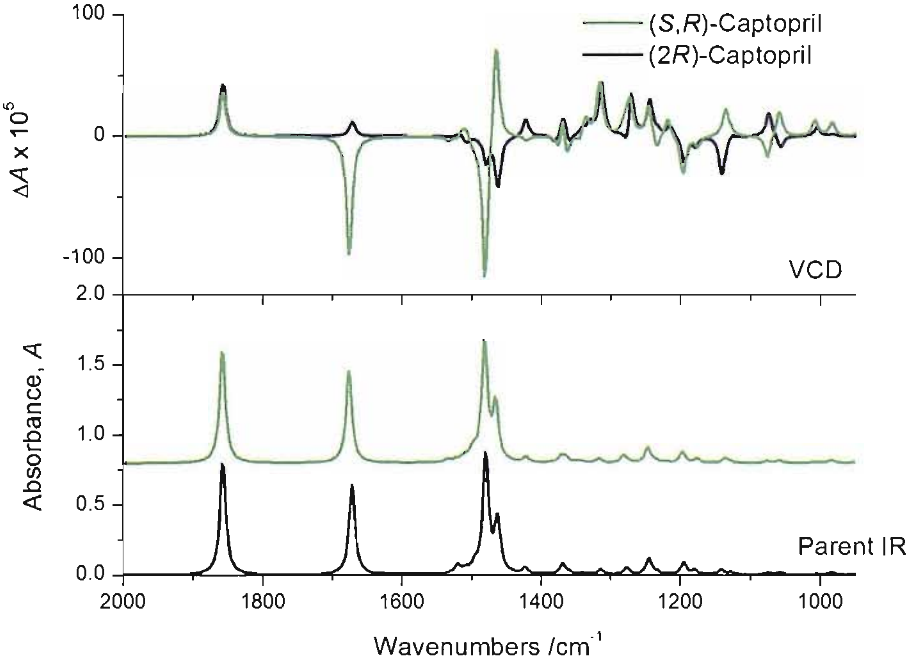

Figure 4.36 Comparison of (*S,R*) and (2*R*)-captopril predicted parent IR (lower frame) and VCD (upper frame) spectra, calculated using DFT B3LYP 6-31G. IR spectra offset for clarity.**

Assessment of which chiral centres are responsible for which bands in the VCD spectrum of a two chiral centre compound has proven very informative and it is interesting to see how the VCD bands interact. Choice of starting structure has again been shown to be important, but in this case using no prior information gave the best results. Fulfilling the hydrogen-bonding possibilities of a molecule can improve the match of the predicted spectra to the experimental spectra and is important to consider when hydrogen-bonding is possible.

4.5 Atenolol and related molecules

Atenolol (figure 4.37) is a fairly complex molecule; it contains just one chiral centre but has a lot of conformational flexibility about that chiral centre due to the chain that it is positioned on. Experimentally atenolol has proven a problematic system since the start of this research. It was chosen due to the availability of both enantiomers and the fact that when using single crystal XRD the absolute stereochemistry is undeterminable, due to both poor crystal quality and the lack of heavy atoms (chapter 1, figure 1.7). However, the VCD measurements have also proven extremely difficult; this is due to issues with solubility and concentration, using the solution state sampling method. Atenolol is completely insoluble in $CDCl_3$, and it is only soluble in deuterated methanol, which is not as good a solvent as it has a large absorption band in the infrared at ~1100 cm^{-1}, which limits the range of study to 1800 – 1200 cm^{-1}.

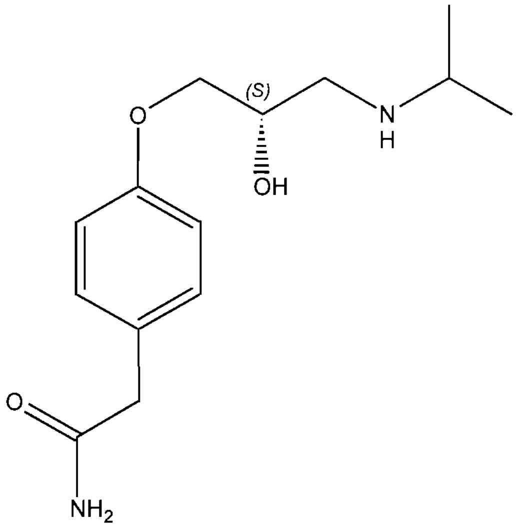

Figure 4.37 (*S*)-Atenolol

The quality of data obtainable from a solution of (*S*)-atenolol in D_4 methanol is shown in figure 4.38 (left hand side), along with a comparison of the solution data of the (*S*) and (*R*) enantiomers (figure 4.38, right hand side). These spectra were collected from 0.11 M solutions in CD_3-OD, on the dual PEM spectrometer, in a 94 μm BaF_2 cell, with a 10 hour collection time, at a resolution of 4 cm^{-1}, solvent spectra subtracted.

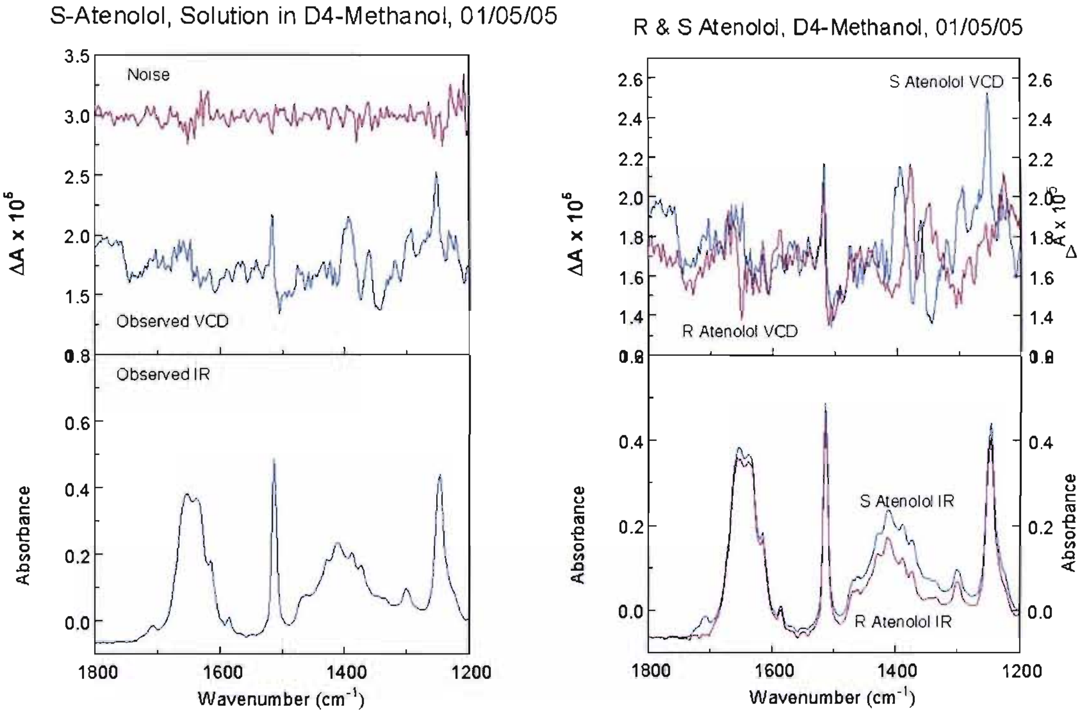

Figure 4.38 Solution state data from (*S*)-atenolol (left hand side) and comparison of (*S*) (blue line) and (*R*)-atenolol (red line) (right hand side). Parent IR (lower frame), VCD and associated noise (upper frame) spectra of atenolol as solutions in D_4 methanol. Solvent spectra subtracted.

The collection of a nujol mull spectrum of atenolol gave an excellent VCD spectrum (figure 4.39). Data collections were taken on both single and dual PEM spectrometers; a comparison of the (*S*)-atenolol spectra from the two spectrometers is shown in figure 4.39. The single PEM spectrometer spectra for both enantiomers are shown in figure 4.40, they show mirror image spectra, which is very encouraging for the single PEM spectrometer.

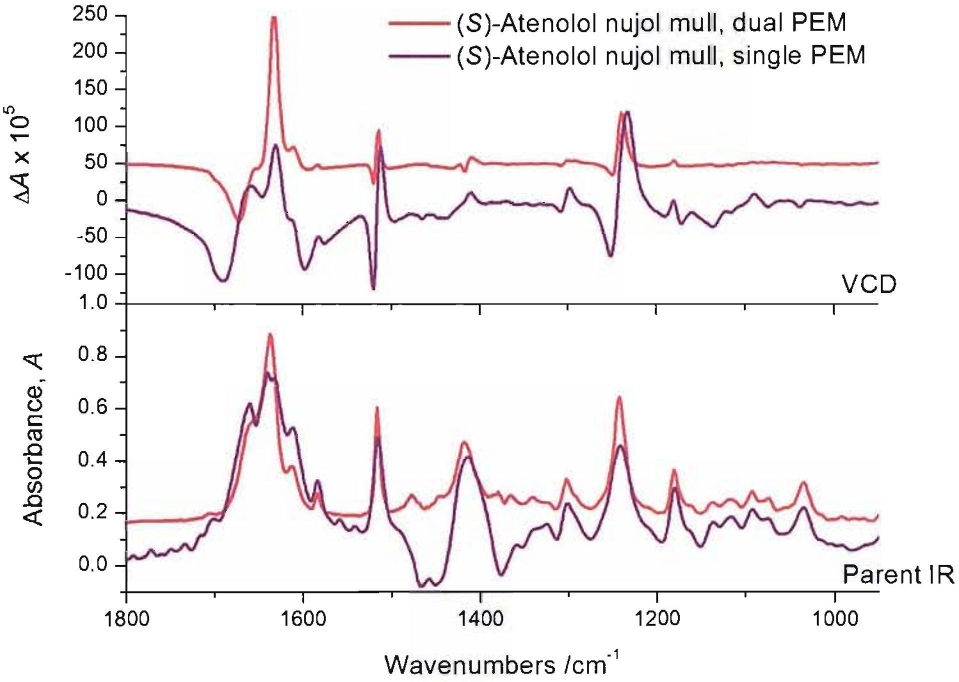

Figure 4.39 Comparison of (S)-atenolol parent IR (lower frame) and VCD (upper frame) spectra from the single (purple line) and dual (red line) PEM data collections. Spectra offset for clarity.

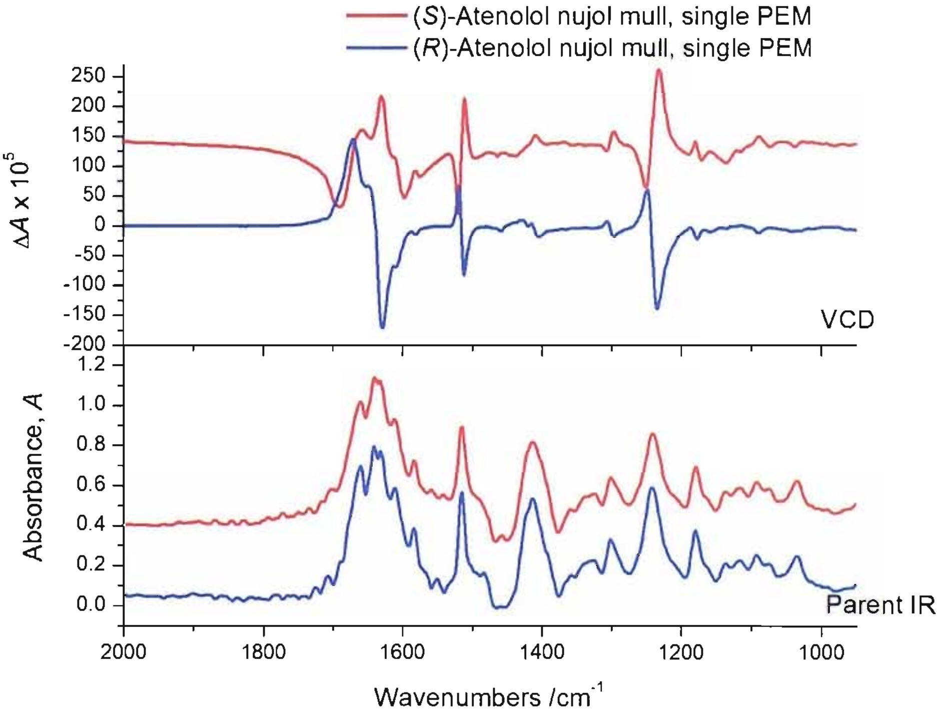

Figure 4.40 Comparison of the parent IR (lower frame) and VCD (upper frame) spectra of (*S*) and (*R*)-atenolol (red and blue lines respectively). Data collected on the single PEM spectrometer, 4096 scans, 16 cm^{-1} resolution, nujol subtracted. Spectra offset for clarity.

The best method so far for determining the starting geometry for a calculation is by performing a search of conformational space using a program such as Spartan.

The optimised geometry for (*S*)-atenolol from this search of conformational space is shown in figure 4.41 below. The calculation using Gaussian was then performed using this starting geometry and a comparison of the results with the experimental spectra is shown in figure 4.42.

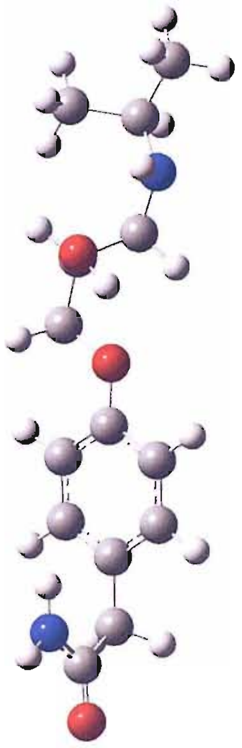

Figure 4.41 Optimised geometry of (*S*)-atenolol from search of conformational space using Spartan.

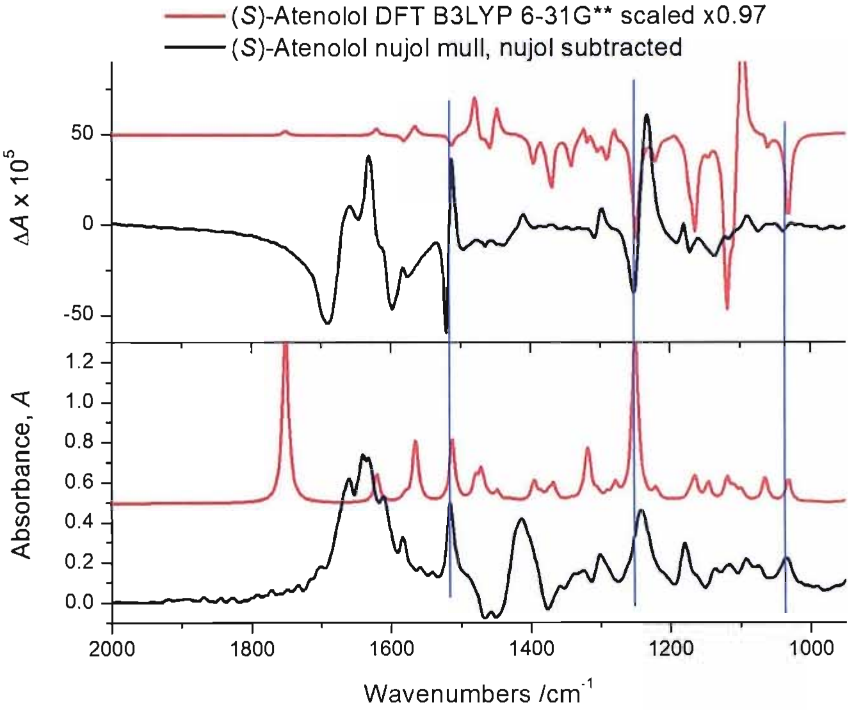

Figure 4.42 Comparison of parent IR (lower frame) and VCD (upper frame) spectra of (*S*)-atenolol predicted and experimental spectra. Predicted spectra from optimised Spartan geometry with DFT B3LYP 6-31G level calculation, scaled by 0.97. Experimental spectra from nujol mull on single PEM spectrometer, nujol subtracted. Spectra offset for clarity. Corresponding bands highlighted by blue lines.**

This comparison shows some good correlations between the experimental and predicted IR spectra, which are highlighted by the blue lines in figure 4.42. However, the IR correlations do not really carry through to the VCD spectra. One very prominent problem is the lack of a VCD band in the predicted spectrum to correspond to the large VCD peak seen in the experimental spectrum at ~1650 cm^{-1}. A confident assignment of absolute stereochemistry is not possible from this calculation.

Many further calculations have been performed on atenolol, but like the measurement of the experimental spectra, these predictions have not been straightforward. Dimer pairs and systems fulfilling the hydrogen-bonding potential of atenolol have been modelled, and information from the incomplete XRD investigations has been used. However, none of these predictions has given a better match than that seen in figure 4.42. The complexity of these calculations is due to the flexibility of the structure, which give the potential for many possible minimum energy conformers. It is quite possible that in the nujol mull (the solid state) there is a combination of a number of different conformers that leads to the VCD spectrum observed.

Atenolol shares the same structural backbone as many other compounds. For example the structures of pindolol (figure 4.43) and propranolol (figure 4.44) are shown below. Analysis of the VCD spectra of compounds using fragments has been used where a smaller fragment of a molecule which contains the same chiral centre and any prominent features, can reduce the computational time required to obtain an accurate predicted VCD spectrum.

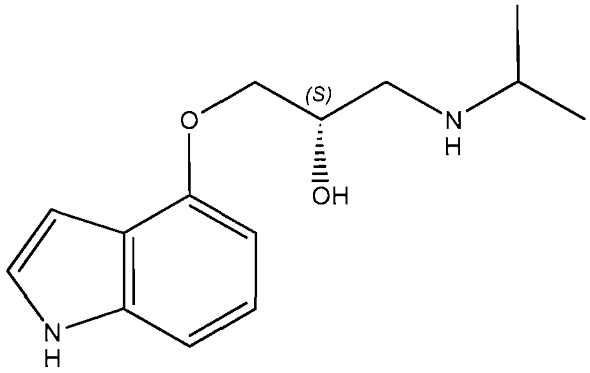

Figure 4.43 (*S*)-Pindolol

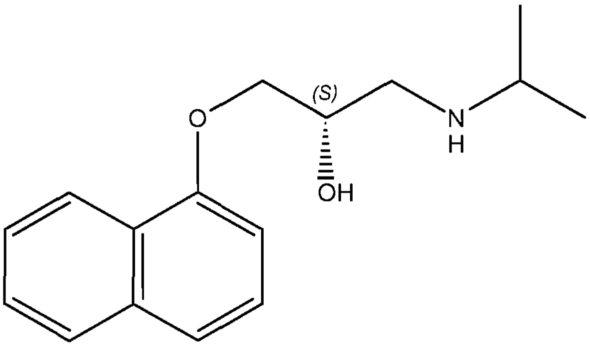

Figure 4.44 (*S*)-Propranolol

A calculation using the shared structural backbone of these compounds (figure 4.45) was performed at the DFT B3LYP 6-31G level and the scaled predicted spectra were compared to the experimental spectra of the compounds sharing this backbone. Comparisons of this calculation with the experimental spectra are shown in figure 4.46 for (*S*)-atenolol, in figure 4.47 for (*S*)-pindolol and in figure 4.48 for (*S*)-propranolol.

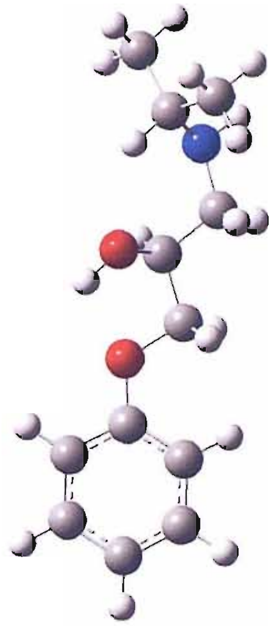

Figure 4.45 Structural backbone shared by atenolol, pindolol and propranolol, shown in the (*S*)-configuration.

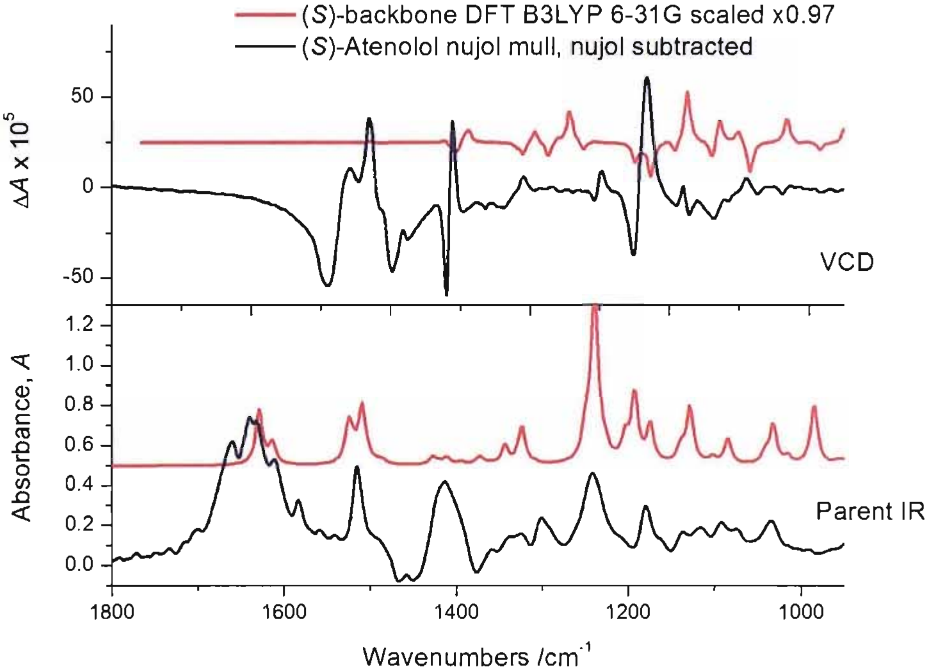

Figure 4.46 Comparison of the (*S*)-backbone calculation parent IR (lower frame) and VCD (upper frame) spectra with the experimental spectra of (*S*)-atenolol from nujol mull. Predicted spectra calculated at the DFT B3LYP 6-31G level. Spectra offset for clarity.

The comparison of the predicted spectra from the backbone calculation (figure 4.46) with the (*S*)-atenolol experimental spectra from the nujol mull does not show a good correlation especially for the VCD spectra. The IR spectra appear to show several corresponding bands, but the VCD at these bands do not correlate.

It may be that a higher level of calculation is necessary to achieve the correlation in the VCD spectrum.

Comparison of the predicted spectra from the backbone calculation with the (*S*)-pindolol and (*S*)-propranolol experimental spectra from the nujol mull (figures 4.47 and 4.48 respectively) show a better correlation than seen with the atenolol spectra.

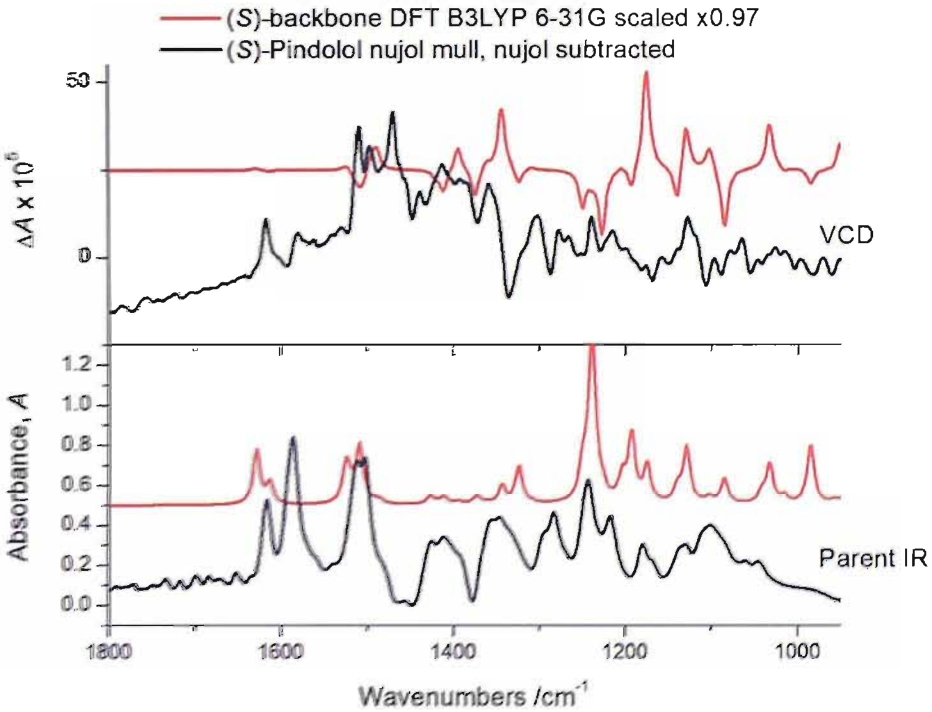

Figure 4.47 Comparison of the (*S*)-backbone calculation parent IR (lower frame) and VCD (upper frame) spectra with the experimental spectra of (*S*)-pindolol from nujol mull. Predicted spectra calculated at the DFT B3LYP 6-31G level. Spectra offset for clarity.

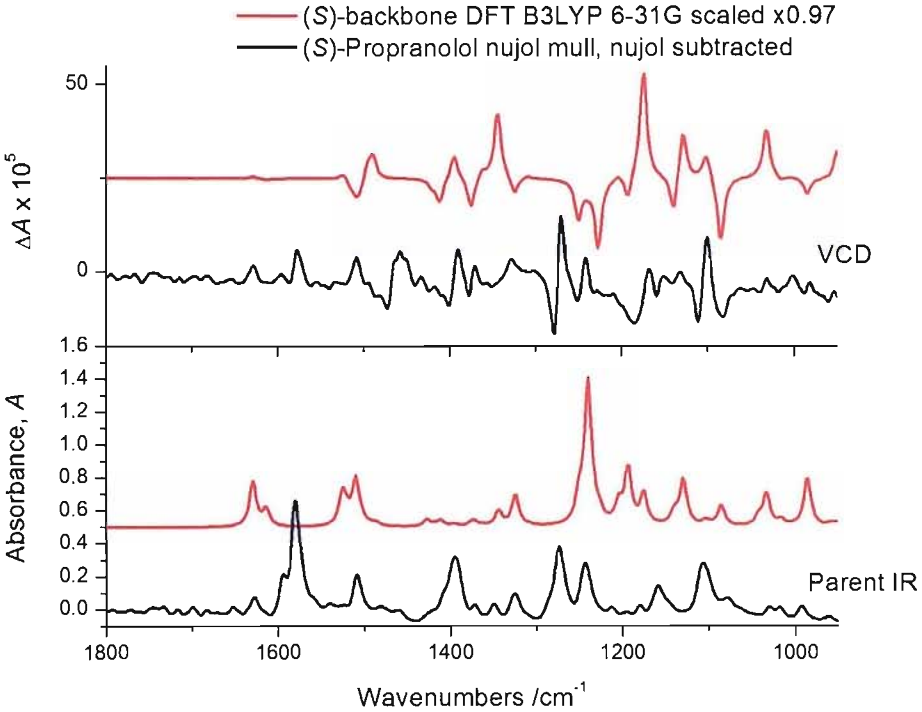

Figure 4.48 Comparison of the (*S*)-backbone calculation parent IR (lower frame) and VCD (upper frame) spectra with the experimental spectra of (*S*)-propranolol from nujol mull. Predicted spectra calculated at the DFT B3LYP 6-31G level. Spectra offset for clarity.

This fragment calculation technique appears to be more effective for two of the compounds, than the other. Calculation at a higher level, using the 6-31G** basis set was performed and the resultant predicted spectra are compared to the experimental spectra from the three compounds in figures 4.49, 4.50 and 4.51 below. The predicted spectra are scaled by 0.97 for easier comparison to the experimental spectra. Use of a higher level calculation has not significantly improved the match to the experimental spectra, although the match with (*S*)-pindolol, looks better than before.

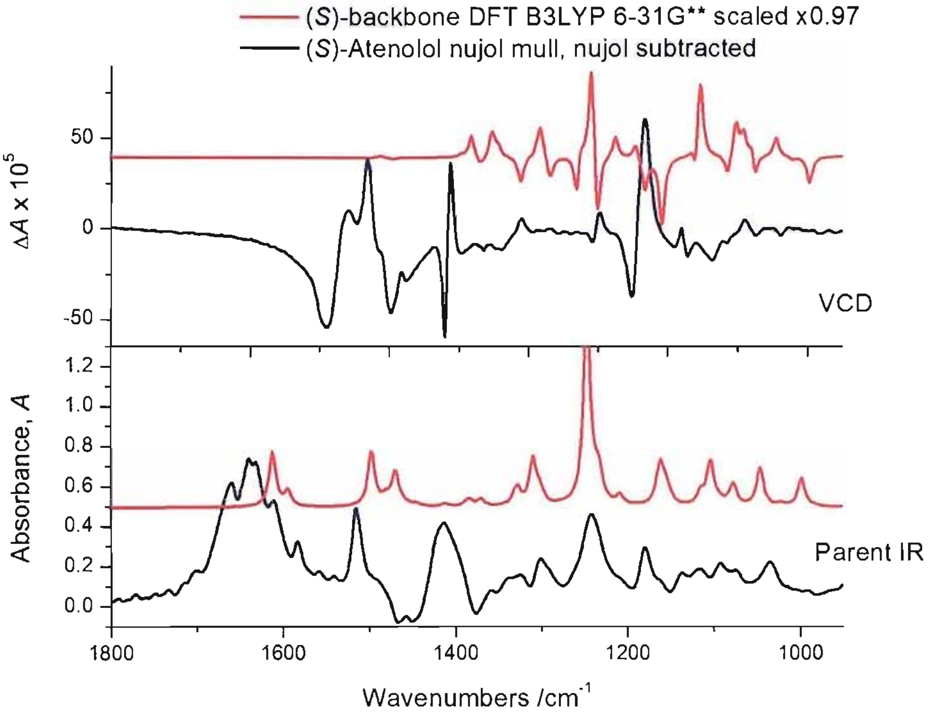

Figure 4.49 Comparison of the (*S*)-backbone calculation parent IR (lower frame) and VCD (upper frame) spectra with the experimental spectra of (*S*)-atenolol from nujol mull. Predicted spectra calculated at the DFT B3LYP 6-31G** level. Spectra offset for clarity.

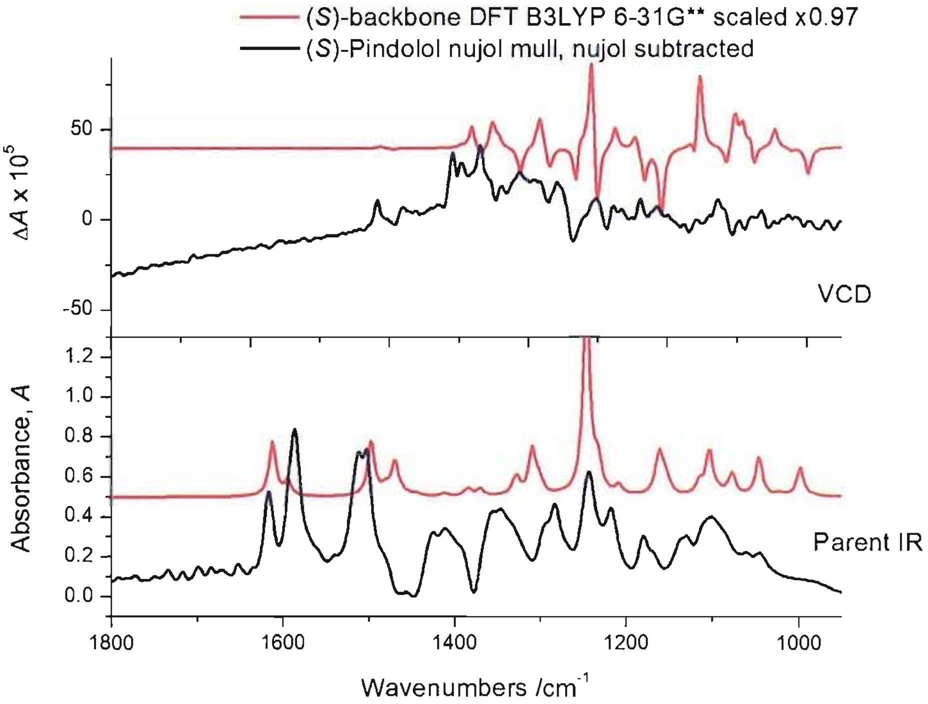

Figure 4.50 Comparison of the (*S*)-backbone calculation parent IR (lower frame) and VCD (upper frame) spectra with the experimental spectra of (*S*)-pindolol from nujol mull. Predicted spectra calculated at the DFT B3LYP 6-31G** level. Spectra offset for clarity.

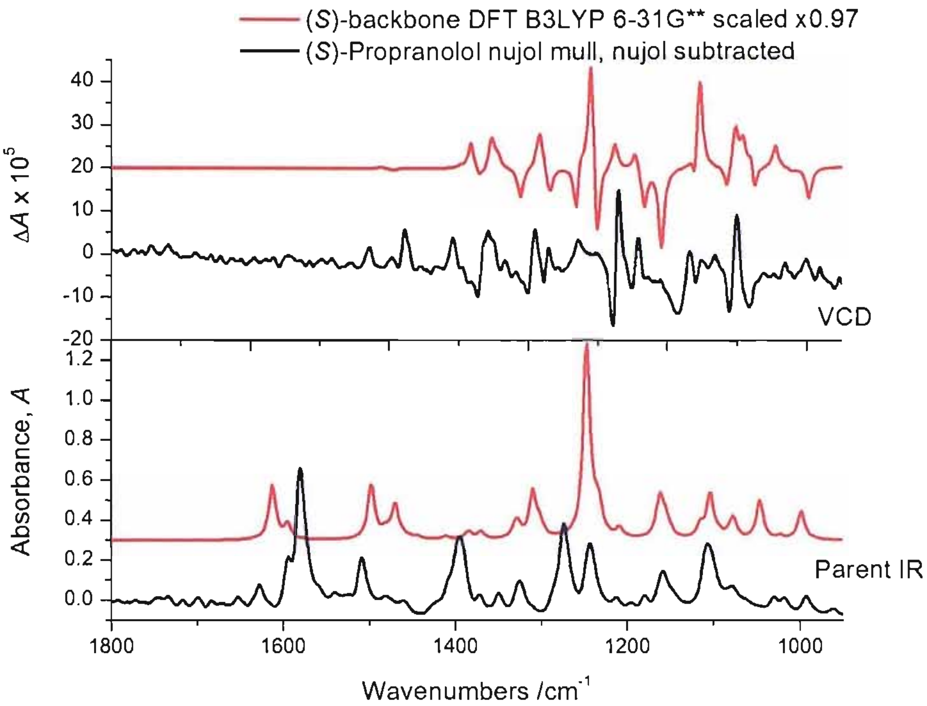

Figure 4.51 Comparison of the (*S*)-backbone calculation parent IR (lower frame) and VCD (upper frame) spectra with the experimental spectra of (*S*)-propranolol from nujol mull. Predicted spectra calculated at the DFT B3LYP 6-31G level. Spectra offset for clarity.**

4.6 (*S*)-Ibuprofen and related molecules

(*S*)-Ibuprofen (figure 4.52) is slightly less conformationally flexible than atenolol as the chiral centre is on a shorter chain. However, there is the possibility of hydrogen bonding with the carboxylic acid group. This hydrogen bonding can be seen from the XRD data, where a dimer pair forms the asymmetric unit in the crystal structure (chapter 5). This dimer formation will increase the complexity of the calculations needed to predict an accurate VCD spectrum.

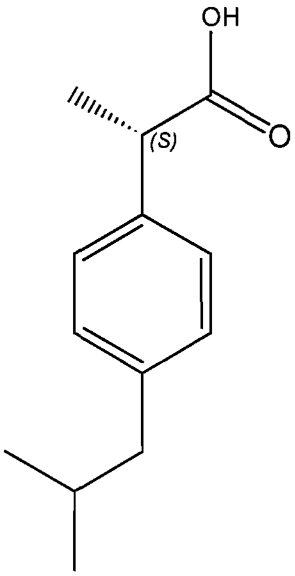

Figure 4.52 (*S*)-Ibuprofen

Published spectra have made use of marker bands and key reduced structural features of larger molecules for absolute stereochemistry determinations that otherwise would have been extremely computationally expensive.[9, 10] The use of marker bands for identification of the absolute stereochemistry of specific chiral centres would be a useful time saving technique within the pharmaceutical industry, where families of compounds are often made within the drug development process. Each of the compounds within the families needs to be identified for the strict stereochemical regulations that govern pharmaceutical marketing. Figure 4.53 shows the presence of an (*S*)-configuration marker band in the VCD spectra of both (*S*)-ibuprofen and (*S*)-2-phenylpropionic acid.[11] The marker band arises from the common structural fragments of the two compounds and the identical chiral centre environments. For compounds that share these structural features a prediction can be carried out for the smaller fragment and the parameters optimised to obtain the best fit for this structure. The knowledge that comes from this prediction can then be applied to the prediction of the spectra of the other compounds in the family, giving a considerable reduction in the amount of computational time necessary to obtain an accurate prediction.

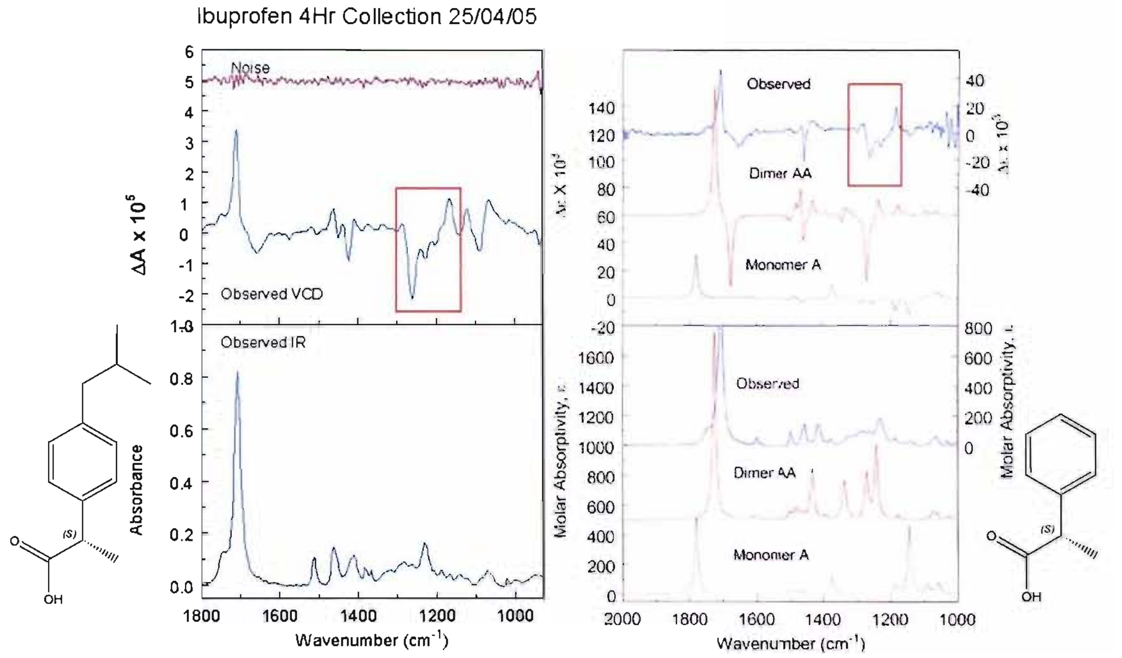

Figure 4.53 (a) VCD marker band found in (*S*)-ibuprofen and (b) marker band from (*S*)-2-phenylpropionic acid,[11] red box indicates the common marker band.

For prediction of the (*S*)-ibuprofen IR and VCD spectra, a method that has been previously published for the prediction of (*S*)-2-phenylpropionic acid spectra was used.[11] (*S*)-2-phenylpropionic acid has the same structural backbone and chiral centre as (*S*)-ibuprofen, hence the same VCD marker bands are seen in their respective VCD spectra (figure 4.53). The method used for prediction of the VCD spectrum for (*S*)-ibuprofen involved calculation with DFT B3LYP 6-31G**, for three separate dimer pairs, made up from two different possible configurations of the carboxylic acid group with respect to the adjacent methyl group A and B. Molecule A has the methyl group on the same side as the C=O of the carboxylic acid group, molecule B has the methyl group on the opposite side to the C=O of the carboxylic acid group. The dimer pairs are shown in figure 4.54 below, with the three possible combinations of the two available conformations of the molecule, AA, AB and BB.

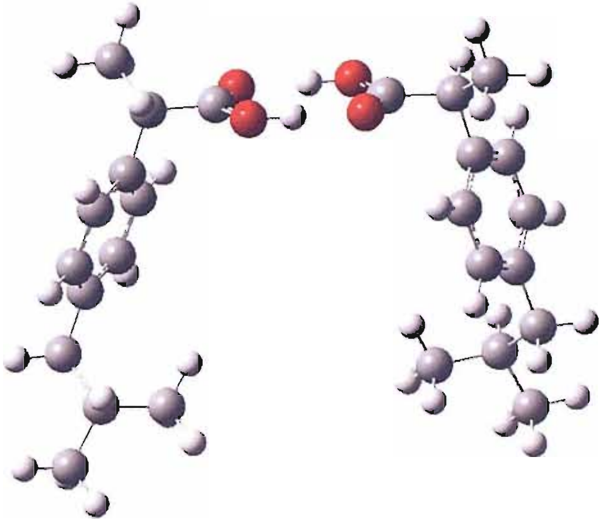

AA Dimer

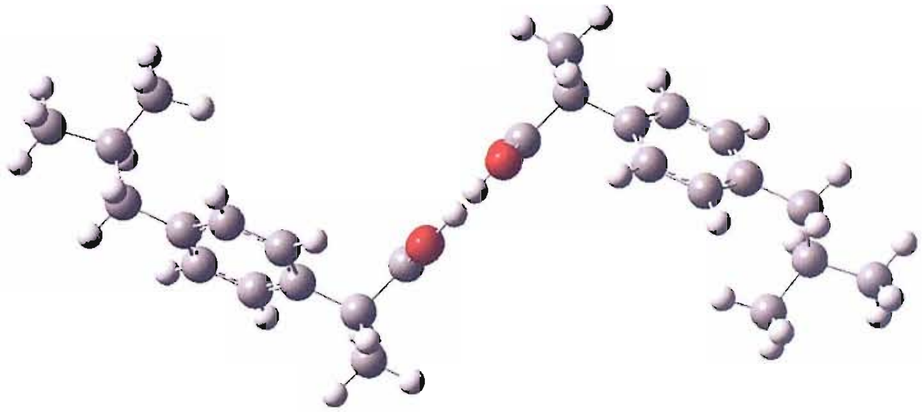

AB Dimer

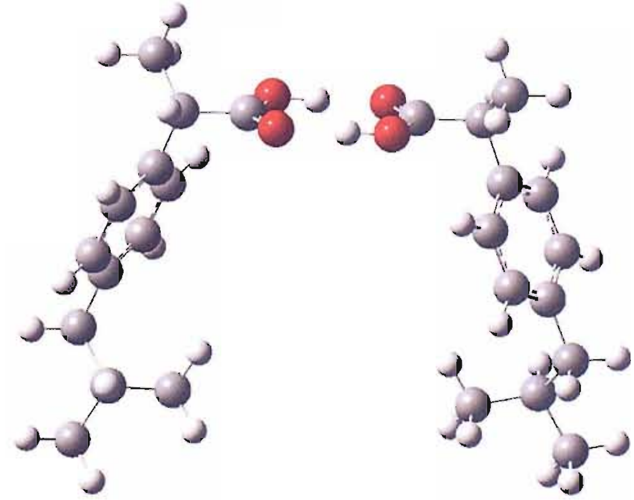

BB Dimer

Figure 4.54 Three possible dimer pairs from the two configurations A and B of (*S*)-ibuprofen.

Combination of the predicted IR and VCD spectra of the three dimers in the paper for (*S*)-2-phenylpropionic acid gave a good fit to the experimental IR and VCD spectra. The Boltzmann population distribution was calculated from the results of the (*S*)-ibuprofen dimer calculations, using a statistical weighting factor of two for the AB dimer. A population distribution of 56% AA, 37% AB and 7% BB is thus obtained from the energy differences between the dimers pairs. This distribution is very similar to the population distribution for the (*S*)-2-phenylpropionic acid. Figure 4.55 shows the individual parent IR and VCD spectra of the three different dimers, as well as the combination spectra for (*S*)-ibuprofen. Comparison of the spectra enables determination of which bands are due to which dimers in the combined spectra.

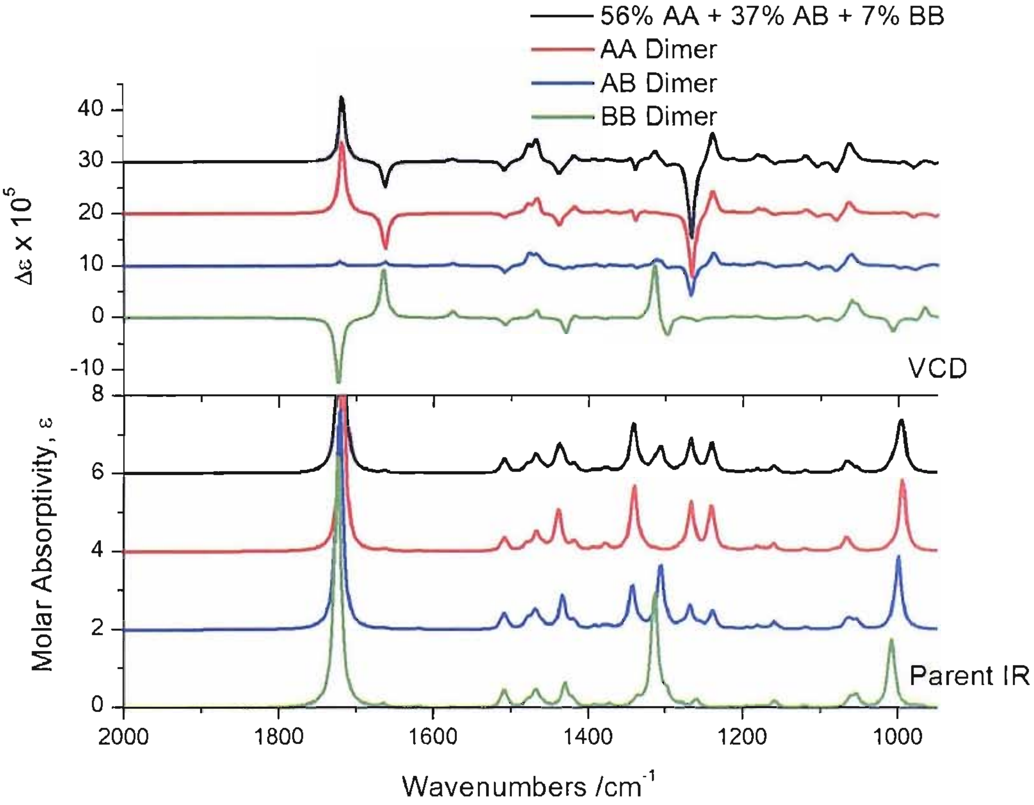

Figure 4.55 Predicted IR (lower frame) and VCD (upper frame) spectra of (*S*)-ibuprofen calculated at DFT B3LYP 6-31G level, black line = combined dimer, red line = AA dimer, blue line = AB dimer and green line = BB dimer. Spectra offset for clarity.**

To compare the experimental and combined predicted IR and VCD spectra, it is necessary to apply a scale factor to the predicted spectra. This scale factor is calculated as described previously (chapter 3, section 3.3.2), through comparison of the corresponding bands of the predicted and experimental IR spectra, followed by calculation of the ratio ν_{exp} / ν_{calc} for each band, the average of these values gives the scale factor to be applied. The experimental and combined predicted (raw) IR spectra are shown in figure 4.56. VCD measurements for (*S*)-ibuprofen were carried out on a dual PEM spectrometer. Sample solution of a 0.29 M concentration of (*S*)-ibuprofen in $CDCl_3$, measured over 10 hours, in a 94 μm BaF_2 solution cell at 4 cm^{-1} resolution.

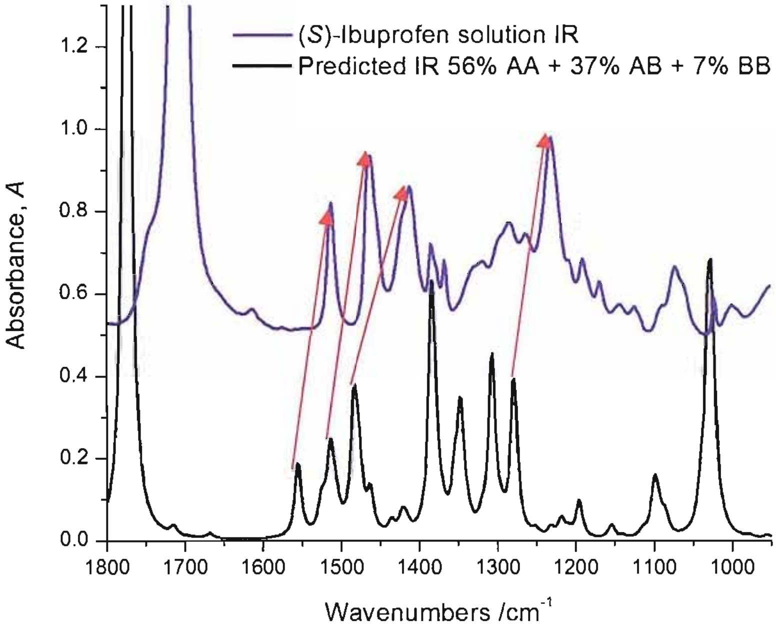

Figure 4.56 Comparison of the experimental IR spectrum (purple line) and predicted combined IR spectrum (black line) of (*S*)-ibuprofen. Spectra offset for clarity.

From this IR spectrum (figure 4.56) the corresponding bands were determined and tabulated (table 4.2). The average scale factor was then determined and applied to the predicted combined IR spectrum (figure 4.57).

Table 4.2 Calculation of scale factor for the predicted spectra of (*S*)-ibuprofen

Predicted Band /cm^{-1}	Experimental Band /cm^{-1}	Scale factor
1280	1230.50	0.9613
1510	1463.87	0.9694
1560	1512.08	0.9693
1770	1708.81	0.9654
	Average Scale Factor	**0.9664**

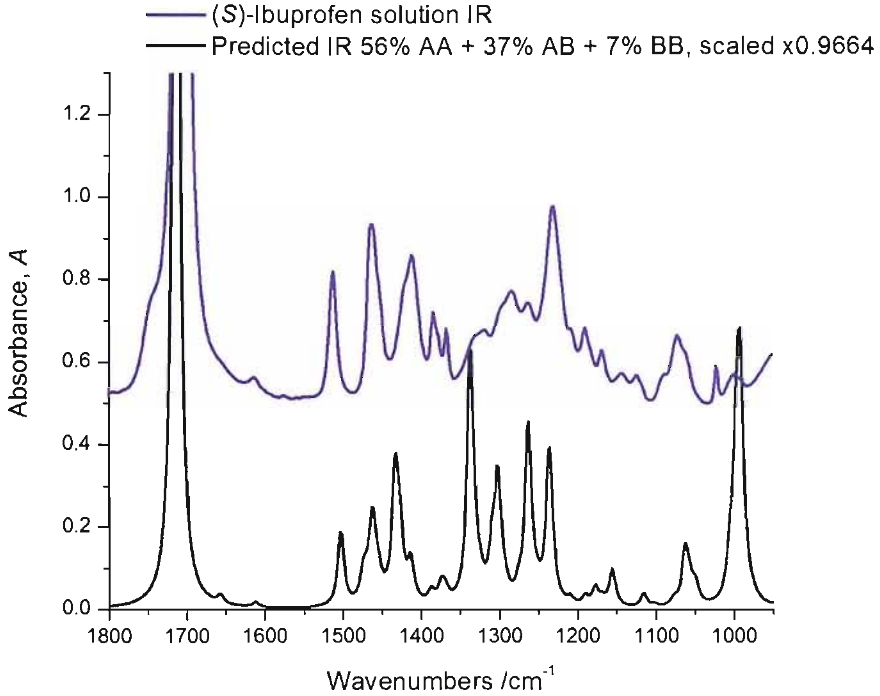

Figure 4.57 Comparison of the experimental IR spectrum (purple line) and the scaled (x0.9664) predicted combined IR spectrum (black line) of (*S*)-ibuprofen. Spectra offset for clarity.

The scaled predicted IR spectrum for (*S*)-ibuprofen shows a good fit to the experimental IR spectrum of (*S*)-ibuprofen, and the scale factor of 0.9664 can be applied to the combined predicted VCD spectrum and compared to the experimental VCD spectrum (figure 4.58).

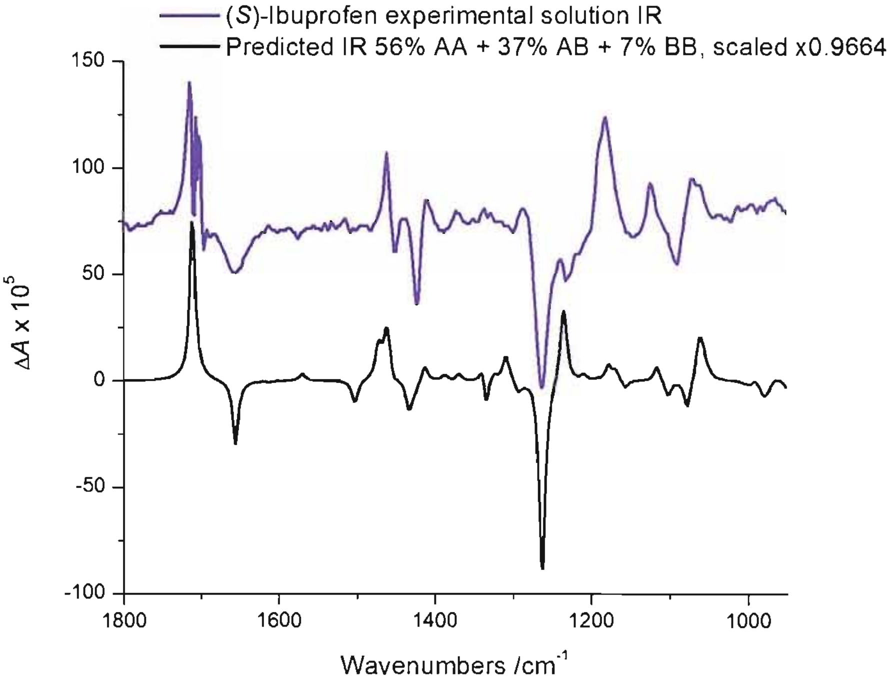

Figure 4.58 Comparison of the experimental VCD spectrum (purple line) and the scaled (x0.9664) predicted combined VCD spectrum (black line) of (*S*)-Ibuprofen. Spectra offset for clarity.

With the scaled combined predicted VCD spectrum for (*S*)-ibuprofen now showing a good fit to the experimental VCD spectrum of (*S*)-ibuprofen, the goodness of fit parameter can be determined as before. Table 4.3 shows the tabulated bands for the comparison and the final *R*-factor determination.

Table 4.3 Calculation of the goodness of fit parameter, *R*-Factor, for (*S*)-ibuprofen

(*S*)-Ibuprofen, Dual PEM VCD Spectrum	**Predicted (*S*)-Ibuprofen DFT B3LYP 6-31G**, Scale factor 0.9664**
1714	1710
1656	1652
1461	1459
1423	1430
1263	1265
1182	1179
1124	1111
1062	1063
***R*-Factor**	**0.02842**

The final determined *R*-factor for the goodness of fit of the combined dimer predicted VCD spectrum to the experimental VCD spectrum of (*S*)-ibuprofen is $R = 2.84\%$.

The method of combining dimers to create a good predicted VCD spectrum appears to work very well, with an excellent *R*-factor. Application of this technique to further possible dimer pairs will improve calculations and it will be especially helpful if the XRD shows a dimer in the asymmetric unit, which may then be put into the calculation with a selected absolute stereochemistry.

Use of published spectra of compounds with similar structural features and chiral centres, has been shown to provide an excellent starting point for new predictions. This can radically reduce the time spent on new calculations. Consideration of the likely formation of dimer pairs and dominant conformers leads to more accurate predictions of VCD spectra, which in turn leads to increased confidence in absolute stereochemistry determinations.

(*S*)-Ketoprofen (figure 4.59) shares the same structural backbone as (*S*)-ibuprofen, and 2-phenylproprionic acid. Therefore it is logical to assume that the (*S*)-ketoprofen spectra should show the same key marker band for the (*S*) configuration as shown for the case of (*S*)-ibuprofen and (*S*)-2-phenylpropionic acid.

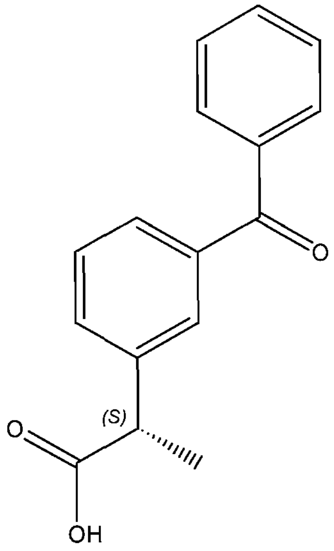

Figure 4.59 (*S*)-Ketoprofen

The experimental nujol mull spectrum for (*S*)-ketoprofen is shown in figure 4.60, and shows good IR and VCD spectra when collected upon the single PEM spectrometer.

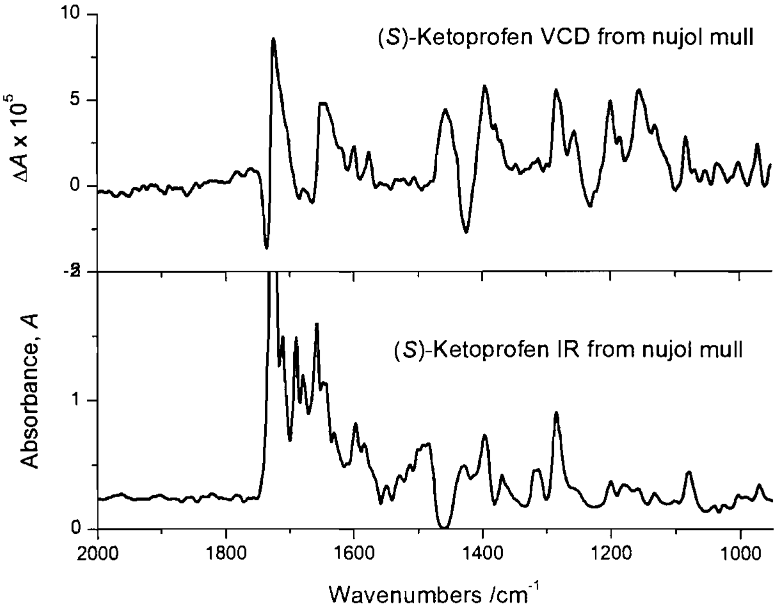

Figure 4.60 (*S*)-Ketoprofen parent IR (lower frame) and VCD (upper frame) spectra, measured from nujol mull data on the single PEM spectrometer, 4096 scans, 16 cm^{-1}, nujol subtracted.

However, comparison of the (*S*)-ketoprofen and (*S*)-ibuprofen nujol mull spectra does not show the same key marker band indicative of the (*S*) configuration (figure 4.61) as seen when the (*S*)-ibuprofen is compared to the (*S*)-phenylpropionic acid.

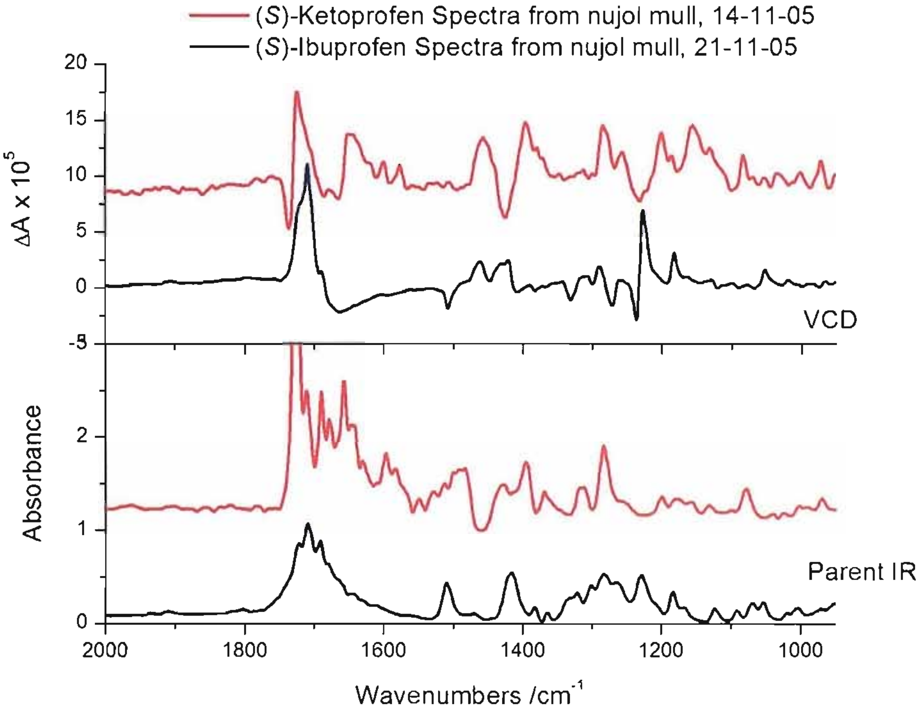

Figure 4.61 Comparison of nujol mull data from (*S*)-ketoprofen (red line) and (*S*)-ibuprofen (black line), parent IR (lower frame) and VCD (upper frame). Spectra offset for clarity.

When the predicted spectra are calculated for the three dimer pairs of (*S*)-ketoprofen, and combined using the Boltzman distribution with the energies from the calculations (figure 4.62), the comparison of the combined predicted spectra with the experimental spectra does not show a good match (figure 4.63). The blue lines highlight the corresponding bands.

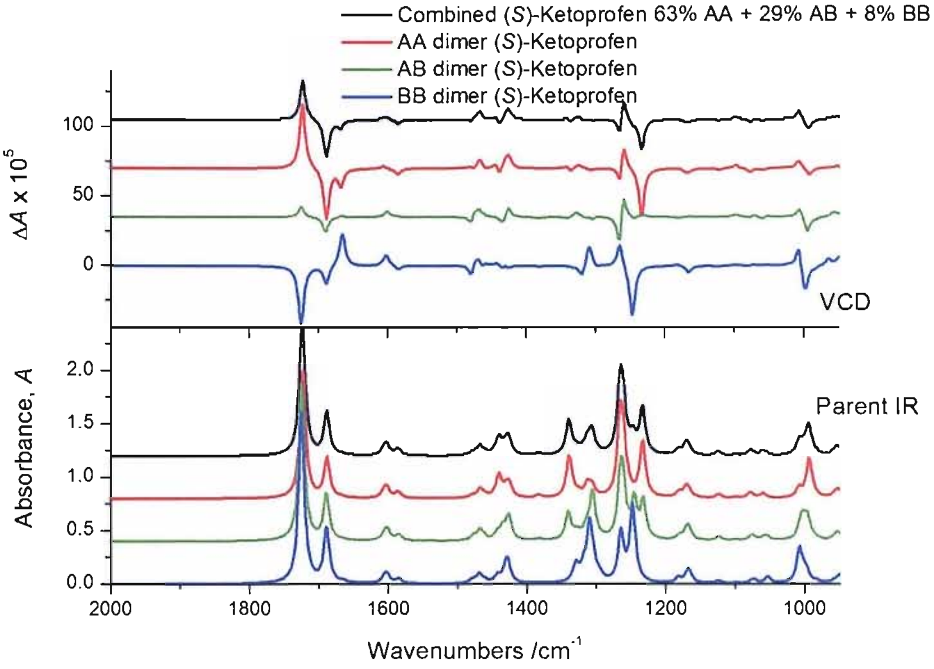

Figure 4.62 Comparison of parent IR (lower frame) and VCD (upper frame) of (*S*)-ketoprofen from the three possible dimer pairs and the combined spectra. Spectra offset for clarity.

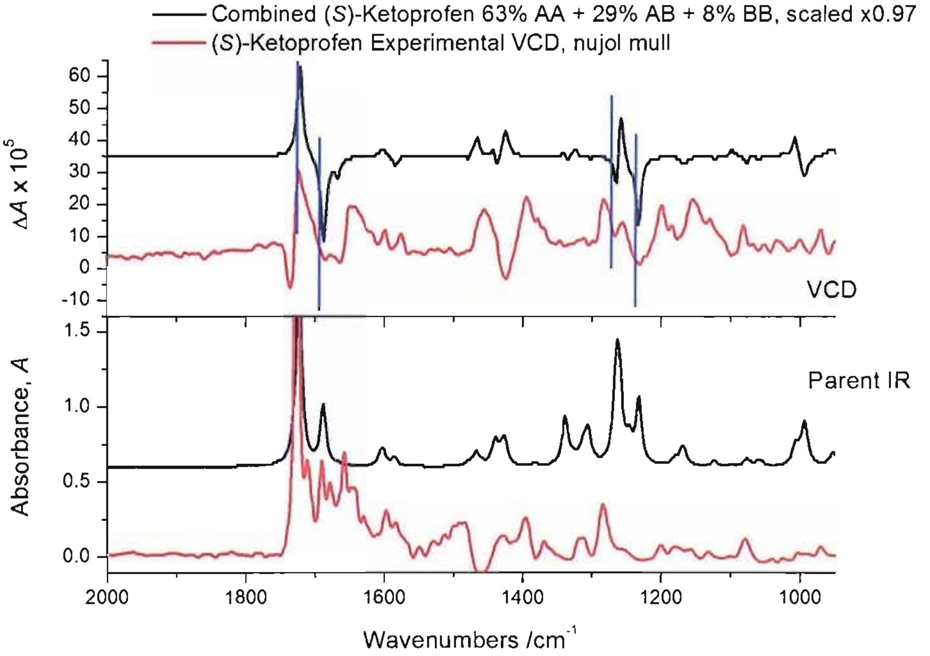

Figure 4.63 Comparison of parent IR (lower frame) and VCD (upper frame) of (*S*)-ketoprofen, combined predicted spectra and experimental spectra from nujol mull. Spectra offset for clarity. Blue lines indicate corresponding bands in the VCD.

There are corresponding bands (indicated by the blue lines in figure 4.63) at 1720 cm^{-1} and the combination of bands at ~1250 cm^{-1}. Rather than the bands being of the same relative intensity, the bands occur in the right directions i.e. positive and negative predicted bands correspond to the positive and negative bands in the experimental spectra.

It was thought that the monomers of (*S*)-ketoprofen may show a better fit to the experimental spectra, and so the calculations were performed for monomers A and B. These results are compared to the dimer spectra in figure 4.64. They show very different bands, with the positions shifted to different wavenumbers as now the carboxylic acid group is not involved in hydrogen-bonding (monomers).

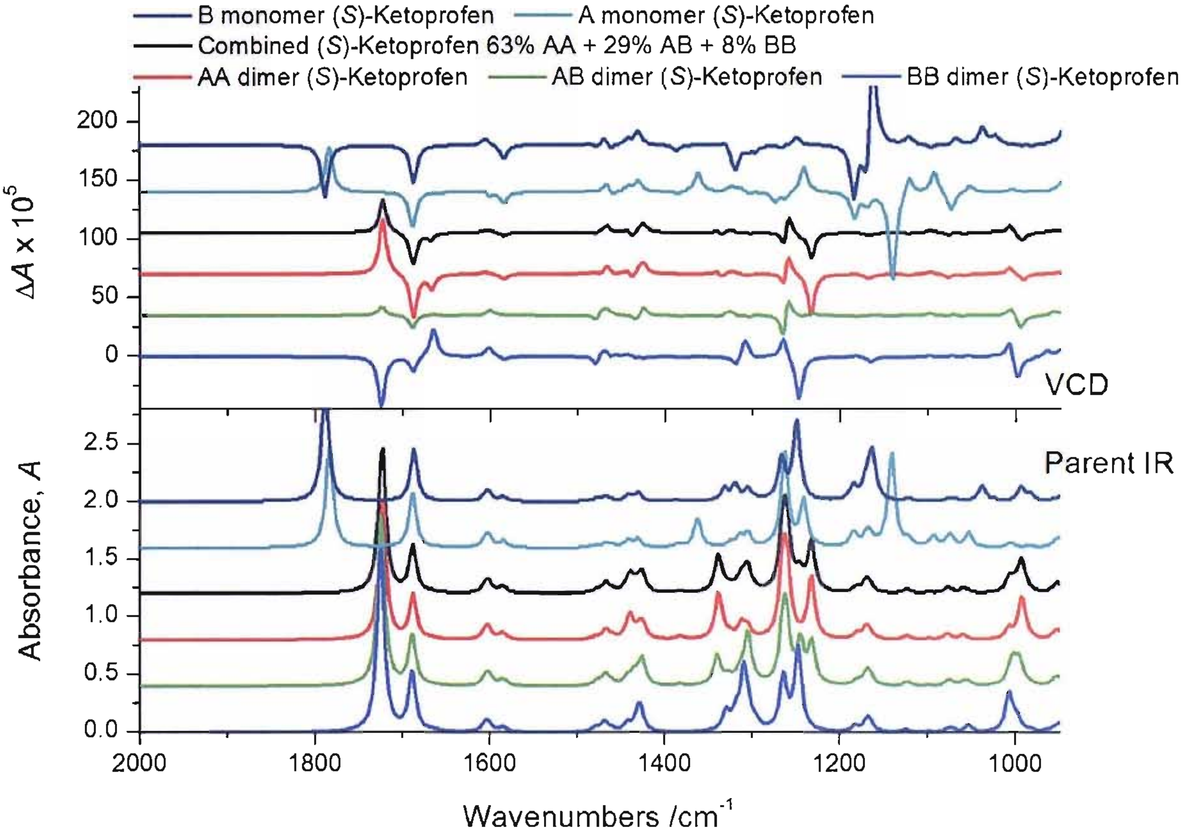

Figure 4.64 Comparison of parent IR (lower frame) and VCD (upper frame) spectra of the predicted spectra of (*S*)-ketoprofen. Monomers and dimer pairs and combined spectra from dimers shown. Spectra offset for clarity.

It is very interesting to look at the effect of the rotation of the carboxylic acid group. Monomer A has the methyl group on the same side as the carbonyl double bond, whereas monomer B has the methyl group on the same side as the hydroxyl group. Differences can be seen as the bands at 1795 cm^{-1} change sign between the A and B monomer, as do the bands at 1150 cm^{-1}. So it is not just change in chirality that can invert the sign of a band, it is also due to the conformation of the bond. This illustrates how important it is to calculate the predicted spectra from the correct conformation of the enantiomer. This was also observed in the case of (*S*)-naproxen highlighted earlier.

Looking at the BB dimer, the predicted spectra seem to show a good match to the experimental spectra. It may be that increasing the proportion of BB dimer in the combined spectra, would produce a better match to the experimental spectra. This was done through an arbitrary linear combination of the dimers predicted spectra with the proportions 40% AA dimer, 20% AB dimer and 40% BB dimer. A comparison of this newly combined predicted spectrum (scaled by 0.97) with the experimental spectra is shown in figure 4.65.

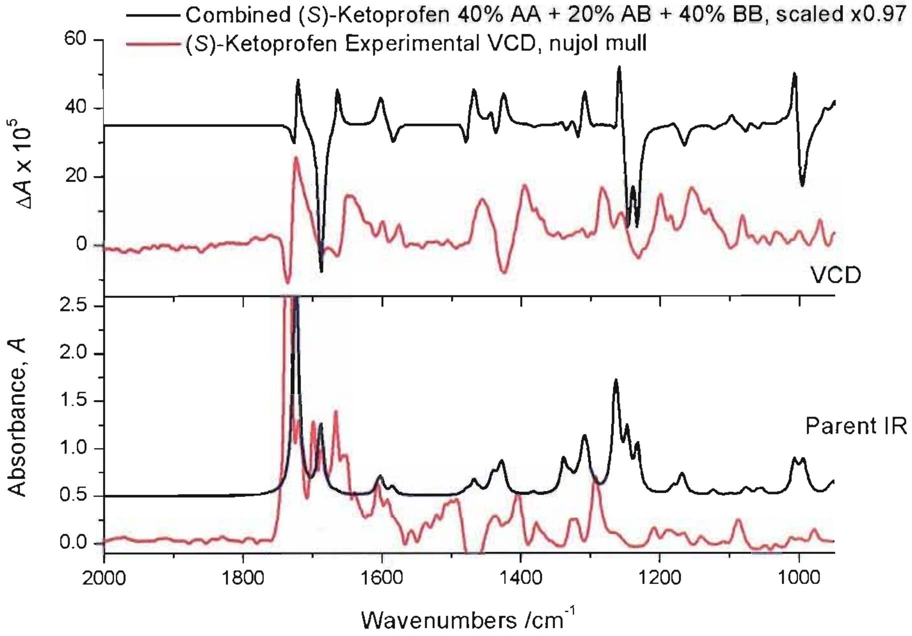

Figure 4.65 Comparison of parent IR (lower frame) and VCD (upper frame) of (*S*)-ketoprofen, scaled combined predicted spectra and experimental spectra from nujol mull. Spectra offset for clarity.

Increasing the proportion of the BB dimer in the combined spectra above has improved the fit to the experimental spectra. This is especially noticeable about the peak at 1720 cm^{-1} where there is now a negative band before the large positive band, as seen in the experimental spectrum. From this match the absolute stereochemistry can be confidently assigned as (*S*). The Boltzmann energy distribution did not give the correct proportions for an accurate combined VCD spectrum, this is probably due to the fact that the calculations are performed on gas phase molecules and so do not accurately represent conditions in the solution state, where certain conformations, or in this case dimers, may be favoured. It is interesting that this is the case for one compound but not for the others. Further investigation into this family of compounds would indicate which scenario is more common.

4.7 Conclusions

The progression of the development of the VCD technique has been shown in this chapter and some important information has been discovered. Experimentally the impact of the concentration and choice of solvent on the quality of the solution state VCD spectra obtained has been shown to be very important. It can determine if the spectra measured are of good enough quality to compare to the predicted spectra. The nujol mull technique has been shown to provide good quality spectra that are simple to measure experimentally. They tend to show clearer, stronger VCD peaks that are easily compared to the predicted spectra. Also for challenging compounds that have solubility issues, the nujol mull technique will always be available, as was seen in the case of atenolol. Influence of the choice of type of spectrometer used on the VCD spectra attainable has been shown and greatly alters the quality of baseline and noise on the VCD spectrum measured. The dual PEM provides better quality spectra particularly in the solution state but measurement times are typically four to fives times longer than with the single PEM spectrometer. Using the nujol mull technique the choice of spectrometer becomes less important, as this sampling technique tends to give a stronger signal.

With regards to the prediction of accurate VCD spectra the influence of changing basis sets and prediction level has been shown very simply with the case of α-pinene. The larger the basis set and the more complicated the prediction level the more accurate the predicted VCD spectra are. The addition of polarisability to the basis set is essential for accurate prediction of VCD vibrational frequencies. Component analysis to determine which chiral centre in which configuration is responsible for which VCD bands in the spectrum was extremely informative for the case of captopril, and analysis gave a better understanding of the VCD interactions.

Choice of starting geometry was shown to be influential on the success of the calculation, as the geometry optimisation within Gaussian [12] does not tend to alter the starting geometry significantly. A search of conformational space alters the configuration much more and is far more likely to find a minimum energy structure. Hence if the calculation starts from a minimum energy conformation (from the search of conformational space) then the predicted spectra are more likely to show a better match to the experimental spectra. However, the calculations are performed on molecules in the gas phase and so the minimum energy conformation may not be the minimum energy structure present in either the solution state or solid state (nujol mull). In this case using XRD data can provide a better starting geometry. As mentioned it is unlikely that the molecule will be completely isolated (as it is in the gas phase) so addition of a group to fulfil the hydrogen bonding capabilities of the molecule can lead to more accurate predicted spectra. However, by far the best method is to start by using data from previous successful predictions of structurally related molecules, as was the case for (*S*)-ibuprofen. This method used published data as a starting point for the calculations, using the same dimer pairs and the same method for combination of the predicted spectra, which resulted in extremely accurate predicted spectra and gave a very good match to the experimental VCD spectrum.

With the issue of predicting spectra it is important to note that rotation of a bond can lead to inversion of the VCD band due to the vibration of the bond. This was seen in the cases of (S)-naproxen and (S)-ibuprofen. Calculations, therefore, need to be performed very carefully and comparison of predicted spectra for different conformers may provide very interesting information.

For scaling predicted spectra, the groups involved in hydrogen-bonding, especially the carbonyl bands (as we have seen) need their predicted positions to be scaled by a larger amount than the rest of the compound in general. As the presence of hydrogen-bonding in the experimental spectra has resulted in a shift of these bands to a lower wavenumber.

4.8 References

1. F.J. Devlin, P.J. Stephens, J.R. Cheeseman, and M.J. Frisch, *Ab initio prediction of vibrational absorption and circular dichroism spectra of chiral natural products using density functional theory: alpha-pinene.* Journal of Physical Chemistry A, 1997. **101**(51): p. 9912-9924.
2. L.A. Nafie, G.S. Yu, X.H. Qu, and T.B. Freedman, *Comparison of IR and Raman Forms of Vibrational Optical- Activity.* Faraday Discussions, 1994(99): p. 13-34.
3. X.L. Cao, R.D. Shah, R.K. Dukor, C.N. Guo, T.B. Freedman, and L.A. Nafie, *Extension of Fourier transform vibrational circular dichroism into the near-infrared region: Continuous spectral coverage from 800 to 10 000 cm(-1).* Applied Spectroscopy, 2004. **58**(9): p. 1057-1064.
4. A.P. Scott, Radom, L., *Harmonic vibrational frequencies: An evaluation of Hartree- Fock, Moller-Plesset, quadratic configuration interaction, density functional theory, and semiempirical scale factors.* Journal of Physical Chemistry, 1996. **100**(41): p. 16502-16513.
5. T.B. Freedman, X.L. Cao, R.V. Oliveira, Q.B. Cass, and L.A. Nafie, *Determination of the absolute configuration and solution conformation of gossypol by vibrational circular dichroism.* Chirality, 2003. **15**(2): p. 196-200.
6. T. Buffeteau, L. Ducasse, A. Brizard, I. Huc, and R. Oda, *Density functional theory calculations of vibrational absorption and circular dichroism spectra of dimethyl-l- tartrate.* Journal of Physical Chemistry A, 2004. **108**(18): p. 4080-4086.
7. J. Hehre W, *A Guide to Molecular Mechanics and Quantum Chemical Calculations*. 2003: Wavefunction Inc.
8. *Spartan '02*. 2002, Wavefunction Inc.: Irvine.
9. V. Andrushchenko, H. Wieser, and P. Bour, *B-Z conformational transition of DNA monitored by vibrational circular dichroism. Ab initio interpretation of the experiment.* Journal of Physical Chemistry B, 2002. **106**(48): p. 12623-12634.

10. T.B. Freedman, F.J. Long, M. Citra, and L.A. Nafie, *Hydrogen-stretching vibrational circular dichroism spectroscopy: Absolute configuration and solution conformation of selected pharmaceutical molecules.* Enantiomer, 1999. **4**(2): p. 103-119.
11. T.B. Freedman, X.L. Cao, R.K. Dukor, and L.A. Nafie, *Absolute configuration determination of chiral molecules in the solution state using vibrational circular dichroism.* Chirality, 2003. **15**(9): p. 743-758.
12. G.W.T. M. J. Frisch, H. B. Schlegel, G. E. Scuseria, , et al., *Gaussian 03.* 2003, Gaussian, Inc.: Pittsburgh PA.

Chapter 5 - Development of the Single Crystal XRD Method

The technique of single crystal X-ray diffraction (XRD) [1, 2] in conjunction with anomalous scattering methods and the Flack parameter [3, 4] is the preferred method of absolute configuration determination for chiral molecules in the pharmaceutical industry. In chapter two the effect of increasing the wavelength of the X-ray radiation on the size of the anomalous scattering differences was shown, with the outcome that the longer the wavelength of the radiation the larger the anomalous scattering difference and so the more likely it is that the absolute configuration will be confirmed. The anomalous scattering differences also depend on the atomic weight of the atom, the lower the atomic weight of the atom the smaller the anomalous scattering differences observed, hence compounds containing only light atoms can be problematic. In this chapter the effect of changing various parameters, on the success of the single crystal XRD collection and the subsequent absolute stereochemistry determination were observed. Firstly, the effect of changing the percentage of heavy atoms (in this case oxygen and nitrogen) in the molecule, on the ease of absolute stereochemistry determination and the reliability of the Flack parameter was observed. This is presented through single crystal XRD collections of benzyl-(*S*)-mandelate, (*S*)-ibuprofen and (-)-ephedrine. Secondly, the results of single crystal XRD collections for (2*S*)-captopril and atenolol are discussed, with a polymorph screen performed on (2*S*)-captopril. Finally the effect of redundancy on the Flack parameter was investigated with a very large data collection for (*S*)-ibuprofen. Additional single crystal XRD collections have been performed and the results of these are presented in the appendix.

5.1 Effect of Heavy Atoms on the Absolute Stereochemistry Determination

The aim of this first investigation is to observe the effect of the percentage of heavy atoms in the molecule on the results of absolute stereochemistry determinations carried out via single crystal XRD. The percentage of heavy atoms (oxygen and nitrogen) as compared to the total number of atoms (excluding hydrogen) in the compound is first calculated for the three compounds under investigation. These are benzyl-(*S*)-mandelate, (*S*)-ibuprofen and (-)-ephedrine (figure 5.1) and the respective proportions of heavy atoms to the total number of atoms are 3/18, 2/15 and 2/12, which equate to the percentages 17 %, 13 % and 17 %. However, it has to be considered that for the (-)-ephedrine one of the heavy atoms is nitrogen, which is a poorer anomalous scatterer than oxygen. From these percentages benzyl-(*S*)-mandelate is likely to give the best results, whilst (*S*)-ibuprofen and (-)-ephedrine should give slightly poorer results.

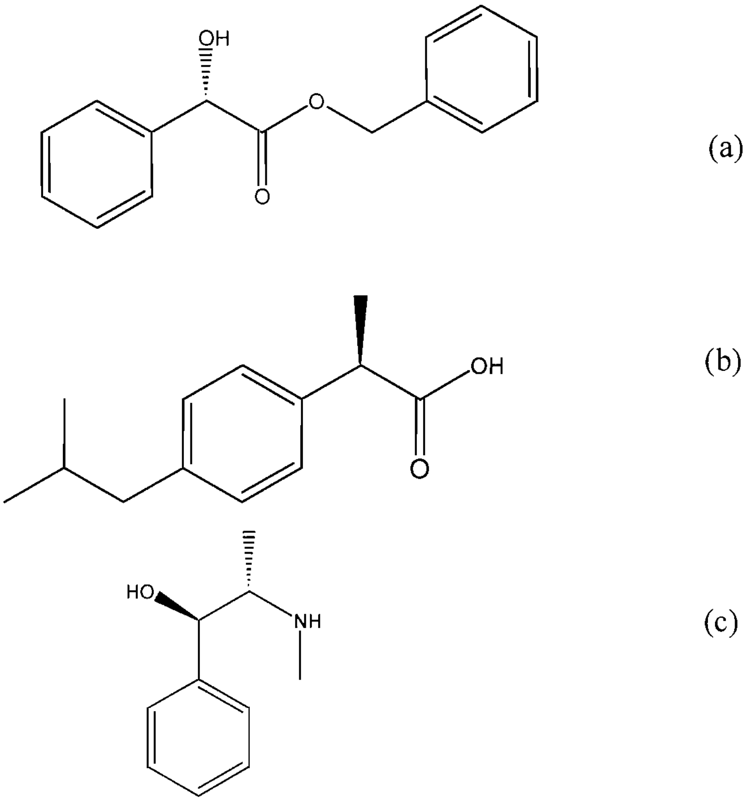

Figure 5.1 (a) Benzyl-(*S*)-mandelate, (b) (*S*)-ibuprofen and (c) (-)-ephedrine

The data collections for these three compounds were performed at Bruker AXS, Delft on the Bruker AXS Proteum, with Microstar generator and Cu *K*α radiation. After reprocessing the R_1 values and the Flack parameter with its associated error were compared. It is expected that as the number of anomalous scatterers decreases it becomes more difficult to view the differences between the Friedel pairs and so the likelihood of being able to determine the absolute stereochemistry to any level of accuracy will decrease.

5.1.1 Benzyl-(*S*)-Mandelate

Benzyl-(*S*)-mandelate contains 17% oxygen and neither the crystal structure nor absolute stereochemistry has been reported previously to our knowledge. A single crystal was obtained through re-crystallisation from methanol/acetone employing the evaporation technique. Single crystal X-ray crystallography, at low temperature 100 K, showed that benzyl-(*S*)-mandelate ($C_{15}H_{14}O_3$) crystallises in the monoclinic system, space group $P2_1$. With $a = 8.0310(3)$ Å, $b = 5.6303(2)$ Å, $c = 13.4909(4)$ Å, $\alpha = \gamma = 90°$, $\beta = 94.901(1)$ °, $V = 607.79$ Å^3 and $Z = 2$. After processing the data using SHELXTL [5] a value of $R_1 = 0.0249$ was obtained, which is a very good margin of error, and $S = 1.116$, with Flack parameter $x = 0.0186$ (0.1522).

The crystal structure obtained is shown in figure 5.2 below. We can see from the X-ray data above, that the absolute stereochemistry has not been proven unequivocally. Ideally for proven absolute stereochemistry we require a Flack parameter of less than 0.10 with esd (estimated standard deviation) of less than 0.15 is required. Increasing the redundancy of the data may help to improve the Flack parameter to within acceptable values for absolute stereochemistry determination. The effect of redundancy on the Flack parameter will be considered in section 5.4. Since the estimated standard deviation is within the acceptable limits there is some confidence that the absolute stereochemistry can be assigned as that of the *S*-enantiomer.

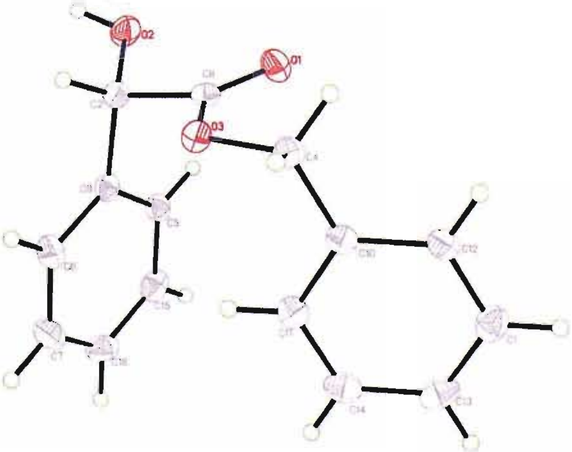

Figure 5.2 Benzyl-(*S*)-mandelate, crystal structure from Cu *Kα* single crystal XRD collection.

5.1.2 (*S*)-Ibuprofen

The crystal structure of (*S*)-(+)-ibuprofen has been previously published, but without comment on the absolute stereochemistry.[6] Single crystal X-ray crystallography, at low temperature 100 K, showed that (*S*)-ibuprofen ($C_{13}H_{18}O_2$) crystallises in the monoclinic system, space group $P2_1$. With $a = 12.1240(2)$ Å, $b = 7.9558(2)$ Å, $c = 13.3756(3)$ Å, $\alpha = \gamma = 90$ °, $\beta = 111.990(1)$ °, V = 1196.30 $Å^3$ and Z = 4. After processing the data using SHELXTL a value of $R_1 = 0.0370$ was obtained, and S = 1.000, with Flack parameter x = 0.0029 (0.2405). The crystal used was obtained from evaporation from methanol.

The crystal data collected is in agreement with the data previously published [6] and the hydrogen bonded dimer is shown in figures 5.3 and 5.4. The Flack parameter for this data collection is within accepted limits; however, its associated error is too high to be confident in the absolute stereochemistry determination. This is not entirely unexpected as the compound contains only 13 % oxygen atoms, and so very little anomalous scattering is present.

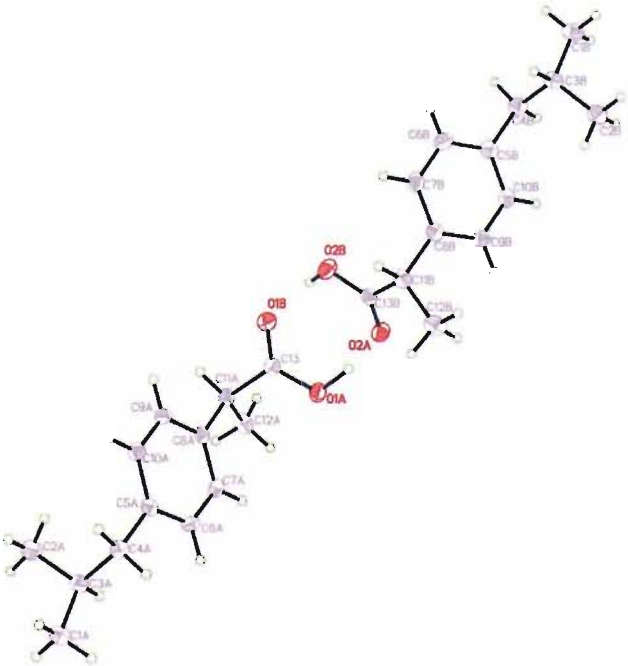

Figure 5.3 (*S*)-ibuprofen from Cu *Kα* single crystal XRD collection.

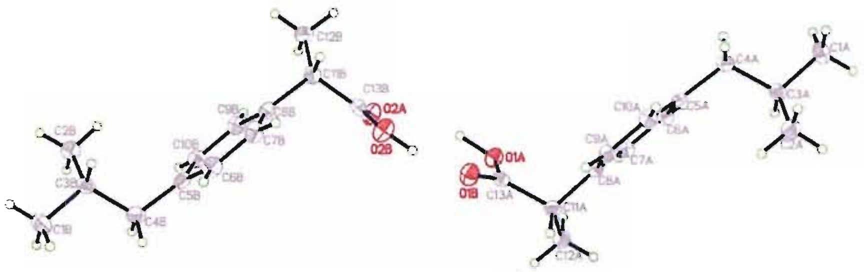

Figure 5.4 (*S*)-ibuprofen from Cu *Kα* single crystal XRD collection.

It is interesting to note that such a small change in the percentage of heavy atoms (17 – 13 %) means that the Flack parameter is now not a confident assignment of the absolute stereochemistry.

5.1.3 (-)-Ephedrine

The crystal structure of many derivatives of (-)-ephedrine have been previously published [7] but contain no direct reference to the absolute stereochemistry. (-)-Ephedrine contains 17 % heavy atoms, composed of one oxygen and one nitrogen atom. Single crystal X-ray crystallography, at low temperature 100 K, showed that (-)-ephedrine ($C_{10}H_{15}O_1N_1$) crystallises in the orthorhombic system, space group $P2_12_12_1$. With a = 7.3481(9) Å, b = 11.2203(14) Å, c = 24.093(3) Å, $\alpha = \beta = \gamma = 90$ °, V = 1986.38 Å^3 and Z = 8. After processing the data using SHELXTL a value of R_1 = 0.0696 was obtained, and S = 1.000, with Flack parameter x = 0.6980 (0.4876). The crystal used was obtained from re-crystallisation with methanol/water, employing the evaporation technique.

The crystal structure obtained is shown in figure 5.5, where two ephedrine molecules are complexed to one water molecule. The Flack parameter is very poor for this structure and inverting it (to see if it was the other enantiomer) gave even worse results. So despite (-)-ephedrine having a higher percentage of heavy atoms than (*S*)-ibuprofen, the effect of having only one oxygen atom and one nitrogen atom was significant and meant that the absolute stereochemistry determination could not be proven.

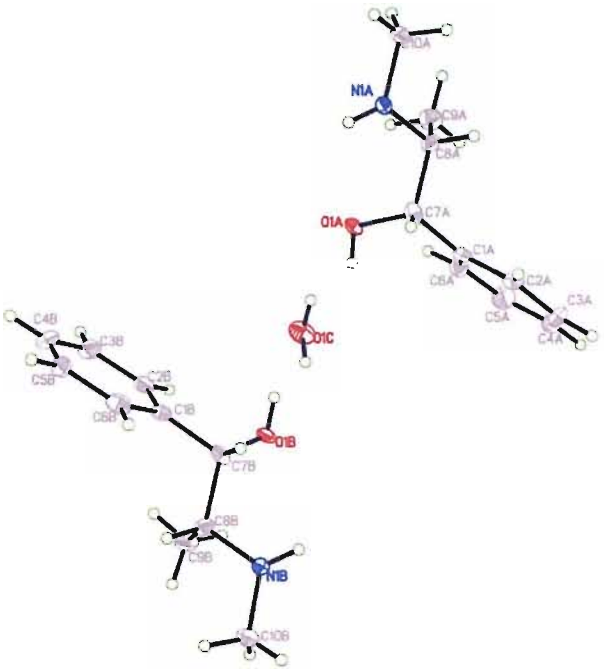

Figure 5.5 (-)-Ephedrine, complexed to water molecule, from Cu *Kα* single crystal XRD collection.

5.1.4 Conclusions

The effect of the percentage of anomalous scatterers to the total number of atoms, excluding hydrogen, in the compound is mostly as expected. The higher the percentage, i.e. the more anomalous scatterers there are, the better the Flack parameter observed. However, this was only the case when the anomalous scatterers were the same, i.e. benzyl-(*S*)-mandelate and (*S*)-ibuprofen both contained only oxygen atoms and when the percentage of these decreased the Flack parameter worsened. When (-)-ephedrine and (*S*)-ibuprofen are compared from percentage heavy atoms alone (-)-ephedrine would be expected to give better results than (*S*)-ibuprofen, but this was not the case. The Flack parameter for (*S*)-ibuprofen was significantly better than for (-)-ephedrine, because the (*S*)-ibuprofen contains two oxygen atoms, whilst (-)-ephedrine contains one oxygen and one nitrogen atom. So when considering the percentage of heavy atoms in a molecule it is also important to consider what these atoms are when trying to assess if the absolute stereochemistry will be determinable.

It would be very interesting to expand this investigation further to see what percentage of nitrogen atoms is equivalent to what percentage of oxygen atoms. This would give a further guide to whether an absolute stereochemistry determination is likely to work (barring poor crystal quality, etc.) before it was performed and so could save valuable XRD resources.

5.2 (2*S*)-Captopril

Captopril is an angiotensin converting enzyme (ACE) inhibitor used in the treatment of high blood pressure and heart failure [8, 9] (figure 5.6). It was the first potent and orally active ACE inhibitor. ACE inhibitors inhibit the converting enzyme peptidyl dipeptidase that hydrolyses angiotensin I to angiotensin II. Where angiotensin I has no biological effect, angiotensin II causes vaso constriction, which regulates blood pressure and also regulates the thickness of the blood, through kidney function.[10]

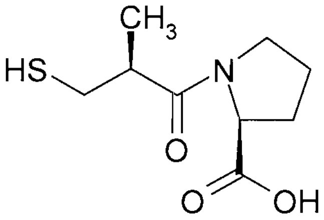

Figure 5.6 (2*S*)-Captopril

Two single crystal XRD collections were carried out using Mo and Cu radiation, and these results are compared. Also presented are the results of a polymorph screen carried out at AstraZeneca, using standard pharmaceutical techniques.

5.2.1 Single Crystal XRD Structure

The crystal structure of (2*S*)-captopril has only one entry in the Cambridge crystallographic database,[11] this paper contained no mention of the absolute stereochemistry of the compound and was run at room temperature. Captopril, (2*S*)-1-(3-Mercapto-2-methylpropionyl)-L-proline ($C_9H_{15}NO_3S$), was purchased from Sigma Aldrich. Several re-crystallisation processes were employed, having saturated solutions in varying solvents, and then allowing evaporation at room temperature. The crystal employed for the single crystal x-ray diffraction work was produced using methanol as the solvent.

Single crystal X-ray crystallography, using the SMART diffractometer, Mo *Kα* (0.71 Å) radiation, at low temperature 123 K, showed that (2*S*)-captopril crystallises in the orthorhombic system, space group $P2_12_12_1$. With a = 6.8056(13) Å, b = 8.8106(18) Å, c = 17.535(4) Å, α = 90 °, β = 90 °, γ = 90 °, V = 1051.4(4) $Å^3$ and Z = 4 molecules. After processing the data using SHELXTL a value of R_1 = 0.0266 was obtained, with a Flack parameter of -0.0210 (0.0585). Figures 5.7 and 5.8 show a single molecule and the crystal packing in the unit cell, respectively, for (2*S*)-captopril.

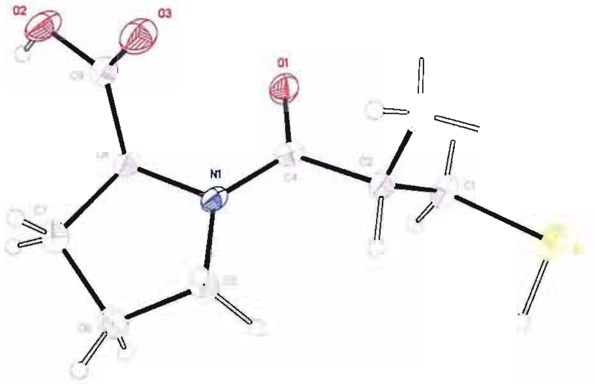

Figure 5.7 (2*S*)-Captopril in the orthorhombic crystal system $P2_12_12_1$, from Mo *Kα* single crystal XRD collection.

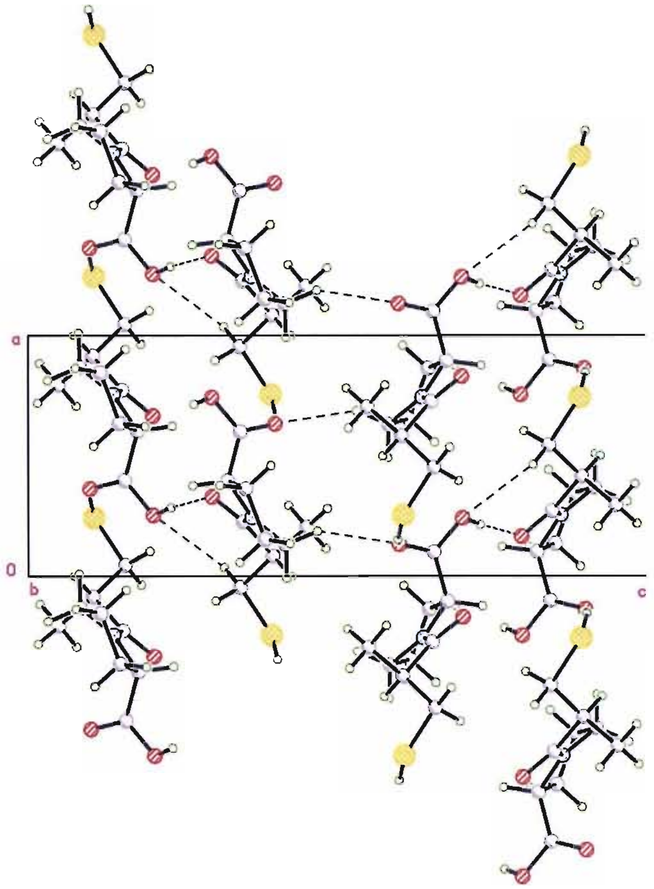

Figure 5.8 Four molecules of (2*S*)-captopril within the unit cell, from Mo *Kα* single crystal XRD collection.

The designation of the absolute stereochemistry of (2*S*)-captopril did not require Cu *Kα* radiation for use with the anomalous scattering technique. The Flack parameter obtained allowed the absolute stereochemistry to be confidently assigned. The sulphur atom present in the compound dominates the anomalous scattering when using Mo radiation, and provides large enough anomalous scattering differences to allow confident determination of the absolute stereochemistry.

A single crystal XRD collection was also performed using Cu *Kα* radiation, in order to compare the differences seen between the two types of data collection. Single crystal X-ray crystallography, using the Rigaku diffractometer Cu *Kα* (1.54 Å) radiation, at low temperature 123 K, showed that (2*S*)-captopril crystallises in the orthorhombic system, space group $P2_12_12_1$. With a = 6.7995(16) Å, b = 8.7944(14) Å, c = 17.4622(16) Å, α = 90 °, β = 90 °, γ = 90 °, volume=1044.20(25) Å^3 and Z = 4 molecules. After processing the data using

SHELTXL a value of $R_1 = 0.0496$ was obtained, and the Flack parameter was shown to be -0.1597 (0.0589. The crystal structure obtained is shown in figure 5.9.

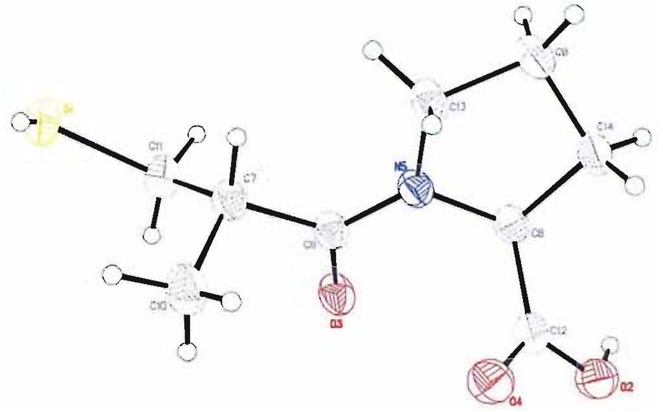

Figure 5.9 X-ray crystal structure of (2*S*)-captopril from Cu *Kα* radiation single crystal data collection

The Flack parameter obtained from this collection is significantly larger than that seen in the Mo radiation collection, but still provides fairly reliable enantiomeric discrimination. The differences in these collections are mainly owing to the change to softer X-rays i.e. using Cu *Kα* instead of Mo *Kα* which are longer wavelength X-rays and also the quality of the diffractometer that the data collection was taken on. The actual differences between the lattice parameters from the two data collections are very slight. In order to obtain better information from an absolute stereochemistry determination using Cu *Kα* radiation, a larger data collection is necessary.

The crystal structure of (2*S*)-captopril has also been reported by Kadin [12] which showed the existence of two polymorphs, Form I and Form II. A polymorph screen was performed (see Appendix I) in order to obtain Form II and thus examine whether changes in the structure affect the Flack parameter for the same molecule. However the polymorph screen failed to find the crystallisation conditions that gave Form II and therefore this aspect was abandoned.

5.3 Atenolol

Atenolol contains just one chiral centre and three oxygen and two nitrogen atoms; it is a difficult compound to deal with for single crystal X-ray diffraction using the anomalous dispersion method, figure 5.10. The proportion of heavy atoms to total number of atoms is 26 %, three of which are oxygen and two of which are nitrogen. Perhaps more importantly the percentage of oxygen atoms present is 16 %. Thus from the investigation in section 5.1, it is expected that the absolute stereochemistry would be determinable when using Cu *Kα*, but not Mo *Kα*.

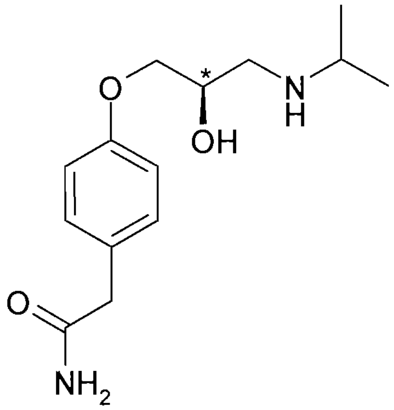

Figure 5.10 (*R*)-atenolol

Re-crystallisation of atenolol tends to produce thin plate-like crystals, shown in figure 5.11 below. These crystals are also often highly mosaic and contain a large amount of disorder, providing difficult specimens for single crystal X-ray diffraction measurements, even when low temperature techniques are employed to try and minimise thermal motion. The disorder is highlighted in figure 5.11 (a), where the crystals are observed through a polarising microscope. If the crystals were uniform they would exhibit a uniform colour, the highly coloured variations in the crystals here show a large amount of disorder.

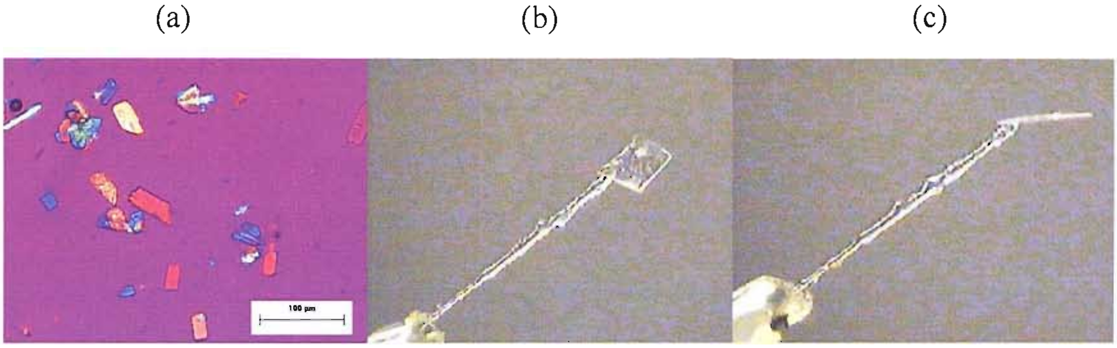

Figure 5.11 (a) Different colours show stress and strain in atenolol crystals, (b) front and (c) side view of a single crystal of atenolol, shows thin, plate like nature

The crystal structure for (*R*)-atenolol has been obtained by Sohrab Karami using Mo *Kα* radiation. The results gave unit cell dimensions of a = 53.421(14) Å, b = 5.673(1) Å, c = 9.612(3) Å, β = 99.064°, monoclinic C2, Z = 8, and R_1 = 9%. There are two molecules in the asymmetric unit, one of which is ordered, the other of which is disordered. The disorder is seen about the isopropyl amine group, shown in figure 5.12. For regulatory submission further data would have to be collected using Cu radiation, in order to determine the absolute stereochemistry. However, this data collection can only be performed if good quality single crystals can be obtained, and this has not been possible. Owing to the disorder and problems with thermal motion it is likely that the Flack parameter would not give a confident measure even when using Cu *Kα*.

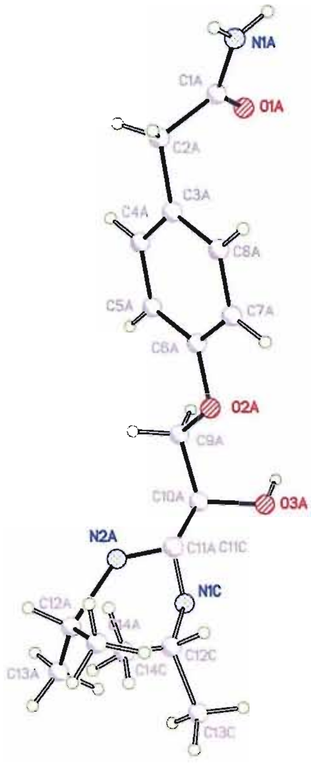

Figure 5.12 One of the molecules in the asymmetric unit cell, which exhibits disorder about the isopropyl amine group

The result of this XRD collection meant that achieving the absolute stereochemistry determination via VCD spectroscopy would be an extremely important result. However, as we saw in chapter 4, atenolol is also a problematic compound for VCD spectroscopy and although a reliable experimental VCD spectrum was eventually collected using the nujol mull technique, the predicted spectra have not yet given a good match to the experimental spectra.

5.4 The Effect of Redundancy on the Flack Parameter

In chapter two the Flack parameter was defined and its use in single crystal XRD for determining the confidence in the absolute stereochemistry determination was described. It was shown that with longer wavelength radiation, greater anomalous scattering differences can be detected, leading to more accurate and reliable absolute stereochemistry determinations. The presence of atoms of a higher atomic weight (i.e. that give rise to larger anomalous scattering differences) in the molecule will lead to an increased accuracy in the absolute stereochemistry determination. There are other parameters that can influence the data collection and cause the result to be more or less reliable; these include crystal quality and collection conditions such as temperature. If we assume we have a good quality crystal, containing one or more oxygen atoms in the molecule, with copper radiation, there is another factor that will play a part in determining whether or not the data collection will produce a reliable Flack parameter for accurate absolute stereochemistry determination. This factor is part of the data collection process itself and is called redundancy.

Within X-ray crystallography, the integrated intensities of the diffraction peaks are used to reconstruct the electron density map within the unit cell in the crystal. To achieve high accuracy in this reconstruction, which is carried out through Fourier transformation of the diffraction intensities using an appropriate phase assignment, a high degree of completeness as well as redundancy in the diffraction data is necessary. Redundancy meaning that all possible reflections are measured multiple times which then reduces the systematic and statistical error.

The effect of collecting highly redundant data with regards to the Flack parameter has not been published to our knowledge. Data becomes redundant when more than one sphere of reflections has been collected; this one sphere of data is all that is necessary to solve the crystal structure of a compound in the most basic space group. As the complexity of the space group increases, so more spheres of data are required in order to solve the crystal structure. Once the data necessary to solve the crystal structure for that compound has been collected, any further spheres of data collected are redundant. It is thought that having highly redundant data will lead to a lowering of the uncertainty u on the Flack parameter x. As the determination of the absolute stereochemistry will be using more Friedel pairs to calculate the differences in reflections, it should have a lower error and give a better overall figure. An investigation was undertaken to determine the effect of redundancy on the Flack parameter for a data collection with (*S*)-ibuprofen, which contains only two oxygen atoms in a framework of 13 carbon atoms. The absolute stereochemistry of (*S*)-ibuprofen was not proven (see Section 5.1.2) since the estimated standard deviation associated with the Flack parameter was large and therefore this material was thought to be a good candidate to test the effects of collecting different levels of redundancy.

As the redundancy of the data-set increases, the symmetry related reflections are measured several times and so the precision of the calculation of the Bijvoet differences improves. In other words the anomalous signal obtained from each data-set can be measured with greater accuracy when highly redundant data is collected. X-ray diffraction data is thus to some extent influenced by counting statistics, the averaged measurement should become more accurate as more individual measurements are made. A highly redundant data set will therefore be intrinsically of higher quality than a data set in which every reflection has only been measured once.

Previous studies [13] have shown that the anomalous *R* factor based on intensities from the XRD data collection (R_{anom}) decreases with increasing redundancy of data and reaches a minimum, past which further redundancy of the data has no effect. A possible reason for this trend is that the statistical errors influencing the small anomalous differences are averaged out the more often these differences are observed. So that in the higher redundancy data sets the anomalous differences are as close to the true values as they can get. It will be interesting to see if this is also the case for the effect of redundancy on the Flack parameter.

5.4.1 (*S*)-Ibuprofen Data Collection

The crystal structure of (*S*)-ibuprofen (figure 5.13) was collected via single crystal X-ray crystallography, using the Bruker-AXS Prospector, with Microstar generator, Cu *Kα* radiation, at low temperature 100 K. (*S*)-Ibuprofen ($C_{13}H_{18}O_2$) crystallises in the monoclinic system, space group $P2_1$ and the data was collected from a crystal obtained from an evaporation from methanol.

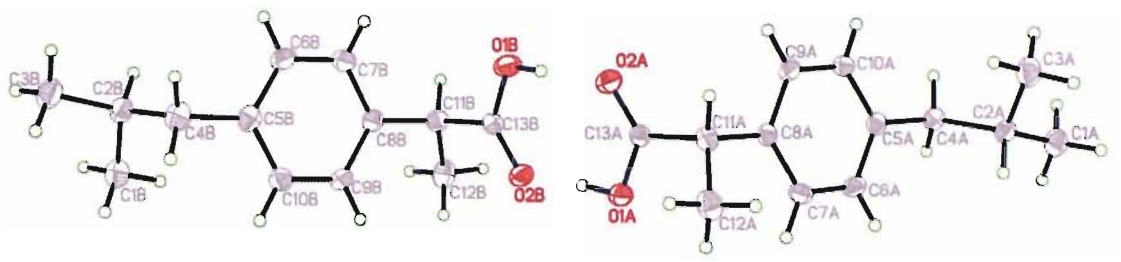

Figure 5.13 (*S*)-Ibuprofen asymmetric unit of the unit cell, after 15 runs, from Cu $K\alpha$ single crystal XRD collection.

In total 15 runs were performed which used differing scans to collect increasingly redundant data. After collection the reflection files from the runs were combined using SADABS, with increasing number of runs i.e. run 1, run 1 & 2, runs 1, 2 & 3, runs 1, 2, 3 &4 etc. This enabled the data collection to be solved for an increasing number of reflections, and allows the effect of increasing redundancy observed.

The lattice parameters and the R_1 values are compared for run 2 and run 15 below. For run 2, a = 12.1240(2) Å, b = 7.9558(2) Å, c = 13.3756(3) Å, $\alpha = \gamma = 90$ °, β = 111.990(1) °, V = 1196.30 Å^3 and Z = 4. After processing the data using SHELXTL a value of R_1 = 0.0370 was obtained, and S = 1.000, with Flack parameter x = 0.0029 (0.2405). For run 15, the lattice parameters were exactly the same and after processing the data using SHELXTL a value of R_1 = 0.0294 was obtained, and S = 1.000, with Flack parameter x = 0.0238 (0.1250). So the increasing the redundancy of the data collection has improved the R_1 factor from 3.7 – 2.94 %, and has halved the error on the Flack parameter from 0.2405 – 0.1250. Hence using the data from all 15 runs has meant that the absolute stereochemistry can now be confidently assigned as the *S*-enantiomer.

A comparison of the Flack parameter and its estimated standard deviation (esd) are tabulated below (table 5.1) for an increasing number of total runs, i.e. increasing redundancy. Also shown in table 5.1 are the total number of reflections and the number of unique reflections for each run. The redundancy for each run is calculated from these values, by dividing the total number of reflections by the number of unique reflections.

Table 5.1 Tabulated Flack parameter, with its estimated standard deviation (esd) for data from an increasing number or runs, 2 – 15. Shown with total number of reflections, the number of unique reflections and the redundancy of the data collection for each run

Run Number	Flack Parameter	Esd	Total Number Reflections	Number Unique Reflections	Redundancy
2	0.0029	0.2405	2560	2100	1.22
3	0.0761	0.1770	3980	2982	1.33
4	0.0240	0.1672	5413	3503	1.55
5	0.0880	0.1670	6417	3728	1.72
6	0.0532	0.1488	7863	4104	1.92
7	0.0772	0.1416	9334	4222	2.21
8	0.0791	0.1364	10727	4288	2.50
9	0.0472	0.1351	11694	4311	2.71
10	0.0731	0.1323	13108	4362	3.01
11	0.0605	0.1297	14545	4385	3.32
12	0.0402	0.1291	15952	4396	3.63
13	0.0414	0.1284	17075	4409	3.87
14	0.0429	0.1259	18508	4433	4.18
15	0.0238	0.1250	19529	4441	4.40

As expected the estimated standard deviation reaches a minimum at the largest number of total runs where the redundancy is highest, figure 5.14. This is a smooth progression, with a large drop in the esd seen initially, followed by a more steady decrease as the redundancy increases from 2.5 - 4.5.

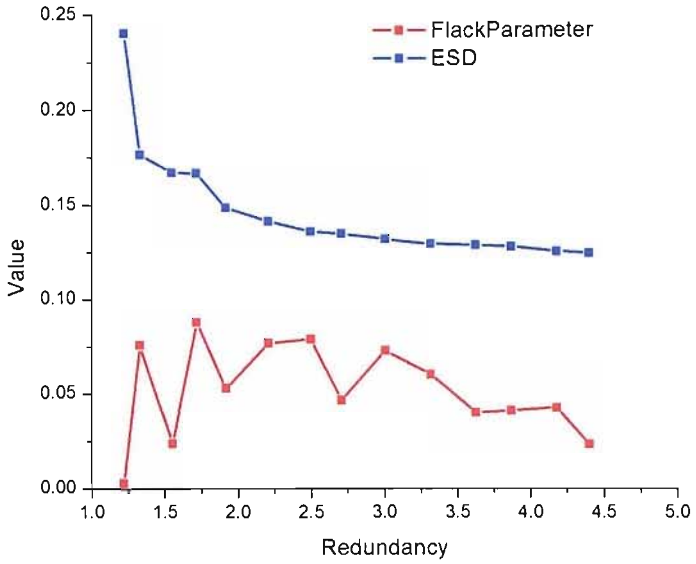

Figure 5.14 Variation of the Flack parameter (red line) and its associated esd (blue line) with increasing redundancy of the data collection for (*S*)-ibuprofen.

Figure 5.15 shows the Flack parameter graph but with error bars on the Flack parameter values that are equivalent to the esd of that Flack parameter. This shows that although the Flack parameter from run 2 appears to have a very good value close to zero, the error on that Flack parameter is large.

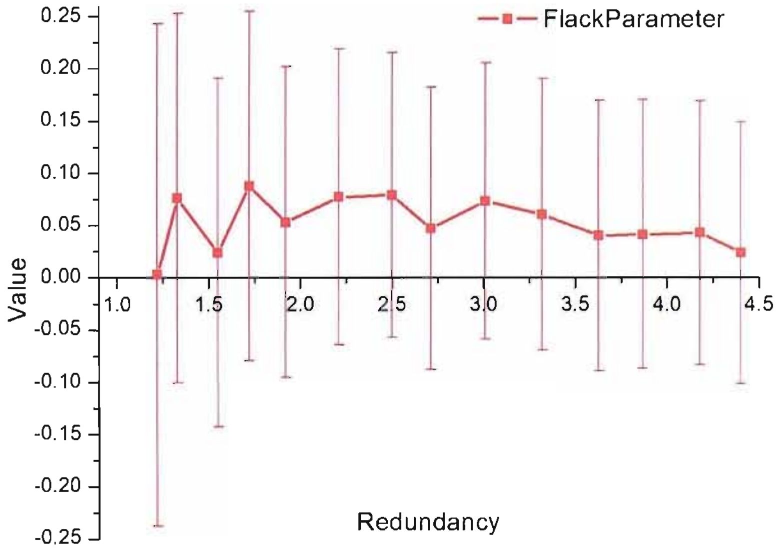

Figure 5.15 Variation of the Flack parameter (red line) with increasing redundancy of the data collection for (*S*)-ibuprofen. Errors bars on Flack parameter are equivalent to the esd value for that Flack parameter.

The results from the study of the effect of increasing redundancy on the Flack parameter and its associated esd are very promising. They show that as the redundancy of the data collection is increased the reliability of the Flack parameter (i.e. the esd) improves and the Flack parameter itself decreases i.e.

becomes closer to zero for the correct enantiomer. This enables more confident assignment of absolute stereochemistry for compounds with only a few light atoms. However, the data collection is very time consuming, but if the results give a reliable Flack parameter which can be used for FDA regulatory submission of new pharmaceuticals, it would be a worthwhile procedure.

It would be interesting to increase the data collection further, in order to increase the redundancy of the data collection, to see if the Flack parameter and its associated esd keep decreasing. There may well be a point at which further data collection does not make a significant improvement to the Flack parameter. Data collections also need to be performed for several different compounds to see how the number of light atoms present affects the decrease in Flack parameter seen with the increasing redundancy.

5.5 References

1. J.M. Bijvoet, A.F. Peerdeman, and J. Van Bommel, *Determination of the Absolute Configuration of Optically Active Compounds by means of X-rays.* Nature, 1951. **168**: p. 271 - 272.
2. W. Clegg, *Crystal Structure Determination.* 1998: Oxford Chemistry Primers.
3. H.D. Flack and G. Bernardinelli, *Absolute structure and absolute configuration.* Acta Crystallographica Section A, 1999. **55**: p. 908-915.
4. H.D. Flack and G. Bernardinelli, *Reporting and evaluating absolute-structure and absolute- configuration determinations.* Journal of Applied Crystallography, 2000. **33**: p. 1143-1148.
5. *SHELXTL.* 1997, Bruker AXS, Inc: Madison, Wisconsin.
6. A.A. Freer, J.M. Bunyan, N. Shankland, and D.B. Sheen, *Structure of (S)-(+)-Ibuprofen.* Acta Crystallographica Section C-Crystal Structure Communications, 1993. **49**: p. 1378-1380.
7. D.C. Phillips, *The Crystal and Molecular Structures of Ephedrine Hydrochloride.* Acta Cryst., 1954. **7**: p. 159 - 165.
8. D.W. Cushman, Cheung, H.S, Sabo, E.F & Ondetti, M.A, *Design of potent competetive inhibitors of angiotensin-converting enzyme. Carboxyalkanoyl and mercaptoalkanoyl amino acids.* Biochemistry, 1977. **16**: p. 5484-5491.
9. M.A. Ondetti, Rubin, B & Cushman, D.W, *Design of Specific Inhibitors of Angiotensin-Converting Enzyme: New Class of Orally Active Antihypertensive Agents.* Science, 1977. **196**: p. 441-444.
10. M. Bradley, *CH324 Medicinal Chemistry Lecture Notes.* 2003.
11. M. Fujinaga and M.N.G. James, *SQ 14,225: 1-(D-3-Mercapto-2-methylpropionyl)-L-proline.* Acta Cryst. B, 1980. **36**: p. 3196-3199.
12. H. Kadin, *Captopril*, in *Analytical Profiles of Drug Substances*, K. Florey, Editor. 1982, Academic Press.
13. M.S. Weiss, *Global indicators of X-ray data quality.* Applied Crystallography, 2001. **34**: p. 130 - 135.

Chapter 6 – Conclusions and Future Work

6.1 Conclusions

Many important issues relating to the determination of absolute stereochemistry of chiral pharmaceuticals have been discussed in this thesis. These include VCD sampling methodology development, optimisation of sampling conditions for available VCD spectrometers and calculation optimisation for VCD spectral prediction and development of the method. For single crystal XRD the limitations of the method with respect to heavy atoms were investigated for a standard data collection, and through increasing the redundancy of the data collection, the effect on the Flack parameter and its associated estimated standard deviation (esd) was observed.

VCD has already proven itself a reliable technique as a tool for absolute stereochemistry determination for specific small to medium sized chiral molecules and for determination of secondary structures of proteins. However, it is currently still regarded as a pursuit for experienced vibrational spectroscopists and molecular modellers. Within the pharmaceutical industry there is a great call for quick, reliable, accurate absolute stereochemistry determinations, which are currently undertaken via single crystal XRD.

In the work presented in this thesis advances have been made in the sampling methodology from the established method of using solutions, to KBr discs and the nujol mull technique. All of these methods are all commonly used within the field of conventional IR spectroscopy. The KBr disc technique proved unreliable when used in conjunction with the single PEM spectrometer, and the spectra contained less information than the equivalent solution state spectra. The dual PEM spectrometer was found to allow collection of excellent solution state VCD spectra, whilst the single PEM spectrometer operates most effectively with the nujol mull sampling method. There are relative advantages and disadvantages with both of the sampling techniques; the nujol mull method is generally quicker for both collection of spectra and preparation of the samples. However, the solution state sampling with the dual PEM spectrometer has the advantage of needing no data reprocessing and presenting a noise reading associated with the VCD spectrum measured. For problematic compounds, those with solubility issues or re-crystallisation problems, the nujol mull technique is ideal and very simple to perform, and would work well in the pharmaceutical industry. Especially when considered with the single PEM spectrometer, which is a module unit that attaches to an existing FT-IR spectrometer and so is the cheaper option. One feature that could greatly improve the potential of the single PEM spectrometer would be an improvement of the data reprocessing step. If this could be automated, as with the dual PEM spectrometer, it would make data collection a routine procedure, and significantly reduce the amount of training necessary to produce an effective VCD spectroscopist.

The other essential component for absolute stereochemistry determinations using VCD spectroscopy is the prediction of accurate VCD spectra. Several different techniques to improve the calculation results were experimented with in this research; these involved choice of starting structure and combination of several predicted spectra to more accurately match the experimental spectra. The greatest improvement of predicted spectra was seen when the hydrogen-bonding possibilities of the compound were fulfilled, either by addition of a water or acetic acid molecule, or through dimerisation. The best fit to the experimental spectra was seen when the predicted spectra for several dimer pairs or conformers were combined. This technique was borrowed from a published paper [1] of a structurally related compound, and shows that published calculations can provide an extremely useful starting point, saving valuable computer resources. For ease of application, the feature of greatest potential is the presence of key VCD marker bands in families of compounds that share the same chiral backbone. This reduces the need for separate VCD calculations for each member of the family, as the marker band is indicative of the absolute stereochemistry. In the area of accurate prediction of VCD spectra, experience has proven to be vital and drawing on other peoples experience is extremely useful.

Pharmacologically important compounds are often members of families that share the same backbone and chiral centre. If these are shown to share marker bands in the VCD spectrum indicative of the stereochemistry then predicting the spectra would be worthwhile and could prove the absolute stereochemistry of the entire family. Thus it could be shown that the determination of their absolute stereochemistry may be quicker through VCD rather than single crystal XRD.

However, a couple of important discoveries have been found which may affect the ease of use of VCD for routine analysis. Rotation of non-chiral centre groups has been shown to cause inversion of bands (as seen in the case of (*S*)-naproxen), which is traditionally only thought to occur when switching from one enantiomer to the other. This added complexity is bound to cause problems for absolute stereochemistry determination, particularly for compounds with greater conformational flexibility. Problems due to this complexity are most likely to occur within the calculation stage of the absolute stereochemistry determination. So it may well be the case that using VCD to determine the absolute stereochemistry is only practical for certain classes of compounds, especially those that have a more rigid structure.

Single crystal XRD is a well practiced technique and its limitations in determination of absolute stereochemistry were explored with regards to the presence of heavy atoms for a standard data collection. These limitations are expected from knowledge of the anomalous scattering differences achievable with varying radiation. An effect that has not previously been investigated to our knowledge is the effect of redundancy with regards to the Flack parameter. Increasing the redundancy has now been shown to lower the Flack parameter and its associated esd, thus increasing the reliability of the absolute stereochemistry determination. This could prove an extremely useful technique within the pharmaceutical industry as the single crystal XRD technique is an accepted proof of absolute stereochemistry for regulatory submission. Although, the data collection took several days even on a state-of-the-art diffractometer, it is still very useful to have a method that improves the Flack parameter and its accuracy. Especially as VCD spectroscopy is currently only widely predicted for small – medium sized molecules.

Overall it has been shown that by using VCD spectroscopy, in combination with the correct sampling method and instrument, a good quality VCD spectrum can be measured for virtually any sample. Calculations, to prove the absolute stereochemistry, are best started from prior knowledge and using previous experience. Dimerisation can play a major role, as can combination of dimers or conformers, in obtaining a better match to the experimental spectra. It is essential to consider the structure of the compound and what its conformational preference in the solution or solid state might be. However, the complexity of the predictions may prove off-putting for the method to become used routinely.

The goodness of fit parameter developed in this research enables the confidence in the comparison of the experimental and predicted VCD spectrum to be determined. This measure of confidence is equivalent to the Flack parameter in single crystal XRD and with more research and further proof of the method it is possible that this would aid the case of using VCD spectroscopy for proof of absolute stereochemistry for regulatory submission. If this were to occur then the technique would drastically increase in popularity in the pharmaceutical industry. The research in this thesis has made a definite start towards this target.

6.2 Future Work

For the future there are many opportunities for VCD spectroscopy; application of the technique to new classes of compounds should continue and with further research VCD should become increasing popular. The accessibility of the nujol mull sampling technique should prove appealing due to the shear simplicity of the method and the reliability of the results, especially as it is a well recognised method within the field of infrared spectroscopy.

A library of both experimental and predicted VCD spectra, such as those available for other vibrational spectroscopy techniques, would prove extremely useful, and could make significant cuts in computer time and resources necessary to determine the absolute stereochemistry of a chiral compound. Comparison of spectra from compounds sharing similar structural backbones could become routine.

If the FDA were to accept VCD spectroscopy as a proof of absolute stereochemistry determination in the process of regulatory submission, then research in this area is bound to increase. VCD would also become a back-up for single crystal XRD absolute stereochemistry determinations, when the Flack parameter calculated gives inconclusive results. So when used in combination, the absolute stereochemistry for a compound containing solely light atoms could be easily proven.

For the future, investigation into more complex molecules with a larger number of chiral centres needs to take place. This was briefly touched upon with the study of (2*S*)-captopril, where the predicted spectra for the two possible enantiomers and two diastereoisomers were compared in order to see which chiral centres contributed to which bands in the VCD. As the number of chiral centres increases, the complexity of the interactions is bound to increase, and these effects are likely to cause some interesting anomalies. Use of the fragment calculation technique in these types of investigations will most likely prove extremely useful. However, because of the possible inversion of VCD bands without changing the absolute stereochemistry, addition of more chiral centres may make prediction of accurate VCD spectra virtually impossible or at least too computationally expensive to be worthwhile.

VCD may prove most useful as a quality control tool within the pharmaceutical industry. If the absolute stereochemistry of the compound is known and the VCD spectrum of a known proportion of one of the enantiomers has been obtained, then the proportion of (*R*) or (*S*) in an unknown sample can be determined. This procedure is very quick, as only an experimental VCD spectrum is required, and either a solution or nujol mull sample can be used.

Expansion of the field of VCD will continue, but probably with the focus on protein conformation rather than small molecule absolute stereochemistry determination. Drug development is also moving to larger more complex biotechnology molecules in the fight to combat an increasing number of diseases. With the complex nature of the VCD calculations routine analysis of small - medium sized chiral molecules is unlikely for all but a very specific subset. If in the future these predictions can be controlled to a higher degree the technique will become more desirable, as the experimental sampling methodology and spectrometers are there to support it.

6.3 References

1. T.B. Freedman, X.L. Cao, R.K. Dukor, and L.A. Nafie, *Absolute configuration determination of chiral molecules in the solution state using vibrational circular dichroism.* Chirality, 2003. **15**(9): p. 743-758.

Appendix I - Polymorph Screen

Polymorphism is an interesting phenomenon which occurs when a compound is able to adopt more than one crystal packing arrangement. This different crystal packing system can then have different space group and lattice parameters (unit cell) which lead to the compound in that polymorphic form having different physical properties to the compound in the other polymorphic form. The concept of polymorphism is an important one for the pharmaceutical industry, as if an active pharmaceutical ingredient can be in a variety of different polymorphs the solubility, density and melting point of the drug can change. This can then lead to possible differences in the activity and potency of the drug and it may be preferable for the pharmaceutical company to produce one polymorphic form in preference to the other. The two polymorphs of (2*S*)-captopril are distinguished by having different lattice parameters and melting points. The single crystal XRD data above proves that the polymorph studied is the high melting polymorph (Form I) and the lattice parameters obtained correspond to those given in the book. The second polymorph is low melting, and unfortunately the method for obtaining it was not described. Hence a polymorph screen was performed to try and obtain the second form of (2*S*)-captopril.

To try and obtain the Form II polymorph (low melting point) several techniques were employed. Slurries were prepared of ~200 mg (2*S*)-captopril in ~1 ml solvent; these were then left to stir at 50 °C for two days (section 1). It was hoped that the compound may convert from Form I to Form II under these conditions. A hot re-crystallisation from methanol was attempted in which the saturated solution was heated then stirred, then allowed to cool and crystals formed (section 2). An anti-solvent solvent method was then practiced initially with an addition of anti-solvent to (2*S*)-captopril in methanol, moving on to an addition of anti-solvent to (2*S*)-captopril in ethyl acetate (section 3). Here the (2*S*)-captopril is at a highly concentrated solution in the solvent (methanol, ethyl acetate) and addition of an anti-solvent (i.e. a solvent which (2*S*)-captopril is not very soluble in) is hoped to crash the (2*S*)-captopril out of solution. Crash cooling with anti-solvent addition was attempted with saturated solutions of (2*S*)-captopril in ethyl acetate (section

4), in which ethyl acetate was heated in order to dissolve as much (2*S*)-captopril in solution as possible. This hot solution was then added to anti-solvent on ice, with the hope that Form II may crystallise out. Another method attempted was crash cooling of a hot saturated solution of (2*S*)-captopril in ethyl acetate, through addition of liquid nitrogen. From these methods the crystals obtained were used to collect powder X-ray diffraction patterns PXRD, which were then compared with the two PXRD patterns given for Form I and Form II polymorphs. At the beginning of the polymorph screen the PXRD, DSC and thermo gravimetric analysis (TGA) were also collected for the two separate batches of (2*S*)-captopril obtained from Sigma Aldrich, in order to ensure the consistency of the results.

1 Slurry Results

Table 1 Slurries, stirred at 50 °C for two days

(2*S*)-Captopril, / mg	Solvent	Amount of solvent / ml	Result
200	Water	0.2	Form I
400	Methanol	1	Form I
330	Isopropyl alcohol	0.2	Form I
310	Ethyl acetate	0.4	Form I
220	Tetrahydrofuran	0.2	Form I
200	Toluene	0.3	Form I
200	Cyclohexane	0.2	Form I

No conversion of Form I to Form II was observed here, and also no hydrates were formed, as would be possible with the slurry in water.

2 Hot Re-crystallisations

Table 2 Hot re-crystallisation, heated solution whilst stirring, allowed to cool.

	Solvent	Results
(2*S*)-Captopril	Methanol	Amorphous, sticky
(2*S*)-Captopril	Ethyl acetate	Bottom of beaker, Form I, side of beaker, Form I

3 Anti-solvent Re-crystallisations

Table 3 Anti-solvent re-crystallisations, results from on the day and overnight

	Solvent	Anti-solvent	Results
(2*S*)-Captopril	Methanol		Crystals grown, Form I
(2*S*)-Captopril	Methanol	DCM	No crystals
(2*S*)-Captopril	Methanol	Isopropyl acetate	No crystals
(2*S*)-Captopril	Methanol	n - Heptane	Cloudy overnight, Form I
(2*S*)-Captopril	Methanol	Ethyl methyl ketone	No crystals
(2*S*)-Captopril	Ethyl acetate	DCM	No crystals
(2*S*)-Captopril	Ethyl acetate	Isopropyl acetate	No crystals
(2*S*)-Captopril	Ethyl acetate	n - Heptane	Crashed out, Form I
(2*S*)-Captopril	Ethyl acetate	Ethyl methyl ketone	No crystals
(2*S*)-Captopril	Ethyl acetate	Cyclohexane	Crashed out, Form I
(2*S*)-Captopril	Ethyl acetate	Toluene	No crystals
(2*S*)-Captopril	Ethyl acetate	THF	No crystals
(2*S*)-Captopril	Ethyl acetate	Acetonitrile	No crystals

4 Crash Cool Re-crystallisations

Here the (2*S*)-captopril was dissolved in the solvent, whilst being heated, then added to cold anti-solvent.

Table 4 Results of crash cooling with anti-solvents

(2*S*)-Captopril / mg	Solvent	Anti-solvent	Result
108	Ethyl acetate	n-Heptane	Form I
105	Ethyl acetate	Cyclohexane	Form I

Here a saturated solution of (2*S*)-captopril in ethyl acetate was prepared by filtering a slurry of (2*S*)-captopril in ethyl acetate and adding to cold antisolvent.

Table 5 Results of maximum concentrations of (2*S*)-captopril and crash cool

	Solvent	Anti-solvent	Result
(2*S*)-Captopril	Ethyl acetate	Cyclohexane	Form I
(2*S*)-Captopril	Ethyl acetate	n-Heptane	Amorphous

Here a solution was made up, heated and stirred, followed by addition of liquid nitrogen once the (2*S*)-captopril was fully dissolved.

Table 6 Crash cooling with $N_{2(lq)}$

(2*S*)-Captopril / mg	Solvent	Result
330	Ethyl acetate	Form I
300	Isopropyl acetate	Form I
200	DCM	Form I

These crash cools with liquid nitrogen resulted in a sticky amorphous substance being initially formed, which transformed, upon being scraped out of the container, into crystalline Form I.

5 Slow Evaporations

These solutions were made up to be left at AstraZeneca for slow evaporation at room temperature. The powder XRD were collected after six weeks.

Table 7 Slow evaporations left at AZ

(2*S*)-Captopril / mg	Solvent	Result
200	Methanol	Form I
200	n-Heptane / Methanol	Form I
200	THF	Form I
200	Isopropyl acetate	Form I

6 Conclusions of Polymorph Screen

The second polymorph, Form II, of (2*S*)-captopril has not been discovered in this polymorph screening, indicating that it is probably highly metastable and therefore difficult to prepare. This work is not aided by the fact that the initial report,[1] carrying the additional polymorph data, has no mention of how the Form II polymorph was formed. If anything this result illustrates the importance of presenting full experimental details, so that the work is reproducible.

References

1. H. Kadin, *Captopril*, in *Analytical Profiles of Drug Substances*, K. Florey, Editor. 1982, Academic Press.